PHOTO- AND RADIOCHROMIC TRANSFORMATIONS IN Al_2O_3:C,Mg FLUORESCENT NUCLEAR TRACK DETECTORS AND HIGH RESOLUTION IMAGING OF RADIATION FIELDS

By

GARRETT JEFFREY SYKORA

Bachelor of Science in Physics
Creighton University
Omaha, Nebraska
2004

Submitted to the Faculty of the
Graduate College of the
Oklahoma State University
in partial fulfillment of
the requirements for
the Degree of
DOCTOR OF PHILOSOPHY
May, 2010

PHOTO- AND RADIOCHROMIC

TRANSFORMATIONS IN Al_2O_3:C,Mg

FLUORESCENT NUCLEAR TRACK DETECTORS AND

HIGH RESOLUTION IMAGING OF RADIATION FIELDS

Dissertation Approved:

Dr. Mark Akselrod

Dissertation Adviser

Dr. Eric Benton

Dr. Eduardo Yukihara

Dr. Daniel Grischkowsky

Dr. A. Gordon Emslie

Dean of the Graduate College

ACKNOWLEDGEMENTS

First and foremost I would like to thank my advisor, Dr. Mark Akselrod. Dr. Akselrod's knowledge, guidance and friendship are responsible for transforming me from an eager student into a young, enthusiastic, scientist. Dr. Akselrod's passion for scientific discovery has provided the inspiration necessary to complete this doctoral program. Outside of the lab Dr. Akselrod has also been a great friend and mentor, I cannot thank him enough for sacrificing so much (including allowing me to live in his house for the last few months of my studies) for my development as a person.

I would like to thank everyone serving on my committee, Dr. Eric Benton, Dr. Eduardo Yukihara and Dr. Daniel Grischkowsky who all took a great deal of time out of their schedules to help my advancement and to carefully read my thesis.

I very much appreciate everyone at Landauer Inc. who has helped make my time at Landauer enjoyable and productive by providing friendship and technical assistance including Kent Dillin, Thomas H. Underwood and James Allen for their efforts in crystal growth and detector preparation, Dr. Vasiliy Fomenko for fruitful discussions, insights and sharing of his recent experiences, James Bartz for his help with performing spectroscopy experiments and Frances Pearce for hard work in assisting me in any way she could. Thank you especially to Dr. Craig Yoder for having the confidence in Dr. Akselrod and myself to allow and encourage us to pursue this project.

Much of this work has been enhanced by discussions with Dr. Eric Benton and Dr. Eduardo Yukihara, whose friendships and mentoring have proven to be invaluable. Dr. Benton performed several key irradiations as well as acted as a liaison for us to get other important irradiations. Dr. Yukihara allowed me to use his facilities at Venture I for several experiments and provided several irradiation opportunities.

I would like to express my gratitude to all those who collaborated with us on our endeavors especially those who performed irradiations including Dr. Mark Salasky of Landauer, Dr. Nakahiro Yasuda of HIMAC in Chiba, Japan as part of the National Institute of Radiological Sciences collaborative research program, Dr. Filip Vanhavere of SCK-CEN, Dr. Elke Brauer-Krisch of ESRF, Dr. Gabriel Sawakuchi of MD Anderson Cancer Center, Dr. Stephen Marino of RARAF, Dr. Marianne Aznar of Coppenhagen University Hospital and Ms. Sidsel Damkjaer of Risoe.

Thank you to everyone in the physics department at Oklahoma State especially Susan Cantrell and Cindi Raymond for all of their assistance, in particular for keeping my unique internship with Landauer and OSU organized.

I need to express my deepest gratitude to my friends and family. Thank you, mom and dad, for raising me to strive to be who I am today and all that I will become.

And finally, it is impossible to express how much my wife, Debbie, and daughter, Ciara, have meant to me over this period of time. Debbie was able to stay strong and patient, keeping me on track and giving me more love, support and encouragement than I could have ever hoped for even through pregnancy and starting the journey of motherhood. Ciara unknowingly kept me sane, just one look into her precious eyes made me realize how great life truly is.

TABLE OF CONTENTS

Chapter Page

Chapter Page

Chapter Page

Chapter Page

Chapter Page

Chapter Page

LIST OF TABLES

Table Page

Table Page

Table Page

LIST OF FIGURES

Figure Page

Figure Page

Figure Page

Figure Page

Figure Page

Figure Page

Figure Page

Figure Page

Figure Page

Figure Page

Figure Page

Figure Page

Figure Page

Figure Page

Figure Page

Figure Page

CHAPTER I

INTRODUCTION

The risks and rewards associated with ionizing radiation have become two of the most important scientific topics following the discovery of radioactivity by Becquerel in 1896. Ionizing radiation is defined as "any particle such as atomic and sub-atomic nuclei, electrons and neutrons as well as photons with sufficient energy (usually on the order of electron volts or higher for photons) to remove electrons bound to atoms" (Attix, 1986). Ionizing radiation poses severe health risks due to its ability to damage cellular structures including deoxyribonucleic acid (DNA). A double strand break of DNA occurs as a result of ionizing radiation depositing enough energy into the helical structure of the DNA to destroy bonds holding the strands together. The damage caused by the break is irreparable leading to an increased risk of developing cancer.

Nuclear power, medical diagnostics and space exploration are among studied applications needing radiation monitoring. Because applications using nuclear and atomic physics are becoming more popular, quantification of the damage caused by neutrons, photons, betas and heavy charged particles is paramount to protection of workers, bystanders and patients. Exposure to neutrons can be particularly dangerous because they can deposit a lot of energy at one time and in one location. With growing

uses of ionizing radiation, it becomes more important to ensure that individuals exposed to such conditions are safe.

Radiation dosimetry is the measurement and determination of quantities that are relevant to radiation interaction in matter. Absorbed dose is the primary quantity used to describe the amount of energy imparted to matter per unit mass, m and is defined as,

$$D = \frac{d\bar{\varepsilon}}{dm}. \qquad \text{(J/kg or Gy)} \qquad (1.1)$$

Most dosimeters are designed to directly or indirectly determine the absorbed dose in biological tissue.

1.1 Radiation detectors

A large number of detectors have been investigated for the purpose of radiation dosimetry. Every detector has its advantages as well as limitations and there has yet to be a perfect detector developed to encompass all radiation needs. Throughout years of development, radiation detectors have fallen into one of two categories, either active or passive. Active dosimeters provide the user with real time dose information and are self-sufficient, stand-alone devices. Active dosimeters involve intricate electronics to extract radiation information. The main advantage of an active dosimeter is immediate user feedback. Examples of active detectors include ionization chambers, proportional counters, scintillators and semiconductor detectors.

Passive detectors are exposed to radiation and then probed on a separate reader. The dose information builds up on the detectors and is stored until read. Some passive detectors will store the information indefinitely while others lose the information during

read out or over time. A few logistical advantages of passive dosimeters are that they are typically small, lightweight and easy to handle. Passive dosimeters can be made in bulk and readout on a single reader. The main disadvantage of passive dosimeters is the lack of real-time data. Examples of passive detectors include photographic nuclear emulsions, thermoluminescence detectors (TLDs), optically stimulated luminescence (OSL) detectors and solid state nuclear track detectors (SSNTDs) which include plastic nuclear track detectors (PNTDs) and fluorescent nuclear track detectors (FNTDs).

1.2 Neutron dosimetry

Significant damage occurs because of neutron interactions in biological systems. Neutrons can cause a great deal of damage because of their acute nature of energy deposition. The quality factor and radiation weighting factors (quantities used to assess biological risks)[1] for neutrons can range from 5 to 20 depending on the neutron energy (ICRP 60) which is excessively large in comparison with photons whose quality and radiation weighting factors are 1. It is therefore important to know the dose due to neutron exposure. Some of the most common areas of neutron exposure are as follows: nuclear power stations (~60 keV neutrons), particle accelerators that can produce a broad range of neutron energies, space environments (~1-200 MeV neutrons) (Benton et al, 2001), medical treatment facilities (broad spectrum neutrons) and also in battlefield scenarios where there may be large neutron fluences from nuclear weapons (~1 MeV).

Neutron dosimetry is one of the most challenging fields of radiation protection because of the nature of neutron physics. Neutrons are neutral particles and thus do not

[1] Quality factor and the radiation weighting factor are discussed in chapter 2.

directly ionize matter. Energy deposition from neutron irradiation occurs through collisions with target nuclei and nuclear reactions involving the capture of an incident neutron and release of several daughter products. Neutron detectors are designed to measure the ionization produced from reaction products like recoil and daughter nuclei as well as gamma photons produced from nuclear reactions. Because of this, neutron detectors are constructed with materials that have large neutron interaction cross-sections.

It has been common practice in neutron dosimetry to use hydrogen-containing material as both a converter and moderator of fast neutrons. Hydrogen nuclei (protons) and neutrons have similar masses thus making *n-p* scattering more efficient than with heavier nuclei. Most fast neutron interactions occur through elastic *n-p* scattering thus hydrogen-containing polyethylene (PE) is commonly used for fast neutron detection. Recoil protons ionize the sensitive volume of the detector creating measurable signal.

Nuclear reactions are the dominant mode of interaction in matter as the energy of incident neutrons decreases. Converters that contain elements with high neutron capture cross-sections such as ^{3}He, ^{6}Li and ^{10}B are often used.

Passive detectors, mainly PNTDs, bubble detectors and ^{6}Li-based TLDs, are commonly used for personal dosimetry and legal dose of record. Active detectors such as ^{3}He proportional counters, Bonner spheres, BF_3 gas filled tubes and recoil proton telescopes are used as neutron detectors for spectrometry. Semiconductor detectors are often used for immediate personnel monitoring. Detailed discussions of the detectors listed above can be found in the textbooks of Knoll (2000) and Attix (1986).

All of the current neutron detectors have advantages and disadvantages. Some detectors are sensitive to gamma radiation that is present in all neutron fields and most

are dependent on the energy of the incident neutrons. Some neutron detectors yield detailed results such as full neutron energy spectra, but are complex and expensive to use (Bonner spheres and proportional counters for instance), while others are simple and inexpensive but do not have the functionality like spectrometry. PNTDs require chemical etching processes, bubble detectors are good for low dose measurements, but have very low saturation doses and TLDs are erased during readout. In light of these considerations, a new type of neutron dosimeter that is better than existing ones is needed. FNTDs are investigated in this work as a next-generation passive neutron dosimeter offering attractive features discussed in this thesis.

1.3 Plastic nuclear track detectors

The use of SSNTDs has been well established in personal neutron dosimetry by quantifying the result of secondary charged particle interactions in the dielectric material. Interaction of ionizing particles in SSNTDs occurs mainly through the Coulomb interaction. Heavy charged particles damage the molecules comprising the material along their trajectory (latent ion tracks). PNTDs undergo chemical, or electro-chemical, etching procedures to break down the surface of the dielectric. Damage caused by ionizing particles acts like a catalyst in the etching procedure causing the area of ion propagation to etch faster. The result of etching is a surface with pits that are visible using conventional microscopy. These visible pits are the tracks in the material. The original size of a pre-etched track is considered a few tens of nanometers in diameter depending on the ion's charge and energy. The size of the track after etching can range

from a few micrometers to several tens of micrometers depending on the etching conditions and relative energy loss of the ions. Figure 1.1 shows a microscope image of a post-etched PNTD after irradiation with 2 MeV protons.

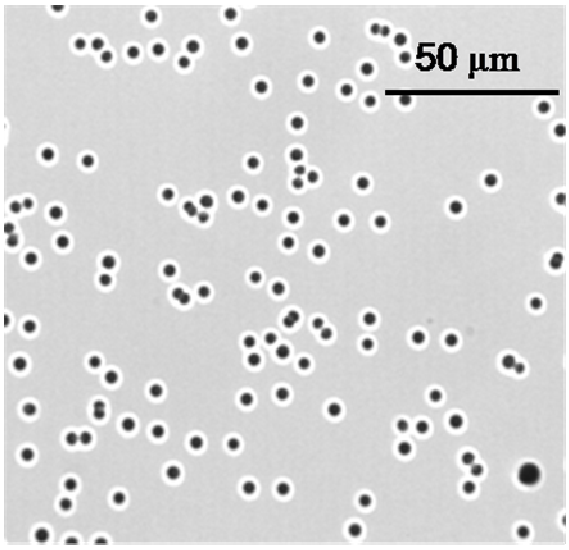

Figure 1.1 Image of etched tracks caused by 2 MeV protons in a CR-39 plastic nuclear track detector (courtesy of Mark Salasky at Landauer Inc.)

PNTDs have a damage threshold that leads to a lower limit of unrestricted linear energy transfer (LET_∞) detection. LET_∞ is the average amount of energy deposited in the material per unit length (in units of keV/μm). If the incident particle does not cause enough damage in the material, then there will be no difference in etching rate from the bulk material to the track. PNTDs are insensitive to lightly ionizing particles like secondary electrons caused by gamma ray interaction. Only in extreme cases when the dose of gamma or x-ray is large enough such that thousands of secondary electrons overlap to cause a large amount of damage in the bulk of the material do PNTDs register features after etching.

In terms of LET, the most sensitive PNTDs are made of plastics, most commonly polyallyldiglycolcarbonate (PADC or CR-39) and are able to register heavy ions with

LET in water ≥ 5 keV/μm (Benton et al, 1986), or the equivalent of protons with energy of several MeV. PNTDs can register tracks caused by elastically scattered protons from *n-p* interactions and tracks caused by nuclear reaction products from thermal neutron interaction with other nuclei in the plastic making PNTDs attractive for neutron dosimetry. Insensitivity to secondary electrons is also a great advantage when it comes to neutron dosimetry because the struggle to separate the always-present gamma contribution from the neutron signal is completely avoided.

Another beneficial application for PNTDs is heavy charged particle spectroscopy. It was found that the ratio of the track etch rate to the bulk etch rate ($V = V_t/V_b$) is dependent on the LET of the incident charged particles (Benton et al., 1986) making PNTDs good candidates for LET spectroscopy.

PNTDs have a broad set of applications that are made possible by their low cost, small size, simple read out device and the experience that many researchers have gained. Another appealing characteristic of PNTDs is their insensitivity to low LET particles. Insensitivity may also be construed as a disadvantage in terms of LET spectroscopy because of the inability to detect high energy protons. A disadvantage of PNTDs is the chemical etching requirement.

1.4 Fluorescent nuclear track detectors

Fluorescent nuclear track detectors (FNTDs) were originally developed as a passive detector to circumvent some of the shortcoming of common track detectors (PNTDs, bubble detectors, etc.). FNTDs began with optically stimulated luminescence (OSL)

technology and evolved through a seemingly unrelated application of Aluminum Oxide (Al_2O_3) crystals (Akselrod et al, 1998). The original idea of using Al_2O_3 as a radiation dosimeter was to measure optically or thermally stimulated luminescence resulting from the trapping of electrons generated by ionizing radiation. The useful trapping occurs in pre-engineered F (neutral oxygen vacancies with two electrons) and F^+ (a positively charged oxygen vacancy with only one electron) color centers due to a carbon dopant in the crystals. This radiation sensitive material served as the basis for a new material with similar optical properties. The addition of a second dopant, magnesium, created new lattice defects and thus new color centers (Akselrod et al., 2003c).

The motivation behind adding magnesium to Al_2O_3:C was to create a crystal with fast luminescence centers (~ns lifetimes), rather than slow (~35 ms lifetime) F centers, suitable for optical data storage. The material was first developed and tested as a holographic data storage medium (Akselrod et al., 2003b) and later was realized as a more novel volumetric fluorescence data storage medium (Akselrod et al., 2003a, 2003c and 2004).

It was suggested to try to image the result of irradiation with alpha particles in the same optical data storage material using the same readout method. Initial success of imaging tracks caused by alpha particle penetration stimulated the development of this new Al_2O_3:C,Mg material as a viable radiation dosimeter.

There were two ideas for the application of Al_2O_3:C,Mg to radiation dosimetry. One was the replacement of CR-39 PNTDs as a possible neutron dosimeter and the second as a heavy charged particle spectrometer. Initial work and testing to these ends began as early as 2004 (Akselrod et al., 2006). Irradiations were performed at the Landauer

irradiation facility in Glenwood, IL and at the Heavy Ion Medical Accelerator in Chiba (HIMAC), Japan. The detectors were imaged on the same test stand that was used for optical data storage technology. Promising and interesting results were achieved with these irradiations. The results showed that this newly engineered material has the ability to be a nuclear track detector for the purpose of radiation dosimetry. Figure 1.2 is an image of neutron induced recoil proton tracks in an FNTD.

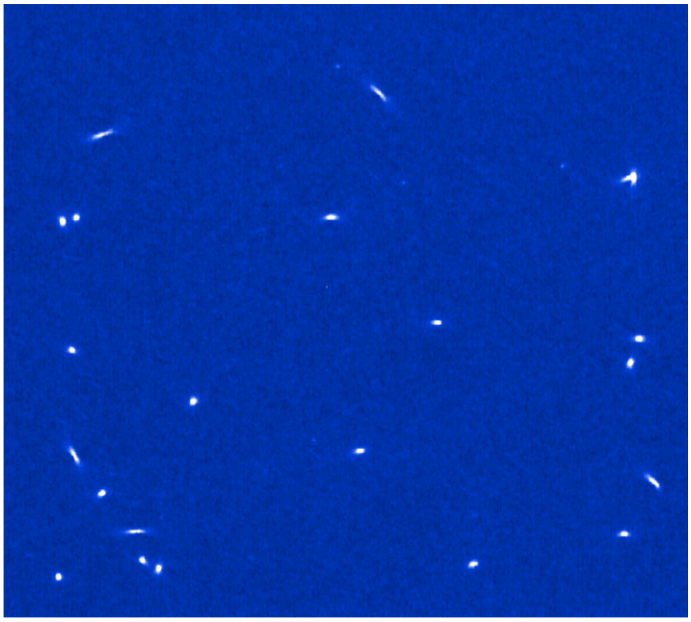

Figure 1.2 100x100 μm^2 Image of recoil proton tracks created in Al_2O_3:C,Mg after irradiation with neutrons.

This work is a continuation of the investigation of FNTDs as viable radiation detectors with multiple applications focusing on neutron dosimetry. A portion of our work was devoted to exploring as many applications of FNTD technology as possible because it is brand new and has never been investigated in detail. Therefore this investigation also included heavy charged particle spectroscopy, gamma, x-ray and beta dosimetry, applications in radiotherapy, microbeam imaging and microdosimetry.

1.5 Dissertation structure

The main goal of this dissertation research was to develop a unique radiation detection system that is useful for both dosimetric measurements as well as scientific investigations with the primary focus on neutron dosimetry. A complete investigation of material physics (optical properties), radiation interaction in the sensitive volume, dose and energy response to different types of radiation and different applications of FNTDs was necessary to develop them as reliable radiation detectors. This dissertation is intended to demonstrate necessary progress in all facets of FNTD technology including basic materials research, instrumentation development, characterization of the FNTD in multiple radiation fields and novel developments in FNTD processing. Even though many applications of this new technology are investigated here, the primary focus was developing FNTD technology for neutron dosimetry and as such the majority of the discussion will revolve around neutron dosimetry.

This work is structured to give the reader an initial review of the background and theory necessary to supplement the results detailed in subsequent chapters. The second chapter discusses luminescence theory, optical properties of Al_2O_3 and Al_2O_3:C,Mg, quantities pertinent to radiation interaction in matter that were not discussed earlier in this chapter as well as track structure theory and the initial results achieved by our group before I was involved in the research.

The remaining chapters detail only the work in which I was directly involved. The goal of chapter three is to present a general understanding of the physical mechanisms in Al_2O_3:C,Mg during and after exposure to ionizing radiation for the purpose of improving the material for future use. Chapter three presents results on the physics of Al_2O_3:C,Mg

obtained using spectroscopic methods. Results include thermal aggregation, photoconversion of defects, designation of excitation/emission bands to color centers and kinetics of charge transfer during irradiation as well as suggestions for further studies.

The fourth chapter discusses original experimental methods developed for FNTD imaging, image analysis and material processing for improved dosimetric capabilities. The scope of this research required a new FNTD reader to be built for faster scanning and better versatility. The first part of the chapter details the design and construction of this new reader. The second part outlines novel image processing methods used to quantify radiation interactions in FNTDs. One of my most important contributions to FNTD technology was a solution to the problem of neutron-gamma separation which was the development of a new image processing routine to determine high doses of radiation. This new processing method is discussed in chapter four.

The fifth and sixth chapters discuss investigation of FNTDs as radiation detectors. Chapter five discusses the primary focus of the research which was the development of FNTDs as a dosimeter for mixed neutron-photon fields. Results from over 100 irradiations, including thousands of FNTDs, are summarized and presented including results from blind comparisons with other dosimeters. Chapter five also discusses the novel method for neutron-gamma separation using FNTD technology.

Chapter six is a survey of all applications of FNTD technology that were investigated throughout the course of this work. Heavy charged particle spectroscopy, QA in proton therapy, beta dosimetry, x-ray microbeam diagnostics, neutron microbeam imaging and microdosimetry were all investigated as a part of this research. The final chapter summarizes and incorporates all of the major conclusions of this dissertation research.

CHAPTER II

BACKGROUND THEORY AND APPLICATIONS

Tracks appear in FNTDs as a result of ionization of the Al_2O_3:C,Mg lattice. Ionizing radiation deposits energy through statistical interaction processes with individual atoms. The amount of energy transferred per interaction is also statistical. Electrons released from their orbits (ionization) resulting in an electron-hole pair. Electrons and holes can have sufficient energy to travel long distances in matter while most travel only short distances (~100 nm, see section 2.5 below). Ionized electrons are secondary delta electrons that also deposit energy and cause ionizations. Eventually, electrons and holes will lose enough energy to be captured by defects leaving them with a different charge relative to the original crystal lattice. Electron and hole trapping resulting in a defect with different optical properties is called radiochromic transformation of defects. Charged particles induce radiochromic transformations of defects in the crystalline material creating specific luminescent centers that can be imaged in fluorescent contrast.

This chapter discusses theories and background relevant for understanding the processes described above. Luminescence theory, a review of the luminescence of Al_2O_3 (pure crystal and neutron irradiated) and some of the original optical studies on Mg doped Al_2O_3 are discussed because the luminescence mechanisms are paramount for proper understanding of radiochromic transformations and the readout method. Common

quantities needed for radiation detection, the theory of charged particle interaction in matter including a brief overview of track structure theory and microdosimetry are discussed to provide the reader with a basic idea of radiation interaction in matter and how tracks are formed in Al_2O_3:C,Mg. The chapter will conclude with a review of Al_2O_3:C,Mg used as a track detector before my research began.

2.1 Luminescence

Luminescent radiation detectors such as scintillators, thermally stimulated luminescence detectors (TLD) and optically stimulated luminescence (OSL) detectors are based on the emission and collection of photons from the detector material. Some materials efficiently emit photons during irradiation; this phenomenon is called scintillation or radioluminescence (RL). RL occurs when electrons and holes produced during ionization subsequently recombine on a luminescent center followed by radiative relaxation (Fig. 2.1). In the thermoluminescence (TL) and OSL processes, electrons or holes trapped in defects for long periods of time (storage) can be released into the conduction band by stimulating the material with heat (TL) or light (OSL). Carriers of opposite charge are trapped in recombination centers (also called luminescence centers) which emit photons during recombination (Fig. 2.1) (Boetter-Jensen et al., 2003).

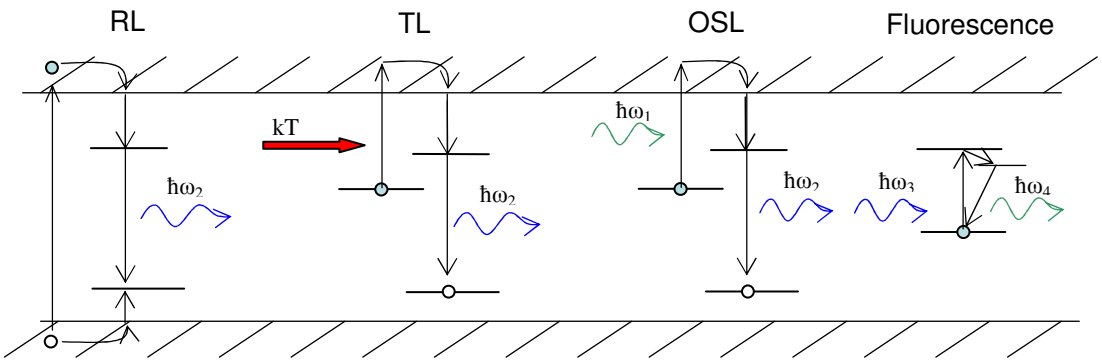

Figure 2.1 Flat band diagram of RL, OSL, TL and fluorescence processes. OSL can emit photons of higher energy while fluorescence emission generally has a Stoke's shift to lower energies.

In the case of FNTDs, trapped electrons are not released from trapping sites, but are stimulated to an excited state with light. The luminescence center is not photo-ionized during stimulation and the electron radiatively relaxes to its ground state emitting a photon (Fig. 2.1). This process is called intra-center luminescence, or fluorescence. The remainder of this section will deal only with fluorescence mechanisms directly related to FNTD technology.

2.1.1 Absorption

Figure 2.2 depicts light absorption in matter. As the absorbing layer thickness, $\Delta x \rightarrow 0$, the amount of change in light intensity, $\Delta I/\Delta x$ is proportional to the light intensity,

$$\frac{dI(x,h\nu)}{dx} = -\alpha(h\nu)I(x,h\nu) \tag{2.1}$$

where $\alpha(h\nu)$ is the energy dependent absorption coefficient. The intensity at any point in the material is then given by

$$I(x,\nu) = I_0(h\nu)\exp[-\alpha(h\nu)x], \tag{2.2}$$

which is known as the Lambert-Beer law. The absorption coefficient, α, is related to the number of absorbing elements, N_{Abs}, in the material and the absorption cross-section, σ_{Abs}, by

$$\int \alpha(h\nu) d\nu = N_{Abs}\sigma_{Abs} \ . \tag{2.3}$$

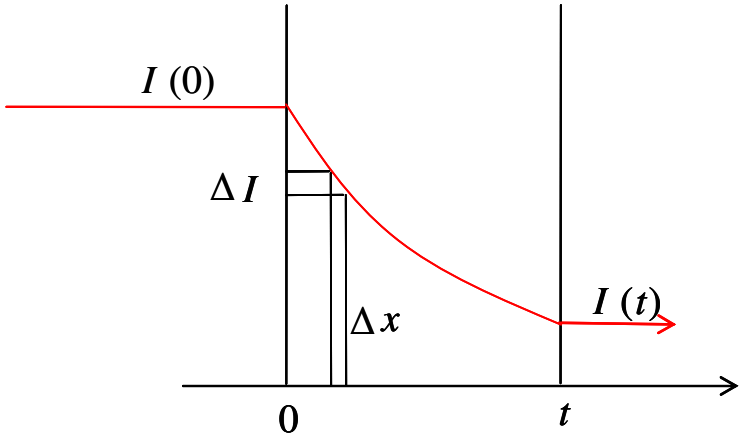

Figure 2.2 Schematic of light absorption in matter

Smakula's relation is used to estimate the color center concentration, N_{abs}, and is

$$N_{Abs} f_{abs} = A\alpha(h\nu_0)\Delta\nu \tag{2.4}$$

where $f_{Abs,}$ is the oscillator strength of the transition, $\Delta\nu$ is the full-width at half maximum (FWHM) of the absorption spectrum centered at $h\nu_0$ in electron volts (eV). A is a constant that depends on the line shape of the absorption spectrum and is 0.87×10^{17} for a Gaussian shape and 1.29×10^{17} for a Lorentzian shape (Vij, 1998). Absorption can occur with and without emission of light, therefore absorption and excitation spectra of various media may be different. Absorption of light occurring without emission results from non-radiative relaxation (i.e. energy loss via phonons or intersystem crossing via tunneling).

2.1.2 Emission

The intensity of light emission is given by

$$I_{em}(\nu) = I_0(\nu) \cdot q \cdot \left(1 - 10^{-\alpha(\nu)l}\right) \tag{2.5}$$

where l is the thickness of the medium and q is the quantum efficiency. The quantum efficiency describes the contribution of nonradiative decay processes and is defined as

$$q = \frac{Number\ of\ \ photons\ emitted}{Number\ of\ \ photons\ absorbed} \ . \tag{2.6}$$

Absorption and emission are commonly seen as transitions to another energy level in electric or magnetic dipoles. Dipole transitions range from allowed to strictly forbidden based on quantum mechanical selection rules for transitions (Henderson and Imbusch, 1989). The lifetime of emission, or the transition rate, is a measure of the probability of the transition to occur. Transition rates on the order of 1ns are generally associated with allowed electric dipole transitions while rates on the order of ms to seconds are associated with forbidden transitions.

The harmonic oscillator is the basic model for the mechanism of luminescence and agrees with the dipole approximation (Stepanov and Gribkovski, 1968). In this model, the energy levels are parabolic in shape, which also agrees with the Born-Oppenheimer approximation and, in its simplest form, uses the configurational coordinate diagram (Fig. 2.3) to explain excitation and emission band shapes in solids (Henderson and Imbusch, 1989).

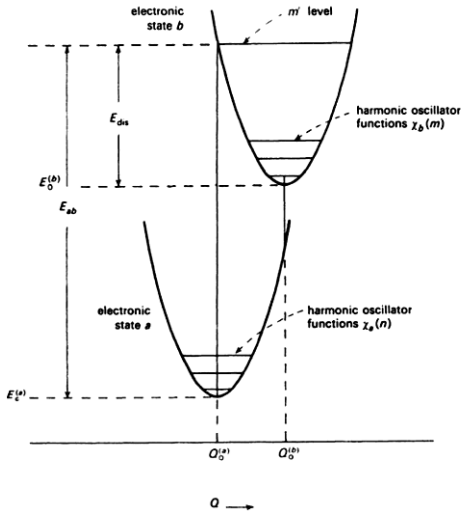

Figure 2.3 Configurational coordinate diagram (Henderson and Imbusch, 1989). The peak position (in energy) is E_{ab}, or the difference in energy between the bottom of the ground state to the point where the vertical line meets the excited state parabola.

2.1.3 Luminescence of F-type centers

Crystal lattices may contain defects consisting of empty lattice sites called vacancies that are charged with respect to the rest of the lattice. These vacancies create traps for electrons or holes depending on whether the anion or cation is vacant. In Al_2O_3, a vacant anion site with two trapped electrons is an F-center and the same vacancy with one electron is an F^+-center. F-type centers have been studied in great detail in alkali halide crystals (Fowler, 1968) and in alkaline earth oxides (Henderson and Imbusch, 1989). In certain cases (thermodynamically or through irradiation), F-type centers will aggregate to next-nearest-neighbors (NNN) creating F_2-type centers (Fig. 2.4).

F-centers are most simply modeled as a particle in a box with the electron trapped by the surrounding lattice structure, but a more realistic model of the F-center is an electron in a finite potential well. A semi-continuum model is also used to describe F-type centers (Huang and Rhys, 1950). The semi-continuum models describe F-type centers as modified hydrogen atoms leading to photonic absorption similar to a 1s→2p transition.

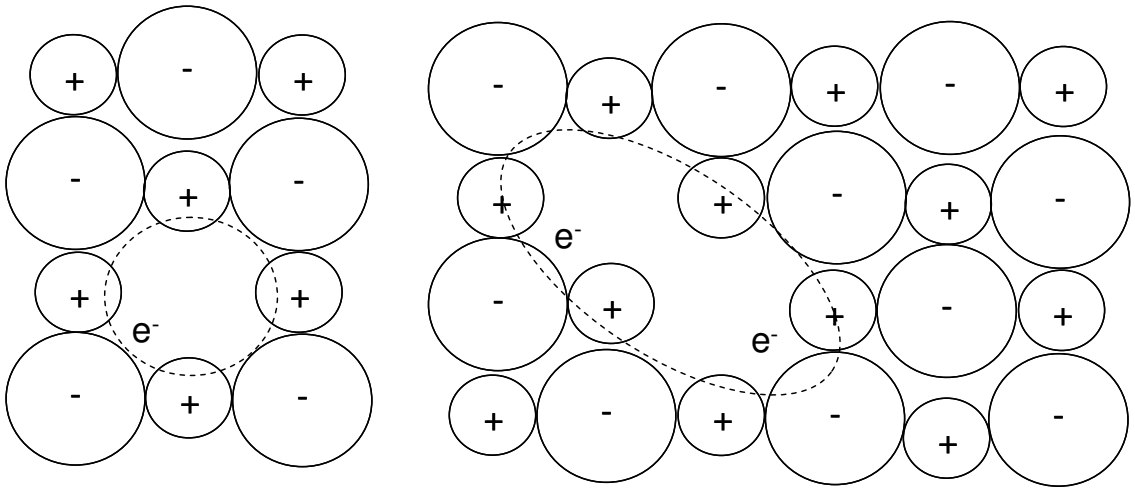

Figure 2.4 Drawing of a single oxygen vacancy - F-center (left) and two nearest neighbor F-centers aggregate F_2-center (right) in an alkali halide crystal (adapted from Henderson and Imbusch, 1989).

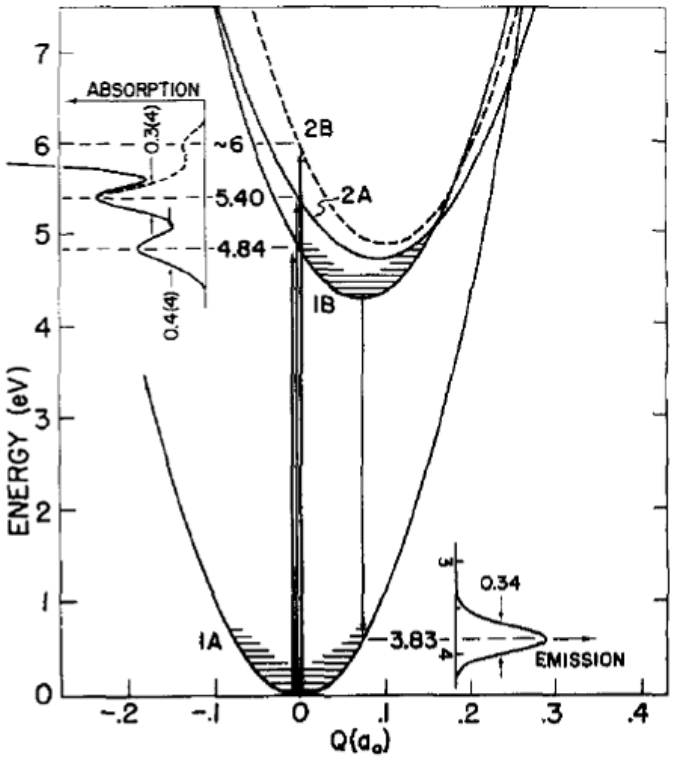

Figure 2.5 Congifurational coordinate diagram of F^+ defects in Al_2O_3 crystals illustrating luminescence mechanisms and electron-phonon interactions (Evans et al, 1995)

Combining the simple models described above with electron-phonon interaction provides a good model of absorption and emission spectra. Electron-phonon interactions account for broad absorption and emission bands in F-type centers (Huang and Rhys, 1950). The electron-phonon interaction characterizes a number of different quantities in the absorption and emission spectra including the displacement energy, E_{dis} (shown in Fig. 2.3), the zero-temperature Franck-Condon factor, $F_m(0)$ which in turn determines the shape of the absorption and emission bands. The displacement energy was found to be

$$E_{dis} = S\hbar\omega_{vib} \tag{2.7}$$

where S is the Huang-Rhys factor and ω_{vib} is the vibrational frequency of the lattice. At T = 0 K, the absorption band shape function of the a→b (m^{th} vibrational state of b) transition is given by (Henderson and Imbusch, 1989)

$$I_{abs}(E) = I_0 \sum_m F_m(0)\delta(E_{bm} - m\hbar\omega - E) = I_0 \sum_m \frac{\exp(-S)S^m}{m!}\delta(E_{bm} - m\hbar\omega - E). \tag{2.8}$$

Likewise, the emission band shape function of the b→a (n^{th} vibrational state of a) transition is given by

$$I_{emi}(E) = I_0 \sum_n \frac{\exp(-S)S^n}{n!}\delta(E_{bm} - n\hbar\omega - E). \tag{2.9}$$

The temperature dependence of the absorption and emission bands can be used to find ω_{vib} and subsequently S. The width of the luminescence band, $W(T)$ is related to ω_{vib} by

$$W^2(T) = W^2(0)\coth\left(\hbar\overline{\omega}_{vib} / 2kT\right) \tag{2.10}$$

and the Huang-Rhys factor, S is determined by

$$S = \frac{\left\langle E^2 \right\rangle}{(\hbar\overline{\omega}_{vib})^2} \tag{2.11}$$

where $<E^2>$ is the second moment of the band. At small values of *S*, vibronic structure can be seen in the absorption and emission bands and at large values of *S*, only smooth bands are observed (i.e. no zero-phonon lines). For single vacancy F-centers in α-Al_2O_3, *S* is large enough to make any zero-phonon lines unobservable (Huang and Rhys, 1950) which was verified by Evans and Stapelbroek (1978) and Brewer et al. (1980). For divacancies, or aggregate centers, *S* should be small enough to distinguish zero phonon lines in absorption and emission spectra (Henderson and Imbusch, 1989).

2.2 Optical properties of F-type centers in Al_2O_3

Al_2O_3 has been investigated for many years for several applications including gain media for lasers (Tippins, 1970), windows in nuclear reactors (Wilks et al, 1967) and in radiation dosimetry (Akselrod et al, 1990). The most comprehensive investigation of the optical properties of Al_2O_3 has been done by Bruce Evans and his collaborators. The majority of work with Al_2O_3 has been performed on crystals with radiation induced defects from neutrons, electrons, protons or gamma photons[2].

2.2.1 Identification of F-type centers

Figure 2.6 is the optical absorption, emission and excitation spectra obtained by Evans et al (1978) for α-Al_2O_3 as-grown (unirradiated) and after irradiation with 3.9×10^{16} neutrons/cm^2. When the polarization of incident light was perpendicular to the optical axis ($\vec{E} \perp \vec{c}$), there were clearly three absorption bands above 4 eV. Electron spin

[2] Chapter 3 of this thesis compares results obtained from neutron irradiated Al_2O_3 crystals to new Al_2O_3:C,Mg.

resonance (ESR) was used to determine the presence of an electron trapped in an anion vacancy (F^+-center) (La et al., 1973). The same group of La, Bartram and Cox (1973) calculated the wave functions, energies and anisotropy for the F^+ center. Anisotropic measurements were performed by Evans and Stapelbroek (1978) and matched to the calculations. These along with excitation-emission measurements and irradiation results led to the identification of the 4.8 eV, 5.4 eV and 6.3 eV absorption bands to F^+ centers. Lee and Crawford (1978) attributed the 6 eV absorption band to F-centers by virtue of photoconversion of the 6 eV band into the 4.8 and 5.4 eV bands by stimulating with 6 eV light and the reverse process was observed by stimulating with 4.1 eV.

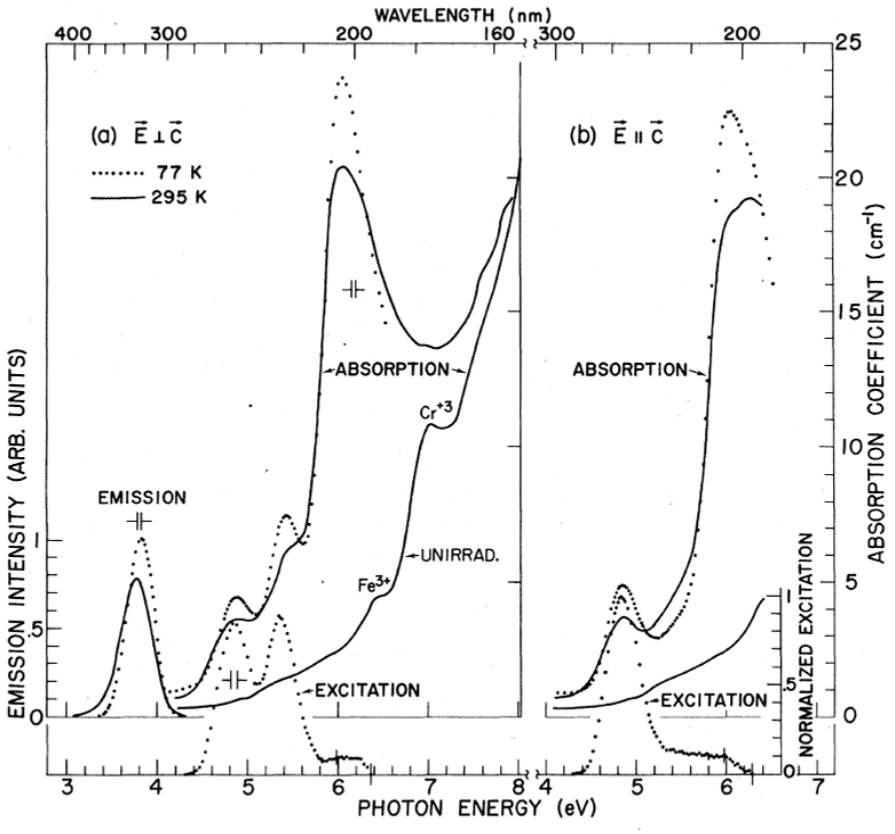

Figure 2.6 Absorption, excitation and emission spectra in the ultra-violet to visible photon energies for neutron irradiated Al_2O_3 crystals (Evans and Stapelbroek, 1978)

Lower energy absorption bands were also observed in neutron irradiated Al_2O_3 crystals. Attempts to study and identify lower energy bands were undertaken by Welch et al. (1980) Martynovich et al. (1985), Springis and Valbis (1985) and Pogatshnik et al. (1987). These lower energy defects were assigned to aggregate oxygen vacancy defects, i.e. F and/or F^+ centers as next nearest neighbors. Table 2.1 is a list of defects that were assigned to optical absorption and excitation emission bands by the above authors.

Table 2.1 Assignment and optical properties of absorption/emission bands in neutron irradiated Al_2O_3 (Evans, 1995)

Color center	Excitation, eV	Emission, eV	Lifetime
F	6.1	3.0	35 ms
F^+ (1A→1B)	4.8	3.8	< 7 ns
F^+ (1A→2A)	5.4	3.8	< 7 ns
F^+ (1A→2B)	6.0	3.8	< 7 ns
F_2	4.1	2.4	
F_2	4.8	3.85	
F_2^+	3.5	3.26	
F_2^{2+}	2.7	2.2	

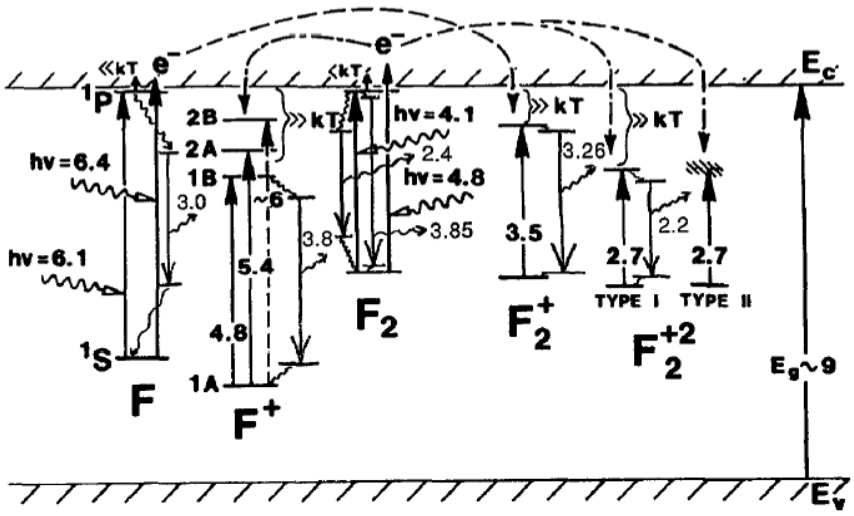

Figure 2.7 Flat band diagram of F-type centers in Al_2O_3 depicting excitation and emission of the assigned defects (Evans et al, 1978)

Evidence for their assignments was based on thermal annealing experiments, presence of zero-phonon lines, anisotropy measurements and similarities with MgO crystals. Theory predicts the presence of zero-phonon lines for aggregate anion vacancies, but not for single vacancies (Henderson and Imbusch, 1989). Figure 2.7 is a diagram of energy levels of defects in Al_2O_3 in the band gap. Pogatshnik et al. (1987) reported that another group, Baryshnikov and Martynovich, showed evidence that the 2.7 eV absorption band should be associated with a negatively charged defect as opposed to the currently assigned F_2^{2+} center.

Assignment of defects needs verification as there is little physical evidence and some discrepancy among researchers. Crystals develop higher order defects (aggregates) as well as a number of other undesirable defects such as interstitial ions and dislocations during irradiation with large fluences of neutrons or charged particles. Further evidence of the nature of these optically active centers includes photoconversion of defects by optically bleaching and also radiation induced conversion of defects. ESR studies on centers with unpaired electrons would provide further evidence, but ESR is beyond the scope of this study.

2.3 Properties of Mg doped Al_2O_3

The motivation behind adding magnesium to Al_2O_3:C was to create a crystal with fast luminescence centers (~ns lifetimes), rather than slow (~35 ms lifetime) F centers, suitable for optical data storage. The material was first developed and tested as a holographic data storage medium (Akselrod et al, 2003b) and later was realized as a more

novel volumetric fluorescence data storage medium (Akselrod et al, 2003a, 2003c and 2004).

Adding Mg to the melt during crystal growth in a highly reducing atmosphere stimulated the production oxygen vacancies (F and F^+ centers). In addition to F and F^+ color centers, Al_2O_3:C,Mg contains a large number of aggregate F_2^{2+}(2Mg) defects - two oxygen vacancies that are charge compensated by two Mg^{2+} ions containing two electrons - and a relatively small number of F_2^+(2Mg) defects containing three electrons. Figure 2.8 shows the structure of the F_2^{2+}(2Mg) defect (Akselrod et al., 2003a). Optical absorption and excitation-emission studies led to this model. The optical absorption bands related to the aggregate centers are highly anisotropic. Anisotropy of the absorption bands is due to the angle between the transition dipole moment (defect axis) and the optical *c*-axis, θ, and the anisotropy ratio, A, is related to θ by

$$A = 2\cot^2\theta. \tag{2.12}$$

Sanyal et al (2005) found A=2.97 for the 435 nm absorption band leading to θ=39.4° which is close to the next-nearest neighbor oxygen divacancy pair of 33° (Mitchell et al, 1960). The difference in angle can be attributed to presence of Mg^{2+} ions. Excitation-emission spectra demonstrated that these aggregate centers have an absorption band centered at 435 nm with an emission band centered at 520 nm (fig. 2.9); the 520 nm fluorescence has a lifetime of 9 ± 3 ns (Sanyal et al., 2005).

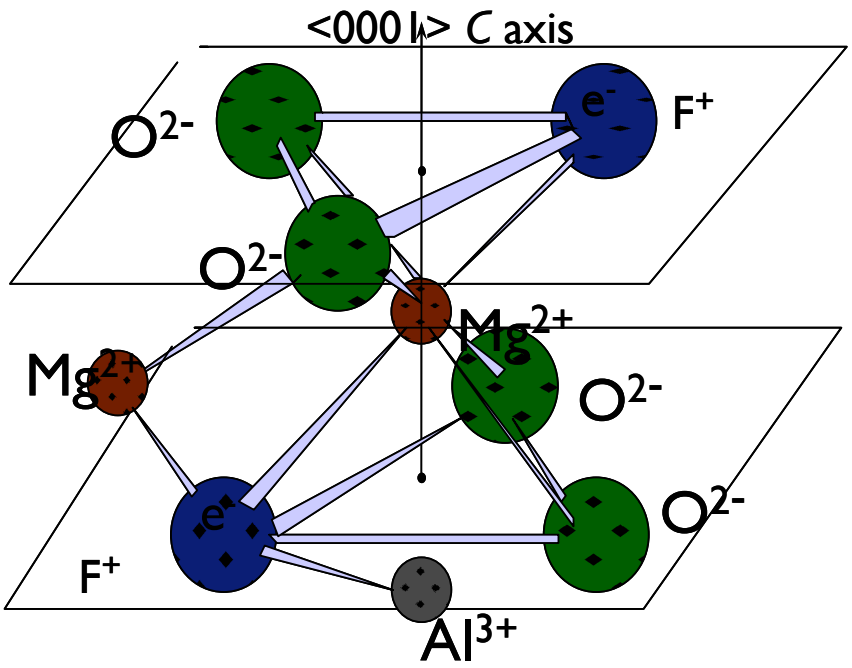

Figure 2.8 Model of the F_2^{2+}(2Mg) defect structure with two oxygen vacancies charge compensated by two Mg^{2+} ions (Akselrod et al, 2003).

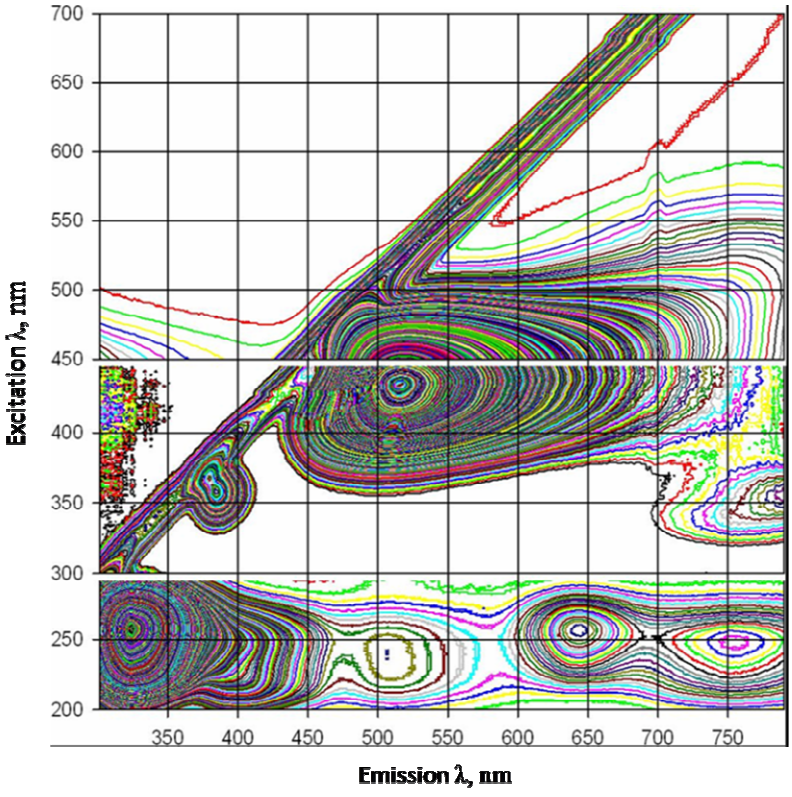

Figure 2.9 Excitation-emission spectrum of a thermally enhanced Al_2O_3:C,Mg crystal (Sanyal et al, 2005).

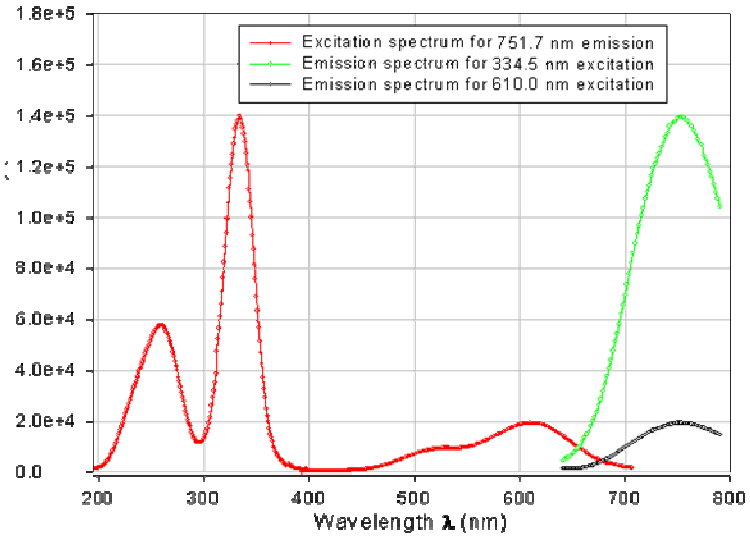

Figure 2.10 Excitation and emission spectra of the F_2^+ (2Mg) center showing three excitation bands at 255 nm, 335 nm and 620 nm and one emission band at 750 nm (Akselrod et al, 2003).

Optical absorption and excitation-emission studies have shown that the F_2^+(2Mg) centers have absorption bands centered at 260 nm, 335 nm and 620 nm (Fig. 2.10). When the color center is stimulated with one of these three wavelengths, one of the three electrons is promoted to a higher energy state. The electron then undergoes a non-radiative, phonon assisted, relaxation and radiative transition to its ground state through the emission of a 750 nm photon with a lifetime of 75 ± 5 ns. The energy of a 620 nm photon (2 eV) is sufficient to excite the three electron color center without photoionization thus allowing for multiple nondestructive readouts.

Thermal stability tests of the F_2^+(2Mg) were also performed on Al_2O_3:C,Mg (Akselrod et al., 2006b). The 750 nm fluorescence was stimulated by 635 nm laser light and the fluorescence intensity was measured after step annealing of the crystal. These tests showed that the fluorescence did not begin to fade until an annealing temperature of 580°C was reached. Optical absorption measurements showed that all F_2^+(2Mg) traps

were emptied and reverted to F_2^{2+}(2Mg) color centers at 680°C. These results show that F_2^{+}(2Mg) color centers are stable to high temperatures, but can also be thermally annealed to their original condition.

The group of Ramirez and Tardio have also been investigating Mg doped Al_2O_3 (Tardio et al, 2003, Ramirez et al, 2005 and Ramirez et al, 2007). Al_2O_3:Mg crystals studied by this group were grown in an oxidizing atmosphere with flowing N_2 gas which is a different growth process than the one used to produce Al_2O_3:C,Mg. Exact crystal growth conditions and their consequences are beyond the scope of this paper; it is recommended to consult the above references for more details. It is, however, important to compare optical properties of Al_2O_3:Mg from the works of Ramirez and co-workers to Al_2O_3:C,Mg from the works of Akselrod and co-workers and to the results presented in chapter 3.

Ramirez et al assumes the presence of Mg in all absorption and emission, so bands are labeled without explicitly specifying the Mg perturbation. They identify an intense absorption/emission band at 435/520 nm as F_2^{2+} centers perturbed by Mg^{2+} ions, which are called simply F_2^{2+} centers in their nomenclature because the presence of Mg is assumed. Figure 2.11 shows optical absorption of Al_2O_3:Mg from their crystals before and after illumination of the crystal with 5 eV (248 nm) light (Ramirez et al, 2007). Defect assignments are shown above the absorption bands. A detailed discussion comparing defect assignments in Al_2O_3:Mg and Al_2O_3:C,Mg can be found chapter 3.

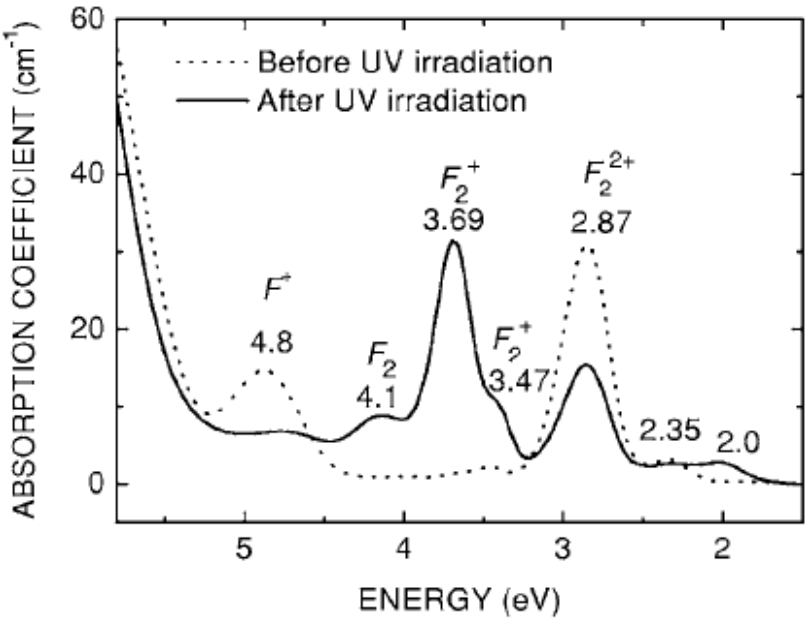

Figure 2.11 Optical absorption spectra of Al_2O_3:Mg before and after illumination with 5 eV light. The defect assignments are shown above each absorption band (Ramirez et al, 2007).

Ramirez et al (2007) also performed optical spectroscopy of defects in Al_2O_3:Mg at temperatures as low as 10 K to be able to resolve the structure of absorption and emission bands. Intense zero phonon lines were observed in the absorption/emission bands designated as aggregates (Fig. 2.12), consistent with the theory of Huang and Rhys discussed above (Huang and Rhys, 1950). More results from Ramirez et al will be discussed in chapter 3.

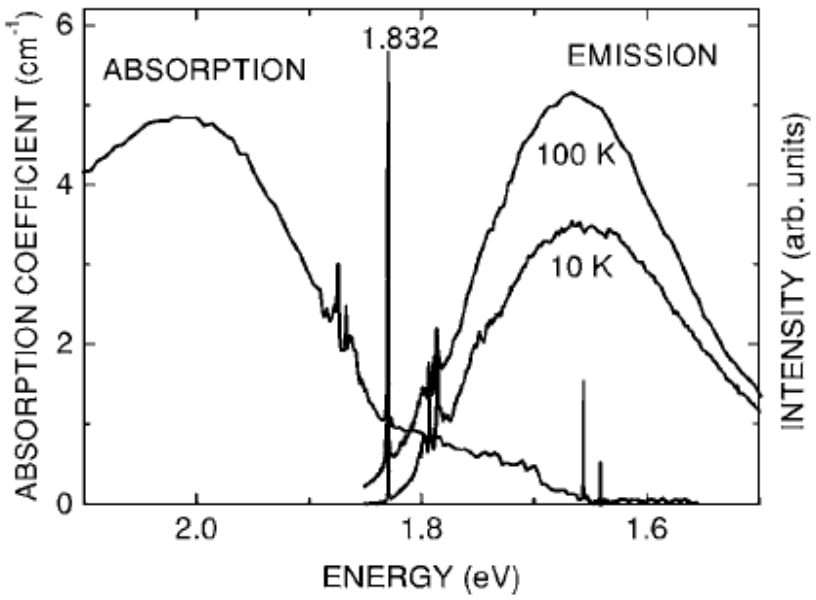

Figure 2.12 Absorption and emission spectra of Al_2O_3:Mg after illumination with 5 eV (247 nm) light at temperatures of 10 K and 100 K (Ramirez et al, 2007).

2.4 Important radiation quantities

2.4.1 Dose

Radiation dosimetry is aimed at the determination of quantities that are relevant to radiation interaction in matter. Absorbed dose is the primary quantity describing the amount of energy imparted to matter per unit mass, *m* and is defined as,

$$D = \frac{d\bar{\varepsilon}}{dm}. \qquad \text{(J/kg or Gy)} \qquad (2.13)$$

2.4.2 Cross sections

Ionizing radiation interacts with matter through a series of stochastic energy deposition events. The primary quantity used to describe the likelihood that an

interaction occurs is given as a cross section, σ. The cross section is defined as the probability of interaction in the material per particle per unit area,

$$\sigma = \frac{P}{\Phi}. \qquad \text{(bn)} \qquad (2.14)$$

P is the probability of interaction and Φ is the particle fluence. The interaction cross section is a general term and can be used to describe any interaction event such as scattering (σ_s), energy transfer (σ_{en}), absorption (σ_{abs}), ionization (σ_{ion}) or emission (σ_{em}).

2.4.3 Quantities for photons and neutrons

Photons impart energy to charged particles or atomic nuclei through either absorption or scattering and charged particles primarily impart energy to matter through the Coulomb interaction; charged particles colliding directly with nuclei occurs but has a smaller cross section. There are five major mechanisms for photon interaction in matter, the photoelectric effect, Compton scattering, pair production, Rayleigh scattering and photonuclear interactions. Of these types of photon interaction, the photoelectric effect, Compton scattering and pair production are the most dominant modes of energy transfer. Rayleigh scattering is an elastic collision of the photon with an atom that results in a small change in the direction of propagation without appreciable energy transfer. Photonuclear interactions are important when the energy of the photon exceeds several MeV when nuclei absorb photons driving the nucleus into an excited state and then decays into a neutron and another daughter nucleus (this is the (γ,n) reaction). Energy absorption/transfer is described in terms of the mass attenuation coefficient (μ/ρ) and mass energy-transfer coefficient (μ_{tr}/ρ) depending on the interaction cross sections for

each particular mode of interaction. The total mass attenuation coefficient for Al_2O_3 is given in Fig. 2.13.

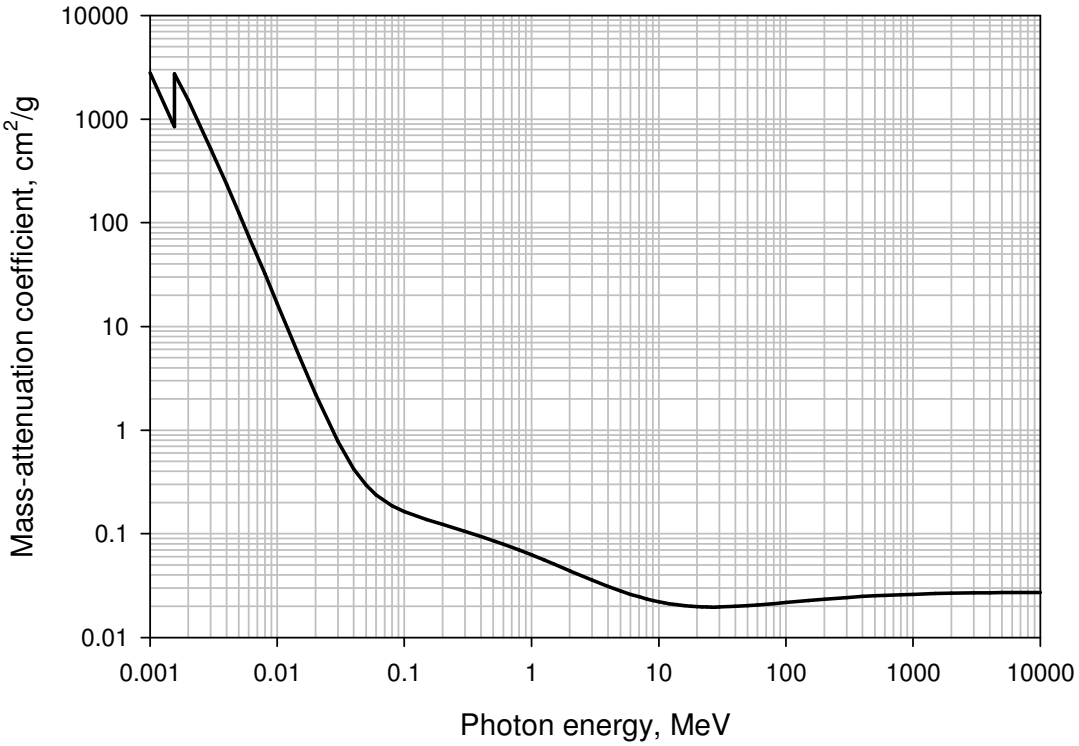

Figure 2.13 Mass attenuation coefficient for Al_2O_3 as a function of photon energy (taken from NIST.gov).

Determining dose is oftentimes more difficult than directly calculating the energy imparted per unit mass. Kerma is the expectation value of the energy transferred by uncharged particles to charged particles per unit mass *dm* in an infinitesimal volume, i.e.

$$K = \frac{d\varepsilon_{tr}}{dm}. \qquad \text{(J/kg)} \qquad (2.15)$$

For photons, the kerma is proportional to the fluence of photons with energy E by the mass energy-transfer coefficient $(\mu_{tr}/\rho)_{E,Z}$, which depends on the atomic number Z of the absorbing material. Therefore, for a spectrum of photon fluence $\Psi'(E)$, the kerma at the point of interest will be

$$K = \int_{E=0}^{E_{\max}} \Psi'(E) \cdot \left(\frac{\mu_{tr}}{\rho} \right)_{E,Z} dE \,. \qquad \text{(J/kg)} \qquad (2.16)$$

Similarly for a spectrum of neutrons with fluence *Φ'(E)* (Attix, 1986),

$$K = \int_{E=0}^{E_{\max}} \Phi'(E) \cdot \left(\frac{\mu_{tr}}{\rho} \right)_{E,Z} \cdot E dE \,, \qquad \text{(J/kg)} \qquad (2.17)$$

where $(\mu_{tr}/\rho)_{E,Z} \cdot E$ is the neutron kerma factor.

The energy transferred to charged particles is dissipated through the Coulomb interaction resulting in ionizations or excitations and through radiative interactions such as brehmsstrahlung radiation. Because of the difference in energy deposition, kerma is split into two components, collision kerma (K_c) and radiative kerma (K_r). The total kerma is the sum of the two components. In charged particle equilibrium, kerma is equal to the absorbed dose.

Exposure is another fundamental quantity in radiation dosimetry. Exposure, *X*, is defined as the total amount of charge, *dQ*, of the ions of one charge (either electrons or positrons) produced in air of mass *dm*, i.e.

$$X = \frac{dQ}{dm} \,. \qquad \text{(C/kg)} \qquad (2.18)$$

Exposure is proportional to the collision kerma by the charge of an electron per mean energy expended per ion pair, $\overline{W}$, i.e.

$$X = K_c \left(\frac{e}{\overline{W}} \right). \qquad \text{(C/kg)} \qquad (2.19)$$

Some dosimeters measure kerma or exposure directly and relate that to absorbed dose, where others measure the absorbed dose directly and relate that to kerma or exposure. The absorbed dose can only be related to kerma or exposure if the condition of

charged particle equilibrium (CPE) exists. CPE exists if every charged particle of a given energy that leaves a volume of interest is replaced by the same charged particle with the same energy. Under CPE, the absorbed dose is equal to the collision kerma. This has practical implications on the design of a dosimeter such as the need for a layer of material that is not part of the sensitive volume of the detector to provide CPE.

2.4.4 Quantities for charged particles

Heavy charged particle interaction in matter is usually described by the stopping power of the material for a particle with charge, *Z,* and energy, *E*. Unrestricted stopping power, which is also the unrestricted linear energy transfer (LET_∞), is defined by ($dE/\rho dx$). The amount of energy deposited in matter is

$$E = \Phi\left(\frac{dE}{\rho dx}\right)\rho t\,, \qquad \text{(MeV)} \qquad (2.20)$$

where Φ is the particle fluence and t is the thickness of the absorbing material. Plugging eq. (2.20) into the definition of absorbed dose, eq. (2.13),

$$D = \frac{\Phi\left(\frac{dE}{\rho dx}\right)\rho t}{\rho t} = \Phi\left(\frac{dE}{\rho dx}\right), \qquad \text{(MeV/g)} \qquad (2.21)$$

The absorbed dose in SI units is

$$D = 1.602\times10^{-10}\,\Phi\left(\frac{dE}{\rho dx}\right). \qquad \text{(J/kg or Gy)} \qquad (2.22)$$

Apart from LET_∞, energy deposition from charged particles can be described by ionization density. Ionization density is the number of electron hole pairs ($N_{e\text{-}h}$) created in a volume, *dV*, that absorb energy, *dE*. The quantity commonly used to describe

ionization density is Z/β where Z is the charge (atomic number) of the incident particle and β is its relativistic velocity. Ionization density is proportional to charge because ionizations occur through Coulomb interactions and inversely proportional to velocity because the ion is allowed to interact with nearby electrons for a longer amount of time.

2.4.5 Dose to biological systems

The biological effect of radiation is not quantified by absorbed dose because it is affected by the type, or quality of radiation, its LET_∞ and the body part exposed to radiation. Dose equivalent weights the absorbed dose to a unit-less quantity called the quality factor, Q. Dose equivalent is defined as

$$H = QD . \qquad \text{(J/kg or Sv)} \qquad (2.23)$$

The quality factor weights the dose based on the distribution of energy deposition in tissue for different types and energies of radiation; Q is a function of LET_∞. Equivalent dose, H_T, describes the dose averaged over the volume of an organ of tissue T by weighting absorbed dose by a radiation weighting factor to tissue w_R.

$$H_T = \sum_R w_R D_{T,R} , \qquad \text{(J/kg or Sv)} \qquad (2.24)$$

where R denotes the type of radiation and D_T is the absorbed dose in tissue. A quantity that better describes the biological effectiveness of radiation is effective dose. Certain body parts are more sensitive to radiation than others resulting in an assigned tissue weighting factor, w_T for each organ. Effective dose is defined as

$$E_T = \sum_T w_T H_T . \qquad \text{(J/kg or Sv)} \qquad (2.25)$$

It is important to note that absorbed dose is a fundamental quantity and the dimensions of J/kg are given the name Gray (Gy). Dose equivalent, equivalent dose and effective dose have the same dimensions but are not fundamental quantities, but are more biologically relevant so they are given in units of Sieverts (Sv). All of the doses discussed in this dissertation will be in terms of dose equivalent unless otherwise specified.

2.5 Track structure theory

Radiochromic transformations (and thus creation of measurable fluorescent tracks) in Al_2O_3:C,Mg occur as a result of ionizations caused by charged particles. Because we are looking at the results of these ionizations on a sub-micrometer level it is necessary to describe charged particle interaction with the crystal in more detail than absorbed dose. It is therefore more instructive to think of charged particle interaction in terms of track formation theory. Researchers began thinking of the result of charged particle interaction in matter as track formation in the 1940's (Nikjoo et al, 2006). Since then, the notion of energy deposition of radiation in matter has evolved from an average energy loss along the track in the 1940's to the stochastic Monte-Carlo delta ray approach of present (Nikjoo et al, 2006).

The original notion of the track consisted of an average energy loss along a straight trajectory through matter and was good enough to describe much of the macroscopic phenomenon observed. The understanding of radiation induced tracks in matter evolved when Howard-Flanders (1958) proposed a non-random clustering of energy deposition along the track of an ion based on cloud chamber measurements. In 1967 Butts and Katz introduced the idea of radial dose distribution where the dose varies as a function of $1/r^2$

at intermediate distances from the core of the ion track outward (Butts and Katz, 1967). The work of Butts and Katz (1967) and Kobetich and Katz (1968 and 1969) popularized the delta ray theory of track structure. Berger introduced one of the first widely used Monte Carlo transport codes for electrons and photons in 1973 (ETRAN, 1973) that led to a widespread interest in Monte Carlo track structure calculations.

Microdosimetry began to gain momentum around the same time with the invention of the Rossi counter (Rossi and Rosenzweig, 1955) and the first Symposium on Microdosimetry in 1968 (Goodhead, 2006). Throughout the last several decades, the Monte Carlo approach has been used in conjunction with various forms of delta ray theories (Butts and Katz, 1967, Zhang et al, 1994, Kieffer and Straten, 1986, Waligorski et al, 1986 and Chatterjee and Schaeffer, 1976) and microdosimetry to describe energy deposition in matter. Several Monte Carlo codes have been developed recently (Nikjoo et al, 2006). Examples of Monte Carlo transport codes are PENELOPE, FLUKA, GEANT4, MCNP5 and MCNPX. Katz's delta ray theory and microdosimetry will be discussed here because they are needed to describe results obtained with FNTD technology.

2.5.1 Katz's delta ray theory

Kobetich and Katz attributed the damage to matter from heavy ions to secondary electrons (delta electrons) ejected from the material. In their theory, delta electrons are assumed to be the dominant form of energy deposition in matter and thus contribute the most to the spatial distribution of dose around a charged particle track. The energy transferred at a depth, t, by one electron is defined as (Cuccinota, 1995)

$$E = \frac{d}{dt}(\eta W) \tag{2.26}$$

where η is the transmission probability of electrons and W is the residual energy of an electron after penetrating a slab of thickness t and is given by

$$W(r,t) = \omega(r-t) \tag{2.27}$$

where r is the practical range of an electron with energy ω after ionization. The range of the electron is given by the range-energy relationship determined by fitting experimental data with a power law relation of the form

$$t = k\omega^{\alpha} \tag{2.28}$$

where $k = 6\text{x}10^{-6}$ g·cm^{-2}·keV$^{-\alpha}$. The exponent has two forms, when $\omega < 1$ keV, $\alpha = 1.079$ and when $\omega > 1$ keV, $\alpha = 1.667$.

The transmission function is given by (Cuccinota, 1995)

$$\eta(r,t) = \exp\left[-\left(\frac{qt}{r}\right)^{p}\right] \tag{2.29}$$

with

$$q = 0.0059Z_T^{\,0.95} + 1.1 \tag{2.30}$$

and

$$p = 1.8(\log Z_T)^{-1} + 0.31 \tag{2.31}$$

Z_T is the atomic number of the target material.

The number of free electrons with energies between ω and $\omega + d\omega$ resulting from an ion interacting with the target material is estimated by

$$\frac{dn}{d\omega} = \frac{2\pi N_e Z^{*} e^4}{mc^2\beta^2}\frac{1}{\omega^2}\left[1 - \frac{\beta^2\omega}{\omega_m} + \frac{\pi\beta Z^{*2}}{137}\sqrt{\frac{\omega}{\omega_m}}\left(1 - \frac{\omega}{\omega_m}\right)\right] \tag{2.32}$$

where e is the electron charge, m is the electron mass, N_e is the number of electrons per cm^3 in the target, $\beta = v/c$, Z^* is the effective charge number of the incident ion and is

$$Z^* = Z\left[1-\exp\left(-\frac{125\beta}{Z^{2/3}}\right)\right] \tag{2.33}$$

ω_m in eq. (2.32) is the maximum energy that an ion can impart to a free electron which is given by

$$\omega_m = \frac{2mc^2\beta^2}{1-\beta^2} \tag{2.34}$$

Eq. (2.32) must be summed when the target material is composed of more than one material with different ionization potentials (Al_2O_3 for example). Electrons with energy ω are ejected at an angle θ given by

$$\cos^2\theta = \frac{\omega}{\omega_m} \tag{2.35}$$

for a classical collision between the ion and free electron. The dose, *D(r),* as a function of distance away from the center of the track, r, can be calculated by the integral (Waligorski et al, 1986)

$$D(r) = \frac{N_e e^4}{\alpha m\, c^2 \rho_m}\frac{Z^{*2}}{\beta^2}\frac{1}{r}\int_{\omega_0}^{\omega_m}\frac{\omega}{t}\left(1-\frac{r}{t}\right)^{1/\alpha-1}\frac{d\omega}{(\omega+I)^2} \tag{2.36}$$

where ρ_m is the density of material, m. Solution of the integral above gives (Waligorski et al, 1986)

$$D(r) = 6.50\times10^{-22}\frac{N_e}{\alpha\rho_m}\frac{Z^{*2}}{\beta^2}\frac{1}{r}\left[\frac{\left(1-\dfrac{r+r_0}{R_{\max}+r_0}\right)^{1/\alpha}}{r+r_0}\right], \quad r_0 < r < R_{max} \tag{2.37}$$

where

$$\alpha = \begin{cases} 1.079, & for\ r_0 = 0.426/\rho_m < r < 61.3/\rho_m \\ 1.667, & for\ 61.3/\rho_m < r < R_{\max} = \dfrac{6.24\times10^6}{\rho_m}\left(\dfrac{\beta^2}{1-\beta^2}\right)^{1.667} \end{cases} \tag{2.38}$$

D(r), is given in terms of Gy for all quantities in CGS units except for r_0 and R_{max} which are in nm.

Recently, Sawakuchi (2008) has slightly modified the Butts and Katz radial dose distribution model to include a flat region near the core of the ion track and applied the results to Al_2O_3. Figure 2.14 is the calculated amount of dose deposited in Al_2O_3 as a function of distance from the track.

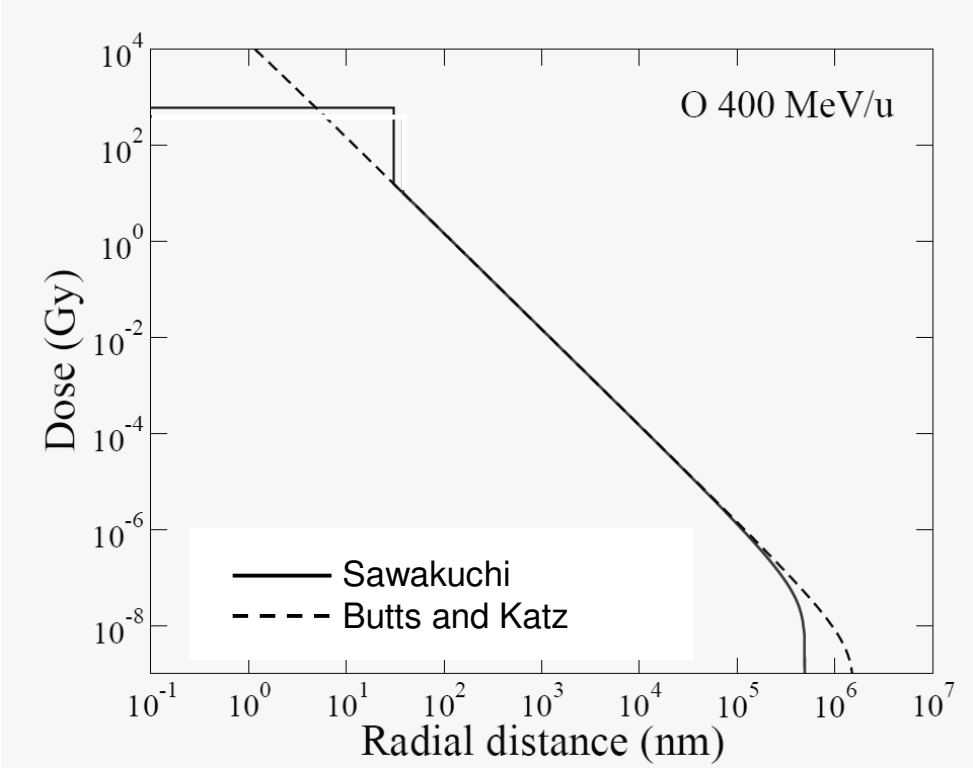

Figure 2.14 Radial dose distribution of 400 MeV/u O in Al_2O_3 as calculated by Sawakuchi (2008) (solid line) and the Butts and Katz model (dashed black line)

2.6 Microdosimetry

Confocal imaging of FNTDs ensures that the quantification of energy deposition in Al_2O_3:C,Mg is measured in a volume confined by only a few cubic micrometers making the data inherently microdosimetric. Microdosimetry was first conceptualized as an attempt to quantify the energy deposition of ionizing radiation on a microscopic level. Microdosimetry, as defined by Rossi and Zaider, "…is the systematic study and quantification of the spatial and temporal distribution of absorbed energy in irradiated matter" (Rossi and Zaider, 1996). The amount of energy deposited in one event may be hundreds of times greater than the average energy absorbed per unit mass. Some factors influencing energy deposition include the atomic structure of matter and the fact that ionizing events occur from charged particles. It is therefore important, especially for radiobiology, to understand the microscopic distribution of energy deposition.

2.6.1 Stochastic quantities

Stochastic quantities will often be of the same units as non-stochastic quantities, but their values can be very different. An example of the difference between stochastic and non-stochastic quantities is the actual number of disintegrations occurring in radioactive material per unit time (stochastic) versus the activity of the material which is the mean number of disintegrations per unit time (non-stochastic). The actual number of disintegrations in a time interval, τ, varies in a Poisson probability distribution given by

$$P(N, A\tau) = e^{-A\tau} \frac{(A\tau)^N}{N!} \tag{2.39}$$

where N is the number of disintegrations and A is the activity. Similarly, energy deposition in matter is probabilistic. The actual number of events per unit length and the actual energy deposited per unit mass have their own distributions.

Absorbed dose (eq. 2.13), is a non-stochastic quantity, and its stochastic analog is specific energy, z which is the amount of energy absorbed in a finite volume, V, surrounding the point at which energy is transferred:

$$z = \frac{\varepsilon}{\rho V} = \frac{\varepsilon}{m} \qquad \text{(J/kg or Gy)} \qquad (2.40)$$

where ρ is the density of the absorbing material and ε is the deposited energy. The average of the specific energy is equal to the absorbed dose.

Lineal energy, y, is the stochastic analog to linear energy transfer and is defined as the amount of energy deposited in the material per unit length, l:

$$y = \frac{\varepsilon}{l}. \qquad \text{(keV/μm)} \qquad (2.41)$$

2.6.2 Microdosimetric spectra

Microdosimetric spectra are the probability distributions of the quantity or quantities of interest. These spectra are assumed to be continuous even though it is only possible to calculate the spectra based on discrete measurements. The moments of these distributions are used to derive useful microdosimetric quantities such as the dose average of lineal energy, y_D.

All detectors currently used for microdosimetric measurements provide the number of ionizations that occur within the sensitive volume of the detector. The number of ionizations can be converted into energy by multiplying the number of ionizations by the mean energy per ion pair. The mean energy per ion pair is called the W value. The

actual spectrum is a result of smoothing the data into a continuous spectrum instead of the original discrete spectrum. Most detectors account for only ionizations, but charged particle interactions can also produce excitations which may affect the overall spectrum.

The resulting data from these detectors are plotted as histograms with the lineal or specific energy on the horizontal axis and the frequency distribution (number of ionization events) on the vertical axis. A number of representations of the data can be used, but the standard format in which microdosimetric spectra are presented is one in which the frequency is multiplied by the lineal energy on the vertical axis and the horizontal presentation of *y* is logarithmic. In other words, the standard format is a semi-log representation with *y*f(y)* or *y*d(y)* on the vertical axis and *log(y)* on the horizontal.

The basic treatment of the moments of the lineal energy spectrum will be outlined as an example. The frequency average, y_F, is the first moment of the distribution and the dose average is the ratio of the second moment to the first moment:

$$y_F = \int_0^\infty y f(y) dy \tag{2.42}$$

and

$$y_D = \frac{1}{y_F} \int_0^\infty y^2 f(y) dy \tag{2.43}$$

where *f(y)* is the probability distribution, or microdosimetric spectrum, of the lineal energy. The event frequency is defined as

$$\Phi^* = \frac{1}{y_F} \ . \tag{2.45}$$

The full mathematical treatment of microdosimetric spectra and their moments is beyond the scope of this paper, but it can be found in Rossi and Zaider.

Microdosimetry is most useful when the actual value of the quantity in question varies greatly from its mean value. It is generally accepted that significant deviation from the mean of the specific energy is "when z is 0 in half of the sites and 2 times the absorbed dose in the other half" (Rossi and Zaider, 1996). The size of the site in which microdosimetry is useful also varies with the ionization density, the delivered dose and the system of interest. For example, in radiobiology, the main volumes of interest are in the cell nucleus (on the order of micrometers) and the DNA inside the nucleus (on the order of a few nanometers). The site size decreases as the amount of absorbed dose reaches large values. When the site size approaches that of individual atoms, quantum mechanical uncertainties start to take effect and thus it is impossible to determine the location of energy transfer.

Most applications of microdosimetry revolve around biological effects. It was suggested that microdosimetric spectra be used to calculate quality factors by way of lineal energy. Kellerer and Hahn (1988) empirically related the quality factor, Q, to y on the recommendation of the ICRP and ICRU. This equation is

$$Q(y) = 0.3y\left[1+\left(\frac{y}{137}\right)^5\right]. \tag{2.46}$$

The site diameter was recommended to be 1 μm in tissue to combine accuracy with ease of measurement. The concept of the quality factor was needed to relate the absorbed dose to the biological effect. This relation is dose equivalent, H and is defined in eq. (2.24). The definition of dose equivalent is more appropriately defined as

$$H = \int_0^\infty Q(y)D(y)dy \tag{2.47}$$

where *y* is the lineal energy of the particles. This formulation is necessary because of the statistical distribution of energy deposition in tissue. The complete role of microdosimetry in radiobiology is a vast subject and will not be detailed here, noting that FNTDs have the potential to act as microdosimeters (see section 6.6).

2.7 Fluorescent nuclear track detectors

The original idea of using Al_2O_3 as a radiation dosimeter was to measure optically or thermally stimulated luminescence. Trapping occurs in pre-engineered F and F^+ color centers due to crystal growth in a highly reducing atmosphere involving carbon. Additional doping with magnesium, created new lattice defects and thus new color centers discussed in section 2.3.

It was suggested to try to image the result of irradiation with alpha particles in Al_2O_3:C,Mg using the same readout method as in optical data storage. Initial success of imaging tracks caused by alpha particle penetration instigated the development of this new Al_2O_3:C,Mg material as a viable radiation dosimeter.

A large number of electrons and holes are generated during the interaction of ionizing radiation with the crystal lattice. There are probabilities for the electrons and holes to undergo a number of different trapping and recombination processes. One process is electron-hole recombination which yields no noticeable change in the properties of the crystal. Another possibility is hole trapping in which certain defects (color centers) trap holes to form a state with a net charge of one less electron. The last process is electron trapping in which defects trap electrons to change the charge state of

the defect to one with a net charge of one additional electron. During irradiation of the crystal, F_2^{2+}(2Mg) defects capture an electron and undergo radiochromic transformation into a different charge state – F_2^{+}(2Mg) (see chapter 3). Figure 2.15 shows a simplified band diagram of the irradiation and non-destructive readout processes.

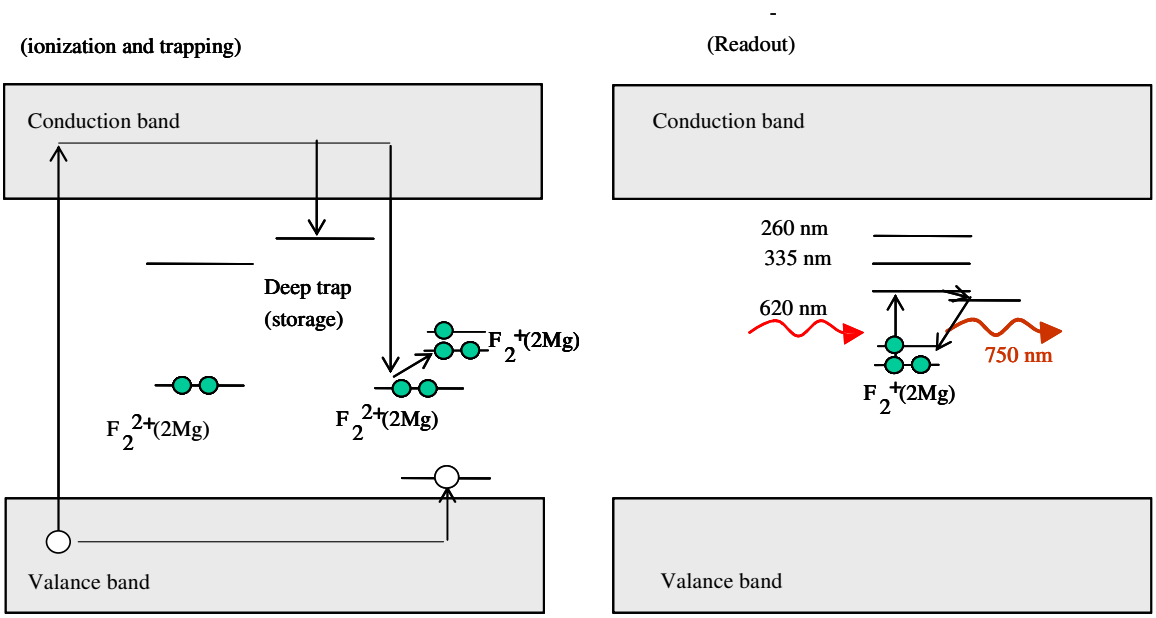

Figure 2.15 Flat band diagram of irradiation and readout of Al_2O_3:C,Mg

Readout of FNTDs was performed with a confocal fluorescence imaging system designed to test methods for optical data storage (Akselrod et al, 2003a-c). Confocal imaging allows detection of the fluorescence only from the volume of the focal spot of the excitation laser light with diffraction-limited 3-D spatial resolution. A schematic diagram of the confocal fluorescence readout system is illustrated in Fig. 2.16. Laser-induced fluorescence is detected in an infinite conjugate confocal geometry. The confocal detection scheme allows rejects fluorescence from areas of the crystal adjacent to the focal spot of the stimulation light that also produce fluorescence. Scanning was performed by moving the FNTD with respect to the objective with a piezo-electric

positioning cube. The time to scan one image with dimensions 100x100 μm^2 was 6 minutes which was too long for practical application as is discussed in chapter 4.

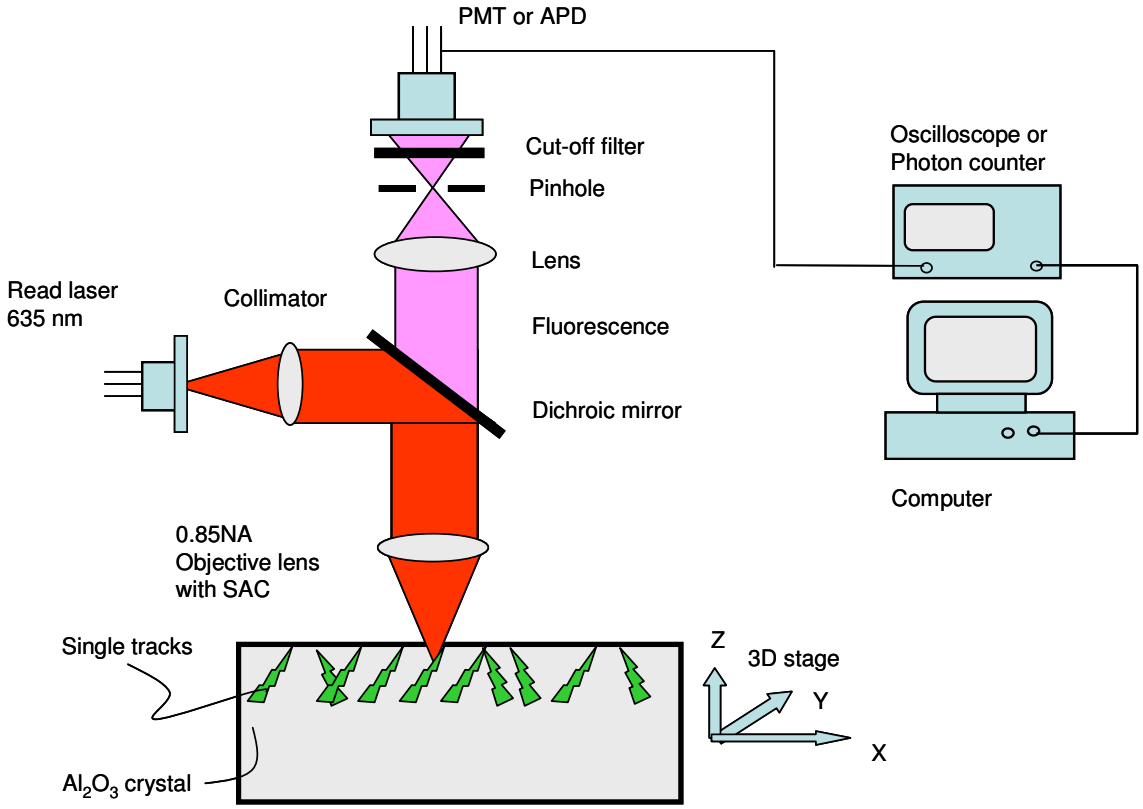

Figure 2.16 Diagram of the original confocal imaging system used for obtaining the first results (alpha particle images and preliminary LET dependences) with FNTDs (Akselrod et al, 2006). The time required to scan one 100x100 μm^2 image was 6 minutes.

Al_2O_3:C,Mg was proposed to replace CR-39 plastic nuclear track detectors as possible neutron dosimeters and also to be used as a heavy charged particle spectrometer. Initial work and testing to these ends began as early as 2004 (Akselrod et al, 2006b). Irradiations were performed at the Landauer irradiation facility in Glenwood, IL and at the Heavy Ion Medical Accelerator in Chiba (HIMAC), Japan. Promising and interesting results were achieved with these irradiations. The results showed that this newly engineered Al_2O_3:C,Mg was a viable nuclear track detector for the purpose of radiation dosimetry.

CHAPTER III

OPTICAL PROPERTIES OF Al_2O_3:C,Mg

Development of Al_2O_3:C,Mg as a radiation detector required detailed investigations of its optical properties and understanding the physics of electronic transitions in Al_2O_3:C,Mg. The purposes of investigating the physics of Al_2O_3:C,Mg were to provide feedback for improving crystal growth, to explain radiation effects on the optical properties of Al_2O_3:C,Mg (i.e. define competing processes for electrons and holes) and to use this information for improving track detection performance. Crystal growth parameters including temperature of the melt, growth rate, doping concentrations and presence of gases, affect the optical and physical properties of the crystal. Investigations of the optical properties of Al_2O_3:C,Mg is therefore important for optimizing crystal growth conditions. Actual correlations with crystal growth parameters are beyond the scope of this paper and will not be discussed in detail here.

A basic understanding of the affect of ionizing radiation on the optical properties of Al_2O_3:C,Mg is important for its application in radiation detection. The nature of charge trapping and transfer in Al_2O_3:C,Mg will affect the performance of any radiation detector. As an example, the first tracks in Al_2O_3:C,Mg were imaged by exciting the crystal with 635 nm light and measuring 750 nm fluorescence (Akselrod et al, 2006). The questions that arise from this are as follows: 1) What are the most efficient wavelengths of excitation and emission for practical radiation –induced imaging? 2) What defect is being

probed and in what charge state is it in? 3) What are competing for free charge carriers? And, 4) Is it possible to enhance the ability to measure tracks? Investigating the optical properties of Al_2O_3:C,Mg should help answer the questions posed above. Understanding the physics of the material can also help validate the technology for use in radiation detection. A good scientific foundation for luminescent detectors includes characterizing their optical properties.

This chapter describes defects in Al_2O_3:C,Mg and their optical properties with photoluminescence (PL) and optical absorption (OA) measurements. The response of Al_2O_3:C,Mg to thermal annealing, optical bleaching and X-ray and beta radiations were examined. Thermal and optical treatments of the crystal were proposed and tested based on optical measurements and results obtained in Akselrod's group works (Akselrod et al., 2001, 2006 and Sanyal et al., 2003). New data on photochromic and radiochromic transformations of color centers are discussed in this chapter.

3.1 Experimental methods and materials

3.1.1 Spectroscopic measurement equipment

Spectroscopic investigations of Al_2O_3:C,Mg were performed using a spectrophotometer for optical absorption and two PL measurement systems. Optical absorption measurements were carried out using a Shimadzu UVPC spectrophotometer. The UVPC spectrophotometer employed a tungsten lamp for measurements between 800 nm and 330 nm and a deuterium lamp between 330 nm to 195 nm. A monochromator separated and scanned the wavelengths of the

illumination light. The beam was split into two paths, a reference beam and a signal beam. The signal and reference beams are measured by a photomultiplier tube (PMT). Transmission through the sample was measured and recalculated into absorption and given in arbitrary units of signal intensity divided by reference intensity. Light from the spectrophotometer is only partially polarized so a polarizer was placed in the beam path for measurements of defect symmetry.

Two fluorescence measurement systems were used for optical spectroscopy. One system was a Jobin Yvon Fluorolog at Oklahoma State University/Venture I research center made available by Dr. Eduardo Yukihara. The second was a fluorescence measurement system assembled from two ARC Research monochromators and an ARC Research Spectrumm CCD camera at Landauer.

The Fluorolog at is a spectrofluorometer using a Xenon arc lamp, two scanning monochromators, one for excitation and the other for emission, and a PMT for light detection. This system monitors a reference beam to correct for the spectral characteristics of the Xenon lamp. The lamp spectrum is shown in Fig. 3.1. The range of wavelengths for the Xenon arc lamp is from 190 nm to 750 nm. The emission intensity is given in terms of counts and is not internally corrected for the spectral sensitivity of the PMT.

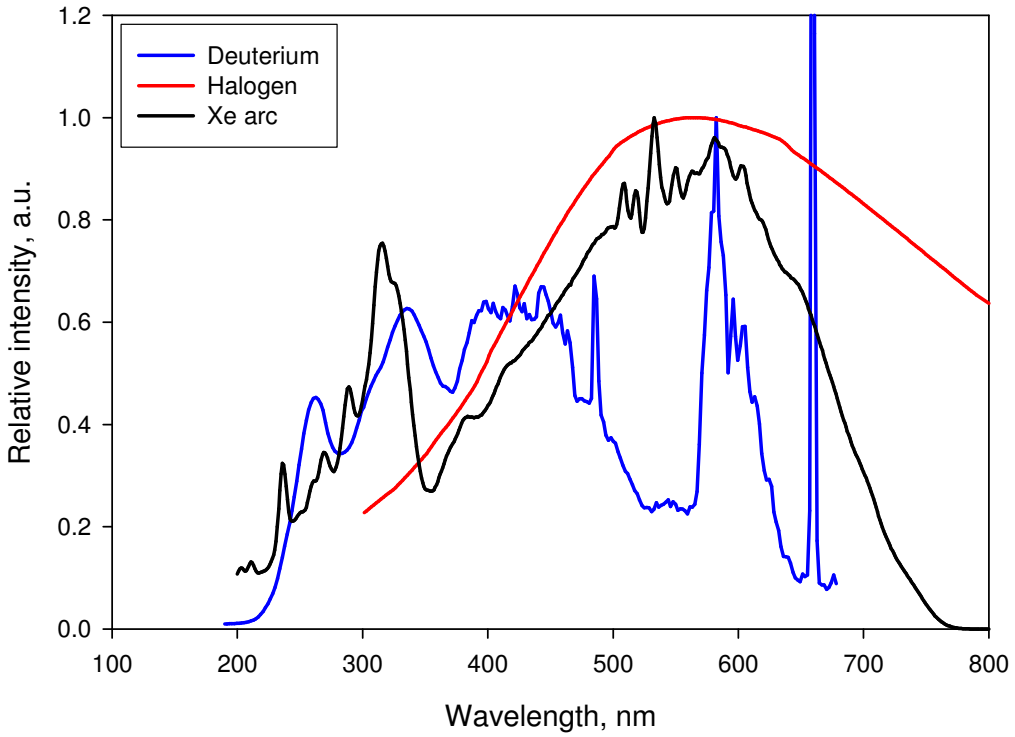

Figure 3.1 Normalized emission spectra of the deuterium, halogen and Xenon arc lamps used for fluorescence measurements of Al_2O_3;C,Mg.

The fluorescence measurement system at Landauer was a fluorometer assembled from separate commercial components. Major components of the Landauer fluorescence system were used in the work of Sanyal *et al* (2003) reviewed in Chapter 2. The fluorometer consisted of an arrangement of two excitation sources, an excitation monochromator, a sample holder, an emission monochromator, a CCD camera and intermediate optics (Fig. 3.2).

The excitation lamps were a Titan Halogen lamp for wavelengths in the range of 800 nm to 350 nm and an Oriel Deuterium lamp for stimulation with 400 nm to 200 nm light. The emission spectra for these lamps can be seen in Fig. 3.1. Excitation and emission spectra were corrected for the efficiency of the monochromator gratings and the quantum efficiency of the CCD camera.

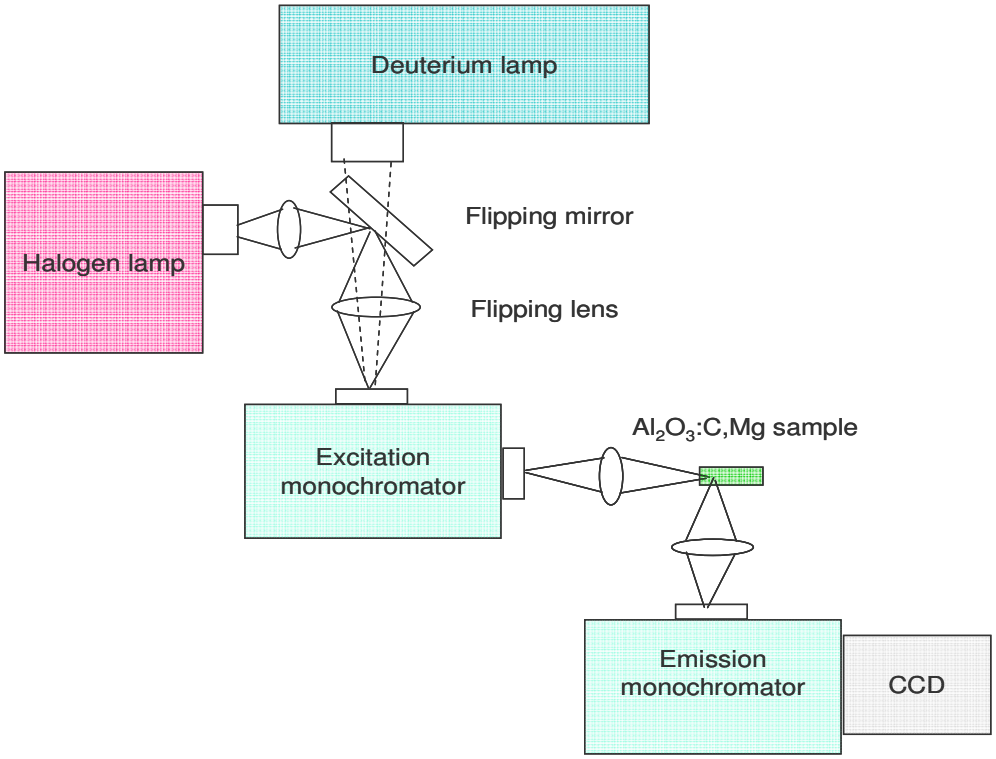

Figure 3.2 Diagram of photoluminescence measurement system used at Landauer Inc.

Both monochromators were similar ARC Research monochromators. They consisted of two turrets containing one blaze grating of 300 lines/mm and the other with a blaze grating of 1200 lines/mm. A grating of 300 lines/mm was used for measurements needing less spectral resolution and the 1200 lines/mm grating was used for high-resolution measurements. Efficiencies of the monochromators were used to normalize the data.

An ARC Research Spectrumm CCD camera was used for spectral imaging. The CCD camera has a back-illuminated chip cooled to -30°C, designed for high quantum efficiency over a broad spectral range (greater than 45% for wavelengths from 190 nm to 950 nm) and low noise measurements. The CCD consisted of a two-dimensional array of 1024 x 128 pixels. Spectral images were acquired by integrating

the intensity of four pixels in the horizontal dimension and all 128 pixels in the vertical dimension. All measurements were corrected for the quantum efficiency of the CCD camera.

3.1.2 Methods of defect transformation

Step annealing experiments were performed to verify defect assignments and to increase the concentration of F_2^{2+}(2Mg) color centers. Thermal annealing was also used to show aggregation of F and F^+ centers and dissociation of F_2^+(2Mg) and F_2^{2+}(2Mg) centers. Thermal aggregation experiments were performed using Vulcan 3-130 and Vulcan 3-550 programmable ovens.

Photochromic transformations of defects in Al_2O_3:C,Mg were performed using an optical parametric oscillator (OPO) pumped by a frequency tripled neodymium yttrium aluminum garnet (Nd:YAG) laser from Continuum. The Nd:YAG laser was pumped by a flash lamp at a frequency of 10 Hz. 7 ns pulses were produced by an optical Q-switch. The fundamental wavelength (1064 nm) of the Nd:YAG laser had an energy of 1.55 J; the doubled frequency (532 nm) had an energy of 650 mJ and the tripled frequency (355 nm) had an energy of 150 mJ. The three wavelengths were separated using a series of high energy dichroic mirrors

The pump laser was injected into a crystal oven containing a birefringent BBO crystal used for tuning the wavelength between 400 nm and 790 nm. High energy pulses were achieved by phase matching the crystals. A set of doubling crystals allowed for a total wavelength range of 215 nm to 790 nm. The OPO was tuned to specific wavelengths corresponding to absorption bands during photoconversion

experiments. The output beam was focused by a UV enhanced aspheric lens to provide high power density and uniform irradiation of the crystal. The beam area was 0.12 mm^2. Specific choice of wavelengths for photoconversion experiments are discussed in the appropriate subsections.

3.2 Differences between Al_2O_3:C and Al_2O_3:C,Mg

It is important to compare Al_2O_3:C, the material engineered for radiation dosimetry using OSL, with Al_2O_3:C,Mg, the material engineered for FNTDs, because Al_2O_3:C has been studied extensively and is the basis for Al_2O_3:C,Mg. Al_2O_3:C has high concentrations of neutral oxygen vacancies with two electrons, F centers, because of crystal growth in a highly reducing atmosphere. There are small concentrations of F^+ centers in Al_2O_3:C compared to F centers (Fig. 3.3a).

A variety of absorption/emission bands are created in Al_2O_3:C,Mg due to crystal growth in a highly reducing atmosphere and the presence of magnesium impurities. Magnesium stimulates production of F^+ centers evidenced by the difference in F^+ center concentration in regular dosimetric Al_2O_3:C from Al_2O_3:C,Mg. Figures 3.3 and 3.4 illustrate the differences in OA and PL spectra from Al_2O_3:C and Al_2O_3:C,Mg. OA and PL spectra show a complex of optically active structures in Al_2O_3:C,Mg compared to the original Al_2O_3:C material. As discussed later, magnesium stimulates production of aggregate oxygen vacancies responsible for the additional absorption and emission bands.

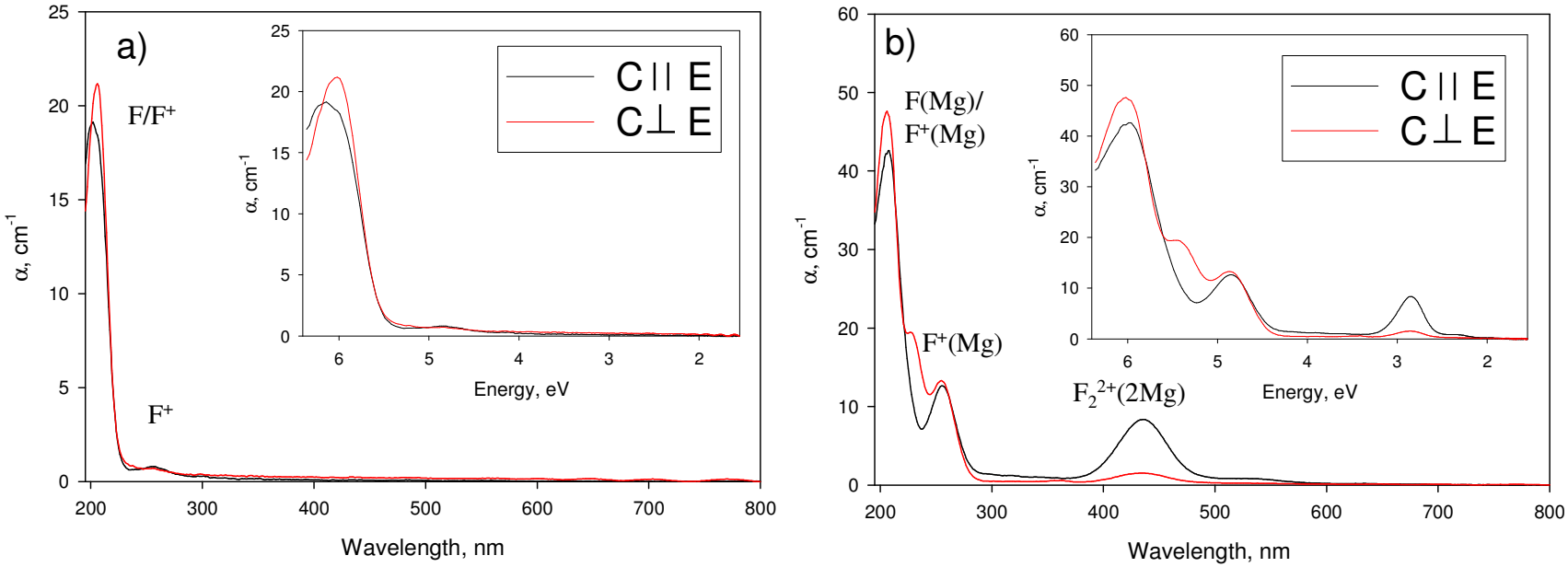

Figure 3.3 Optical absorption spectra of a) Al_2O_3:C with the crystal's optical c-axis parallel (black) and perpendicular (red) to the light polarization direction and b) Al_2O_3:C,Mg with the crystal's optical c-axis parallel (black) and perpendicular (red) to the polarization illustrating both the role of magnesium in creating new color centers and the anisotropy of the color centers. The insets are the same spectra but in terms of photon energy.

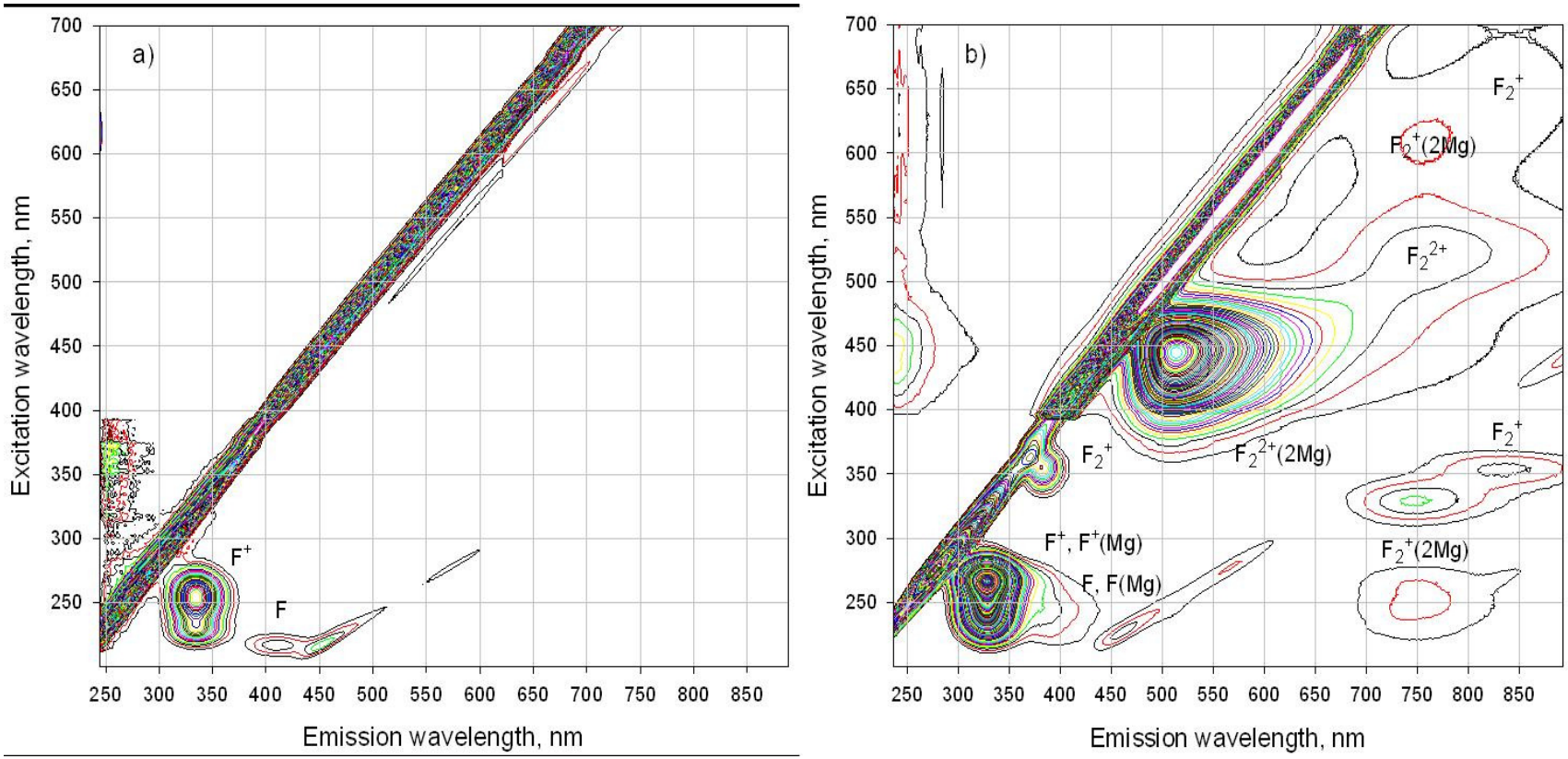

Figure 3.4 Comparison of the photoluminescence spectra of a) Al_2O_3:C and b) Al_2O_3:C,Mg both after thermal annealing at 600ºC showing the role of Mg in forming aggregate defects and the complex of defects in Al_2O_3:C,M in comparison with Al_2O_3:C.

Several combinations of single and double vacancy defects, which ultimately form luminescent color centers, are possible in Al_2O_3:C,Mg. Potential luminescent centers are single oxygen vacancy centers without magnesium such as F and F^+ centers, single oxygen vacancies perturbed by magnesium – F(Mg) and F^+(Mg) and their aggregates which, in different combinations, are F_2, F_2^+, F_2^+(2Mg), F_2^{2+} and F_2^{2+}(2Mg).

The excitation/emission bands in the spectra are preliminarily assigned (and discussed later) as follows: 255/325 and 230/325 are single oxygen vacancies charge compensated by Mg impurities - F^+(Mg) centers, the 300/500 band is attributed to F_2 centers, 435/520 is attributed to aggregate F_2^{2+}(2Mg) centers, 355/385 is attributed to F_2^+ centers and the 620/750, 335/750 and 260/750 are attributed to F_2^+(2Mg) centers (Akselrod et al, 2003, Sanyal et al, 2005). Preliminary assignments were made based on comparisons with neutron irradiated Al_2O_3 from literature data (Evans et al, 1994 and Kulis et al, 1981) and our experiments with thermal and photochromic transformations of color centers in Al_2O_3:C,Mg which are discussed in detail in section 3.3.

3.3 Thermal aggregation of single oxygen vacancies

Thermal aggregation occurs during crystal growth leading to the appearance of additional absorption/emission bands associated with aggregate centers in as-grown crystals. Aggregate centers can then be identified by relating changes in

concentration of the absorption/emission centers after thermal annealing (i.e. one band is created that expense of another).

Thermal aggregation of single oxygen vacancies (F^+(Mg) into F_2^{2+}(2Mg) centers) by long time annealing at low temperatures compared to crystal growth temperatures has been observed before (Akselrod et al, 2003 and Ramirez et al, 2007). Identification of other aggregate centers was based on photoconversion of F_2^{2+}(2Mg) (Akselrod et al, 2003 and Ramirez et al, 2007) and F_2^{2+} (Evans, 1995) centers. Thermal annealing experiments have historically been carried out using OA as the primary measurement tool (Evans, 1995). Likely explanations for not observing aggregation of F^+ and F (or F^+(Mg) and F(Mg)) are that OA measurements are not sensitive enough to detect small changes in defect concentrations and the crystals studied to date have had relatively low concentrations of magnesium (Akselrod et al, 2003).

Thermal annealing experiments were performed to verify identification of bands to aggregate centers and to increase the concentration of aggregate centers. PL and OA measurements were performed on new Al_2O_3:C,Mg crystals with high concentrations of magnesium before and after isothermal annealing at temperatures between 450 and 680ºC. In this study, crystals with absorption coefficients at 435 nm of at least 2.5 cm^{-1} prior to annealing were used. Crystals were isothermally annealed for 25 hours at temperatures of 450, 500, 550, 600, 625 650 and 680ºC and allowed to cool quickly to room temperature.

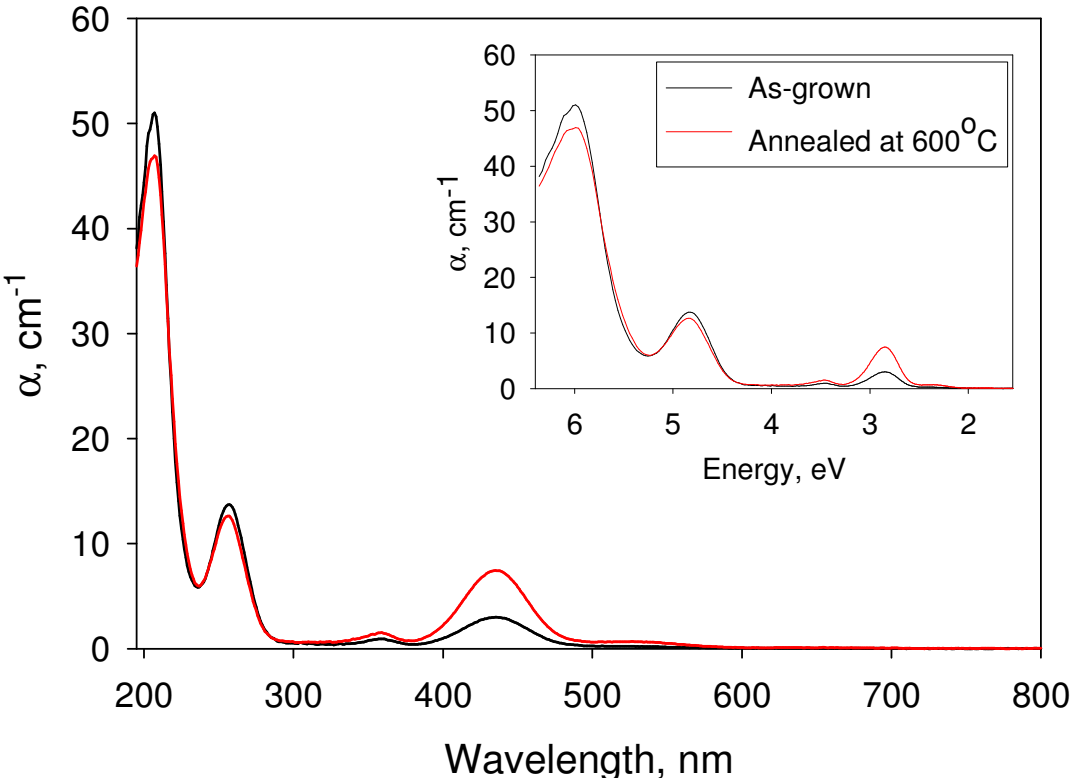

Figure 3.5 Optical absorption spectra for Al_2O_3:C,Mg as-grown (black line) and thermally annealed at 600ºC (red line) demonstrating thermal aggregation of single oxygen vacancies. The inset is the same spectrum but in terms of photon energy.

Figure 3.5 shows the OA spectra before and after isothermal annealing at 600°C and Fig. 3.6 shows the relative changes in absorption coefficients. PL spectra are shown in Fig. 3.7. There was no evidence of thermal aggregation of color centers at 450°C. Annealing temperatures of 500°C and higher induced thermal aggregation which was evidenced by increasing F_2^+(2Mg) (335 nm), F_2^+ (355 nm) and F_2^{2+}(2Mg) (435 nm) absorption at the expense of the 208 and 256 bands. Figure 3.7a demonstrates existing color centers in "as-grown" Al_2O_3:C,Mg. The spectrum shows large concentrations of F^+(Mg) and F_2^{2+}(2Mg) centers with a very small amount of F_2^+(2Mg) centers. Neutral aggregate F_2 centers cannot be seen.

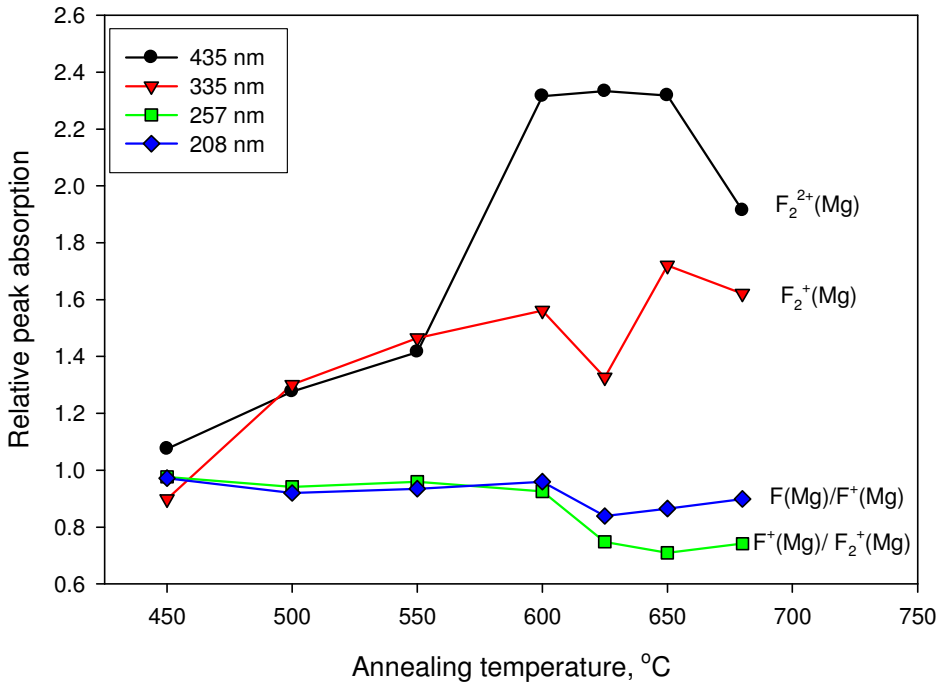

Figure 3.6 Optical absorption peak heights relative to their initial optical absorption coefficient versus isothermal annealing temperature demonstrating thermal aggregation of single oxygen vacancies.

Figure 3.7b shows a PL spectrum of the same crystal after isothermal annealing at 600°C. The spectrum demonstrates a 1.8 times increase in intensity of the F_2^{2+}(2Mg) emission, while the intensity of F^{+}(Mg) luminescence decreased by 10% providing evidence that F^{+}(Mg) centers aggregate to form the 435/520 band. The emission intensity of 620/750, 335/750 and 260/750 bands also showed significant increases. It is suggested that F(Mg) and F^{+}(Mg) centers form aggregate F_2^{+}(2Mg) centers. The decrease in the 208 nm absorption band is attributed to the combination of a net loss of both F(Mg) and F^{+}(Mg) centers. Neutral aggregate, F_2-centers, characterized by a 300/500 nm band, appeared after 600°C thermal annealing but at a concentration that was too low to be measured by optical absorption.

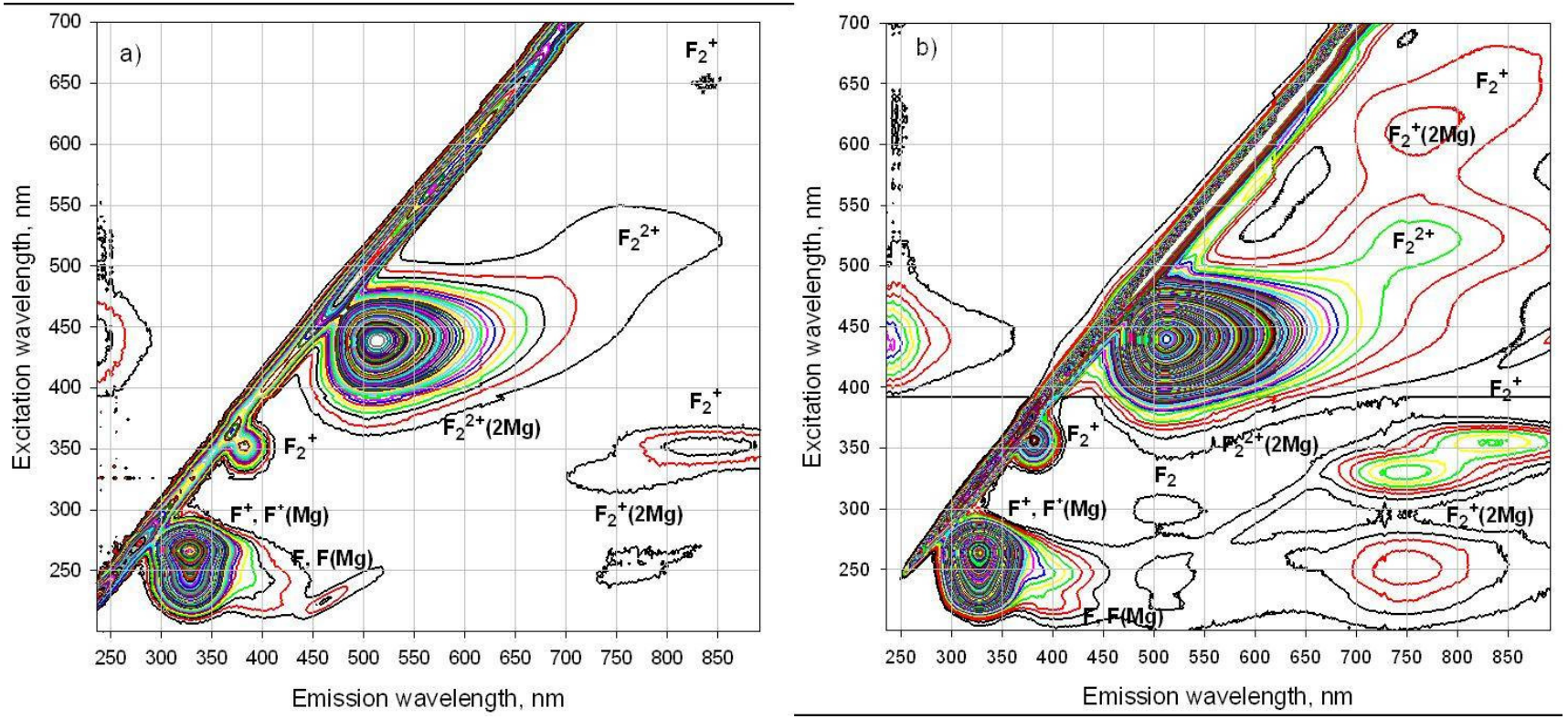

Figure 3.7 Photoluminescence spectra of Al_2O_3:C,Mg a) as-grown and b) after thermal annealing at 600ºC for 25 hours demonstrating the increased concentration of aggregate centers after annealing. Both spectra are on the same scale.

3.4 Photoconversion of defects

Historically, assignment of defects as well as ionization and trapping mechanisms has been investigated utilizing photoconversion of defects. Photoionization of color centers can occur either through single or two-photon absorption. With single photon absorption, the excited state of the color center within the forbidden band-gap lies sufficiently close to the conduction band such that the electron can escape. Sequential two photon absorption occurs as a result of exciting an electron with the first photon and while the electron is still in its excited state, a second photon is absorbed providing enough energy for the electron to escape to the conduction band.

The following section describes results of optical bleaching experiments for defect assignment as well as electron trapping mechanisms. Al_2O_3:C,Mg crystals were optically stimulated with high peak power pulsed laser light from the OPO in an incremental number of pulses incident on the crystal. Optical absorption measurements were performed after every bleaching step. PL spectra were taken prior to the first iteration and after the last. Optical absorption coefficients were used to quantify color center concentrations of optically active bands while PL spectra qualitatively depicted changes in defect concentrations.

3.4.1 435 nm bleaching

The 435 nm absorption band is the most obvious band resulting from the addition of Mg so it was important to verify the assignment of the 435 nm band. It is also assumed that F_2^{2+}(2Mg) centers are the primary electron trap during irradiation that

causes the formation of fluorescent tracks (see section 3.6 below), so it is important to verify that the 435 nm band is correctly attributed to F_2^{2+}(2Mg) centers. 435 nm stimulation specifically targeted F_2^{2+}(2Mg) centers for photoionization and photoconversion. Photoionization of the 435 nm absorption band occurs through sequential two photon absorption. Detailed discussions of sequential two photon ionization of F_2^{2+}(2Mg) centers are found in Akselrod's works (2003a and 2003b).

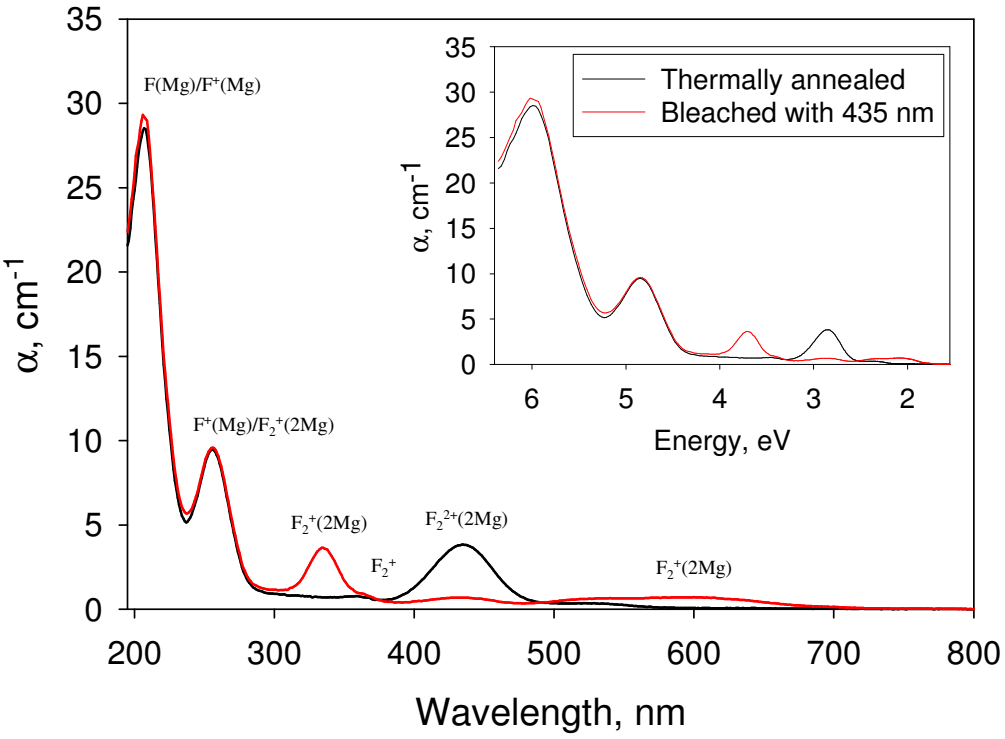

Figure 3.8 Optical absorption spectra for Al_2O_3:C,Mg annealed at 650°C (black line) and optically bleached with high peak power 435 nm, 7 ns pulses to deplete the concentration of F_2^{2+}(2Mg) centers. Annealed Al_2O_3:C,Mg was used to begin with a large concentration of F_2^{2+}(2Mg) centers. The inset is the same spectrum but in terms of photon energy.

Al_2O_3:C,Mg crystals were irradiated with 435 nm light and OA was measured. Figure 3.8 demonstrates OA spectra before and after bleaching. Figure 3.9 shows the absorption coefficients for optically active bands that exhibit noticeable changes as a function of number of delivered pulses. Figure 3.10 shows the PL spectra before and after bleaching with 435 nm light.

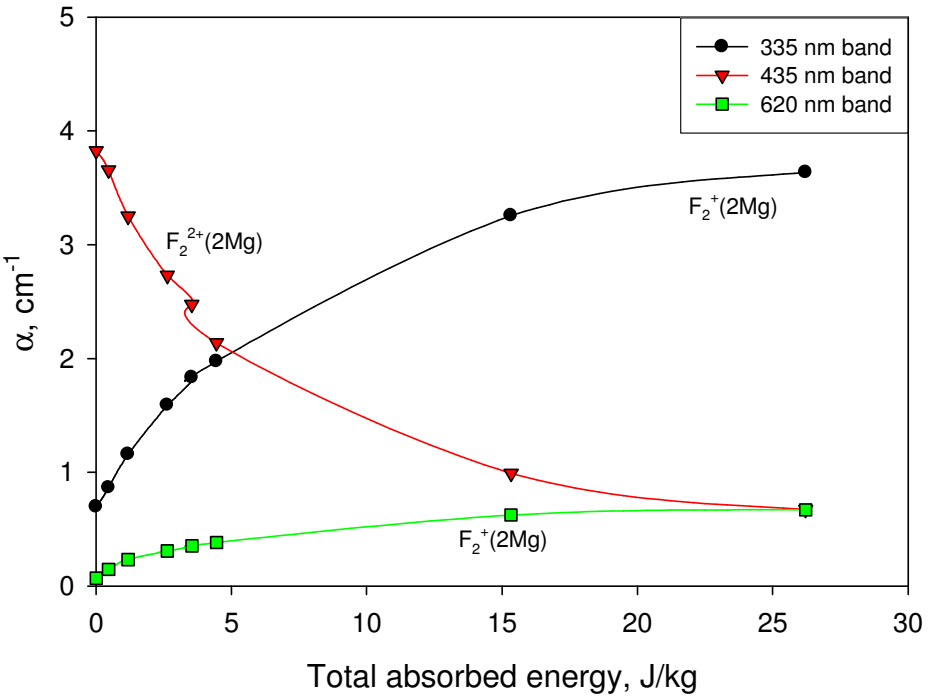

Figure 3.9 Absorption coefficients for Al_2O_3:C,Mg optically bleached with high peak power 435 nm, 7 ns pulses as a function of bleaching pulses demonstrating the kinetics of the bleaching process.

Direct stimulation of the 435/510 nm band resulted in a steep increase of the 256/750, 620/750 and 335/750 nm bands with a simultaneous decrease in the 435/510 nm band. Increases in the 520 nm and 355 nm absorption bands were likely due to the tails of the 620 nm and 335 nm bands respectively. There is also a small increase (compared to the increase in 335 nm absorption) in the 205 nm absorption band suggesting that some electrons photoionized from F_2^{2+}(2Mg) centers are captured on F^+(Mg) centers transforming into F(Mg) centers. The 255 nm absorption band does not decrease because the reduction in F^+(Mg) centers is offset by the increase in F_2^+(2Mg) centers which also absorb 255 nm light (see PL spectra, Fig. 3.10). PL spectra before and after bleaching show a decrease in the 255/325 nm band attributed to F^+(Mg) centers.

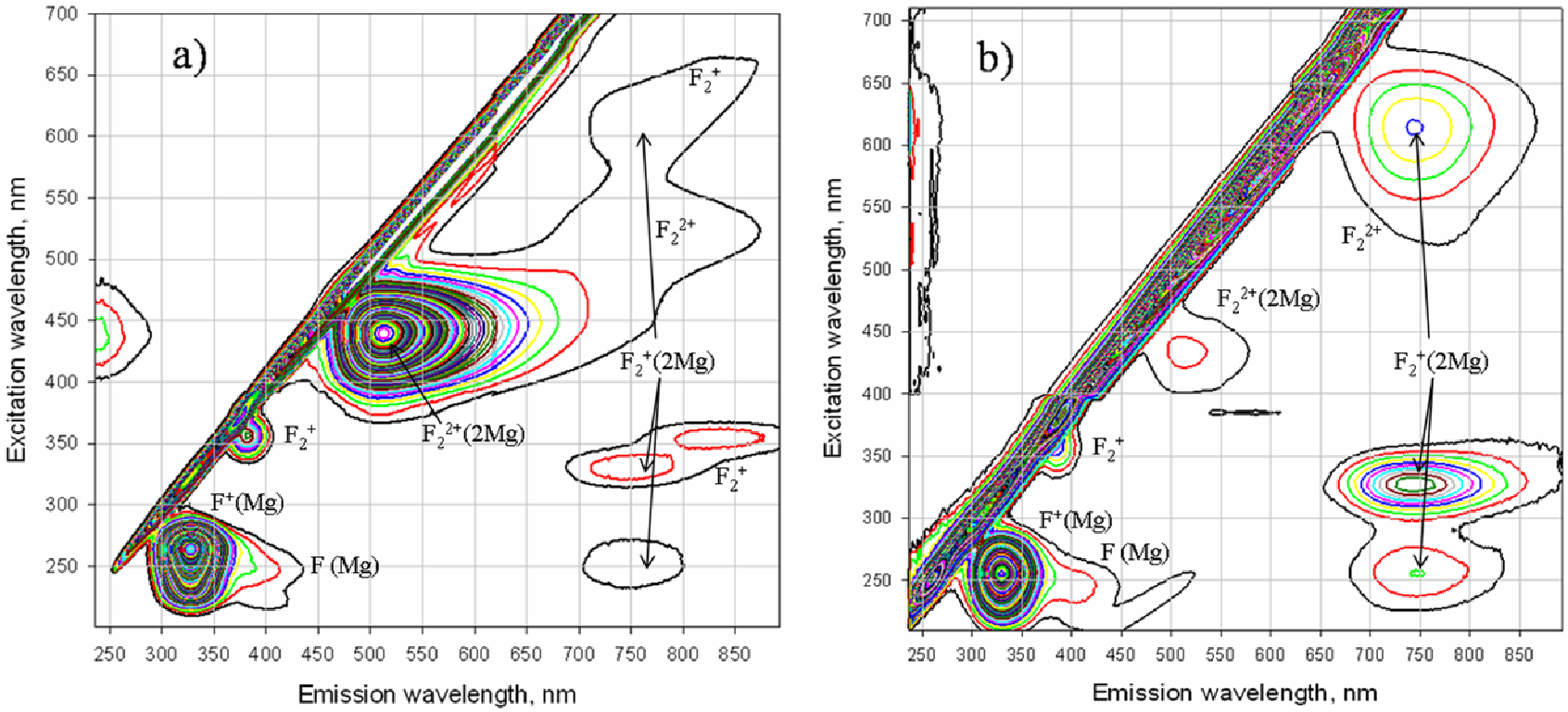

Figure 3.10 Photoluminescence spectra of Al_2O_3:C,Mg a) after thermal annealing at 600ºC for 25 hours (initial state) and b) after optical bleaching with 435 nm light showing the qualitative change in all visible excitation/emission bands. There were noticeable increases in luminescence of the 255/750, 335/750 and 620/750 nm bands with corresponding decreases in the 435/510 and 255/325 nm bands.

Figure 3.11 is the proposed model of bleaching and trapping mechanisms during irradiation with 435 nm light. The Mg perturbed centers are only shown because they are the primary centers for radiation dosimetry described in the remaining chapters.

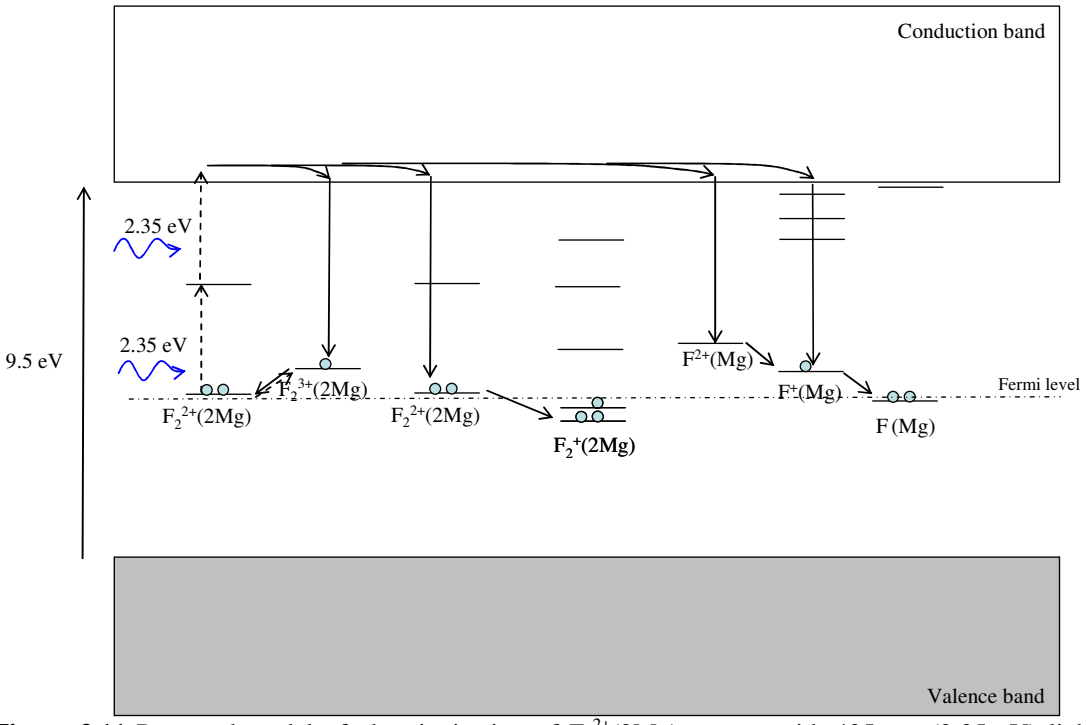

Figure 3.11 Proposed model of photoionization of F_2^{2+}(2Mg) centers with 435 nm (2.35 eV) light followed by subsequent trapping of the photoionized electrons demonstrating photoconversion of optically active, Mg perturbed centers in Al_2O_3:C,Mg. Dashed arrows represent results of photoionization while solid arrows represent results of electron trapping.

3.4.2 310 nm bleaching

Recent results from Ramirez et al (2005 and 2007) have suggested that the 355 nm absorption band is due to a combination of two excited states of the Mg perturbed F_2^+ color center and the third excited state centered at 620 nm. Preliminary results from Akselrod et al (2005) have suggested that the three excited states of Mg perturbed centers have absorption at 255 nm, 335 nm and 620 nm. The purpose of this section is to clarify which luminescence bands are most likely associated with F_2^+(2Mg) centers. It is important to understand which centers belong to this defect

because the 620/750 nm band is the primary luminescence center used for track detection as described in chapters 2 and 4. Illuminating the crystal with 310 nm (4eV) light allowed for direct photoionization of the 335 nm absorption band while avoiding photoionization of the 355 nm band.

Al_2O_3:C,Mg crystals were irradiated with 143 Gy of ^{90}Sr beta to convert F_2^{2+}(2Mg) into F_2^{+}(2Mg) and to obtain high absorption of the 300, 335, 355 and 620 nm bands (see section 3.6). The beta irradiated crystals were illuminated by pulsed, high peak power 310 nm light and OA was measured. Figure 3.12 demonstrates OA spectra throughout before and after bleaching. Figures 3.13 and 3.14 show absorption coefficients of the Mg perturbed and unperturbed color centers respectively as a function of number of pulses and Fig. 3.15 demonstrates PL spectra before and after irradiation with 310 nm light.

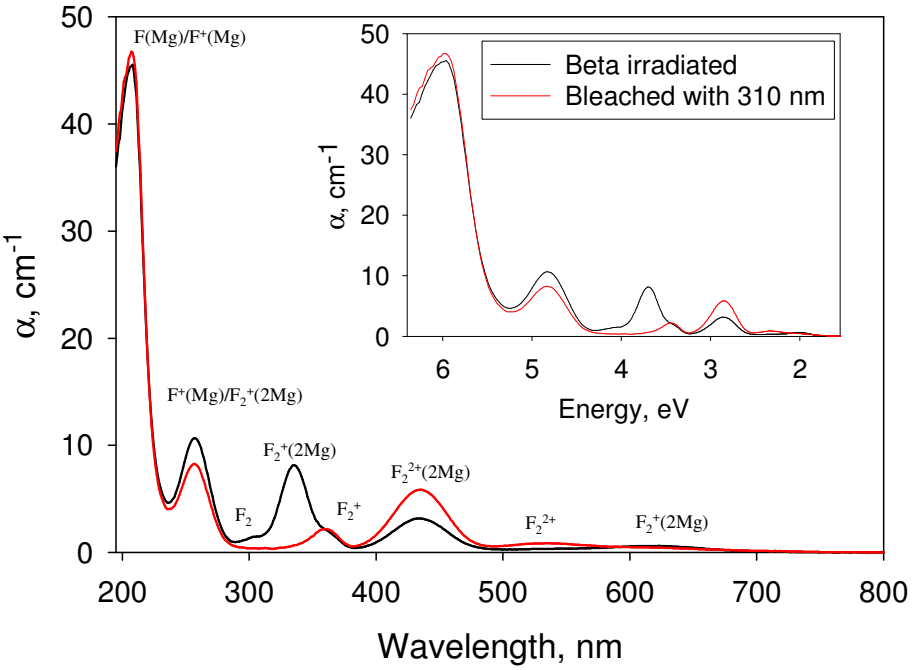

Figure 3.12 Optical absorption spectra for Al_2O_3:C,Mg irradiated with 143 Gy of beta (black line) and optically bleached with high peak power 310 nm, 7 ns pulses to deplete F_2^{+}(2Mg) centers. Beta irradiated Al_2O_3:C,Mg crystals were used to begin with large concentrations of F_2^{+}(2Mg) centers. The inset is the same spectrum but in terms of photon energy.

The change in 335 and 435 nm absorption bands are nearly mirror images of each other (Fig. 3.13) suggesting they are different charge states of the same defect. Direct stimulation of the 335/750 nm band resulted in a steep decline of the 255/750, 620/750 and 335/750 nm bands with a simultaneous increase in the 435/520 nm band. Simultaneous reduction in the 255, 335 and 620 nm absorption/excitation bands provides strong evidence that they belong to the same color center. Furthermore, the increase of the 435 nm band suggests that it is the same defect in a different charge state than one responsible for the 255, 335 and 620 nm bands (i.e. F_2^+(2Mg) was photoionized to produce F_2^{2+}(2Mg)). This is a reverse photochromic transformation of the same defect described in section 3.4.1.

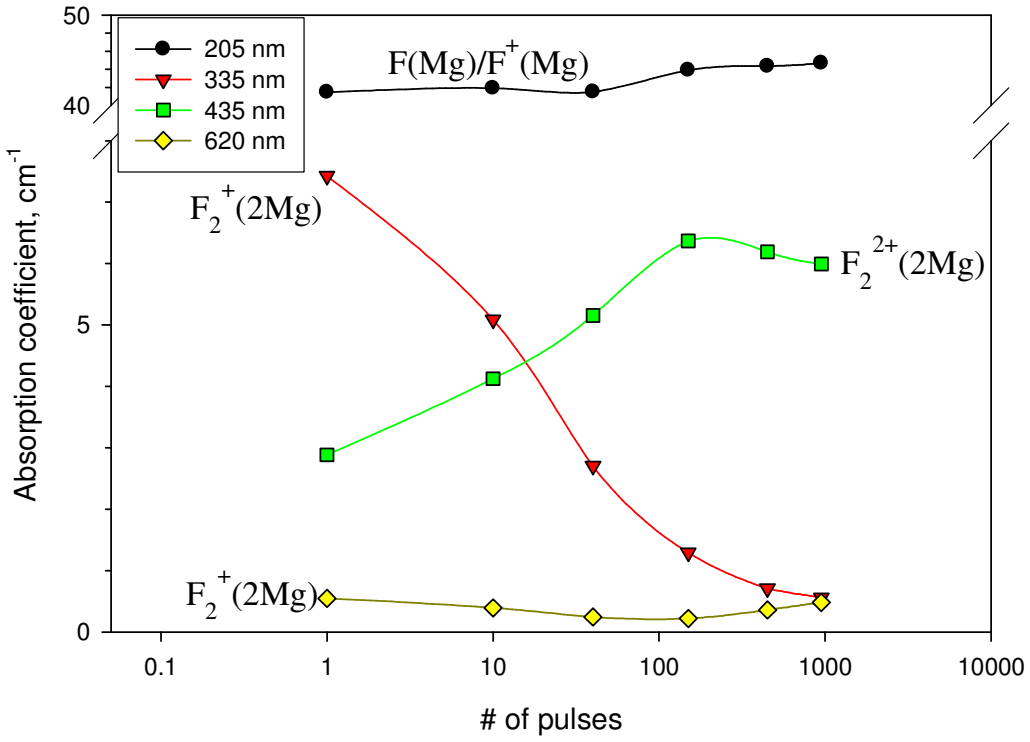

Figure 3.13 Absorption coefficients of the Mg perturbed color centers in Al_2O_3:C,Mg irradiated with 143 Gy of beta and optically bleached with high peak power 310 nm, 7 ns pulses as a function of bleaching pulses.

Changes in the 300, 355 and 520 nm absorption bands (Fig. 3.14) are also important to note. As the 300 nm band decreases, there is a subsequent increase the 355 nm band. Also, the decrease in the 355 nm band can be attributed to a small amount of photoionization. The decrease in 355 nm absorption over the last three bleaching iterations corresponds to the increase in 520 nm absorption. The convolution of absorption coefficients for the 300 and 520 nm bands is shown as a dashed line and is a mirror image of the 355 nm absorption. The 300, 355 and 520 nm absorption bands ought to belong to the same defect (aggregate double oxygen vacancy not perturbed by Mg – F_2, F_2^+ and F_2^{2+} centers) but in different charge states.

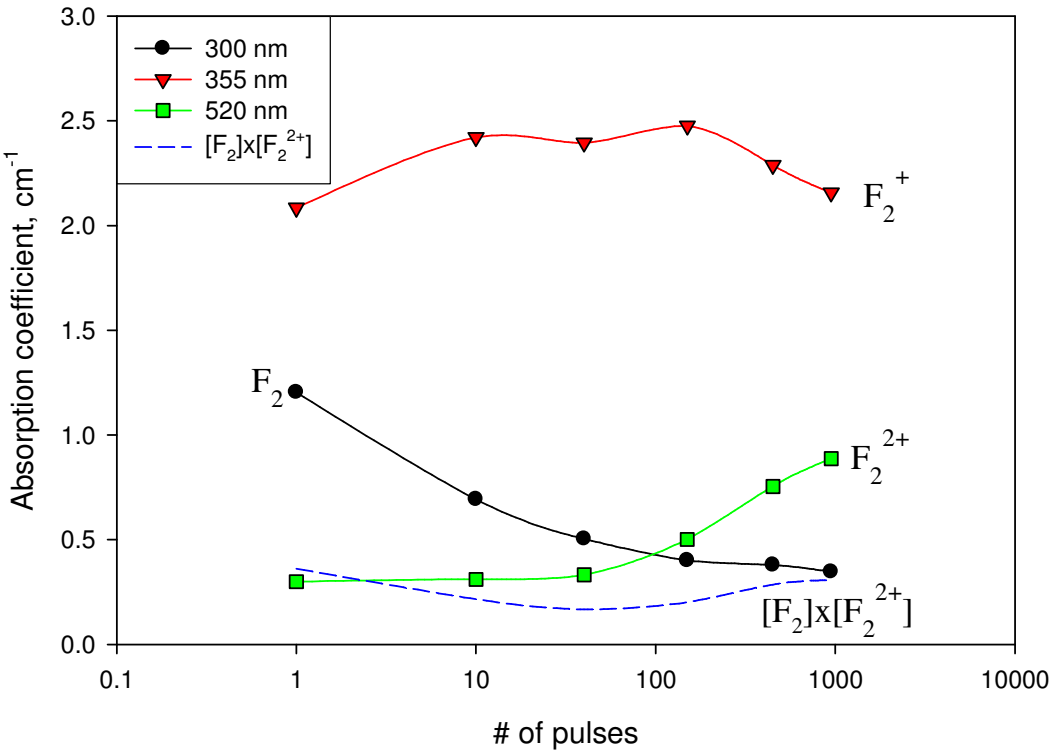

Figure 3.14 Absorption coefficients of the unperturbed aggregate defects in Al_2O_3:C,Mg irradiated with 143 Gy of beta and optically bleached with high peak power 310 nm, 7 ns pulses as a function of bleaching pulses. The dashed line is a convolution of the 300 nm and 520 nm absorption coefficients showing a mirrored image between the convolution and the 355 nm band.

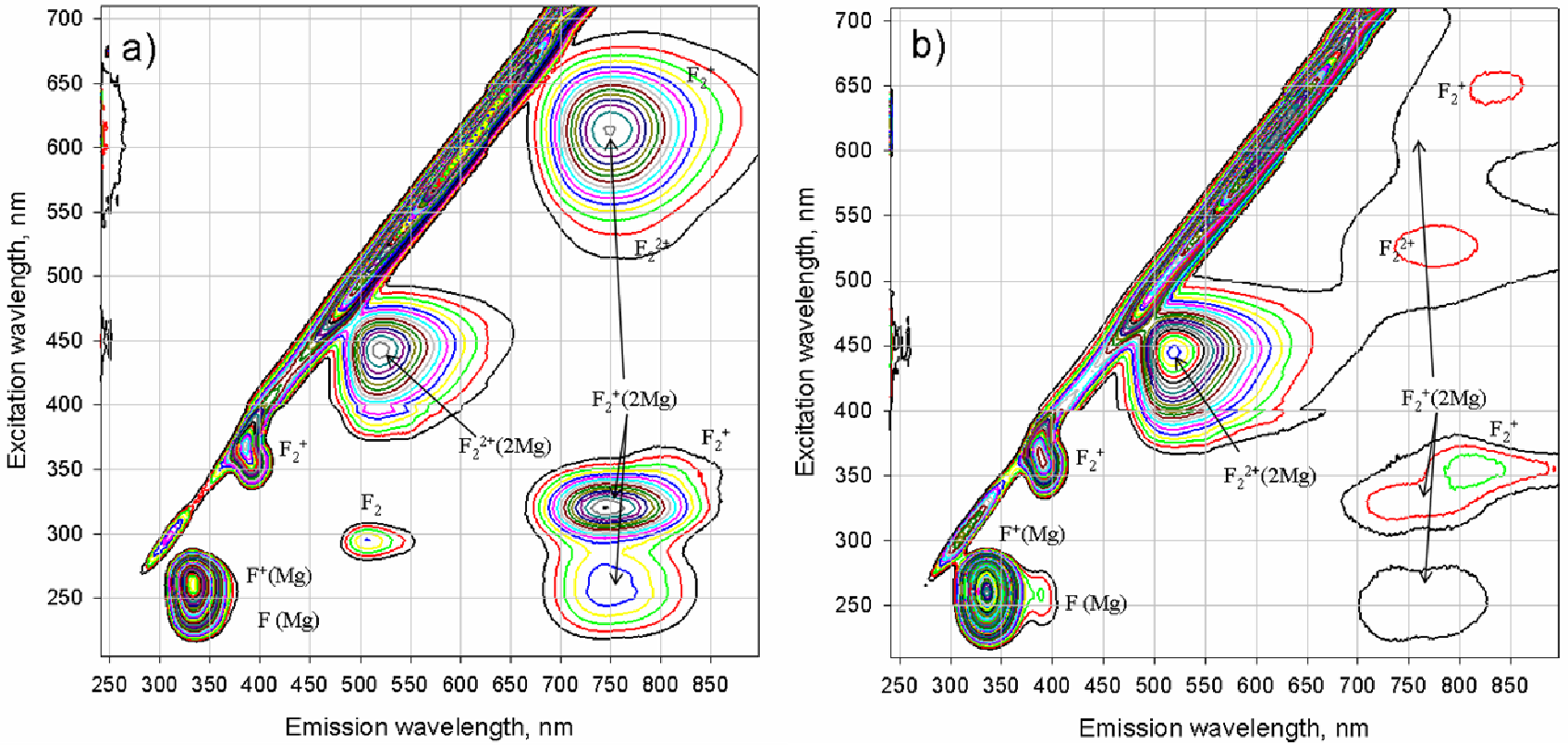

Figure 3.15 Photoluminescence spectra of Al_2O_3:C,Mg a) after irradiation with 143 Gy of beta from ^{90}Sr and b) after photoionization of the same crystal with 310 nm light demonstrating elimination of F_2 and F_2^+(2Mg) centers.

Excitation/emission bands at 355/825 and 650/825 nm became apparent after elimination of F_2^+(2Mg) centers. The 355/385, 355/825 and 650/825 centers are attributed to unperturbed F_2^+ centers. Theoretical predictions as well as spectroscopic measurements have shown that the F_2^+ center has three excited states near the same wavelengths as those observed in Fig. 3.15 (Ramirez et al, 2005 and Evans et al, 1994). The broad 650/825 excitation/emission band accounted for the relative increase in 620 nm absorption in Fig. 3.13. F_2 centers (300/500 nm band) were photoionized as an undesired result of the bleaching procedure to eliminate the 335 nm band. Photoionization of F_2(2Mg) centers (300/500 nm band) initially resulted in an increase of F_2^+ centers until F_2 centers were depleted. After F_2 centers were fully depleted, a small number of F_2^+ centers were photoionized at a low rate as a result of the 310 nm light being absorbed by the tail of the F_2^+ center absorption band accounting for the increase in 520 nm absorption and decrease in 355 nm absorption.

Bleaching mechanisms are illustrated in Fig. 3.16. Photoionization of the F_2^+(2Mg) center is assumed to happen through sequential two-photon absorption but thermally assisted single photon ionization may occur. The actual mechanism of photoionization is currently unknown. The photoionization mechanism is beyond the scope of this paper and will not be discussed further.

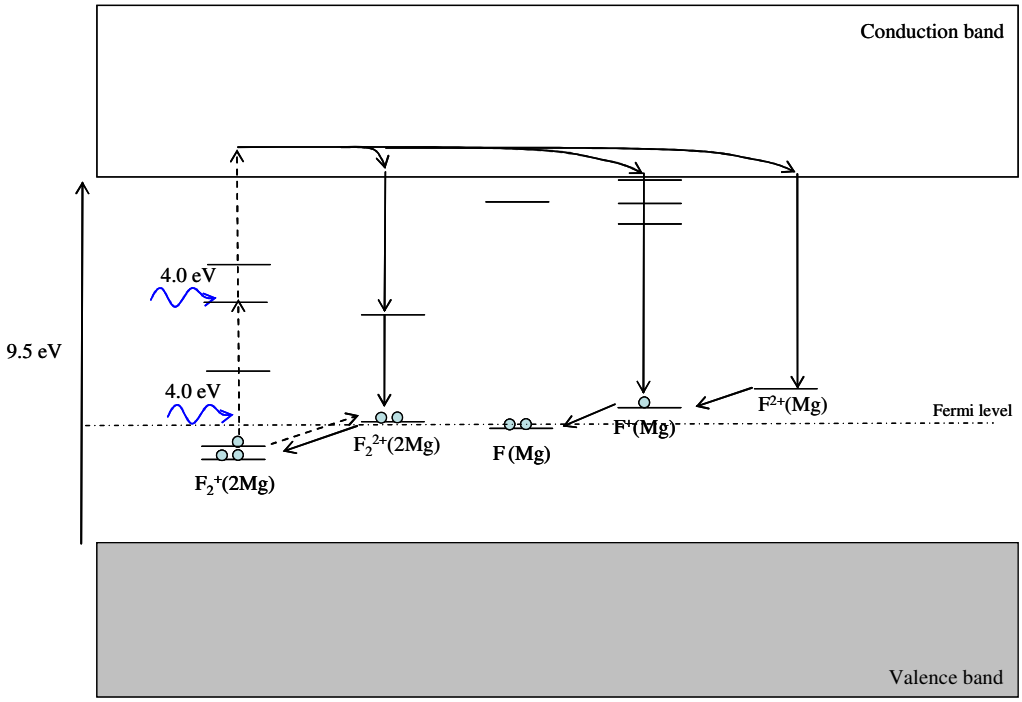

Figure 3.16 Flat band diagram of the proposed model of photoionization of F_2^+(2Mg) centers during irradiation with 310 nm (4.0 eV) light and subsequent trapping of electrons demonstrating photoconversion of optically active, Mg perturbed centers in Al_2O_3:C,Mg. Dashed arrows represent results of photoionization while solid arrows represent results of electron trapping.

3.4.3 Bleaching with 260 nm

Bleaching Al_2O_3:C,Mg with 260 nm light served two purposes, the first was to investigate the photochromic transformation of F^+(Mg) centers and the second was to probe electron trapping on other centers. Photobleaching of F^+ centers has been observed by other groups (Martynovich et al, 1985, Evans et al, 1995 and Ramirez et al, 2005) in neutron irradiated and additively colored Al_2O_3, but no consensus as to the mechanism of F^+ center bleaching has been reached. One theory is that photoionization of F^+ centers occur creating a free-electron and an empty oxygen vacancy (F^{2+}), but there has been no evidence of α-centers[3] in any previous optical

[3] α-centers capture electrons that are stimulated directly from the valence band resulting in a non-radiative absorption process (Fowler, 1968).

absorption measurements. Another theory is that the bottom of the F^+ center lies close enough to the valence band that a 4.77 eV photon has sufficient energy to promote an electron directly into the F^+ ground state; in this theory, popular electron donors include dislocations and interstitials caused by heavy bombardment of radiation. A third theory is that photoionization of the F center occurs leading to an electron being captured by F^+ centers, but direct photoionization of F centers has been shown to increase F^+ center concentration.

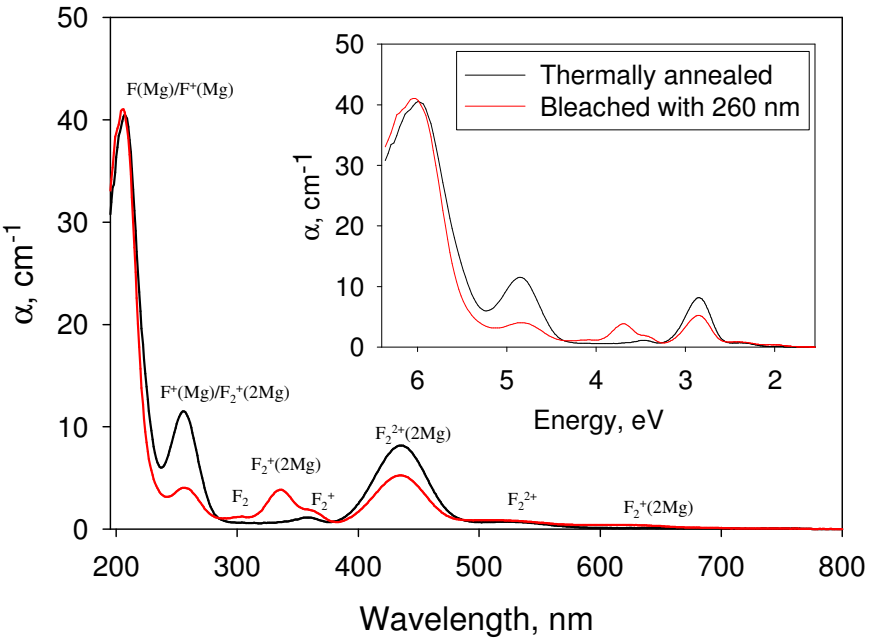

Figure 3.17 Optical absorption spectra for Al_2O_3:C,Mg enhanced by thermal annealing at 600ºC (black line) and optically bleached with high peak power 260 nm, 7 ns pulses to deplete the concentration of F^+ centers providing evidence to support photoionization of F^+ centers. The inset is the same spectrum but in terms of photon energy.

In order to photoionize F^+(Mg) centers, Al_2O_3:C,Mg crystals were illuminated by pulsed, high peak power 260 nm light and OA was measured. Based on studies by Martynovich et al (1985), Ramirez et al (2005 and 2007) and our own unpublished results, it seems likely that photoionization can occur as a result of single photon excitation, but high peak power pulsed laser light was used in this study to ensure photoionization. Figure 3.17 demonstrates the OA spectrum of the crystal before and

after bleaching. Figures 3.18 and 3.19 show absorption coefficients of the Mg perturbed and unperturbed color centers respectively as a function of number of pulses delivered to the crystal. Figure 3.19 demonstrates PL spectra of Al_2O_3:C,Mg before and after bleaching.

The absorption coefficient of the 255 band decreases in the first 200 pulses accompanied by a decrease in the 435 nm absorption coefficient and an initial increase in 620, 335, 355 and 300 nm absorption coefficients. Changes in absorption coefficients plateau for 400 pulses followed by further decrease in the 255 nm band, increasing 435 nm absorption and decreasing 620, 335, 355 and 300 nm absorption.

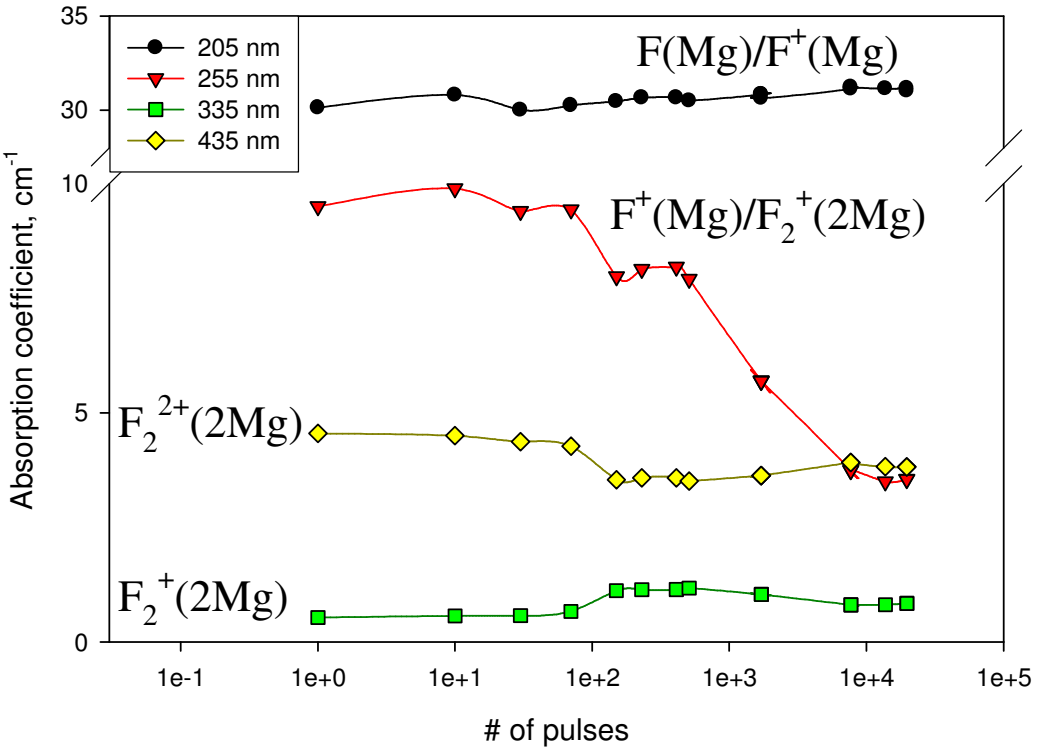

Figure 3.18 Absorption coefficients of the Mg perturbed color centers in Al_2O_3:C,Mg optically bleached with high peak power 260 nm, 7 ns pulses as a function of bleaching pulses demonstrating the redistribution of charge after photoionization of F^+(Mg) and F_2^{2+}(2Mg) centers.

Figure 3.19 indicates that absorption for both F_2^+ and F_2 centers increase as a result of photoionization of F^+(Mg) centers. F_2^{2+} centers capture photoionized electrons creating F_2^+ centers which subsequently capture electrons creating neutral F_2 centers.

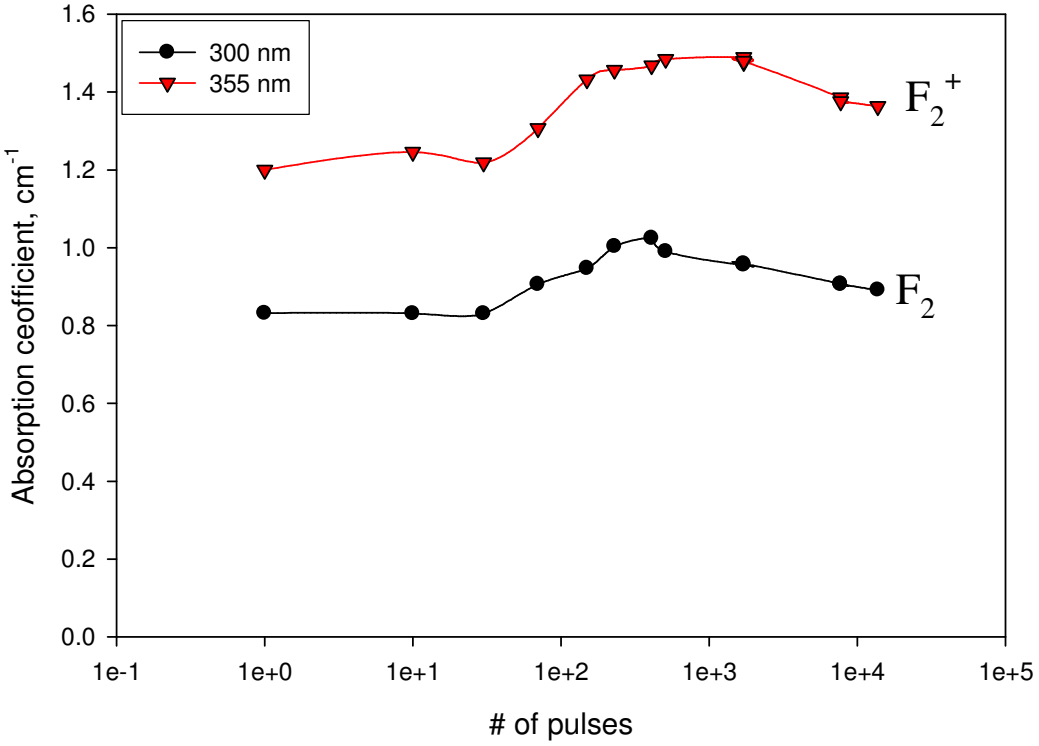

Figure 3.19 Absorption coefficients of the unperturbed color centers in Al_2O_3:C,Mg optically bleached with high peak power 260 nm, 7 ns pulses as a function of bleaching pulses demonstrating the redistribution of charge after photoionization of F^+(Mg) and F_2^{2+}(2Mg) centers.

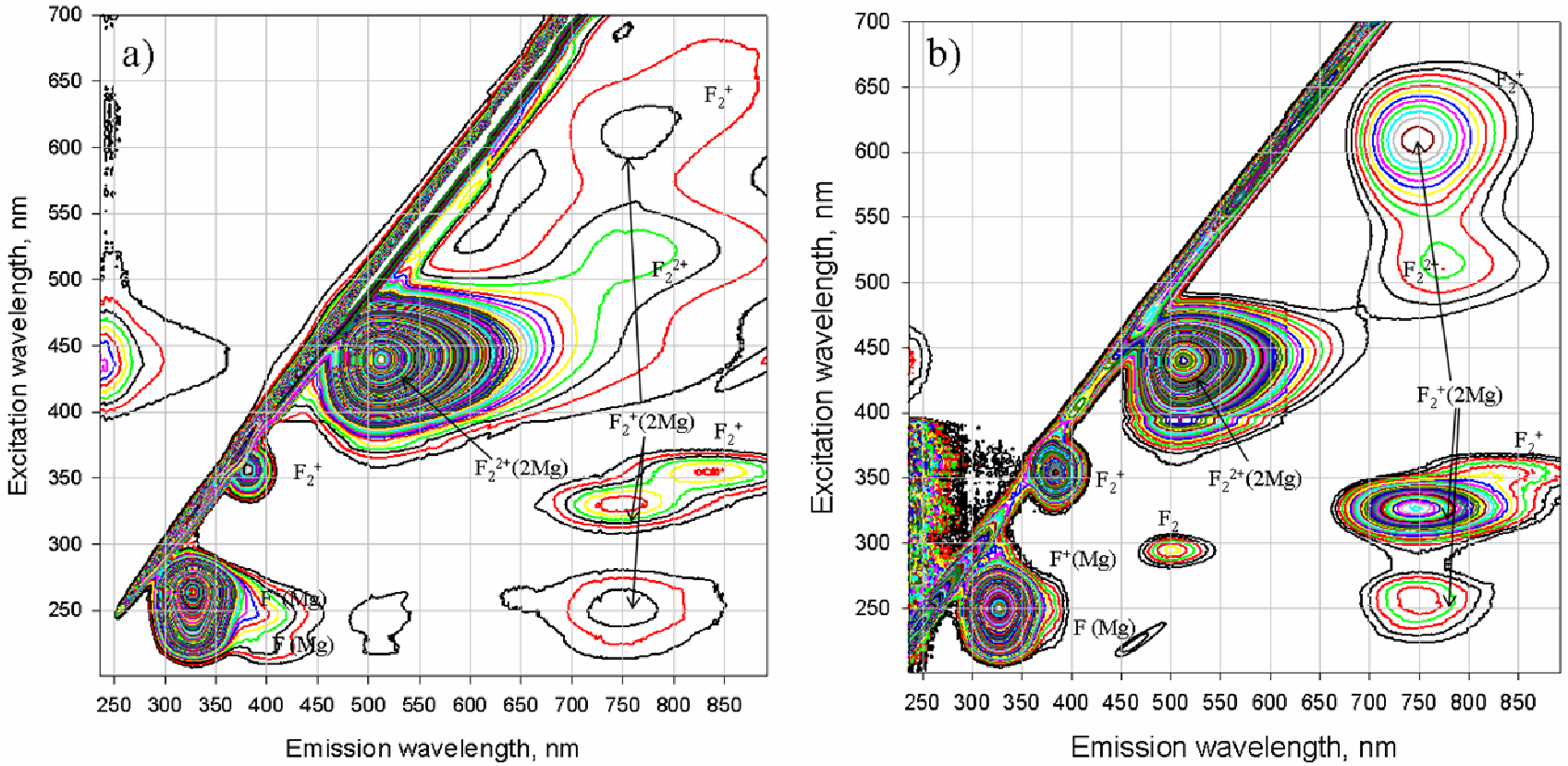

Figure 3.20 Photoluminescence spectra of Al_2O_3:C,Mg a) after thermal annealing at 600ºC for 25 hours (initial state) and b) after optical bleaching with 260 nm light showing the qualitative change in all visible excitation/emission bands. The most noticeable changes are the increases in the 255/750, 335/750, 620/750 (attributed to F_2^+(2Mg) centers) and 300/500 (attributed to F_2 centers) bands; the decrease in 255/325 (attributed to F^+(Mg) centers) and 435/510 (attributed to F_2^{2+}(2Mg) centers) bands is less obvious in this representation.

3.4.3.1 Photoconversion of the F^+(Mg) center

Redistribution of charge during and after bleaching changes the concentrations of the visible color centers suggesting that F^+(Mg) centers and F_2^+(2Mg) centers are photoionized. Also, changes in all absorption/emission bands suggest that electrons are not promoted from the valence band directly into the ground state of F^+ centers. An alternative explanation is that simultaneous 2-photon absorption photoionizes valence electrons. The energy of 260 nm is 4.77 eV and the band gap of Al_2O_3 is approximately 9.5 eV therefore the excitation light would have sufficient energy to ionize valence electrons assuming 2-photon absorption occurs. This explanation is however unlikely because the pulse width of the stimulation beam should be on the order of picoseconds to have sufficient probability of simultaneous 2-photon absorption. The most likely explanation is that F^+(Mg) centers are photoionized creating F^{2+}(Mg) centers.

3.4.3.2 Trapping of photoionized electrons

Figure 3.18 clearly shows an initial decrease in 435 nm absorption with a corresponding increase in 335 nm absorption. The centers with absorption centered at 435 nm capture electrons and transform into centers with 335 nm absorption thus providing further evidence that our assignment of the 435 nm band to F_2^{2+}(2Mg) and the 335 nm band to F_2^+(2Mg) centers is correct. The electron liberated from the F^+(Mg) center is efficiently captured by F_2^{2+}(2Mg) centers initially increasing F_2^+(2Mg) center concentration. The plateau region of Fig. 3.17 occurs as a result of a temporary equilibrium between the number of F_2^+(Mg) centers photoionized and the

number of F_2^+(2Mg) centers created. The final decline of the 255 nm band occurs through photoionization of both the F^+(Mg) and F_2^+(2Mg) centers as evidenced by the decrease in absorption of the 620 and 335 nm absorption bands concomitantly with the small increase of the 435 nm absorption band. F_2^{2+} and F_2^+ centers also trap electrons (less efficiently than F_2^{2+}(2Mg) centers) thus increasing the concentrations of F_2^+ and F_2 centers respectively. A 1% increase in 205 nm absorption indicates that F^+(Mg) centers capture a fraction of the photoionized electrons thus becoming F(Mg) centers. The proposed photoconversion mechanisms of the Mg perturbed centers during and immediately after 260 nm stimulation are shown in Fig. 3.21. Sequential two-photon absorption is shown in the model, but it still may be possible to use single photon absorption to photoionize the F^+(Mg) center.

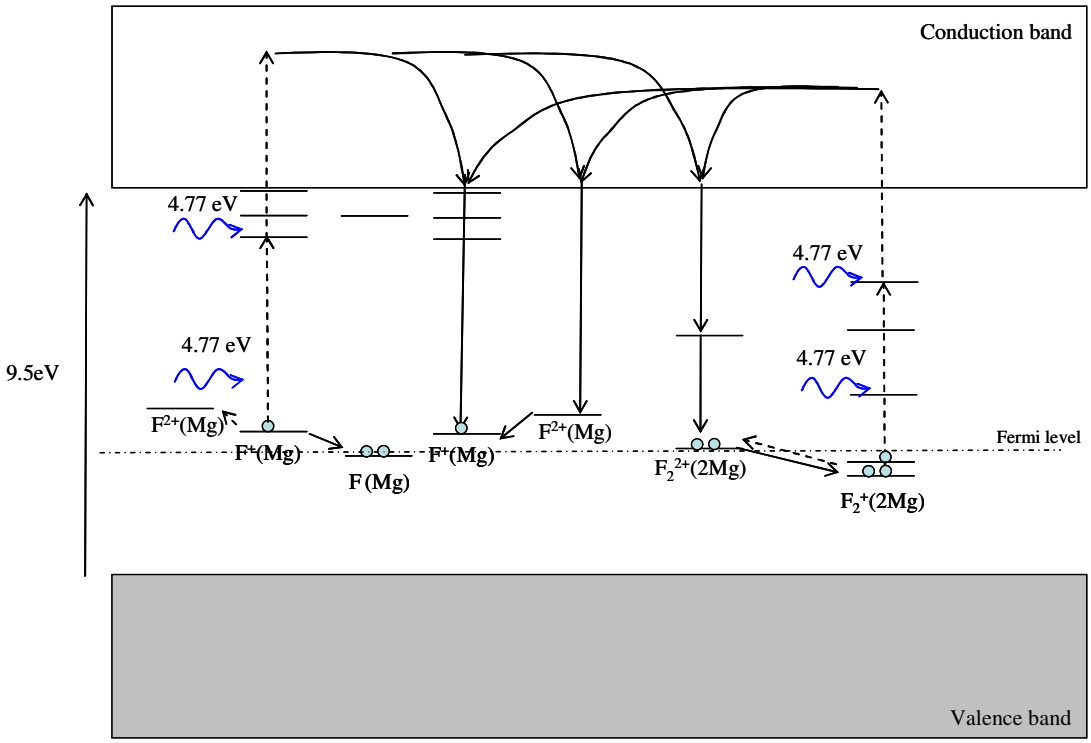

Figure 3.21 Flat band diagram of the proposed method of photoionization of F^+(Mg) and F_2^+(2Mg) centers during irradiation with 4.77 eV (260 nm) light and subsequent trapping of electrons demonstrating photoconversion of optically active centers in Al_2O_3:C,Mg. Dashed arrows represent results of photoionization while solid arrows represent results of electron trapping.

3.4.4 Final assignment of absorption/emission bands in Al_2O_3:C,Mg

One of the primary objectives for performing photoionization experiments was to correctly assign defects to the appropriate absorption/emission bands which will give a better understanding of radiation interaction and track formation in Al_2O_3:C,Mg. Proper defect assignments can also lead to improvements in the crystal properties or processing of the FNTD (see section 4.3). Table 3.1 lists the absorption/emission bands and gives their assignments with references to the evidence of their assignment.

Table 3.1 Assignment of defects to absorption/emission bands in Al_2O_3:C,Mg on the basis of OA, PL, thermal annealing, photoconversion and previous literature data.

Defect	Absorption/emission		Basis
	nm	eV	
F/F(Mg)	205/415	6.00/3.00	OA and Evans et al, 1994
F^+(Mg)	205/325	6.00/3.83	OA polarization dependence, PL spectra and Evans et al, 1994
	229/325	5.40/3.83	
	255/325	4.84/3.83	
F_2^+(2Mg)	255/750	4.84/1.66	Photoconversion with 435, 310 and 260 nm
	335/750	3.70/1.66	
	620/750	2.00/1.66	
F_2^{2+}(2Mg)	435/520	2.85/2.38	Thermal annealing , photoconversion, Evans et al, 1985, Martynovich et al, 1985 and Ramirez et al, 2005
F_2	300/500	4.00/2.48	Photoconversion with 310 and 260 nm and Evans et al, 1994
F_2^+	355/385	3.50/3.22	Photoconversion with 310 and 260 nm and Evans et al, 1994
	355/825	3.50/1.50	
	650/825	1.91/1.50	
F_2^{2+}	520/770	2.38/1.61	Thermal annealing and Photoconversion with 310 and 260 nm

3.5 Optical properties of Magnesium perturbed centers in Al_2O_3:C,Mg

3.5.1 F^+(Mg) centers

Optical absorption and photoluminescence measurements (Figs. 3.3 and 3.4) of Al_2O_3:C,Mg show the absorption and emission bands of F^+(Mg) centers occur at the same energies as F^+ centers in neutron irradiated Al_2O_3 (Evans, 1995) leading to the conclusion that, at room temperature, the presence of Magnesium has negligible effect on the energy levels of F^+ centers (i.e. small perturbation). Negligible perturbation allows us to adopt the configurational coordinate diagram (Fig. 3.22) Evans used to describe F^+ centers in Al_2O_3 (Evans et al, 1995) for F^+(Mg) centers in Al_2O_3:C,Mg.

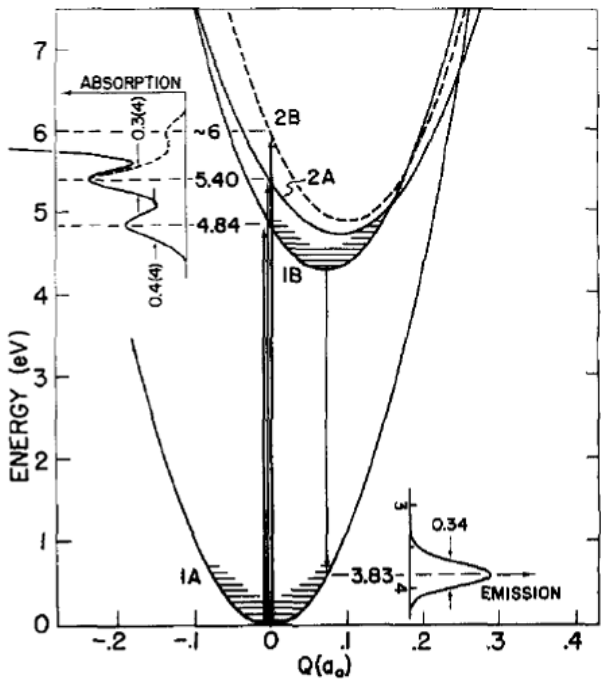

Figure 3.22 Configuration coordinate diagram of F^+ defects in neutron irradiated Al_2O_3 crystals illustrating luminescence mechanisms and electron-phonon interactions (Evans et al, 1995) that can be applied to F^+(Mg) defects in Al_2O_3:C,Mg.

A single emission band for all three excited states of the F^+(Mg) center is explained by the electron-phonon interaction and is illustrated by the intersection of the excited state parabolas in Fig. 3.22. Electron-phonon interaction in F^+ centers is so strong that, even at low temperatures, there is enough thermal energy to result in non-radiative transitions from the 2A and 2B excited states to the 1B state. There is no evidence to suggest that F^+(Mg) centers will behave different from F^+ centers, but further investigations should still be done on F^+(Mg) centers.

3.5.2 F_2^{2+}(2Mg) centers

F_2^{2+} centers have not been investigated in as much detail as the F^+ center except for their identification in neutron irradiated Al_2O_3 by Martynovich et al (1985) with an absorption band centered at 460 nm (2.7 eV) and an emission band at 563 nm (2.2 eV). Similar bands were observed in Al_2O_3:C,Mg and assigned as F_2^{2+}(2Mg) centers with an absorption band centered at 435 nm (2.85 eV) and an emission band at 520 nm (2.38 eV). The difference in absorption and emission energies from neutron irradiated Al_2O_3 can be attributed to the perturbation from the two magnesium ions. More detailed discussions of F_2^{2+}(2Mg) centers can be found in Akselrod et al, 2003 and Sanyal et al, 2005.

3.5.3 F_2^+(2Mg) centers

Three electron aggregate F_2^+ centers have been observed and identified in neutron irradiated Al_2O_3 (Pogatshnik et al, 1987). Experimental observations and current theory suggest that F_2^+ centers ought to have three excited states. In neutron

irradiated Al_2O_3, F_2^+ centers had an absorption/emission band at 355/380 nm (3.50/3.26 eV) (Evans et al, 1994). In this work we suggest that the 355/380 nm band in Al_2O_3:C,Mg is due to unperturbed F_2^+ centers along with absorption/emission bands at 355/825 nm (3.50/1.50 eV) and 650/825 nm (1.91/1.50 eV) which is consistent with the theory of Ramirez et al. (2005).

Magnesium perturbed F_2^+(2Mg) centers appeared in addition to the unperturbed F_2^+ centers. The presence of magnesium not only shifts the ground and excited states to higher energies but also could change the type of transition that occurs between the ground state and first excited state. F_2^+(2Mg) centers have three excited states with 750 nm emission suggesting that absorption and emission for all three states occur as a result of the same type of transition similar to the F^+ centers discussed above. A configurational coordinate diagram of the F_2^+(2Mg) center is seen in Fig. 3.23. At room temperature there is sufficient thermal energy to allow for non-radiative transitions from the 2B and 2A excited states to the 1B excited state accounting for the single emission band centered at 750 nm. It is possible that, at low temperatures, another higher energy emission band may appear from the 2A or even 2B states.

The accuracy of the diagram can be improved by better characterizing the electron-phonon interaction (i.e. performing photoluminescence measurements at low and high temperatures). Investigating the structure (obtaining zero-phonon lines if possible), temperature dependences on the width of the absorption/emission bands and thermal quenching of the F_2^+(2Mg) center will provide sufficient information to fully characterize the optical properties of the F_2^+(2Mg) center. Preliminary thermal quenching measurements suggest that the ground state and first excited state

parabolas intersect sooner than those of the ground state and second and third excited states as depicted in the diagram.

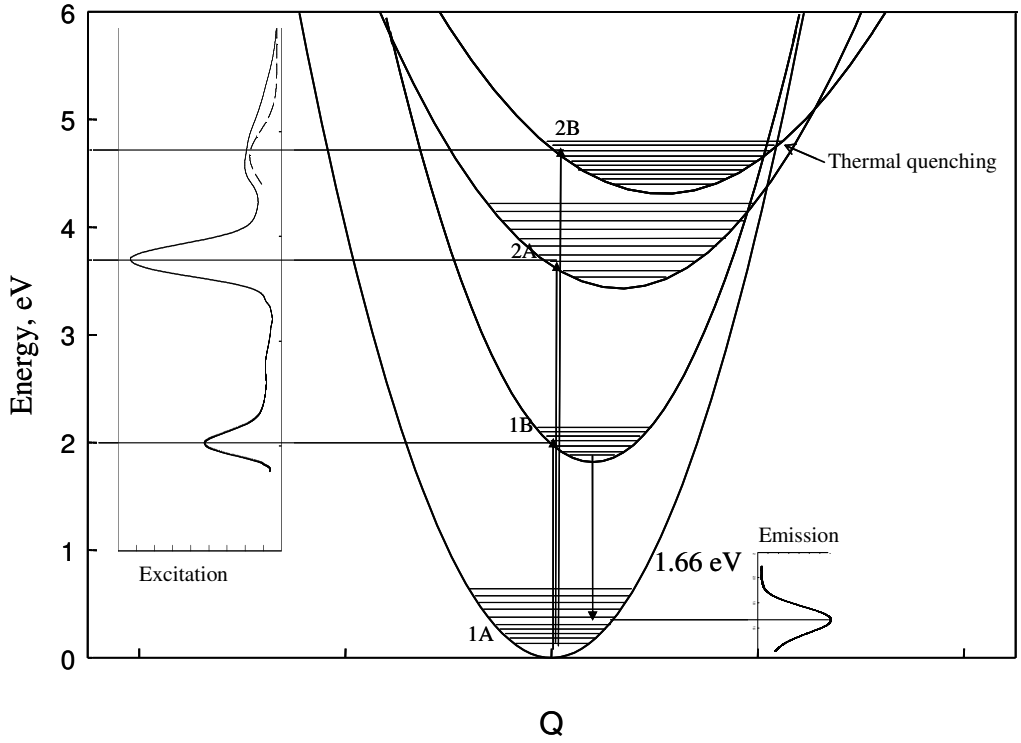

Figure 3.23 Configurational coordinate diagram of an F_2^+(2Mg) defect in Al_2O_3:C,Mg illustrating its luminescence mechanisms. The measured absorption spectrum for 750 nm luminescence is shown on the left and the emission spectrum is shown on the bottom right. The dashed curve in the absorption spectrum is the 255 nm peak deconvolved from an unknown high energy band centered at 240 nm.

3.6 Radiochromic transformations of defects

Imaging of radiation induced fluorescence relies on the ability of the material to trap and store charge resulting from ionizing radiation and to be able to distinguish radiation induced fluorescence from background fluorescence inherent in the material. Investigation of defect transformations in Al_2O_3:C,Mg as a result of ionizing radiation is important to optimize the crystal for radiation detection applications.

Radiation interaction in material generates an abundance of electron-hole pairs as discussed in chapter 2. After thermalization, electrons and holes are captured by electron and hole traps producing a defect with a change of net charge of -1 for electron traps and +1 for hole traps. F centers are historically accepted as hole traps, so during irradiation, F centers will capture holes to become F^+ centers. It was determined, through photoionization of F^+(Mg) centers, that F_2^{2+}(2Mg) centers are electron traps and as such transform into F_2^+(2Mg) centers as a result of irradiation.

Al_2O_3:C,Mg crystals were irradiated with 1 - 800 Gy of x-rays, 4 Gy of ^{137}Cs gamma and 13, 43, 78 and 143 Gy of $^{90}Sr/^{90}Y$ beta. PL and OA measurements were made on the crystals before and after irradiation. Differences in PL spectra for Al_2O_3:C,Mg before and after irradiation are seen Fig. 3.24. The differences in peak absorption coefficients for various bands were plotted as a function of delivered dose in Fig. 3.25 for Mg perturbed centers and in Fig. 3.26 for unperturbed centers. The difference in 750 nm emission for all three absorption bands as a function of dose is plotted in Fig. 3.27. The majority of the discussion will focus on Mg perturbed defects, but it is important to note that there are small changes in the absorption bands in the unperturbed centers for future investigations.

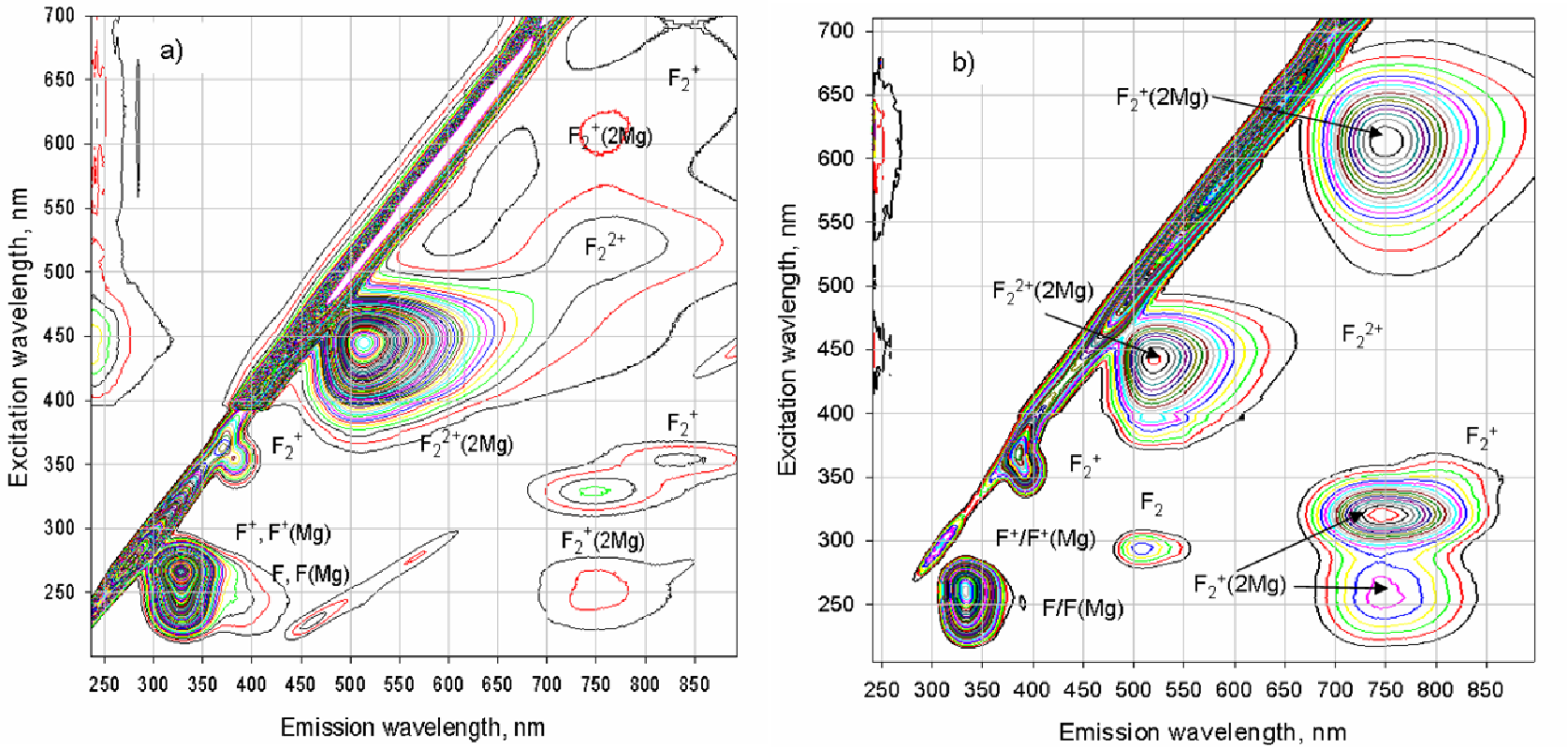

Figure 3.24 2D photoluminescence spectrum of Al_2O_3:C,Mg a) thermally annealed at 600°C and b) irradiated with 143 Gy of beta showing most of the visible excitation/emission bands.

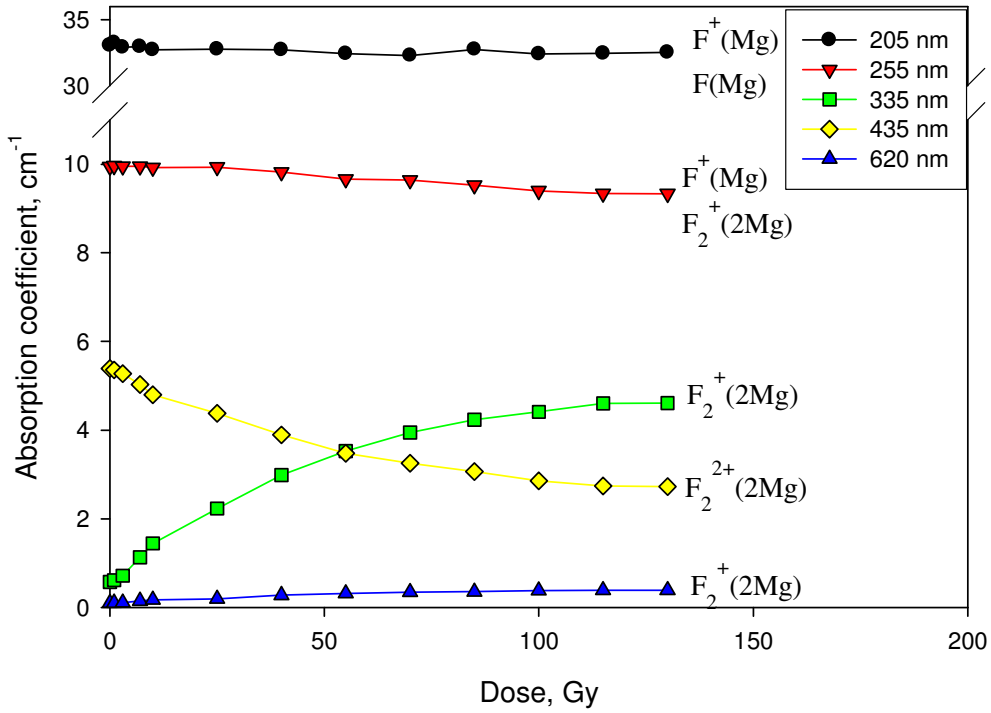

Figure 3.25 Absorption coefficient for Mg perturbed color centers in Al_2O_3:C,Mg as a function of x-ray dose. The absorption coefficients for all bands are shown to change nonlinearly with x-ray dose.

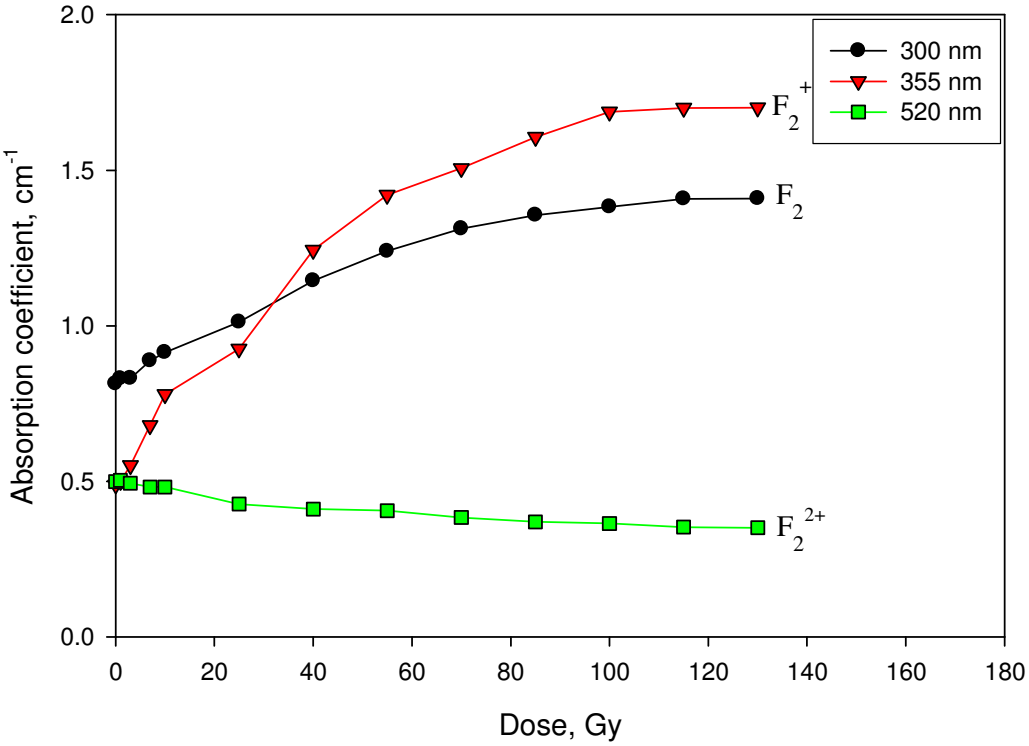

Figure 3.26 Absorption coefficient for unperturbed color centers in Al_2O_3:C,Mg as a function of x-ray dose. The absorption coefficients for all bands are shown to change nonlinearly with x-ray dose.

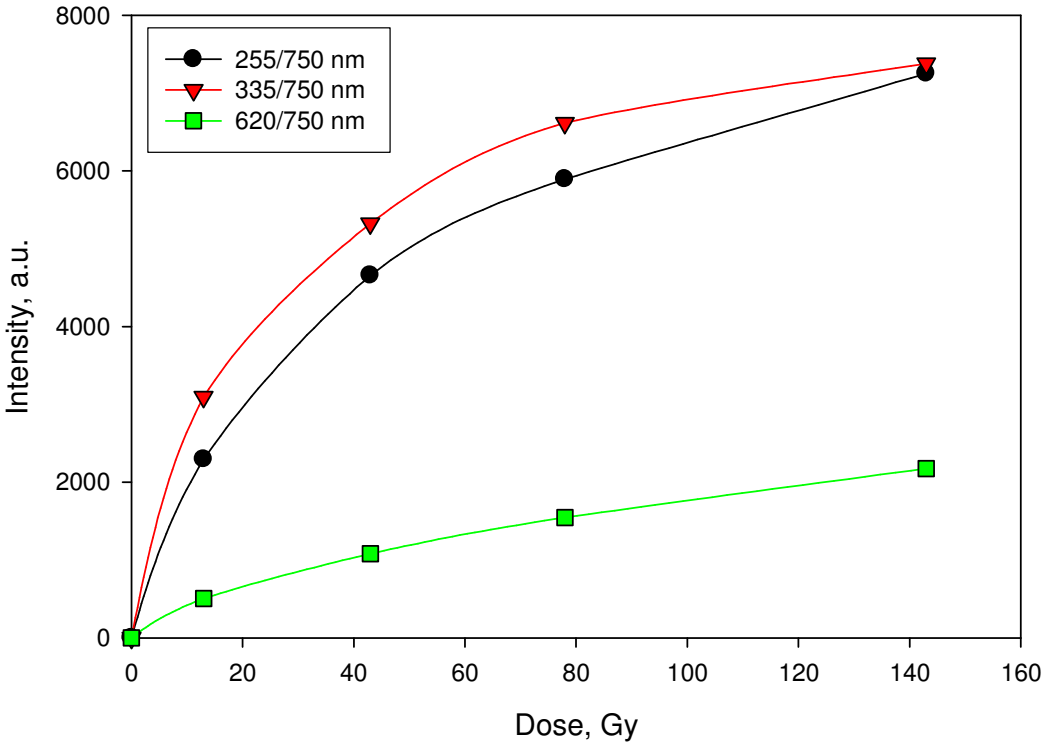

Figure 3.27 Photoluminescence peak heights as a function of dose for the 750 nm emission band. Initial background luminescence was subtracted. 750 nm luminescence is non-linear with dose and saturates near 100 Gy.

Figures 3.25 and 3.26 contain several key features. Changes in color center concentrations stop after approximately 100 Gy which means that the saturation dose of Al_2O_3:C,Mg is around 100 Gy, consistent with Al_2O_3:C. Every absorption band changes as a function of dose meaning that the observable color centers compete with each other for either electrons or holes. The most notable competitors are the F_2^{2+}(2Mg), F_2^{+}(2Mg) and F^{+}(Mg) because they exhibit the largest changes. F^{+}(Mg) centers show large changes in concentration suggesting that they are likely the main competitor for free electrons to F_2^{2+}(2Mg) centers. F_2^{+}(2Mg) centers are created at the expense of F_2^{2+}(2Mg) via electron capture on F_2^{2+}(2Mg) centers consistent with the results from photoconversion with 260 nm light.

It was originally assumed that F_2^{+}(2Mg) centers have a net positive Coulomb potential with respect to the lattice and thus be considered as electron traps. If we assume

the contrary, that F_2^+(2Mg) centers have a negative net Coulomb potential with respect to the crystal lattice, then F_2^+(2Mg) centers may be expected to act as hole traps. Additionally, no radiation induced F_2(2Mg) centers have been conclusively identified suggesting that F_2^+(2Mg) centers may be hole traps. If F_2^+(2Mg) centers are hole traps, then saturation of F_2^+(2Mg) and F_2^{2+}(2Mg) centers can be explained by equilibrium between the transformation of F_2^{2+}(2Mg) centers into F_2^+(2Mg) (F_2^+(2Mg) + $h \rightarrow F_2^{2+}$(2Mg)) center and vise-versa. Non-linear dose response can also be explained by F_2^+(2Mg) capturing holes because the probability of capturing a hole would increase with the concentration of F_2^+(2Mg) centers. A similar argument can be made if F_2^+(2Mg) centers are electron traps. Creation of F_2(2Mg) centers at the expense of F_2^+(2Mg) centers could also lead to non-linear dose response, but this does not sufficiently explain the saturation effect observed in F_2^{2+}(2Mg) centers.

Rate equations (eq. 3.1-3.3) were written and numerically solved for the initial conditions corresponding to the initial absorption measurements shown in Fig. 3.25. In order to duplicate the ratio of final concentrations of F_2^{2+}(2Mg) to F_2^+(2Mg) centers, it was assumed that neutral aggregate centers (also hole traps) exist in as-grown and annealed crystals (i.e. F(Mg)+F(Mg)$\rightarrow F_2$(Mg)) but cannot be observed optically. The change in absorbing centers as functions of dose are given as

$$\frac{d\left[F_2^{2+}(2Mg)\right]}{dD} = -\beta\left[F_2^{2+}(2Mg)\right] + \gamma\left[F_2^{+}(2Mg)\right] \tag{3.1}$$

$$\frac{d\left[F_2^{+}(2Mg)\right]}{dD} = -\gamma\left[F_2^{+}(2Mg)\right] + \beta\left[F_2^{2+}(2Mg)\right] + \delta\left[F_2(2Mg)\right] \tag{3.2}$$

$$\frac{d\left[F_2(2Mg)\right]}{dD} = -\delta\left[F_2(2Mg)\right] \tag{3.3}$$

where D is the dose, β is the electron trapping cross section of F_2^{2+}(2Mg) centers, γ is the hole trapping cross section of F_2^{+}(2Mg) centers and δ is the hole trapping cross section of F_2(2Mg) centers. The numerical solutions are compared to X-ray dose dependences in Fig. 3.28. Very good agreement with OA data provides strong evidence that F_2^{+}(2Mg) centers are actually hole traps.

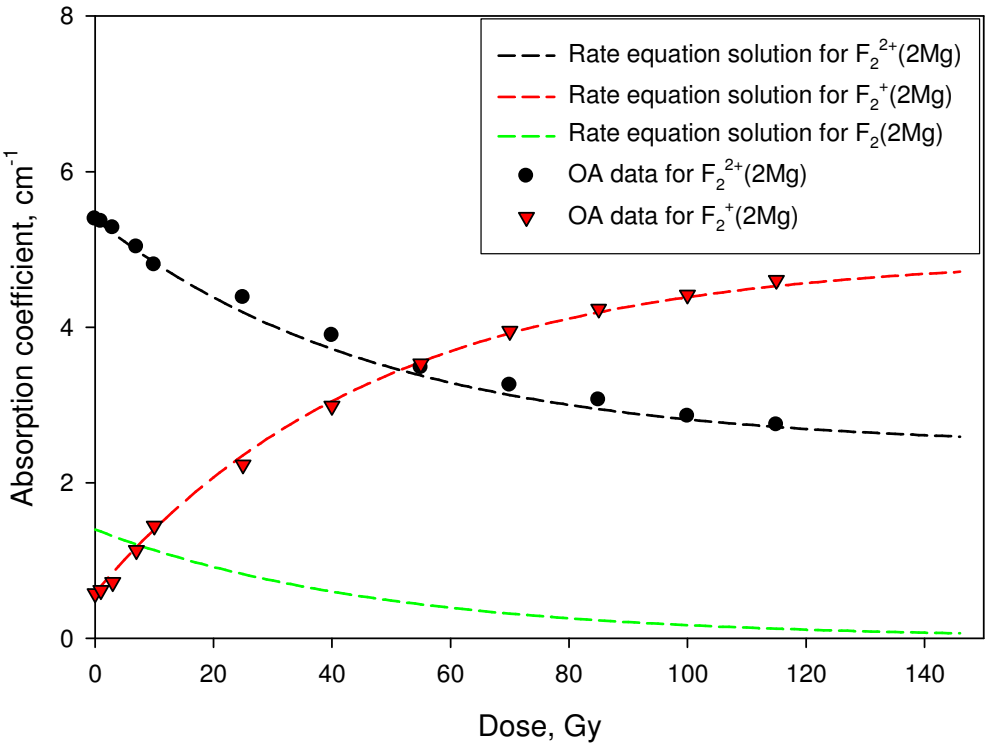

Figure 3.28 Numeric solutions to the rate equations (3.1-3.3) assuming F_2^{+}(2Mg) and F_2(2Mg) centers are hole traps and F_2^{2+}(2Mg) centers are electron traps. Electron and hole trapping cross sections were adjusted to fit optical absorption data.

Figure 3.29 illustrates trapping mechanisms in Al_2O_3:C,Mg during ionization. Transitions resulting from electron trapping are indicated by the solid black arrows and transitions resulting from hole trapping are indicated by dashed arrows. Shallow traps are present in Al_2O_3:C,Mg which are labeled by "Other e^- trap" in Fig. 3.29. It is suggested that F(Mg) centers act as hole traps converting F(Mg) into F^+(Mg) centers during

irradiation. There may be several other hole traps that have not been identified in Al_2O_3:C,Mg and are shown as "Unknown h trap" in Fig. 3.29.

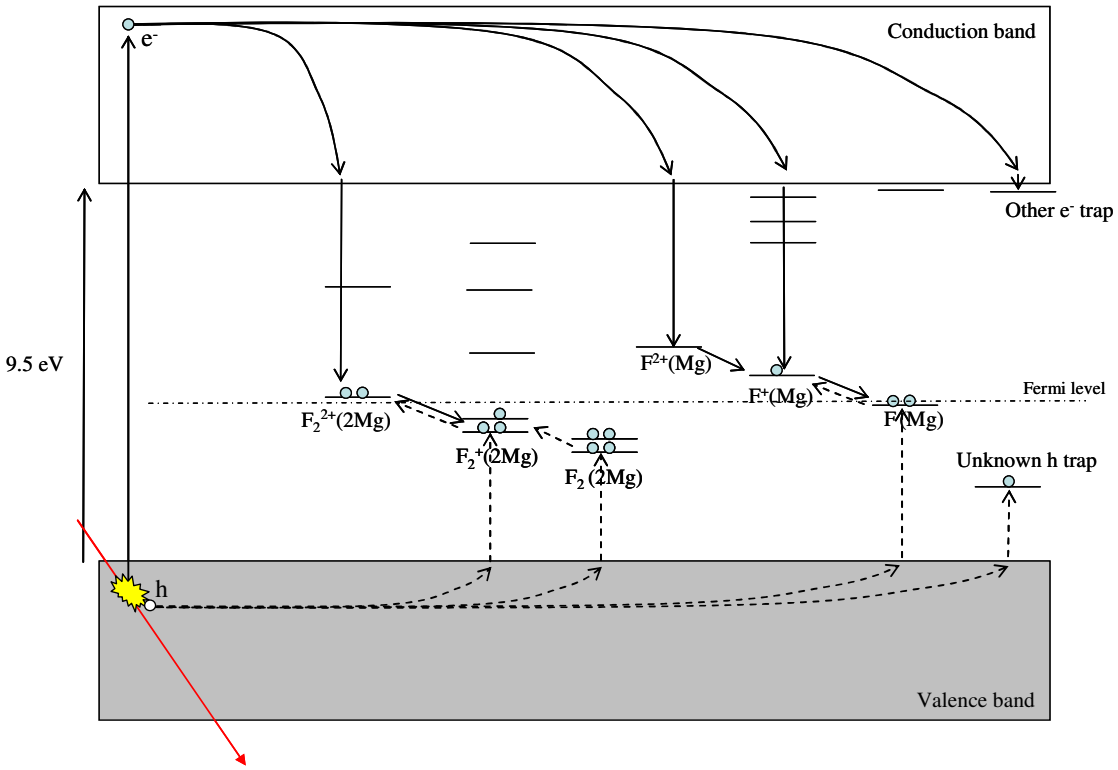

Figure 3.29 Flat band diagram of electron and hole trapping mechanisms in Al_2O_3:C,Mg immediately after energy deposition by ionizing radiation. Solid lines represent electron related phenomenon and dashed lines represent hole related phenomenon. This diagram assumes the existence of F^{2+}(2Mg) centers in Al_2O_3:C,Mg (see section 3.5.1).

3.7 Conclusions

Spectroscopic studies of Al_2O_3:C,Mg have provided several avenues for improving FNTD technology and understanding the properties of new luminescent crystals. Thermal annealing of the crystal at temperatures above the activation energy of single oxygen vacancy diffusion stimulates aggregation and formation of F_2, F_2^+, F_2^{2+}, F_2^{2+}(2Mg) and F_2^+(2Mg) centers. PL studies were performed on Al_2O_3:C,Mg for the first time after exposure to ionizing radiation.

Al_2O_3:C,Mg crystals have a wide variety of absorption and emission bands due to single and aggregate oxygen vacancies that occur as a result of crystal growth in a highly reducing atmosphere in the presence of magnesium. The absorption/emission bands in Al_2O_3:C,Mg were identified through a series of thermal annealing and photobleaching experiments utilizing a combination of optical absorption and photoluminescence measurements. Verifying that the 620/750, 335/750 and 255/750 nm absorption emission bands belonged to the three excited states of the F_2^+(2Mg) center was perhaps the most interesting and useful assignment for application to nuclear track imaging. It was found that F_2^{2+}(2Mg) centers efficiently capture free electrons and undergo radiochromic transformation into three-electron states forming F_2^+(2Mg) centers. F_2^+(2Mg) centers exhibited the largest increase in absorption and luminescence which, when coupled with fast luminescence lifetime of 75 ns (Akselrod et al, 2003), made it the most attractive center to probe for fluorescence track imaging. Significant changes in F^+(Mg) center concentration after irradiation with beta and x-ray suggest that it too is a likely candidate for track imaging, but the ease at which the F^+(Mg) center is photoionized may present problems such as erasure of radiation induced fluorescence.

Several questions about the physics of Al_2O_3:C,Mg have arisen as a result of this study. F_2^+(2Mg) centers were preliminarily assigned as hole traps which explain non-linear dependences and saturation of fluorescence intensity on dose. It is not clear that F_2^+(2Mg) act as hole traps or if there are other mechanisms such as defect creation from irradiation or efficient electron-hole recombination as doses increase. It is important to investigate the trapping mechanisms of the F_2^+(2Mg) center for future improvements of the FTND.

It was shown that F^+(Mg) centers were photoionizeable but the exact mechanism and photoconversion process is questionable. Inability to identify F^{2+} centers seems to contradict the proposed description of photoconversion of F^+ centers, but there have been no high energy (deep UV) absorption measurements performed on Al_2O_3:C,Mg to help verify or deny the existence of F^{2+} centers. Further absorption measurements ought to be performed with higher energy photons to attempt to observe α-centers.

A configurational coordinate diagram of F_2^+(2Mg) centers was developed based on the photoluminescence data presented here and on preliminary thermal quenching results. Improvements in band curvature, placements and intersections can be made by investigating the optical properties of the F_2^+(2Mg) center at temperatures as low as liquid helium temperature (~4 K) all the way to high temperatures (>750 K). Investigating optical properties in the temperature range from 4 K and higher will provide characterization of electron-phonon interactions of the defects.

Photoluminescence measurements need to be performed on Al_2O_3:C,Mg at low temperatures (liquid nitrogen or liquid helium) to determine the effect, if any, of magnesium on the optical properties of F^+ centers. Also, the instrumentation used in this study for photoluminescence measurements had poor sensitivity in the UV (high energy) range of the spectrum which limited the range of wavelengths investigated to greater than 215 nm. More sensitive instruments in the UV region should be used in addition to low temperature measurements. It is also suggested to perform rigorous thermal quenching experiments to determine the Huang-Rhys factor and the overlap of the ground and excited state parabolas (assuming a harmonic oscillator type potential).

CHAPTER IV

READER AND IMAGE PROCESSING DEVELOPMENT

FNTD technology requires high resolution imaging to be able to distinguish radiation induced tracks in Al_2O_3:C,Mg from the background fluorescence while maintaining the ability to process thousands of detectors on a reasonable timescale. Several improvements from the original materials and methods (Akselrod et al, 2003a) were made to increase the efficiency at which data was acquired and extracted from FNTDs. These improvements included development of a new confocal imaging system, new image processing routines and new routines for optical bleaching of FNTDs.

All results pertaining to radiation detection (presented in the remaining chapters) were obtained by imaging FNTDs with diffraction limited spatial resolution and extracting information from those images. In order to accomplish this, a new laser scanning confocal FNTD imaging system and image processing methods were developed. The new image processing method, based on spatial frequency analysis was also one of the most important contributions to FNTD technology that came about as a result of this research. This chapter describes the design and construction of the FNTD reader, innovations in image processing and a new method to improve the performance of FNTDs.

4.1 FNTD reader opto-mechanical design

The readout system constructed for this study was based on the confocal fluorescence approach of the original system that was designed to prove fluorescence based optical data storage concepts (Akselrod et al, 2003a). The first system was successful but limited by scan rate, image field size and lack of several automated features. A number of changes needed to be made in order to make the number and type of measurements necessary for this study. The three major requirements for the upgraded readout system were as follows:

1) Fast scanning
2) Customizability
3) Automatic processing.

The method of scanning for the first readout system was a piezo-electric cube to scan the crystal through the focal spot of the objective lens. The amount of time required to scan an image of 100 x 100 μm^2 area was limited by the frequency response of the piezo-electric cube which resulted in one image every six minutes. The amount of time required to scan one image was too long to be acceptable for the proposed applications.

In order to be competitive with other passive neutron dosimetry techniques, the efficiency of the scanning system needed to be comparable to the readout systems used for plastic nuclear track detectors which is on the order of a minute per detector (Salasky, 2006). Landauer's standard imaging area is 4.4 mm^2 per detector which means that the original FNTD imaging system would require 440 images resulting in a scan time of 44 hours per FNTD.

Software development was also important to allow for automated processing of large batches of detectors. Automated image acquisition and image processing for multiple detectors was added to the software. Image processing routines (to be discussed later) allowed for dosimetric information to be extracted from the FNTD in multiple applications. These routines needed to be developed or enhanced for all applications especially neutron and gamma dosimetry (see section 4.2).

The imaging system was designed to accommodate for mirror scanning and multiple detector imaging. Figure 4.1 is a photograph of the FNTD reader, Fig. 4.2 is a diagram of the scanning system shown from the top. Table 4.1 is a list of all of the major components with a brief explanation of their functions.

The excitation source is a polarization maintaining fiber coupled diode laser with emission at 635 nm from Blue Sky Research. The fiber output is coupled into a 6 mm Blue Sky Research collimator and directed such that the stimulation light is incident on a 750 nm long wave pass (LWP) Lambda Research dichroic mirror oriented at 45° to the incident light[4].

[4] Light incident at an angle to the dichroic mirror shifts the spectral characteristics to the blue meaning the actual cut off wavelength for this particular dichroic was 700 nm.

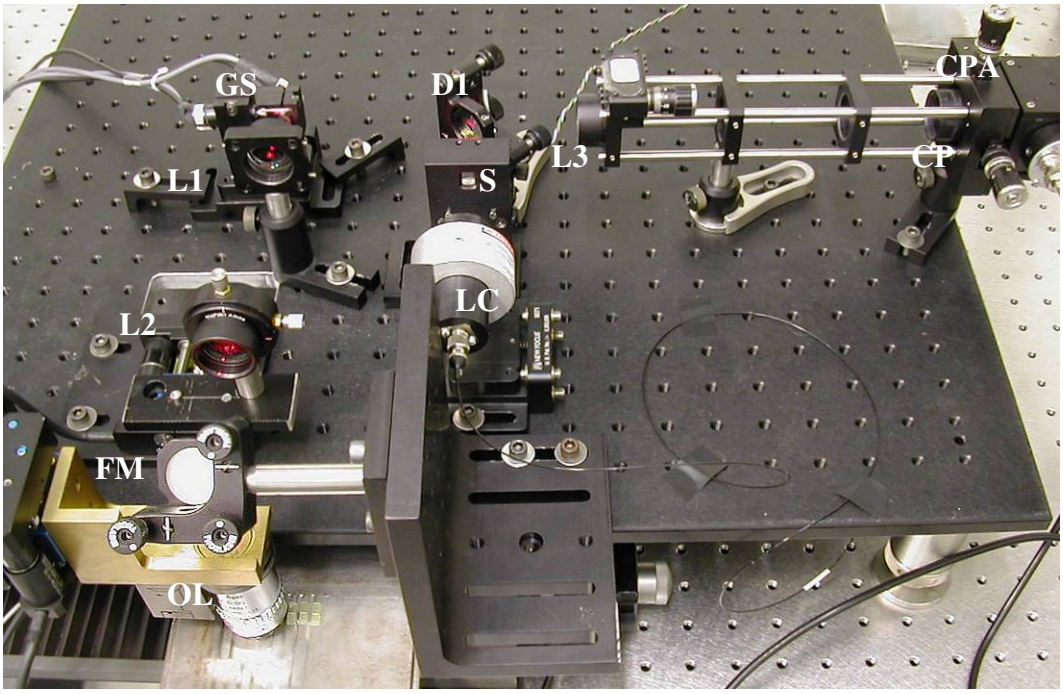

Figure 4.1 Photograph of the imaging system designed for reading Al_2O_3:C,Mg FNTDs. The parts and labels are described in Table 4.1.

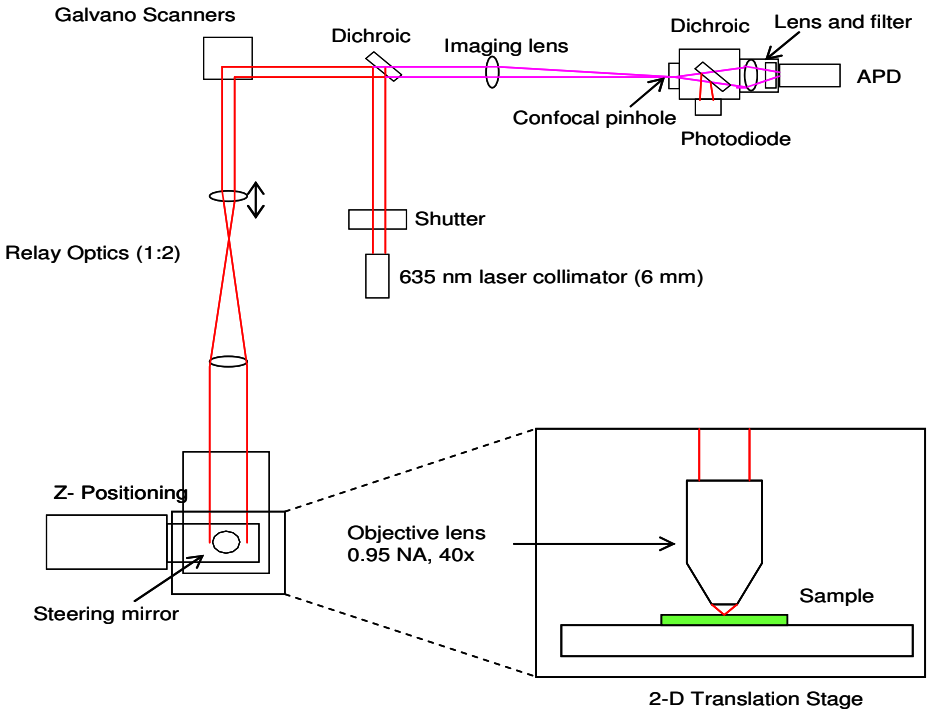

Figure 4.2 Diagram of the FNTD imaging system

Table 4.1 List of components and their abbreviations on Fig. 4.1

Part	Purpose	Code
Red laser diode (fiber coupled)	Stimulation	Not shown
Laser collimator	Collimates stimulation light from the fiber coupled laser	LC
Shutter	Blocks stimulation light when system is not scanning	S
750 nm LWP dichroic	Reflects stimulation light and passes fluorescence	D1 & D2
Galvanometer scan mirrors	Scans stimulation light across the FNTD and de-scans fluorescence	GS
Short focal length relay lens	Images center of scan mirrors	L1
Long focal length relay lens	Images scan beam on objective and expands beam	L2
Folding mirror	Directs stimulation light to the z-plane and fluorescence to the x-y plane	FM
Z positioning stage	Provides coarse positioning of the objective in the z-plane	Not shown
Piezo positioner	Moves objective lens in the z-plane	OL*
Objective lens	Images FNTD	OL
Sample holder	Holds multiple FNTDs for massive scanning	Not shown
Stepper stages	Moves the FNTD from between image locations and from one FNTD to another	Not shown
Tube lens	Focuses fluorescence into the confocal pinhole	L3
Confocal pinhole	Provides diffraction limited spatial resolution by rejecting out of focus light collected by the objective	CP
Confocal pinhole positioning assembly	Positions confocal pinhole	CPA
Focusing lens	Condenses fluorescence onto the sensitive APD area	Not shown
RG695 optical filter	Blocks remaining red stimulation light and passes fluorescence	Not shown
Photodiode	Measures reflected stimulation light	Not shown
Avalanche photodiode	Measures fluorescence from FNTD	Not shown

The dichroic mirror directs the excitation light to the scan mirrors. The mirrors scan the excitation light across a set of relay lenses consisting of two Newport achromatic lenses that expand the beam and image the point between the scan mirrors onto the back focal plane of the objective lens. A 40x 0.95 NA PlanFluor Nikon objective lens focuses the excitation light on the detector and collects the emitted fluorescence. The 750 nm fluorescence is collected through the same optical path and is descanned by the scan mirrors. After the fluorescence is descanned, it passes through the dichroic mirror and is imaged on the confocal pinhole by a Newport 200 mm focal length achromatic lens. The confocal pinhole rejects fluorescence originating outside of the focal volume. The remaining fluorescence passes through the pinhole and through another 750 nm LWP Lambda Research dichroic mirror (which directs residual excitation light to a Si photodiode to measure surface location) oriented at 45° and through an RG695 filter to absorb any remaining excitation light. A Newport 35 mm focal length aspheric lens is used to collect the fluorescence on the sensitive area of a Hamamatsu avalanche photodiode (APD). The imaging system is broken into conceptual sections, light delivery, scanning, objective lens, light detection and motion. These sections are discussed in detail below.

4.1.1 Light delivery

The fiber coupled laser and collimator serve as the light delivery component of the readout system providing a circular TEM_{00} mode beam. This laser provided enough laser power to maximize fluorescence. The amount of fluorescence reaching the detector increases with laser power until the fluorescence output saturates. The current through the laser diode was selected such that the corresponding laser power was enough to reach

fluorescence saturation. The laser power was 12 mW corresponding to 75 mA of current through the diode.

The collimator was matched the fiber termination from the laser and to provide a beam diameter sufficient for the rest of the scanning system. The size of the scan mirrors limited the diameter of the incoming beam. A collimator providing a 6 mm diameter beam was chosen to be small enough for the whole beam to be reflected by the scan mirrors. The back aperture of the objective lens determined the diameter of the beam after expansion. The diameter of the beam needed to be at least 1.5 times the size of the back aperture in order to avoid vignetting in the image. The system was designed such that the relay lens system can be used to change the beam diameter to the desired size. In this case, the size of the back aperture of the objective lens was 8 mm so an expanding ratio of 2 to 1 was chosen. The relay lenses served the dual purpose of beam expander and aberration compensator (see section 4.1.3).

4.1.2 Scanning

The original scanning apparatus (Akselrod et al, 2003a) used a piezoelectric cube to move the detector through the focal spot of the imaging objective with a maximum displacement of 100 μm and a maximum linear velocity of 900 μm/s. Piezoelectric devices were too slow for practical imaging of multiple detectors and so scanning galvanometer mirrors were suggested. The set of galvanometer mirrors were positioned by the manufacturer in orthogonal planes such that one mirror scans horizontally and the other scans vertically. Each mirror was controlled by a separate motor physically decoupled from one another to avoid cross-talk between axes. 8 mm diameter mirrors

were selected to allow for a compromise between maximum resonance frequency (fastest possible scan rate) and large surface area. The mirrors were coated with aluminum.

The galvanometer mirrors and drive electronics selected for scanning were from Cambridge Technology. The mirrors had a resonant scanning frequency of at least 2 kHz. With a 40x, 0.95 NA Nikon objective lens with a 5 mm focal length and a beam expansion of a factor of two, the resonant frequency of the mirrors allowed for a maximum scanning velocity[5] of 400,000 μm/s. The actual scan velocity used was limited by the bandwidth of the avalanche photodiode (APD) and amplification electronics (see part 4, light detection).

4.1.3 Objective lens

Four objective lenses were tested for different applications. Each objective was designed for flat field illumination for fluorescence applications. The objective lenses had different magnifications, numerical apertures and spherical aberration compensation ranges. The four objectives were as follows: a Nikon PlanFluor 40x 0.60 NA with spherical aberration compensation from 0 to 2 mm in glass, a Nikon PlanFluor 60x 0.85 NA with spherical aberration compensation from 110 to 270 μm in glass, a Nikon PlanFluor 40x 0.95 NA with spherical aberration compensation from 110 to 260 μm in glass and the fourth was a Nikon PlanFluor 60x 1.4 NA oil immersion lens with spherical aberration compensation from 110 to 160 μm in glass. The Nikon PlanFluor 40x 0.95 NA objective was used in most applications. The 40x, 0.95 NA objective allowed for lateral resolution of r_{xy} = 400 nm and axial resolution of r_z = 1 μm in conjunction with a pinhole appropriate for diffraction limited imaging.

[5] The maximum displacement of the focal spot on the crystal is determined by the focal length of the microscope objective and the scan angle required to achieve a flat field of view.

4.1.4 Light detection

The detection component of the system consisted of the confocal pinhole, wavelength separating optics and photo-detectors. The diameter of the confocal pinhole was determined by multiplying the magnification of the imaging system by the Airy disk diameter of the beam focused on the sample. Neutron dosimetry required a pinhole with larger diameter than that required for diffraction limited resolution in order to increase the fluorescence intensity of recoil proton tracks. A pinhole diameter of 2 Airy disk diameters was chosen such that signal to noise ratio was maximized in order to optimize track detection.

Residual excitation light not fully filtered by the dichroic passes through the confocal pinhole and must be separated from the fluorescence. The incoming excitation light can be used to determine the location of the crystal surface and to image the surface of the crystal. It is reflected by the dichroic mirror and measured by a photodiode. The fluorescence passes through the dichroic mirror as well as approximately 1% of the excitation light. An RG695 long-pass filter was chosen to absorb the remaining excitation light; filters with shorter cut off wavelengths did not completely block the excitation light.

A Thorlabs Si photodiode was used in conjunction with a trans-impedance amplifier to measure the intensity of the reflected red excitation light as well as image the surface of the detector. An APD was chosen to measure the 750 nm fluorescence because of high quantum efficiency in the near infrared. The APD had a gain of 30 and a bandwidth of 100 kHz which limited the overall scan velocity. An additional amplifier with a gain of 10 and a bandwidth of 40 kHz was used in conjunction with the APD limiting the data

rate. The data rate used for the reading FNTDs (10 kHz for HCP spectroscopy, 80 kHz for neutron dosimetry) was often above the bandwidth of the amplifier, but the cut-off response of the amplifier was slow enough to achieve acceptable signal-to-noise. An additional low-pass resistor-capacitor filter was used to eliminate high frequency noise. The cut-off frequency was ½ the sampling frequency.

4.1.5 Motion

The read out system was designed such that there were five locations for automatic motion utilizing four motorized stepper stages and one piezoelectric positioning device. Large range motion was needed in order to achieve automatic processing of multiple FNTDs thus two Thor Labs high precision linear stepper stages with 250 mm of travel were used. These two stages were placed underneath the objective to move between image locations and from one FNTD to another. The two remaining stepper stages were Physik Instrument (PI) stepper motors and stages with 25 mm of travel. These two stages were used for large range motion of the objective lens and positioning the back relay lens for additional spherical aberration compensation (see section 4.1.2).

A PI piezoelectric positioning device was used to position the objective lens with a precision of 10 nm in a range of 100 µm. The piezoelectric positioner used was specifically designed by PI for microscope objective positioning. Piezo positioning was used to scan the objective lens perpendicular to the detector's polished surface for determining the position of the crystal surface and to precisely position the objective at the desired scan depth (see section 4.1.2 on wavefront aberrations).

4.1.6 Wavefront aberrations

Ideal wavefronts are required in order to achieve quality results with any imaging system. Aberrations must be carefully considered and dealt with because confocal imaging systems reject light originating from outside a diffraction limited focal volume. Any degradation in the wavefront of the excitation or the emission light will corrupt the image.

Most wavefront aberrations in an imaging system result from either improper alignment or imperfect optics. Aberrations resulting from improper alignment are often off-axis aberrations such as astigmatism or coma. Off-axis aberrations as well as small magnitude higher order aberrations can also occur from poorly manufactured optics. Lenses can introduce a significant amount of chromatic aberrations unless they are specifically designed for multiple wavelengths. The majority of these aberrations can be eliminated by tedious alignment and selection of proper optics.

Aberrations also occur as a result of imaging the crystal. First order off-axis aberrations such as coma and astigmatism occur from the surface of the crystal being oriented at an angle other than perpendicular to the direction of light propagation. These aberrations are avoided by ensuring proper alignment of the crystal with respect to the imaging system. Large magnitude third and fifth order aberrations are unavoidable through alignment and require more creative correction methods. The highest magnitude aberration that arises from imaging the crystal is third order spherical aberration.

Spherical aberration is a major concern in biological imaging and optical data storage so several solutions have been made available for dealing with this problem. Some commercial objective lenses have been designed to compensate for spherical

aberrations up to a maximum depth in a common medium, mainly glass. The objective used for the majority of this study (0.95 NA, 40 x Nikon Plan Fluor objective) was designed with a spherical aberration compensation (SAC) collar that corrects for spherical aberrations that occur between 110 µm and 230 µm in glass. Spherical aberrations are a function of the index of refraction of the media in which the light is entering so corrections were made to relate the amount of SAC in glass to the amount of SAC needed for Al_2O_3.

Adjustment of the SAC for commercial objectives was done by physically rotating a SAC collar. This method of SAC proved to be inefficient due to the requirement of human intervention so another method was employed for automatic SAC. Tom Milster originally compensated for the majority of spherical aberrations by adjusting the defocus of the beam entering the objective by moving one lens element in a relay pair (Milster *et al*, 1999). This type of SAC was implemented by placing the back lens of the relay pair on a motorized linear stage allowing for automatic precise control of the defocus of the excitation beam into the objective lens. A detailed discussion and calibration of this method can also be found in appendix A1.

4.2 Hardware control and image processing

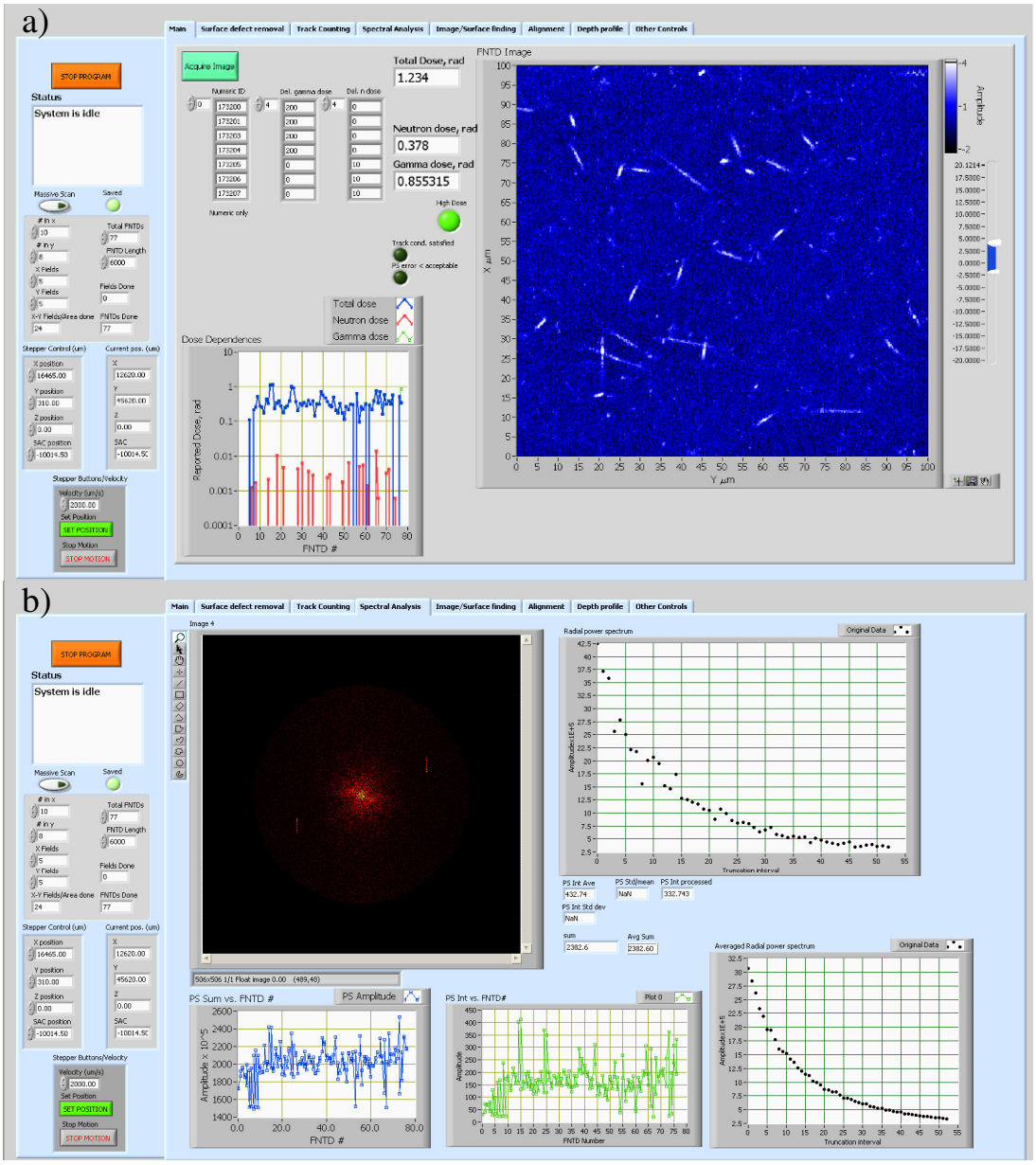

Figure 4.3 Screen shots of image acquisition software a. main page with image and dose reporting, b. image power processing page (see section 4.2.2).

All of the control software for the FNTD reader was developed in the LabView™ programming environment. LabView™ offered an easy to use graphical programming interface that allowed for modifications of the main software routine. Software development was broken into four sub-modules, scanning hardware control, data acquisition, motion and data processing.

The base software developed for scanning FNTDs (hardware control and image acquisition) and the nature of scanning were the same for all of the studied applications. Controls were put into the software to allow for slight variations of scan parameters such as scan time, field of view, image depth and number of images. The scan parameters were changed for every application and will be detailed in subsequent chapters. Motion control was integrated into image acquisition such that every component with motorized translation stages was controlled based on the image acquisition parameters. Two screen shots from the image acquisition software are shown in Fig. 4.3.

4.2.1 Image acquisition sequence

FNTDs were first scanned perpendicular to the crystal surface to determine the location of the surface within an accuracy of 10 nm. After finding the axial surface position, the FNTD was scanned in a plane parallel to its surface - the depth of scanning varied depending on the application which is discussed in chapters 5 and 6. The image areas had dimensions of either 100×100 μm^2 (for applications requiring maximum resolution, i.e. heavy charged particle spectroscopy) or 150×150 μm^2 (for applications requiring fast image acquisition, i.e. neutron dosimetry). After the first image was obtained FNTDs were scanned in the same lateral (xy-plane) position but deeper in the

crystal when 3-dimensional imaging of the FNTD was required (depth profiles – see chapter 5). After all depths were imaged, the FNTD was scanned in a new lateral position and the process repeated. Multiple images were obtained from each FNTD and behind every neutron converter when applicable. The number of acquired images in the xy-plane depended on the measured dose or track density and was adaptively varied between 5 and 100 for each area.

4.2.2 Image processing methods

Every application of FNTDs investigated this study required different processing methods based on their objectives. Processing methods were tailored to optimize the performance of FNTDs in individual applications. Multiple image processing programs were developed in LabView™. Image processing for each application had the same basic structure that consisted of these steps: pre-processing (which included noise and non-radiation induced object removal), radiation induced object enhancement and parameterization of radiation-induced signals. Parameterization of radiation induced fluorescence for individual applications depended on their requirements (Table 4.2).

4.2.3 Noise removal

Pre-processing was the same for all applications of FNTD technology that were explored in this dissertation. The pre-processing steps were as follows:

1. Identify objects on the crystal surface from the photodiode image that could cause bright objects on the fluorescence image,
2. Identify all bright objects on the fluorescence image,
3. Determine if any of the objects identified on the photodiode image correlates with any objects on the fluorescence image,
4. Remove correlated objects,
5. Identify any large (3x the pixel area occupied by a charged particle track), localized objects on the fluorescence image,
6. Remove the identified large objects, and
7. Perform digital filtration using a fast Fourier transform (FFT) and spatial frequency truncation on the fluorescence image.

Radiation induced parameters and their specific image processing routines for every application investigated in this study are identified in Table 4.2. Dr. Vasiliy Fomenko developed a cross-correlation routine to enhance charged particle tracks for track counting. That routine was slightly modified and implemented in the image processing software. The new image processing method for neutron dosimetry, photon dosimetry and beta dosimetry is original and will be discussed in the following section.

Table 4.2 Image processing parameters derived for different applications to determine radiation quantities

Application	Parameter	Purpose
Neutron dosimetry	Track count	Secondary particle density
	Image power	Average dose
	Track angle	Angular distribution of incident neutrons
	Track length	Estimation of neutron energy
Heavy charged particle spectroscopy	Fluorescence amplitude	LET determination
	Track width	LET determination
	Track angle	Ion angle of incidence
	Track length	Ion range
Gamma and x-ray dosimetry	Average fluorescence	Dose
	Image power	Dose
Beta dosimetry	Average fluorescence	Dose
	Image power	Dose
Radon detection	Track count	Radon concentration
X-ray microbeam	Fluorescence Intensity	Modulation/peak to valley dose ratio
	FWHM	Width of microbeam

4.2.4 Individual track analysis

Images of fluorescent HCP tracks provide multiple parameters to describe individual tracks. These parameters can be particularly useful in neutron dosimetry and heavy charged particle spectroscopy. Figure 4.4 demonstrates pre-processing and track identification on a neutron irradiated FNTD. Figure 4.5 shows analysis of an individual track on a single image of an FNTD irradiated with 120 MeV/u ^{56}Fe (see chapter 6 for discussion on energy and LET dependence).

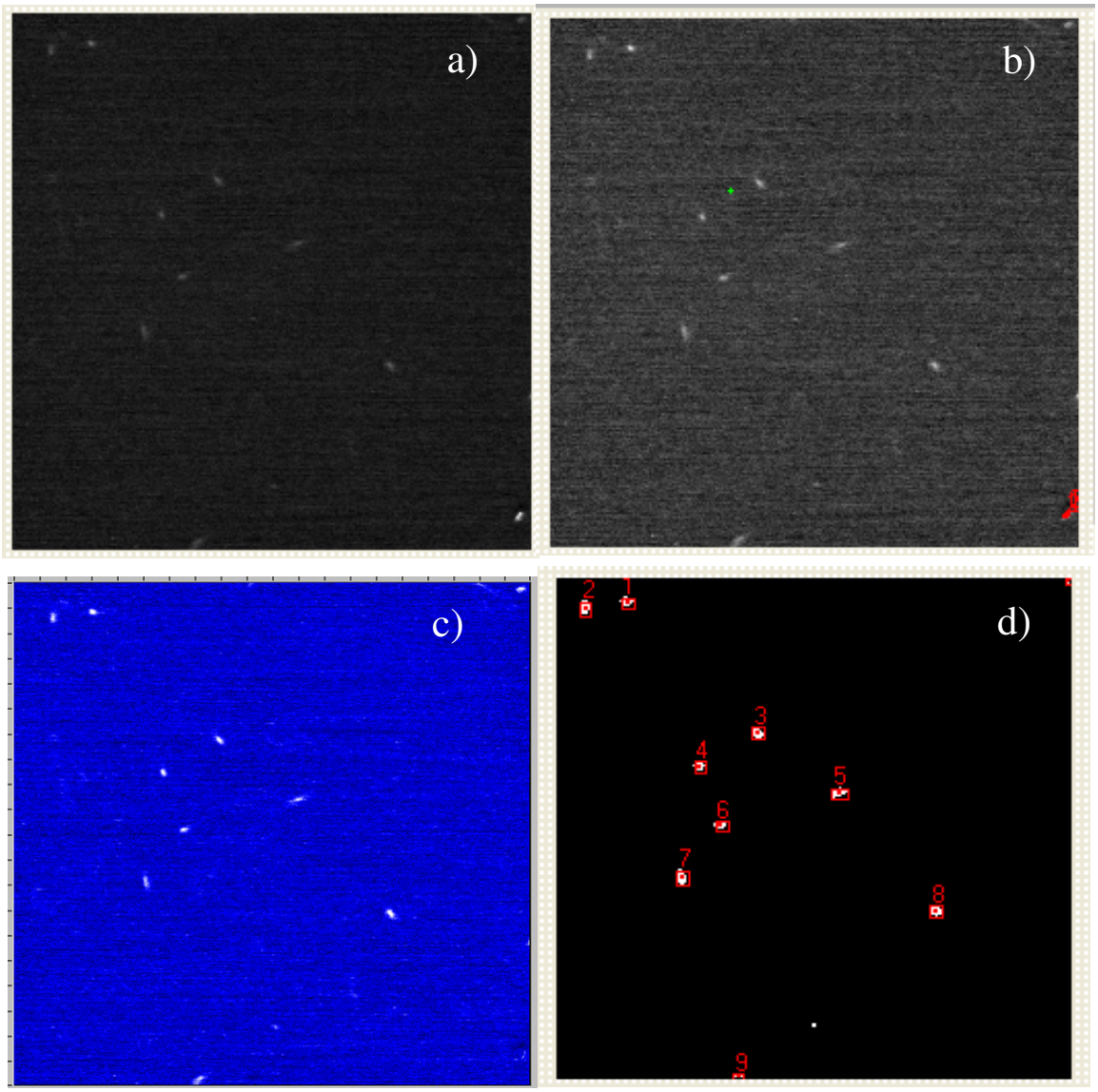

Figure 4.4 Series of images acquired from a neutron irradiated FNTD covered with PE demonstrating automatic pre-processing, track identification and track counting. a) Original fluorescence image, b) after identification and removal of high and low intensity artifacts, c) after FFT truncation and noise removal and d) final image after cross-correlation and track identification.

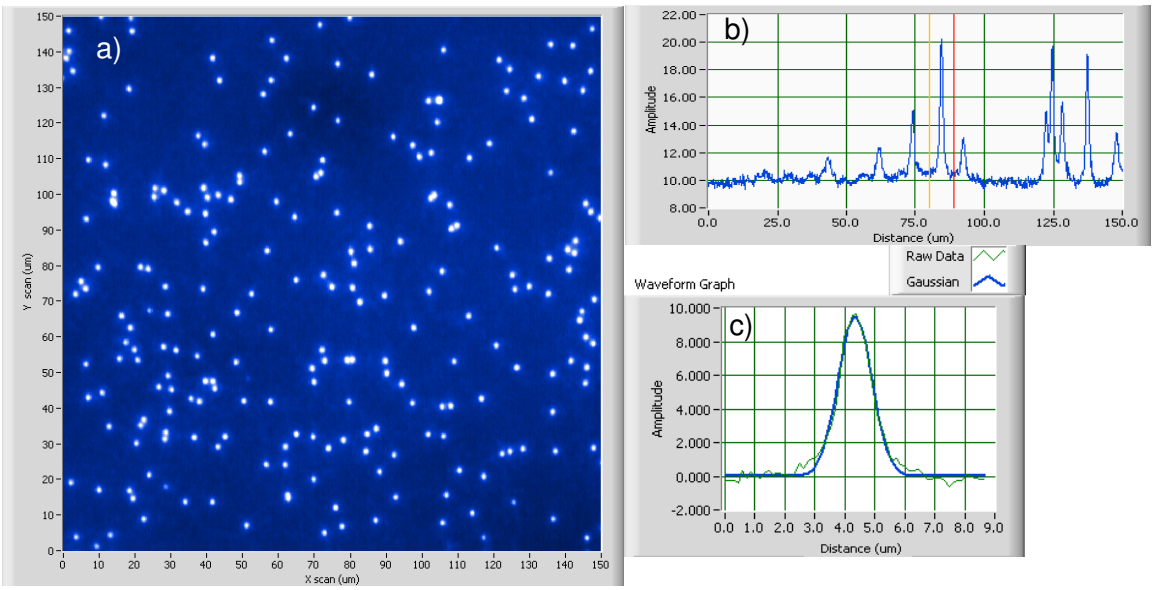

Figure 4.5 a) 150x150 μm^2 image of an FNTD irradiated with 120 MeV/u ^{56}Fe; the bright objects are tracks caused by interaction of ^{56}Fe with Al_2O_3:C,Mg, b) cross section of multiple tracks along one line in the image; an individual track is selected by the vertical lines and c) the cross section of the selected track fit with a Gaussian curve. The maximum amplitude of the track is the fluorescence intensity and the full-width at half maximum of the Gaussian is taken to be the width of the track.

After the pre-processing described above in section 4.2.3, tracks are automatically identified by their contrast (fluorescence intensity relative to the background fluorescence) and overall size (number of pixels). Every track is then counted and processed to obtain fluorescence intensity, and when applicable, track width. The angle of incidence (angle deviating from normal to the surface) of the track can be calculated by acquiring images at two depths and using simple geometry (Fig. 4.6), i.e.,

$$\theta = \tan^{-1}(d/z). \qquad (4.1)$$

The maximum intensity of the track depends on the angle of incidence, so the angle must be accounted for (section 6.1).

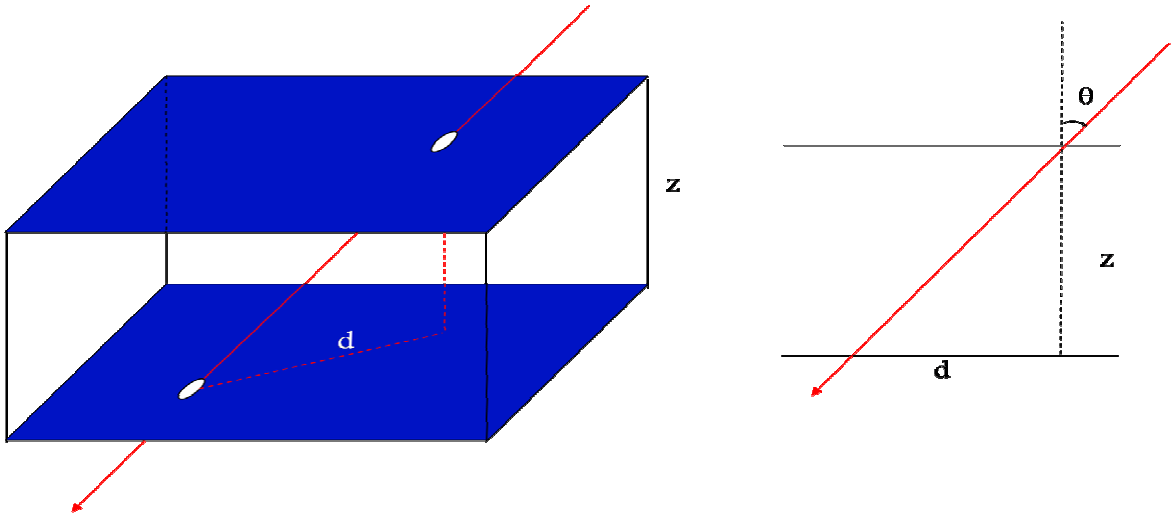

Figure 4.6 Diagram of two image planes used to determine angle of incidence of the ion; z is the distance between image planes in the axial direction and *d* is the distance between the tracks.

4.2.5 Spatial frequency analysis

Usual methods for determining dosimetric information consisted of either track counting (for neutron dosimetry), fluorescence amplitude analysis (for HCP spectroscopy) or measuring luminescence emitted from the bulk of the crystal (for OSL). The method proposed here is essentially a combination of all three methods. Each image taken with the confocal imaging system has a volume of roughly $3x10^{-5}$ mm^3, so the amount of material being sampled is small, but a "bulk" parameter is still used. The bulk parameter is a measure of the "roughness" of the image.

Ionized electrons resulting from radiation are captured by F_2^{2+}(2Mg) color centers transforming the center into an F_2^{+}(2Mg) center so the fluorescence intensity at the points of capture increase and all other points remain the same. The total amount and variation (spatial modulation) of F_2^{+}(2Mg) color centers within each image can then be estimated by evaluating the power of the image. The power of an image is defined as the integral of the square of the magnitude of the image in the spatial frequency domain. The Fourier transform is used in order to convert the image from the spatial domain to spatial

frequency domain. For an image with a size of NxN pixels, the discrete Fourier transform (DFT) is given by

$$F(k,l) = \frac{1}{N^2} \sum_{m=0}^{N-1} \sum_{n=0}^{N-1} f(m,n) e^{-\frac{2\pi i}{N}(km+ln)} \tag{4.2}$$

where *f(m,n)*is the original image in the spatial domain and *F(0,0)* represents the DC offset of the image. The 2-D DFT is separable such that the image need only go through two sets of one dimensional Fourier transforms instead of a double sum. The number of calculations needed to completely transform the image is N^2. A fast Fourier transform (FFT) allows for a reduction in the number of calculations to $N \log_2 N$ while leaving the final result the same. There are many different ways to compute the FFT; the method used in this work is the Cooley-Tukey Radix-2 method (Cooley et al, 1965).

Any Fourier transform will produce a complex number for its output. The complex number can be represented as either its real and imaginary parts or magnitude and phase. Both parts are necessary to fully describe the image. The magnitude of the FFT describes the geometrical pattern, or structure, of the image and contains most of the useful information in the image. The phase of the image generally provides little useful information, but is necessary to reconstruct the image back into the spatial domain.

The magnitude of the FFT is easily represented graphically. There are two different representations of the magnitude, regular and optical. The regular representation places the low frequencies in the corners of the image and the high frequencies toward the center. The optical representation flips the frequencies such that the center represents low frequencies and the outer parts of the image represent the high frequencies. The optical representation is most commonly used (Russ, 2007).

Analysis of images in the spectral domain is a powerful tool to determine patterns that may occur in the image. For instance, vertical stripes in the image will show up as spikes in the frequency spectrum along the horizontal axis and diagonal stripes will show up as spikes in the opposite diagonal direction. Other shapes and patterns can manifest themselves in lines, rays or spots. Figure 4.7b is an example of the power spectrum for an image of a bleached and unirradiated FNTD.

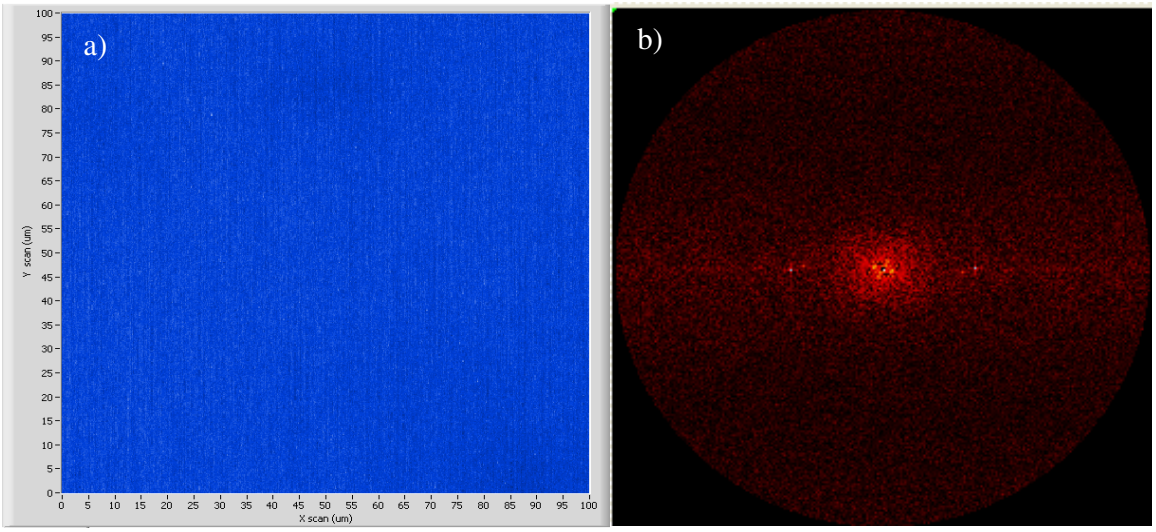

Figure 4.7 a) Image of a bleached, un-irradiated FNTD b) 2 dimensional power spectrum in the optical representation. 0.5% of the low frequencies (offset of the image) and 1% of the high frequencies are removed for visual purposes.

Because of the stochastic nature of energy deposition and the random spatial distribution of radiation there is no discernable pattern within the image. This means that the frequency spectrum will not consist of discrete spikes or lines, but will rather be a continuum of frequencies. The maximum frequency that is possible to obtain in an image is *1/2pixels* (a white stripe and a black stripe each with a thickness of one pixel). Therefore, the radiation induced signal will manifest itself in low frequencies because the point spread function consists of an equivalent of roughly 8 pixels. The maximum frequency of the desired features is *1/8 pixels* which is 1/4 of the maximum frequency.

Because the radiation induced signals can be larger than 8 pixels and are spaced randomly with different shapes, the useful signal will be a continuum in the low frequency range whether it was induced by heavy charged particles or photons. One exception may be an image of purely perpendicular tracks of particles with the same linear energy transfer where the shapes and amplitudes are roughly constant in which case there will be an increase in magnitude in a distinct frequency range.

The frequency spectrum will be center symmetrical because of the randomness within the image. This means that it is possible to square and integrate the frequency spectrum to obtain the power of the image at certain frequencies and plot the power as a function of frequency. The power within a certain frequency range, *dkdl* is given by

$$P = \int_{k_0}^{k} \int_{l_0}^{l} \left| F(k,l) \right|^2 dkdl \tag{4.3}$$

where k_0 and l_0 are the initial frequencies of interest.

Each image is transformed to the frequency domain by performing the FFT. The magnitude of the FFT is then calculated, squared and integrated with respect to frequency. Figure 4.8 shows the steps in processing with an image obtained from an FNTD irradiated with 30 mSv of fast neutrons. The power of the image increases as dose increases, therefore the image power serves as a good parameter of dose. Detailed results of this processing method can be found in chapter 5.

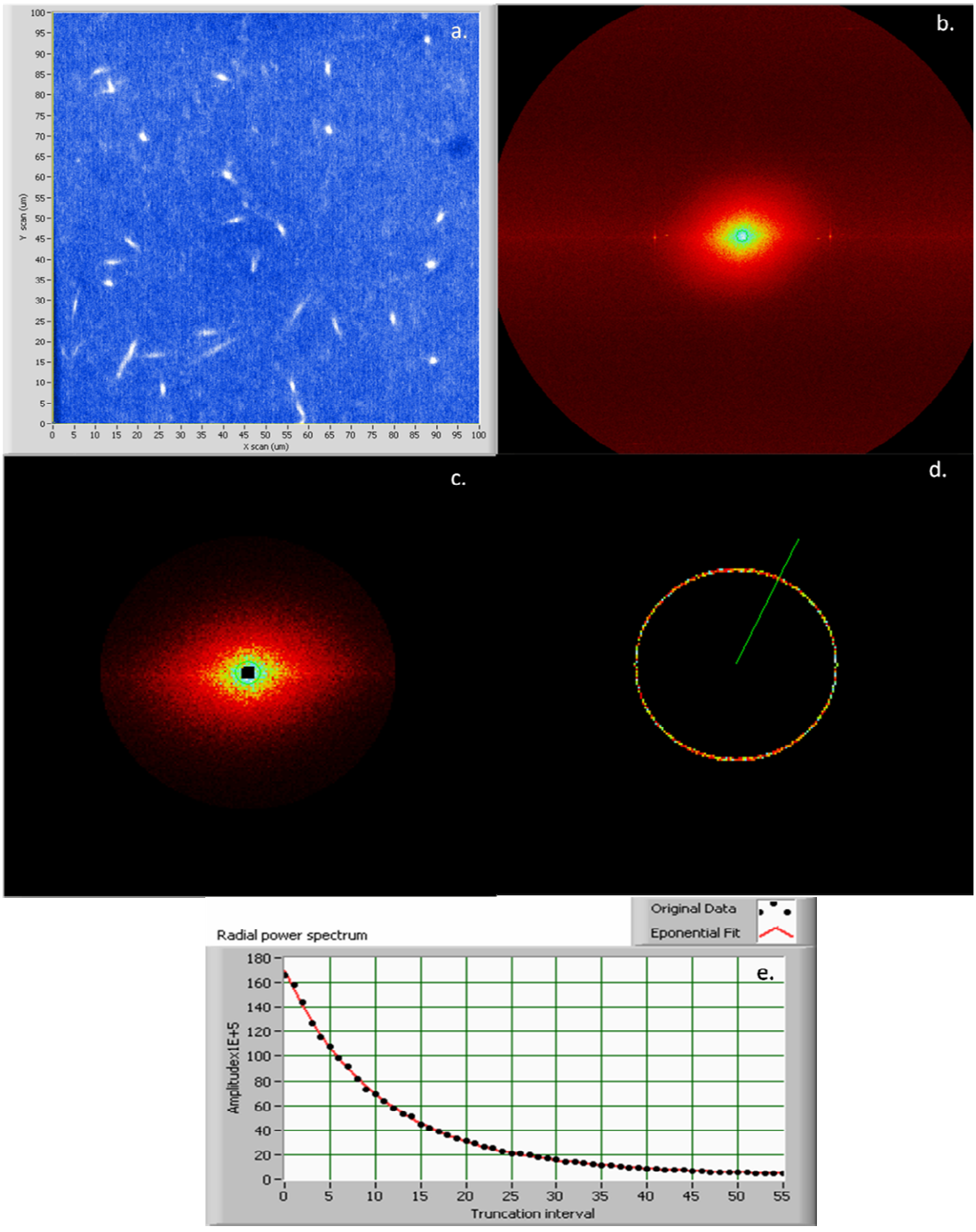

Figure 4.8 Illustration of the image processing routine: a) Image of FNTD irradiated with 30 mSv of fast neutrons, b) FFT with 0.5% low frequencies and 1% high frequencies truncated, c) FFT with 2% low frequencies and 72% high frequencies truncated, d) ring of frequencies during radial integration, e) final integrated power spectrum with fit.

4.3 Conclusions

The demand to image thousands of FNTDs per month required the design and construction of an imaging system suitable for fast scanning while maintaining its flexibility to accommodate multiple applications such as neutron dosimetry and heavy charged particle spectroscopy. The imaging system described in this chapter accomplished that task and is currently limited only by the bandwidth of the data acquisition electronics. Improvements to image acquisition speed are still possible with faster electronics. The lifetime of F_2^+(2Mg) luminescence is 75 ns, so the maximum achievable scan rate is approximately 13 MS/s (calculated by 1/lifetime) which is 200 times faster than the scan rate used in this study. Imaging time is limited to 4 seconds per image by the bandwidth of the avalanche photodiode. An investigation into faster photodetectors is suggested to further increase the efficiency of the imaging system. Further improvements should also consider the fact that there are a low number of photons arriving at the APD during image acquisition.

New image processing methods were developed to quantify energy deposition in FNTDs. Spatial frequency analysis for high fluence applications such as high dose neutron dosimetry and gamma dosimetry was the most notable contribution among the image processing routines developed.

CHAPTER V

NEUTRON AND GAMMA DOSIMETRY USING FNTDS

Personal neutron dosimetry is one of the most challenging problems facing scientists working in radiation fields. Some of the most common areas of neutron exposure are as follows: nuclear power stations (~60 keV neutrons), particle accelerators that can produce a broad range of neutron energies, space environments (~1-200 MeV neutrons), medical treatment facilities (broad spectrum neutrons) and also in battlefield scenarios where there may be large neutron fluences from nuclear weapons (~1 MeV). For the purpose of this work, neutrons with energies on the order of a few meV are considered thermal, from 1 eV to 1 keV are considered "slow" and greater than 1 keV are considered fast. Fluorescent nuclear track detector technology is proposed as a new technology with beneficial features for neutron dosimetry.

Solid state nuclear track detectors (SSNTD), in particular CR-39 plastic nuclear track detectors, are currently being used by some companies such as Landauer Inc. to service personal neutron dosimetry needs. CR-39, like any well established technology has been characterized over many years. FNTD technology needs to be characterized in a similar manner in order to prove its commercial and technical usefulness in neutron detection. This chapter describes detailed characterization of FNTD performance including dose, energy and angular dependences.

Track detectors have traditionally functioned as neutron dosimeters by relating track density of nuclear reaction products to the incident neutron fluence. Unlike most nuclear track detectors, Al_2O_3:C,Mg is sensitive to low LET radiation including secondary electrons resulting from interactions of photons with the crystal. As a result, FNTDs can be used to image overlapping secondary delta electron tracks and the image can be used to determine the photon dose.

Neutron radiation is usually accompanied by gamma radiation, and a high contribution of gamma to radiation-induced fluorescence signal might be a problem. If the equivalent dose of gamma radiation is above several cSv, then the fluorescence induced by overlapping secondary delta electron tracks can interfere with the signal induced by recoil protons making it difficult to detect and count neutron induced tracks. A new image processing method is investigated in this chapter as a technique to determine dose for both low and high LET radiations. The new image processing method is combined with a new detector configuration utilizing three converters of non-ionizing to ionizing radiation to effectively separate neutron and gamma induced signals. The response of FNTDs to photons is also characterized in this chapter in order to effectively separate neutron and gamma signals.

5.1 Experimental methods

5.1.1 Neutron converters

Neutrons have no charge and will not interact with Al_2O_3 through the Coulomb interaction. Therefore, ionization (and thus fluorescent tracks) does not occur in Al_2O_3:C,Mg. There is a finite probability that a neutron will collide with an oxygen

nucleus to create an interstitial oxygen atom and also that a neutron will be captured by an aluminum nucleus. Neutron reactions with aluminum are as follows: $^{27}Al(n,p)^{27}Mg$, $^{27}Al(n,\alpha)^{24}Na$ and $^{27}Al(n,2n)^{26}Al$, all producing characteristic gamma decay. Protons, alphas and gamma from neutron reactions with Al cause detectable effects in the crystal. Neutron interaction cross-sections with O and Al are on the order of several mBarns (Exfor, 2009), so neutron fluences would have to be on the order of 10^{14} neutrons/cm^2 and higher. 10^{14} neutrons/cm^2 is similar to the fluences used to observe single and aggregate defects in the work of Evans described in chapter 2. Observing defect creation is not practical for personal neutron dosimetry due to the need for such high fluences.

It has been common practice in neutron dosimetry to use hydrogen containing material as a moderator and converter of fast neutrons. Hydrogen and neutrons have similar masses thus making neutron-proton (*n-p*) scattering more efficient than with heavier nuclei. *n-p* elastic scattering is efficient for fast neutrons, which is why hydrogen containing polyethylene (PE) has been used as a fast neutron converter and moderator. PE has the largest concentration of hydrogen than any other practical material.

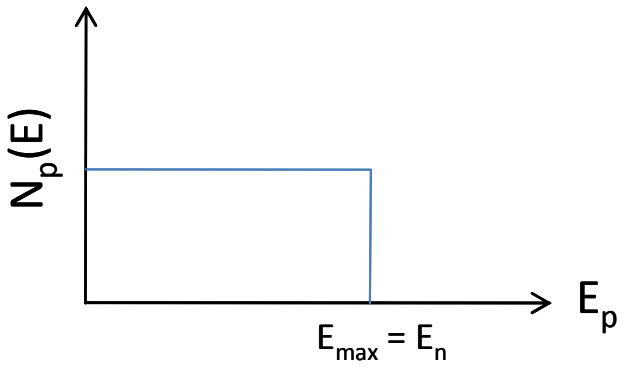

Figure 5.1 Distribution of recoil protons of energy E_p. The maximum recoil proton energy is E_n.

Recoil protons generated at the interface between PE and Al_2O_3:C,Mg have a distinct angular distribution, which is uniform for angles of incidence from 0º to 180º, where 0º and 180º are parallel to the crystal surface and 90º is perpendicular to the surface. In addition to an angular distribution, there is an energy distribution of 0 (at 0º) to E_n (at 90º) where E_n is the energy of the incident neutron (Fig. 5.1). This results in an average energy of recoil protons of $E_n/2$ for monoenergetic neutrons. The distribution of energies is broadened because the incident neutrons are not monoenergetic and the recoil protons originating within the bulk of the PE converter will lose energy while passing through the PE.

Thermal or slow neutrons are commonly "converted" into ionizing radiation by materials that contain elements with high neutron capture cross-sections such as ^{6}Li and ^{10}B. The reactions with Q-values in parentheses are as follows:

$$^6Li + ^1n \rightarrow ^4He(2.05MeV) + ^3H(2.73MeV) \quad (5.1)$$

$$^{10}B + ^1n \rightarrow ^7Li^*(0.84MeV) + ^4He(1.47MeV) \quad (5.2)$$

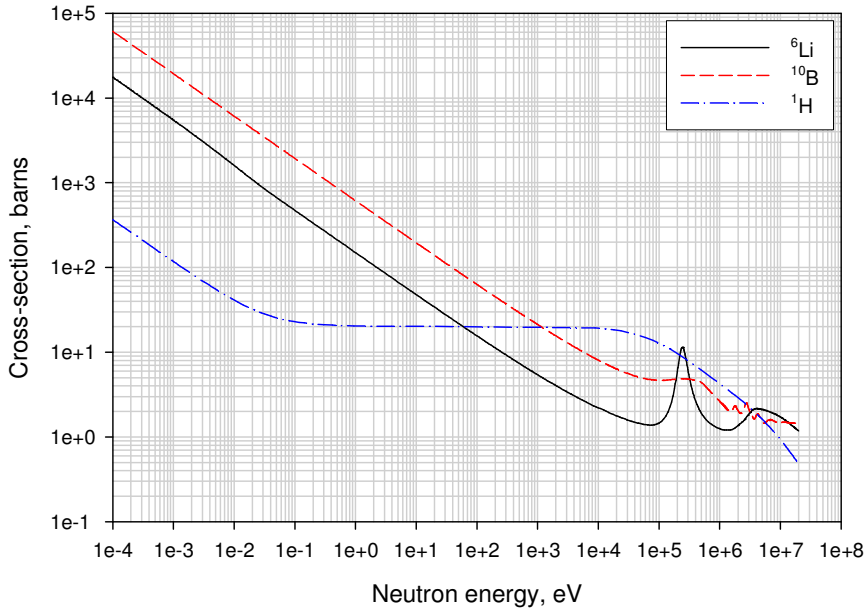

Figure 5.2 Neutron reaction cross-sections for ^{6}Li, ^{10}B and ^{1}H. These cross-sections are taken from the ENDF data base (2006).

Energy dependent neutron capture cross-sections (total cross-section) for ^{6}Li, ^{10}B and ^{1}H are shown in Fig. 5.2. (n,α) reactions dominate in ^{6}Li and ^{10}B which have approximately 2-3 orders of magnitude larger neutron capture cross sections than *n-p* scattering for thermal neutrons (~0.025 eV). The *n-p* scattering cross section is larger and less complex than neutron capture cross sections of ^{6}Li and ^{10}B for $E_n > 1$ keV. Considering the neutron reaction cross-sections and ignoring size constraints, the most efficient way of detecting neutrons is to moderate incident neutrons using PE and convert the moderated neutrons with a thermal neutron converter similar to many active neutron spectrometers such as Bonner sphere detectors (Bramblett et al, 1960). PE is however still useful as a converter because recoil protons provide information on the energy of incident neutrons (section 5.5).

Three converters containing ^{6}Li were used in these experiments. TLDs of two types were investigated, TLD 100 which contained a natural abundance of ^{6}Li and TLD 600 which was ^{6}LiF enriched with ^{6}Li resulting in 6 times larger abundance of ^{6}Li than the TLD 100. TLD 100 chips were 3 mm x 3mm x 1 mm blocks and the TLD 600 chips were circular 3 mm in diameter and 1 mm thick.

Cases enclosing FNTDs in PE (fig 5.3) were designed by Jimmy Lo at Landauer. The cases were designed such that a 1 mm thick slab of PE was in contact with the top half of the polished FNTD with a recess to allow a second converter (^{6}LiF, ^{10}B, PTFE etc.) to contact the bottom half of the FNTD.

Figure 5.4 conceptually illustrates the role of converters in the proposed dosimeter configuration. The result of irradiating FNTDs with neutrons of different energies is demonstrated by the number and length of tracks behind the converters

(see section 5.5). Teflon is used as the neutron insensitive converter providing quasi-charged particle equilibrium for gamma dosimetry and neutron-gamma separation (see sections 5.1.2 and 5.8).

Personal neutron dosimetry is often performed in an albedo configuration. A standard 30 x 30 x 15 cm^3 polymethyl methacrlate (PMMA) phantom was used to simulate the albedo configuration during calibrations.

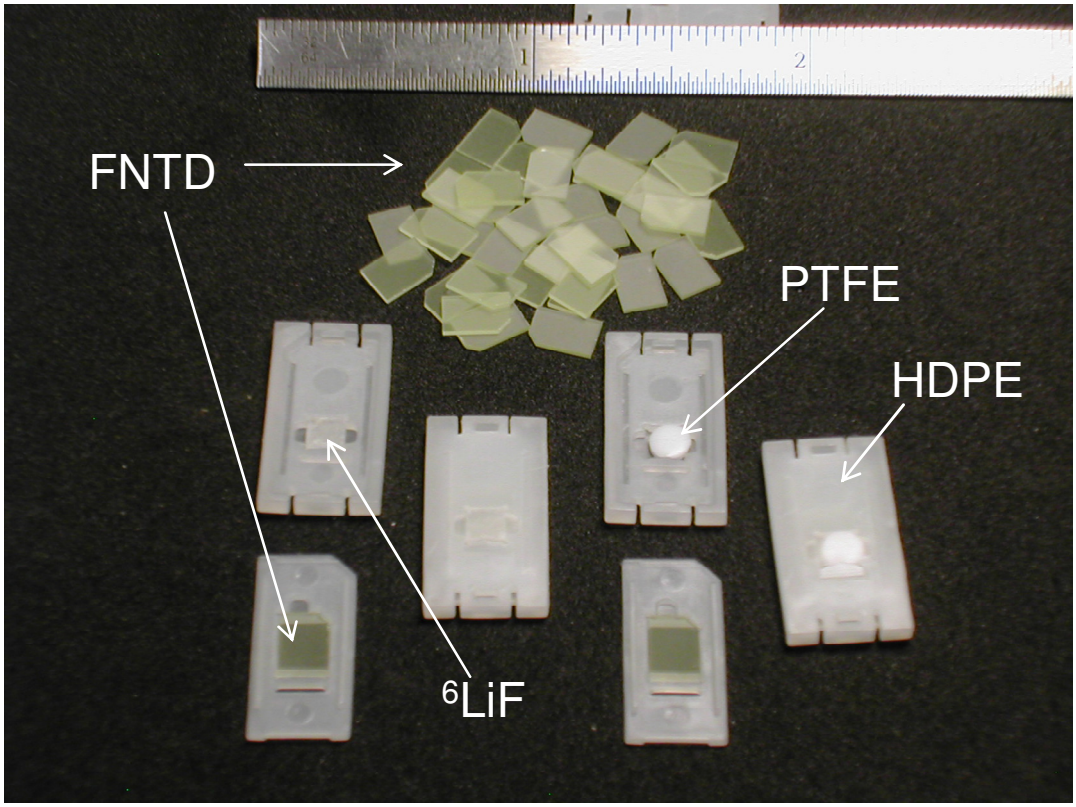

Figure 5.3 FNTDs and the PE converter cases with ^{6}LiF and PTFE chips.

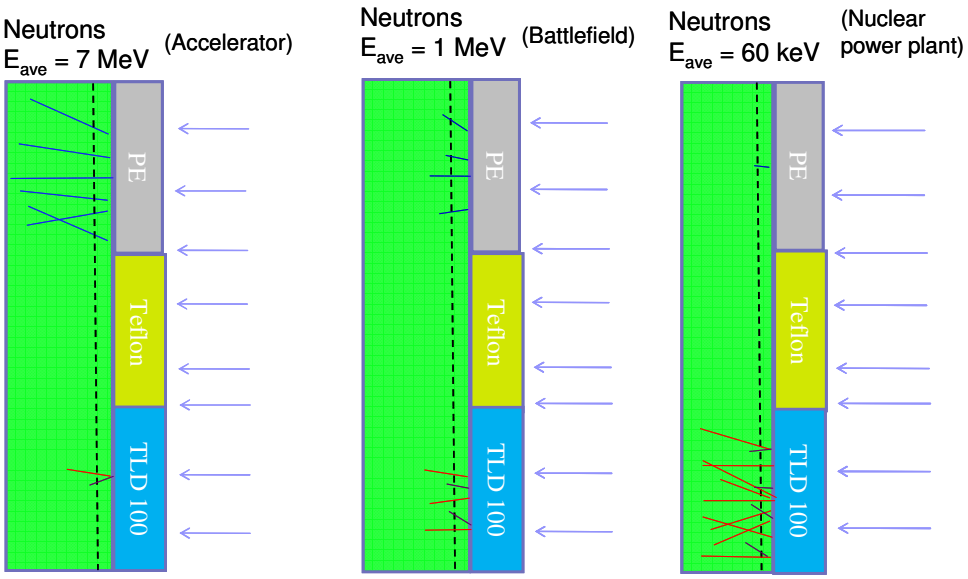

Figure 5.4 Diagram of FNTD-converter combinations illustrating energy response (section 5.4) and neutron-gamma separation (section 5.9).

5.1.2 Charged particle equilibrium layer

Quasi-charged particle equilibrium was created during photon irradiation by placing a converter in contact with the FNTD. Polytetrafluoroethylene (PTFE or Teflon®), which consists of carbon and fluorine (polymer of C_2F_4) having low neutron interaction cross-sections, was used for gamma dosimetry to perform neutron-gamma separation (section 5.4). PTFE was placed on the polished side of the FNTD to provide a build-up layer in front of the crystal. PTFE has similar electron density to the neutron converters and will create similar build up layers of charged particles in FNTDs. 1 mm thick PTFE was used in experiments.

5.1.3 Irradiations

A large number of irradiations and measurements were performed to prove that FNTDs are valid neutron and gamma dosimeters. The irradiation facilities with

sources and their neutron or photon energies are listed in Table 5.1. Specific irradiation details are discussed in the results sections.

Table 5.1 List of neutron and photon irradiation facilities with sources and their average energies used.

Facility	Source	Energies
Landauer – Stillwater, USA	x-ray	40 kVp
Landauer – Glenwood, USA	x-ray	20 kVp-250kVp
	^{241}AmBe neutron	Broad spectrum – 4.4 MeV
	Paraffin moderated ^{241}AmBe neutron	Broad spectrum
	^{137}Cs gamma	662 keV
NPL, England	Mono-energetic neutron	40 keV 59 keV 70 keV 100 keV 160 keV 250 keV 1.1 MeV 2.2 MeV 5 MeV
SCK-CEN, Belgium	Mono-energetic neutron	500 keV 1.0 MeV 3.5 MeV 7.0 MeV 15.9 MeV 19.5 MeV
PTB, Germany	Mono-energetic neutron	14.6 MeV
	Inscattered ^{252}Cf	Broad spectrum – 200 keV
RARAF Columbia University, USA	Mono-energetic neutron	200 keV 500 keV 1.0 MeV 2.0 MeV 5.9 MeV 14.0 MeV
	Microbeam	60-200 keV
PNNL, USA	^{241}AmBe neutron	Broad spectrum – 4.4 MeV
	Paraffin moderated ^{241}AmBe neutron	Broad spectrum
	^{252}Cf	Broad spectrum – 1.2 MeV
	D_2O moderated ^{252}Cf	Broad spectrum – 600 keV
White Sands Missile Range, USA	Fast burst reactor neutrons	Broad spectrum – 1.2 MeV
	REBA gamma	>250 keV
AREVA, France	Nuclear reactor neutrons	Broad spectrum – 1.1 MeV
CUH, Denmark	18 MV LINAC (photoneutrons)	Broad spectrum – 266 keV

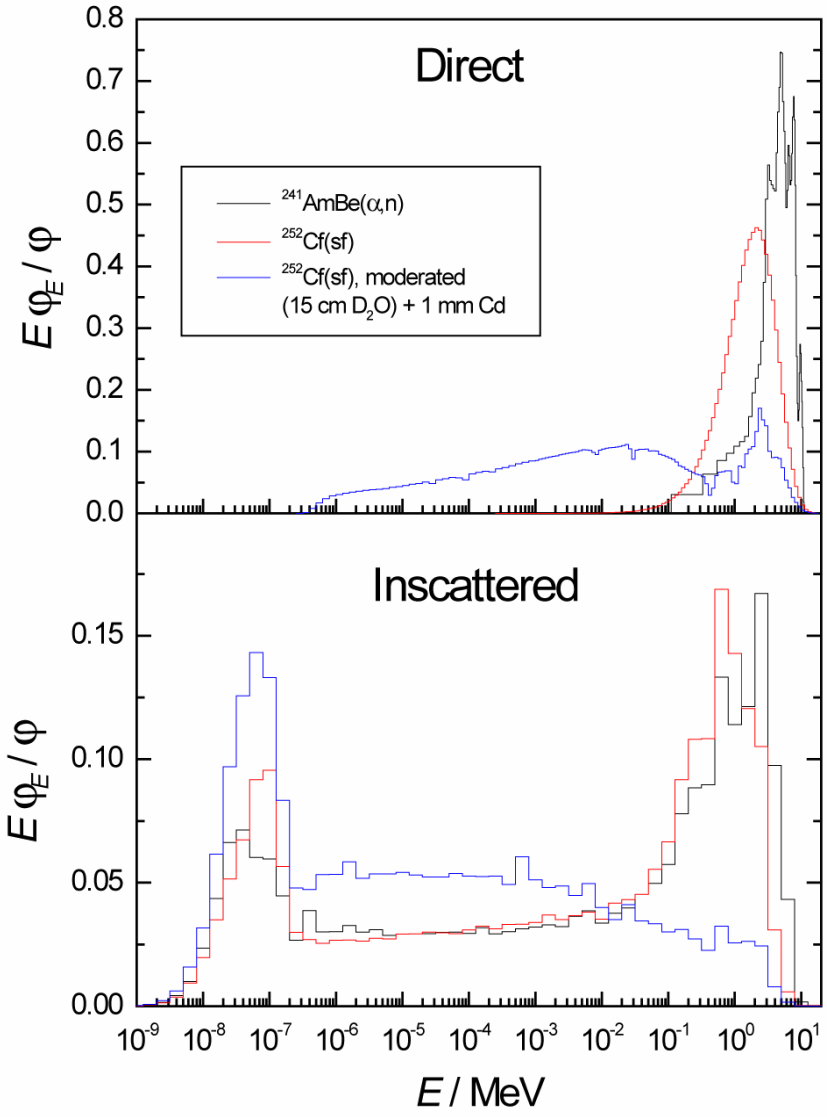

Figure 5.5 Spectra of broad spectrum neutron sources directly in the primary field (top) and scattered from the room (bottom) (Courtesy of Andreas Zimbal at PTB).

The term mono-energetic is used here to describe a spectrum of neutrons peaked at a particular mean energy. Energy spectra for broad spectrum ^{241}AmBe, ^{252}Cf and D_2O moderated ^{252}Cf are shown in Fig. 5.5. Figure 5.5 illustrates neutron spectra directly in the primary radiation field (direct) and the contribution from room scattering (inscattered). D_2O moderated ^{252}Cf shows a significant contribution of fast neutrons in addition to thermalized neutrons.

5.1.4 Track counting

SSNTDs determine neutron dose by relating the number of tracks caused by nuclear reactions either in the detector itself or from a neutron interacting with a converter. Neutron dose is proportional to the track density and is determined by

$$D = \frac{(N' - B)}{S} \quad , \tag{5.3}$$

where N' is the measured track density, B is the background track density and S is the sensitivity of the detector in terms of track density per unit dose.

Track detectors have a distinct advantage over other neutron dosimeters in that the detection parameter is binary, either there is a track or there is not. The binary nature of track detection allows for lower limits of detection because of lower uncertainty in the background noise. The most recent developments in image processing for track recognition and counting were described in detail in section 4.2.

5.1.5 Spatial frequency analysis

Spatial frequency analysis provided a new approach to determine the dose of radiation through evaluation of the spatial modulation of the fluorescence intensity within at least one image acquired from an irradiated FNTD. The modulation of fluorescence intensity is caused by non-uniform distribution of ionization produced by charged particles (either heavy recoils or secondary electrons) through the Coulomb interaction with the FNTD. Quantitative evaluation of fluorescence intensity

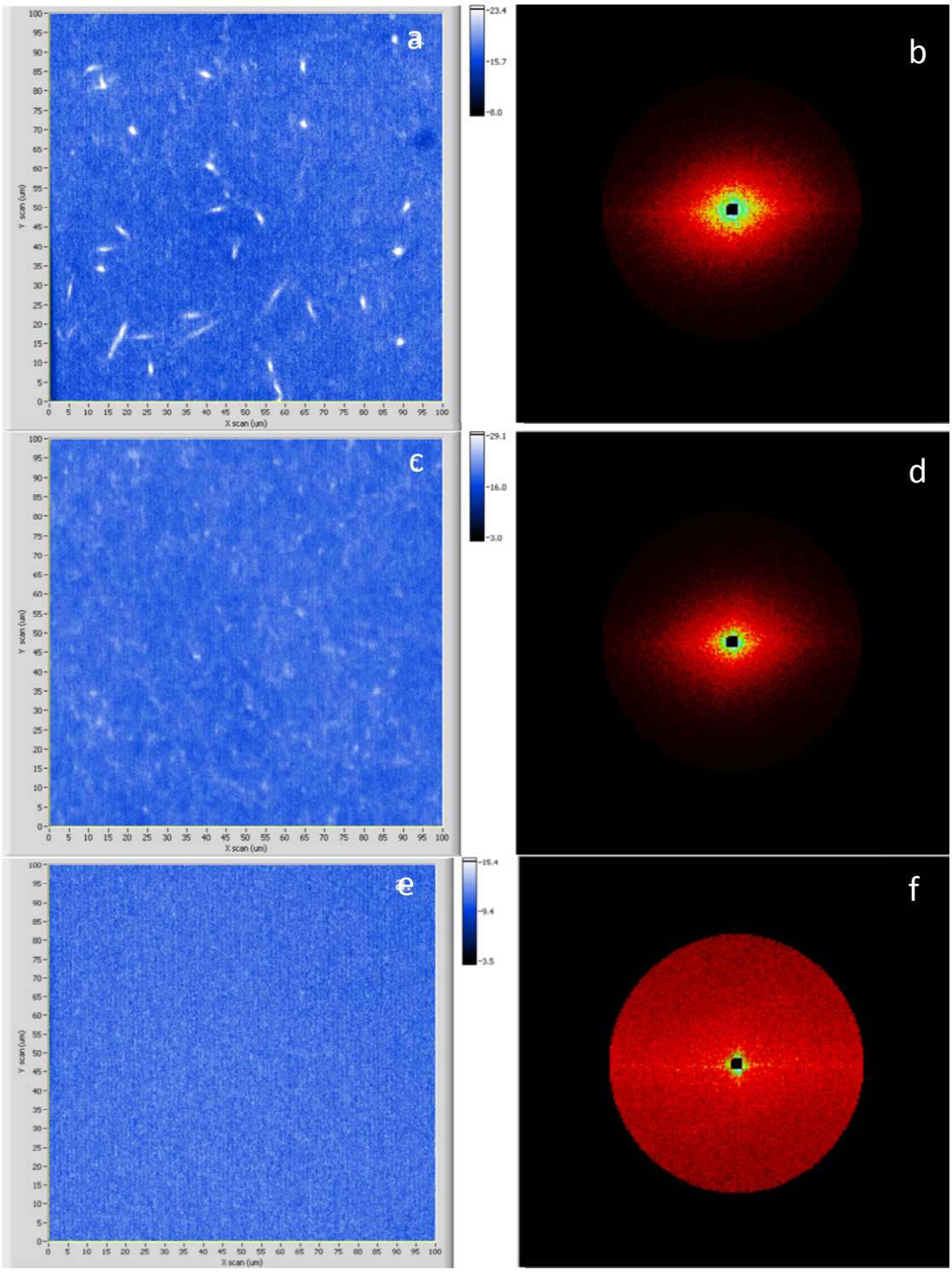

Figure 5.6 100 x 100 μm^2 images and their 2D power spectra of an FNTD irradiated with 30 mSv of fast neutrons (a and b), 3.5 cGy of gamma (c and d) and an optically erased FNTD (e and f). Low frequencies below 2% and high spatial frequencies above 52% were removed because they do not carry any useful information.

modulation can be determined by calculating the spatial power of the image. The power within a spatial frequency range, *dkdl* is given by

$$P = \int_{k_0}^{k} \int_{l_0}^{l} \left| F(k,l) \right|^2 dkdl \tag{5.4}$$

where k_0 and l_0 are the initial spatial frequencies of interest and $|F(k,l)|$ is the magnitude of the Fourier transform of the image with spatial frequencies k and l and is defined in the discrete Fourier transform as

$$F(k,l) = \frac{1}{N^2} \sum_{m=0}^{N-1} \sum_{n=0}^{N-1} f(m,n) e^{-\frac{2\pi i}{N}(km+ln)} \tag{5.5}$$

where $f(m,n)$is the intensity of the original image in the spatial domain at points m and n, $F(0,0)$ represents the DC offset of the image.

Fluorescence images from the Al_2O_3:C,Mg crystal after medium and high doses of fast neutrons show a significant number of bright tracks, that in the spatial frequency domain, should have a certain distinctive power spectrum (Fig. 5.6, a and b). The same is true for medium and high doses of gamma radiation (Fig. 5.6, c and d). Tracks of individual secondary (or delta) electrons are in general invisible because of their low ionization density but with the increase of gamma dose they start overlapping and one can see bright features (which gives the appearance of a “lumpy” texture) on the image that cause difficulty identifying and counting recoil proton tracks. This lumpiness of the image in a spatial frequency domain produces features in a certain frequency range that grow as absorbed dose increases. As-grown crystals also show distinctive power spectra because they contain some equilibrium concentrations of F_2^+(2Mg) color centers which produce non-uniform background fluorescence. In turn, well bleached FNTD crystals have very uniform residual

fluorescence background that produces very small intensities on the spatial frequency power spectrum.

Figure 5.6 shows example images and their 2D power spectra of both neutron and gamma irradiated FNTDs as well as a bleached un-irradiated detector. Each image is transformed to the frequency domain by performing the FFT. The magnitude of the FFT is then calculated and squared to obtain the power per frequency interval of the image. The power of the image is calculated by eq. (5.4).

5.2 Dose linearity

5.2.1 Track counting for neutron dosimetry

The most important parameter for dosimetry is that the dosimeter is proportional to dose. Dose linearity was demonstrated by irradiating FNTDs with fast and moderated neutrons from calibrated ^{241}AmBe neutron sources at the Landauer irradiation facility. Delivered doses were in the range from 0.3 to 300 mSv for fast neutrons and from 0.3 to 10 mSv for moderated neutrons. Irradiations with fast neutrons were performed using the ^{241}AmBe source in two geometries: "free-in-air" at 20 cm from the source and on a 30×30×15 cm^3 PMMA phantom at 50 cm distance. Moderated neutrons were produced by the ^{241}AmBe source moderated with paraffin. Detectors covered with PE, ^{10}B and ^{6}LiF were irradiated with all of the sources and doses; $^{6}Li_2C0_3$ covered FNTDs were irradiated with moderated neutrons and PTFE covered FNTDs were irradiated with fast neutrons free-in-air.

FNTDs exposed to neutrons from unmoderated and moderated ^{241}AmBe both free-in-air and on phantom were imaged at a depth of 3 μm below the surface. 50 images were obtained with a field of view of 100 x 100 μm^2 for each FNTD. Dose dependences presented in Figs. 5.7 - 5.9 show good linearity within four orders of investigated dose range for fast neutrons. There is no significant difference in sensitivity of FNTDs behind PE converters between irradiations performed free-in-air and on-phantom (Fig.5.7 compared to Fig. 5.8), which indicates that albedo neutrons do not affect the sensitivity of the FNTD-PE combination to fast neutrons.

The obtained sensitivity of 21.5 tracks/mm^2/mSv is consistent with preliminary results (Akselrod et al, 2006a). In comparison, the sensitivity of LanTrack CR-39 to fast neutrons is 12.1 tracks/mm^{-2}/mSv (Salasky, 2006). The sensitivity of FNTDs to moderated neutrons with the enhanced ^{6}LiF converters as determined from the slope of the dose dependence in Fig.5.9 is 6500 tracks.mm^{-2}.mSv^{-1} which is also consistent with the sensitivity reported previously by Akselrod et al. The track density per 1 mSv of dose for the thermal component of FNTDs obtained using enhanced ^{6}LiF is 300 times higher than for the PE component making the ^{6}LiF portion almost insensitive to fast neutrons. As a result, it was concluded that the PE component of the detector is sensitive only to fast neutrons and the ^{6}LiF part provides response exclusively to lower energy components of the field. ^{10}B-loaded Teflon converters gave almost 100 times lower track density than the enriched ^{6}LiF (Fig. 5.9).

Significant numbers of tracks measured behind the PE converters after irradiations with the paraffin-moderated ^{241}AmBe source (Fig. 5.9) proves that there is still a large flux of fast neutrons in the field. Using a fast neutron sensitivity of 21.5

$mm^{-2}.mSv^{-1}$ obtained from Fig. 5.7, it was calculated that the dose equivalent of fast neutrons in the moderated field exceeds 5 times the dose equivalent for thermal neutrons. In turn, detectors behind enriched ^{6}LiF and ^{10}B converters allowed us to estimate the contribution of thermal dose during irradiations with fast neutrons free-in-air and on-phantom due to scattering and albedo neutrons (Fig.5.7 and 5.8). Using the sensitivity to thermal neutrons of 6500 $mm^{-2}.mSv^{-1}$, it was calculated that the contribution of thermal neutrons during "free-in-air" irradiations is only 0.1%, whereas during "on-phantom" irradiations their contribution increased almost 10 times. Scattering of fast neutrons from the concrete walls (3-4 m distance) and the ceiling (1.5 m distance) should contribute at least 5% of the total dose.

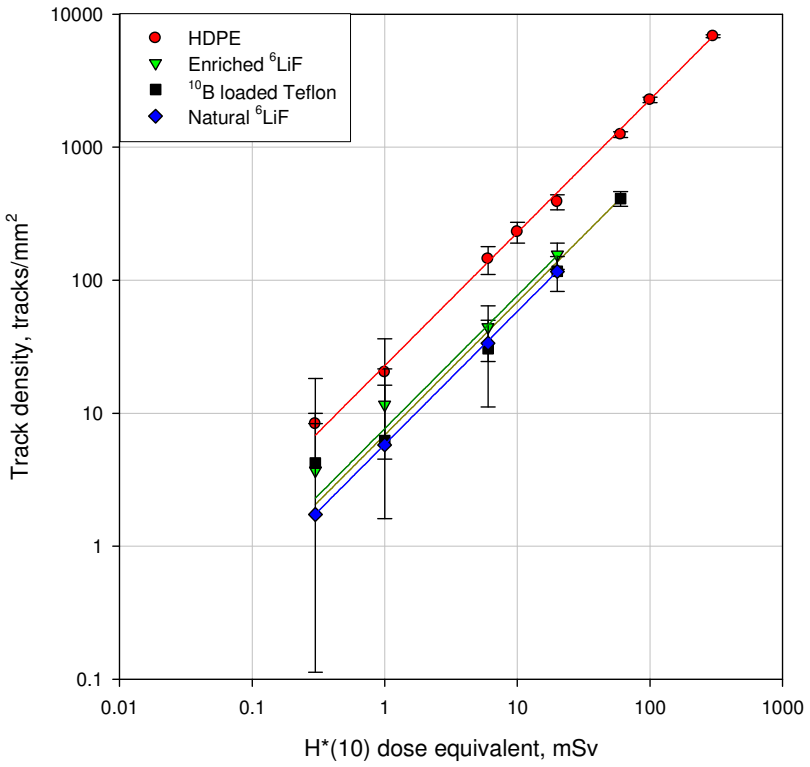

Figure 5.7 Dose dependences for FNTDs covered with PE, enriched ^{6}LiF, ^{10}B loaded Teflon™, and ^{6}LiF with a natural abundance of ^{6}Li irradiated with fast neutrons from $^{241}AmBe$. Ambient dose equivalent, H*(10) is used because the irradiations were free-in-air.

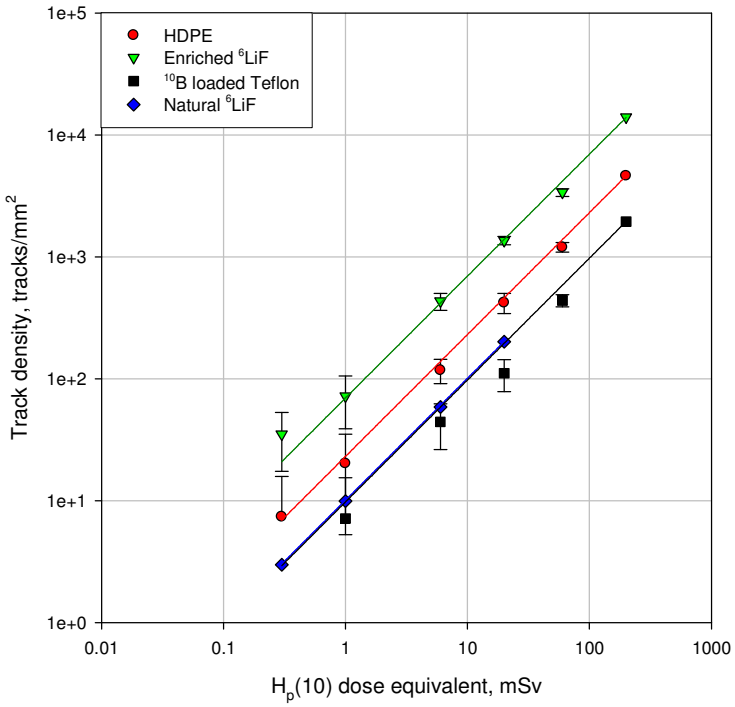

Figure 5.8 Dose dependences for FNTDs covered with PE, enriched ^{6}LiF, ^{10}B loaded Teflon®, and ^{6}LiF with a natural abundance of ^{6}Li irradiated on-phantom (albedo configuration) with fast neutrons from ^{241}AmBe. Personal dose equivalent, $H_p(10)$ is used because of the simulated body behind the FNTDs.

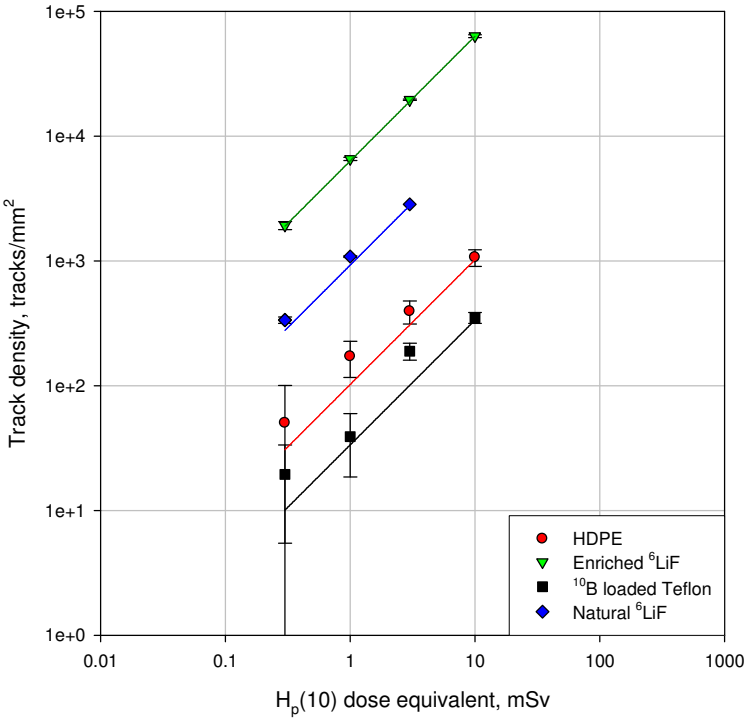

Figure 5.9 Dose dependences for FNTDs covered with PE, enriched ^{6}LiF, ^{10}B loaded Teflon®, and ^{6}LiF with a natural abundance of ^{6}Li irradiated with moderated neutrons from paraffin moderated ^{241}AmBe.

Another important observation is the difference in track density for ^{6}LiF and ^{10}B converters obtained after irradiations in different neutron fields (see Figs. 5.7 and 5.9). For neutrons moderated by paraffin with a large thermal component, the ^{6}Li converter provides significantly higher response than the ^{10}B converter (Fig. 5.9), whereas for "free-in –air" fast neutron irradiations their sensitivity is almost equal (Fig.5.7). The albedo configuration during "on-phantom" irradiations shows the intermediate situation (Fig. 5.8).

The nuclear reaction and product energies for ^{6}Li(n,α) and ^{10}B(n,α) are detailed in equations (5.1) and (5.2) respectively. The thermal neutron capture cross-section for ^{10}B is about four times that for ^{6}Li, but the Q-value of the ^{6}Li(n,α) reaction is about twice that of the ^{10}B(n,α) reaction. Because both products of the ^{6}Li(n,α) reaction have higher energies, their range is longer and thus easier to detect using FNTDs than the products from the ^{10}B(n,α) reaction. The tritium ion has a range of about 24 μm in Al_2O_3 where as the alpha particle has a range of about 4 μm as calculated by SRIM 2006 (Zieglar and Biersack, 2006). In turn, the range of alpha particles produced in the ^{10}B(n,α) reaction is only 2.9 μm and explains the low detection efficiency of this converter.

5.2.2 Image power for neutron and gamma dosimetry

Linearity of the new image power method for determining neutron and gamma doses was tested by irradiating FNTDs with neutrons and gamma. Detectors were mounted in FNTD holders specifically designed to cover half of the polished side of

the FNTD with 800 μm of PE and the other half with either a ^{6}LiF (TLD-100 chip) or a 1 mm thick piece of PTFE.

One set of FNTDs were irradiated with fast neutrons from a ^{241}AmBe source in a range of doses from 1 mSv to 10 Sv. Another set of FNTDs were irradiated with 662 keV gamma photons from a ^{137}Cs source in a range of doses from 3 mGy to 30 Gy. A third set of FNTDs were irradiated with 40 kVp x-rays in a dose range of 300 mGy to 300 Gy[6].

The dose dependences for neutrons and gamma are presented in Figure 5.10. The dose dependences show that the new parameter, image power, is proportional to the delivered dose. The dose dependence for ^{241}AmBe neutrons (E_{av}=4.4 MeV) in terms of absorbed dose (Q = 10) is collinear with the gamma dose dependence. This suggests that the image power is a good parameter for the dosimetry of both neutron and gamma radiation. It should be noted that ^{241}AmBe also has a 59 keV gamma decay component that contributes 2.5% of the overall dose in terms of dose equivalent.

The low dose limit can be calculated from these data and is roughly estimated by

$$LDL = \frac{3\sigma}{S(D)} \tag{5.6}$$

where σ is the standard deviation of the background and *S(D)* is the sensitivity (slope of the dose dependence). The minimum detectable dose, according to the available data obtained from bleached detectors is around 800 μGy. Here, σ = 14.8 and S*(D)* = 53.2 units/mGy of absorbed dose, so the low dose limit = 835 μGy.

[6] The x-ray doses reported were corrected for the over-response of Al_2O_3 to lower energy x-rays (10 keV-200 keV) due to the increased photoelectric effect. See the discussion in section 5.4 for more details.

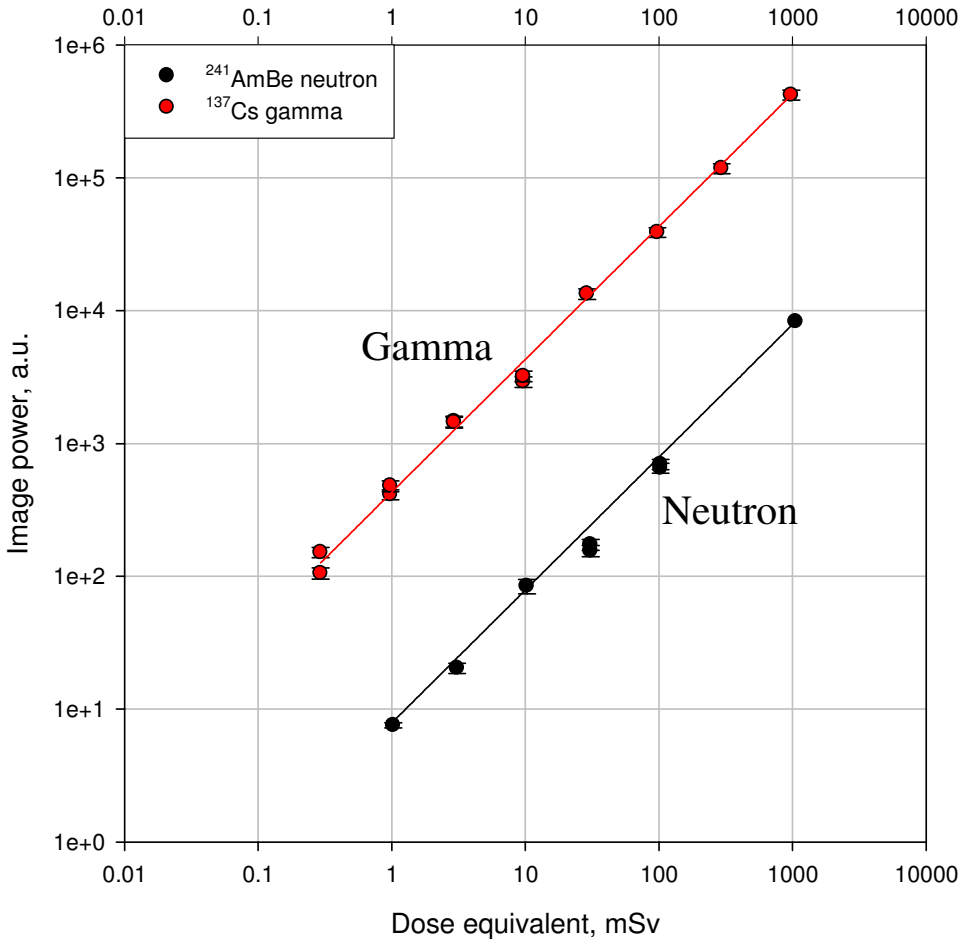

Figure 5.10 Image power dose dependences for FNTDs irradiated with ^{241}AmBe fast neutrons (black symbols) and ^{137}Cs gamma photons (red symbols) in terms of dose equivalent.

The dynamic range of this new image processing technique for high doses of photons was tested on FNTDs irradiated with 40 kVp X-rays at Landauer in Stillwater. The dose dependences for both the image power and conventional average fluorescence intensity of the acquired images are presented in Figure 5.11. The saturation dose for both parameters was approximately 100 Gy, but the new processing technique provided much better linearity and 1:1 slope, whereas the average fluorescence intensity shows sublinear behavior. Data presented in Fig. 5.10

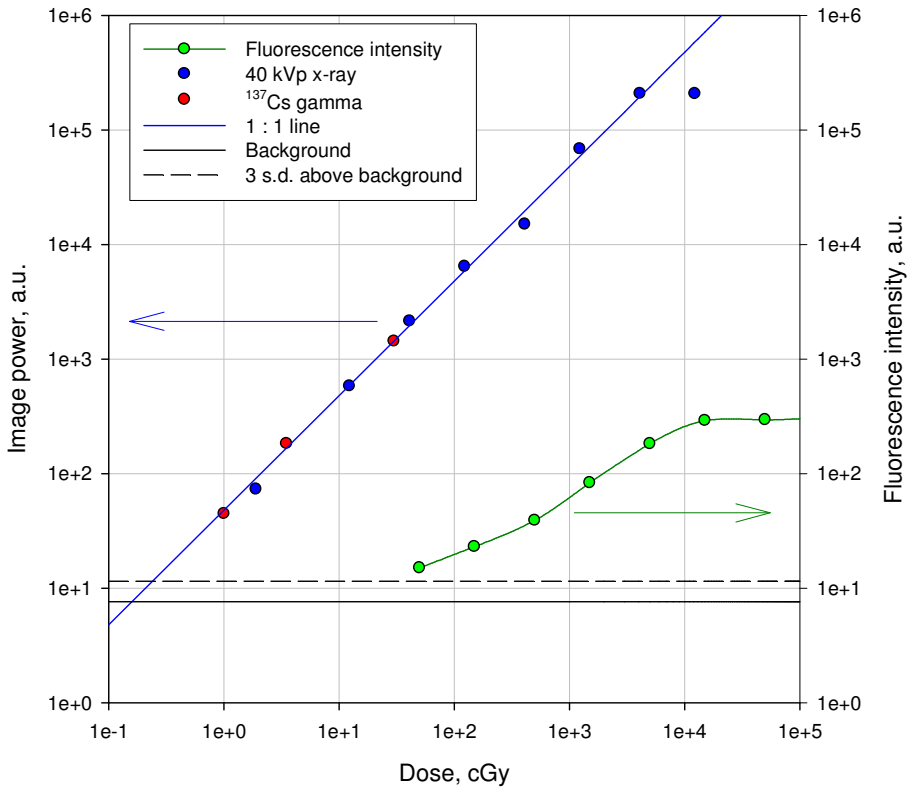

Figure 5.11 Dose dependence for image power and average fluorescence intensity for FNTDs irradiated with ^{137}Cs gamma and 40 kVp x-rays. Image power was corrected for x-ray over response.

combined with data of Fig. 5.11 provide evidence that the new processing method allows for linear dose response for photon radiation within almost 5 decades from 1 mGy to 50 Gy. Investigation of the dynamic ranges for dosimetry of fast neutrons will continue but it is now obvious that this new technology gives unprecedented neutron/gamma ratio for difficult to detect and discriminate fast neutrons. A large dynamic range combined with data presented below on two techniques for neutron/gamma signal separation makes this new dosimetric method extremely promising for a variety of applications.

5.2.3 Combined methods

Track counting fundamentally has a very low LDL because it uses binary mode – track or no track. The LDL of the image power mode is approximately an order of magnitude larger than that for track counting because there are still some variations in analog signal and noise in the imaging readout system. The saturation dose for track counting mode occurs when tracks begin to overlap making it impossible to distinguish individual tracks; this happens before 1 Sv for FNTDs. Saturation occurs at a higher dose in image power mode because it is an analog technique so overlapping tracks does not affect the dose linearity. The dose range for FNTDs can be extended by combining the two methods. Dose dependences for both image power and track counting modes are shown in Fig. 5.12. The effective dose range of FNTDs for neutrons spans at least 5 orders of magnitude by coupling track counting with the new image power processing method.

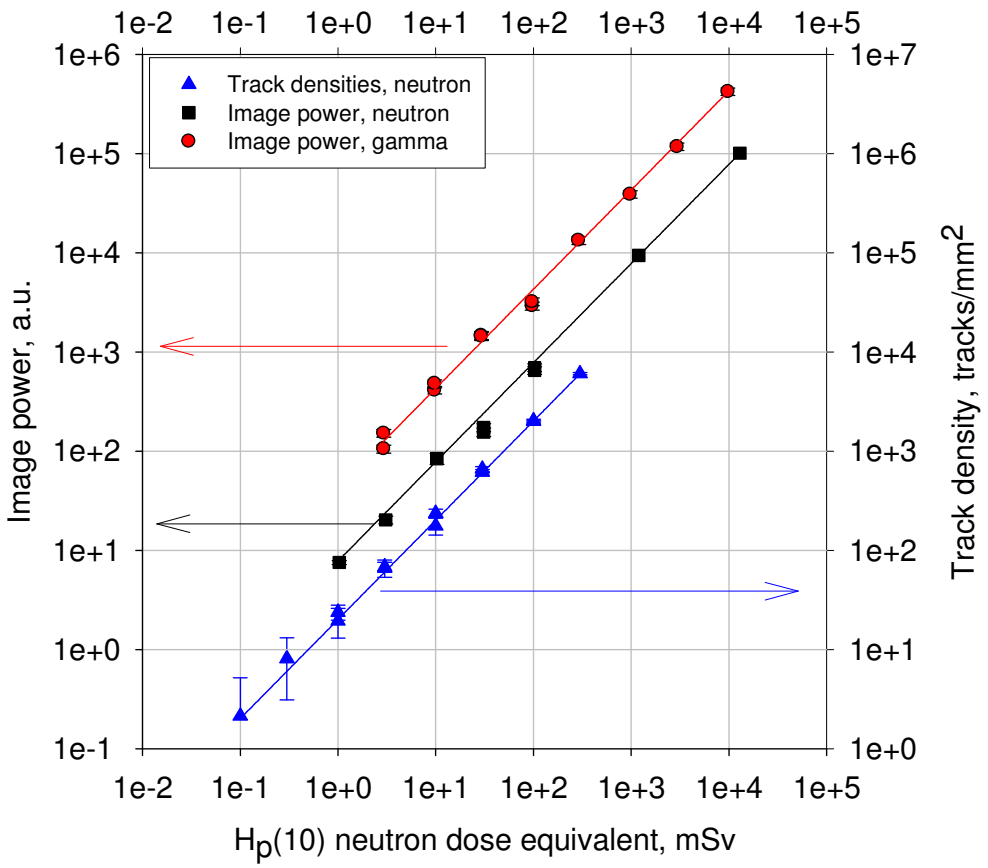

Figure 5.12 Dose dependences for fast neutrons using track counting (triangles) and image power mode (squares). Dose dependence of gamma induced signal using image power mode are shown as red circles.

5.3 Crystal to crystal differences in sensitivity

Dosimeter sensitivity, defined as the slope of the linear portion of the dose dependence, is one of the most important parameters for determining doses. If all dosimeters have the same sensitivity, then only one calibration for all detectors is required. If dosimeters have varying sensitivities, then individual calibrations for every detector, or group of similar detectors, is required. Constant sensitivity among dosimeters is desired to avoid excess calibrations. FNTD sensitivity for both track counting and the new image power mode were tested by irradiating FNTDs with different concentrations of color centers. The results are discussed below.

5.3.1 Track counting

Track counting is a binary system and as such should be insensitive to small variations in crystal properties because the number of tracks is determined by the concentration of neutron conversion elements in the converter (i.e. the amount of hydrogen in PE or ^{6}Li in ^{6}LiF). Figure 5.13 shows dose dependences in track counting mode for FNTDs cut from three crystals with varying coloration. 50 images per FNTD were acquired and processed (total area of 0.5 mm^2). Determined neutron sensitivities varied by 3.4% from the highest coloration to the lowest showing that track counting is nearly insensitive to color center concentration.

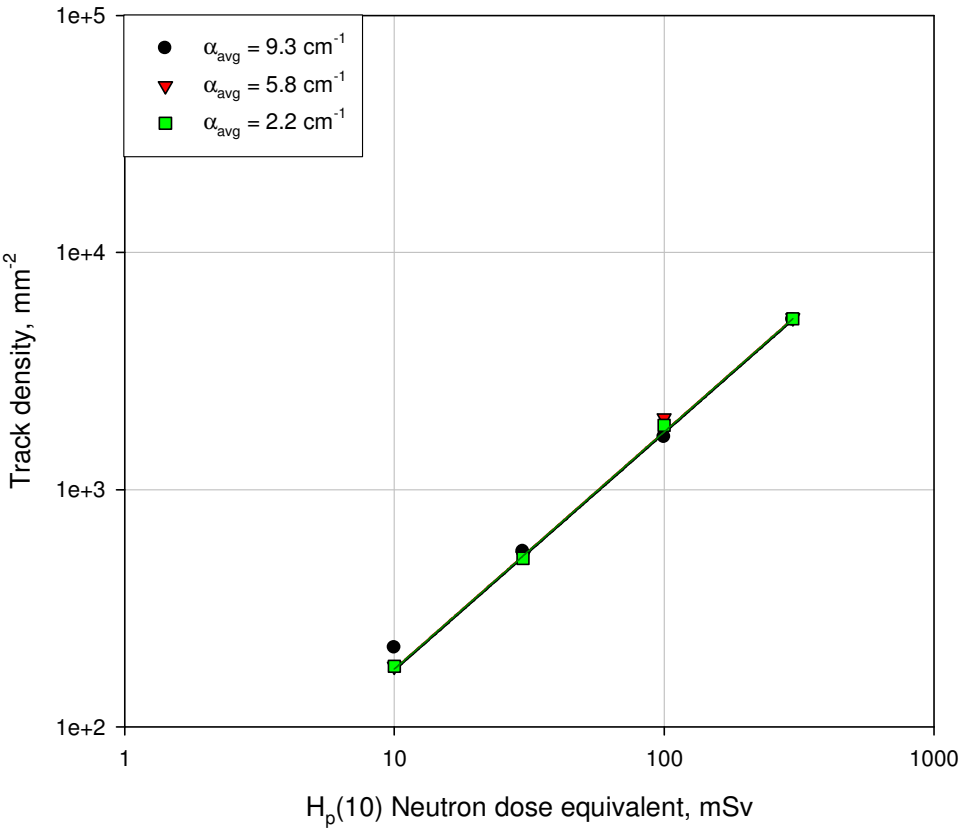

Figure 5.13 Dose dependence in track counting mode for FNTDs cut from crystals with varying coloration (coloration is defined as the absorption coefficient of the F_2^{2+}(2Mg) color center, α). A total area of 0.5 mm^2 was scanned. The difference in sensitivities from the highest to lowest coloration crystals was only 3.4%.

5.3.2 Image power

Track counting is not sensitive to the color center concentration within certain limits because the imaging system finds the track or it does not. Spatial frequency analysis uses an analog parameter that is more sensitive to variation in color center concentration even though the average absolute intensity of fluorescence is not measured. Crystals with different properties have different sensitivities to energy deposition (fluorescence amplitudes vary as a function of F_2^{2+}(2Mg) color center concentration). Because the image power is an analog parameter and partly depends on the fluorescence amplitude, it might respond differently from one crystal to another. Figure 5.14 shows dose dependences for detectors cut from three different crystals. Different crystals all have slightly different slopes (sensitivity) and offsets (background). All samples were optically bleached (erased) prior to irradiation.

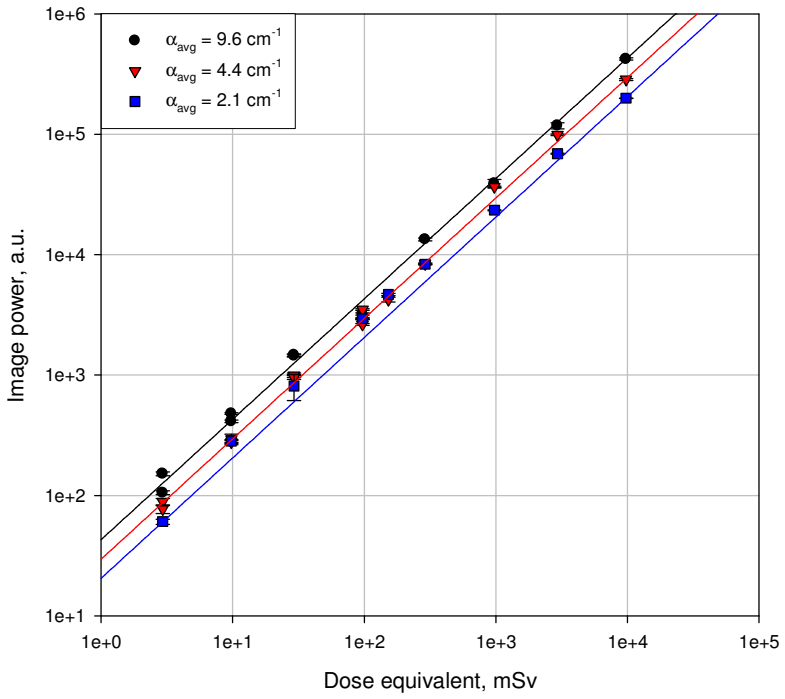

Figure 5.14 Image power dependence on dose for FNTDs cut from three crystals with different coloration. A total area of 0.5 mm^2 was scanned. The difference in sensitivities from the highest to lowest coloration crystals was ~60%.

There is a significant difference in the sensitivity of FNTDs cut from crystals with different color center concentrations. The largest difference is between FNTDs cut from A136 (α_{avg} = 9.6 cm^{-1}) and A173 (α_{avg} = 2.1 cm^{-1}) which is approximately 65%. A153 (α_{avg} = 4.4 cm^{-1}) is in the middle. It is apparent that the sensitivity depends on the number of F_2^{2+}(2Mg) color centers in the crystal. The difference in sensitivity can be corrected in a number of different ways. In commercial operation, FNTDs from different crystals should be checked for quality to ensure that the initial values and response to a reference dose of known radiation (x-rays or gamma) stay within predetermined tolerances. If it is not feasible to "pre-calibrate" the detectors, a post-irradiation calibration can be performed on the few individual detectors with unusually high doses.

The variation of FNTDs cut from the same crystal is small enough to determine the dose if the crystal is known. Evidence of this is that most of the data presented above (dose dependences except for the crystal comparison, x-ray energy dependences and mono-energetic neutron dependences) are results from bleached FNTDs cut from crystal A136. Crystal A136 is one of the most non-uniform crystals used in these investigations. It is therefore reasonable to assume that all other crystals will be as reliable if not better.

5.4 Improving lower limit of detection

FNTDs are cut from multiple crystals all with varying properties (color center concentrations, uniformity of coloration, concentration of crystal defects, etc.); single

crystals also have variance leading to differences in response to ionizing radiation. Differences in sensitivity to ionizing radiation, background fluorescence and variation in the background fluorescence can cause problems in track recognition and inconsistency in power spectrum analysis (see section 5.3 above).

F_2^+(2Mg) color centers, that are normally radiation induced color centers, exist in "as-grown" crystals causing background fluorescence during readout. Non-uniformity of this background fluorescence limits the ability to detect tracks caused by low LET particles. Fluorescence intensity of charged particle tracks and the image power are correlated with the concentrations of F_2^{2+}(2Mg) centers (see section 6.3) meaning the sensitivity of the FNTD depends on the concentration of F_2^{2+}(2Mg) centers. As seen in section 5.3, variation in color center concentration can cause significant problems. Therefore, methods for assessing and improving the performance of FNTDs were needed.

The figure of merit for assessing FNTD performance was the signal to noise ratio (SNR) defined as the ratio of the mean fluorescence intensity of tracks created by normally incident 5.11 MeV alpha particles ($\bar{I}_\alpha$) and the standard deviation of the background fluorescence (σ_{bgrd}), i.e.,

$$SNR = \frac{\bar{I}_\alpha}{\sigma_{bgrd}} \tag{5.7}$$

In order to increase SNR, thermal treatments and an optical bleaching procedure based on the results of photochromic and thermal aggregation experiments in chapter 3 were implemented. Thermal aggregation was performed to increase the concentration of F_2^{2+}(2Mg) centers and optical bleaching of F^+(Mg) and F_2^+(2Mg)

centers was performed to eliminate competitors (F^+(Mg)) and background fluorescence (F_2^+(2Mg)). The thermal aggregation procedure used to enhance the concentration F_2^{2+}(2Mg) was that of Akselrod et al (2003b) and as such will not be discussed here in detail. The following section details new optical bleaching routines used to enhance the performance of FNTDs.

5.4.1 Annealing-bleaching sequences

The most obvious hindrance to reliable track detection and spatial frequency analysis is the presence of pre-existing, non-uniform background fluorescence. Also, investigations of photo- and radiochromic transformations of defects in Al_2O_3:C,Mg detailed in chapter 3 demonstrated that F^+(Mg) centers compete with F_2^{2+}(2Mg) centers for ionized electrons. It is for these reasons that two enhancement procedures were investigated. The first procedure consisted of the following steps:

1) Thermally anneal the crystal to 680°C and cool it slowly at a rate of 0.5°C/minute down to 500°C for 15 hours as described by Akselrod et al (2003b) to increase the concentration of F_2^{2+}(2Mg) centers.

2) Bleach with 325 nm light to eliminate F_2^+(2Mg) centers that cause background fluorescence.

The second procedure consisted of:

1) Thermally anneal the crystal to 680°C and cool it slowly at a rate of 0.5°C/minute down to 500°C for 15 hours as described by Akselrod et al (2003b) to increase the concentration of F_2^{2+}(2Mg) centers.

2) Bleach with 260 nm light specifically to reduce the concentration of F^+(Mg) centers, which are considered undesirable competitors for free electrons during irradiation.

3) Re-anneal the crystal as in step 1 to eliminate excess F_2^+(2Mg) centers created by bleaching with 260 nm light (see explanation below).

4) Bleach with 325 nm light to eliminate F_2^+(2Mg) centers that cause background fluorescence.

Bleaching the FNTD with 260 nm left the crystal in a state with approximately 150% more F_2^+(2Mg) centers than in its original state (see chapter 3). The remaining amount of F_2^+(2Mg) centers were impossible to completely eliminate with 325 nm illumination, so the FNTDs were re-annealed with the same procedure as before. This extra annealing step eliminated excess F_2^+(2Mg) centers and returned the concentrations of F_2^+(2Mg) and F_2^{2+}(2Mg) centers close to their pre-bleached levels. An additional step of bleaching the crystal with pulsed 325 nm laser light was performed to ionize the remaining F_2^+(2Mg) centers. There was also a slight increase in F^+(Mg) luminescence after this 325 nm bleaching step but there was still an overall decrease of F^+(Mg) center concentration by approximately 60%. Figure 5.15 shows a PL spectrum of Al_2O_3:C,Mg after bleaching the crystal with pulsed 260 nm light, re-annealing and bleaching with 325 nm light.

In both procedures, residual F_2^+(2Mg) luminescence was practically eliminated as a result of photo-conversion of F_2^+(2Mg) centers into F_2^{2+}(2Mg) centers. The F_2^+(2Mg) bands, however, could not be completely eliminated due to equilibrium

distribution of free electrons between different color centers during the photo-ionization/bleaching procedure.

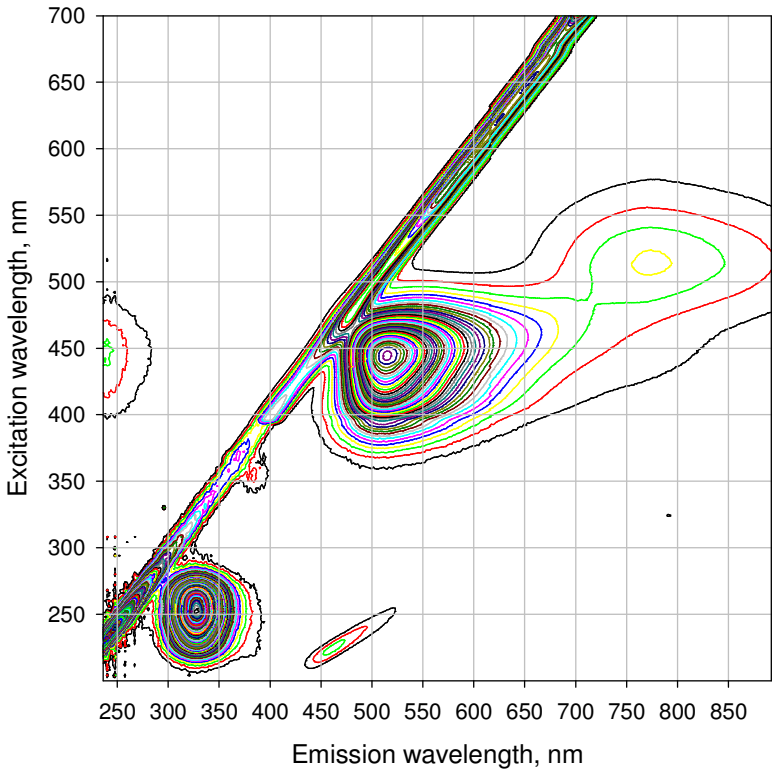

Figure 5.15 Photoluminescence spectrum of Al_2O_3:C,Mg after bleaching with 260 nm, annealing and bleaching with 325 nm light to reduce competing F^+(Mg) centers as well as background producing F_2^+(2Mg) centers.

5.4.2 Alpha particle testing

Alpha particle irradiations were used to evaluate the performance of Al_2O_3:C,Mg crystals after different treatment of the crystals. The results are summarized in Table 5.2. Each preparation step enhanced the SNR of the FNTDs.

Table 5.2 Improvements of SNR (average fluorescence intensity of alpha tracks divided by the standard deviation of the background fluorescence) as a result of different crystal treatment.

Crystal state	Background fluorescence, a.u.	Alpha track fluorescence, a.u.	SNR, a.u.
As grown	65 ± 2.35	22	9.36
Annealed	235 ± 2.79	38	13.6
Bleached 325 nm	21.5 ± 0.95	38	40.0
Bleached 260 and 325 nm	33 ± 0.95	45	47.4

In practical application, the benefit of bleaching with 260 nm is too small compared to the extra time required for the additional annealing step. Therefore, the 260 nm bleaching step was not used for FNTDs in this study. It is, however, important to note the increase in fluorescence intensity for alpha tracks since it may have future implications in low dose measurements by increasing the sensitivity of the FNTD.

Annealing and bleaching with 325 nm light proved to be the best practical combination of pre-irradiation treatments. This procedure increased the SNR by a factor of 4 in a period of time that was practically acceptable. Most FNTDs used in this study were treated with this procedure. Figure 5.16 is a set of images from the same FNTD after thermal annealing and irradiation with alpha particles (Fig. 5.16a), after bleaching with 325 nm light (Fig. 5.16b) and after irradiating again with alpha particles (Fig. 5.16c). Figure 5.16 also clearly demonstrates the ability to erase radiation induced fluorescence by optically bleaching with 325 nm light.

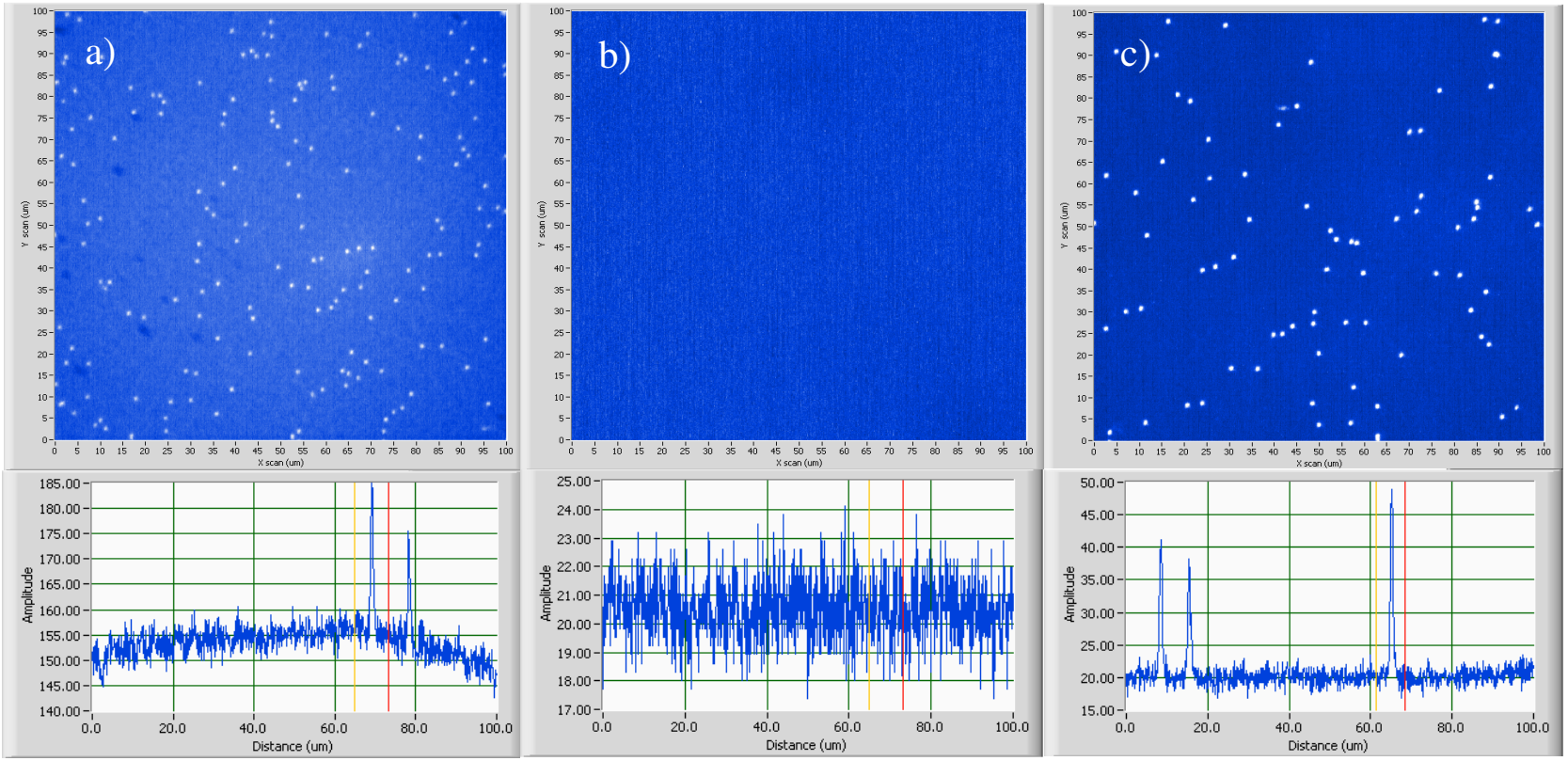

Figure 5.16 Images and cross sections of an FNTD after a) thermal aggregation enhancement and irradiated with alpha particles, b) after bleaching the same crystal with 325 nm light and c) after irradiating the crystal again with alpha particles.

5.4.3 Effect of bleaching on image power

Figure 5.17 shows images of unbleached (a) and bleached FNTDs (b) cut from the same crystal and their subsequent power spectra (c and d are horizontal views of the full 2-dimensional power spectrum; e and f are the powers as a function of spatial frequency). The average intensity of the bleached FNTD is around 10 a.u., almost a factor of 10 smaller than that of the unbleached FNTD. The power spectrum is also much more uniform. The horizontal view of the power spectrum (Fig. 5.17c and 5.17d) for a bleached FNTD is shown in the same scale as the unbleached to show the dramatic effect of bleaching. Defects, scratches and non-uniformity still contribute to the power spectrum, but their effect is now much less pronounced. There is a factor of 20 decrease in the amplitude of the power spectrum after bleaching (Fig. 5.17f). This provides a decrease in LLD and more reliable dose determination at low doses.

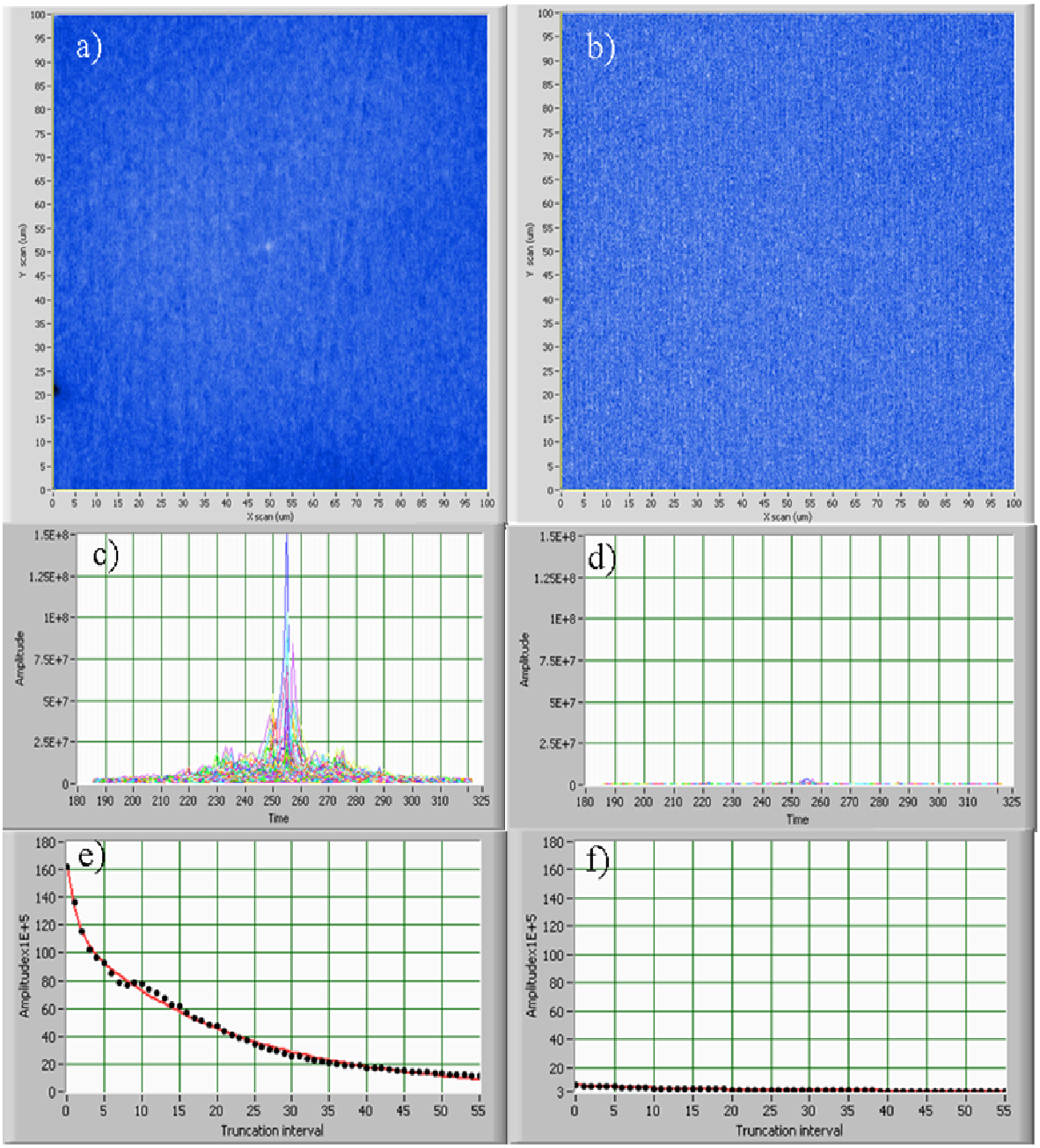

Figure 5.17 Effect of bleaching with 325 nm pulsed laser on background image (a and b) and power spectrum of FNTDs (c-f).

5.5 Neutron-gamma separation

In neutron dosimetry, FNTDs serve the same purpose as CR-39 PNTDs, to detect and count nuclear tracks induced by charged particles. FNTDs have many advantages over PNTDs, but PNTDs have the distinct advantage of being insensitive to low linear energy transfer (LET) radiation such as secondary delta electrons caused by irradiation with gamma or x-rays. FNTDs however, are sensitive to low LET radiation. Because neutrons are usually accompanied by gamma radiation, high contribution of gamma radiation to radiation-induced fluorescence signal might be a problem. If the dose of gamma radiation is above several cGy, the fluorescence induced by overlapping secondary delta electron tracks can interfere with the signal induced by recoil protons making it difficult to detect and count neutron induced tracks. Figure 5.18 shows two images, one of recoil proton tracks on an FNTD irradiated with 100 mSv of fast neutrons from ^{241}AmBe neutrons with 7.5 mGy of accompanying gamma dose and the other of recoil protons and overlapping delta electrons caused by irradiation with 100 mSv of ^{241}AmBe and 100 mGy of gamma from ^{137}Cs. After irradiation with higher doses of gamma, the recoil proton tracks are much less distinct and more difficult to identify and count. This problem leads to inaccurate neutron dose determination. Figure 5.19 shows track detection efficiency as a function of additional gamma dose.

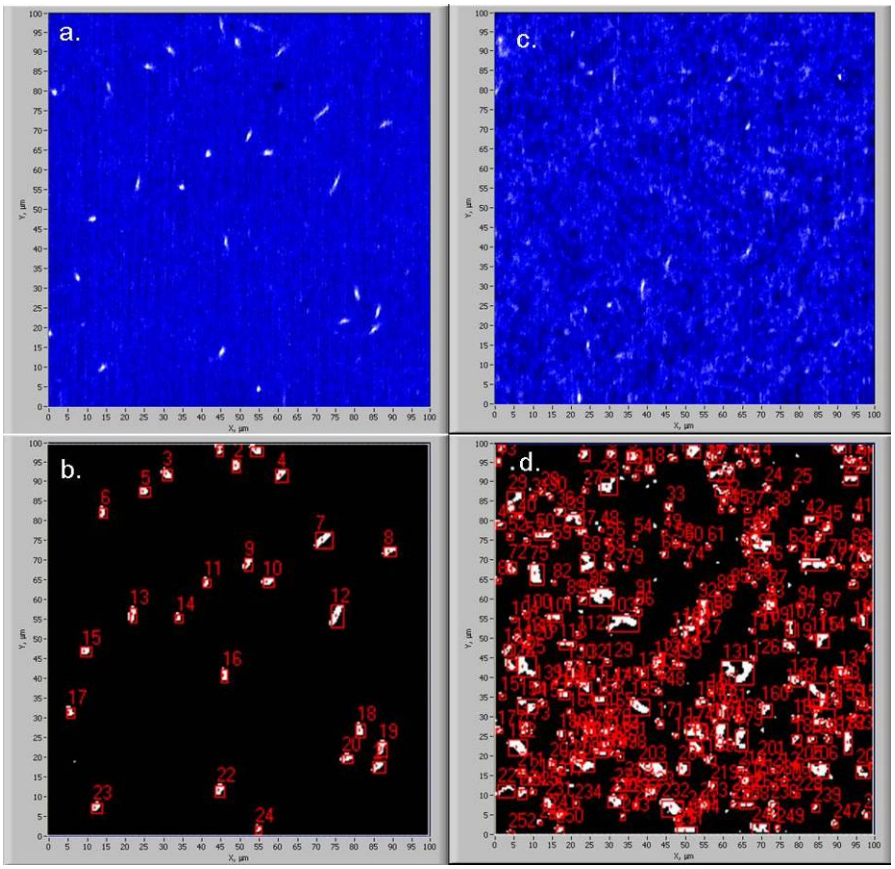

Figure 5.18 Images before and after image processing for FNTDs irradiated with 100 mSv of fast neutrons with 7.5 mGy accompanying gamma dose (a and b) and 100 mSv of fast neutrons with 100 mSv of ^{137}Cs gamma (c and d). This demonstrates the inability to count tracks when the FNTD is irradiated with large gamma doses.

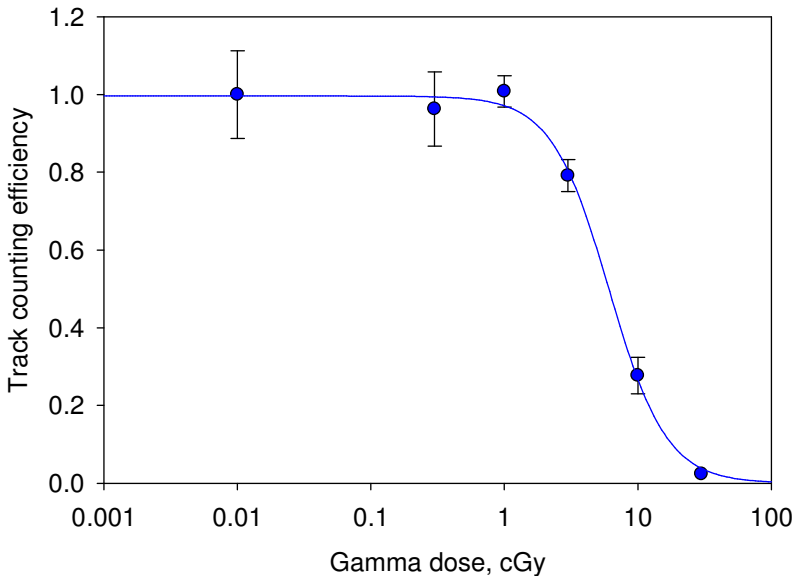

Figure 5.19 Detection efficiency as a function of gamma dose for recoil proton tracks irradiated with excess gamma from ^{137}Cs.

5.5.1 Experimental methods

Investigations of the neutron-gamma separation technique were performed with detectors mounted in the FNTD holder with half of the FNTD covered with 800 µm of PE and the other half with a 1 mm thick piece of PTFE The purpose of the PTFE was to provide charged particle equilibrium reducing the build-up layer at the surface of the FNTD after gamma irradiation. PTFE also has a similar density to PE so it is a viable material to compare with PE. PTFE and PE are needed for neutron-gamma separation. The carbon and fluorine atoms in PTFE have neutron interaction cross-sections that are orders of magnitude lower than hydrogen and ^{6}Li and thus produce a negligible number of nuclear recoils. Table 5.3 shows the track densities per unit neutron dose ($H_p(10)$) for PE and PTFE converters. The ratio of delivered neutron dose to gamma dose was from 3:1 to 1:3 in terms of dose equivalent.

Table 5.3 Track densities comparing the number of recoil nuclei from PE and PTFE.

Neutron dose, $H_p(10)$	Track density behind PE	Track density behind PTFE
100 mSv	2100 tracks/mm^2	5 tracks/mm^2
300 mSv	6180 tracks/mm^2	20 tracks/mm^2
1.21 Sv	~24000 tracks/mm^2	84 tracks/mm^2

It is common practice in neutron dosimetry to use two detectors to separate neutron and gamma signals, one that is sensitive to both neutrons and gammas and one that is sensitive only to gammas. The neutron dose is then extracted according to

$$D_n = \frac{Q_{n,\gamma} - A(\gamma)D_\gamma}{B(n)}, \tag{5.8}$$

where $Q_{n,\gamma}$ is the response of the detector sensitive to both neutrons and gamma, $A(\gamma)$ is the sensitivity of the detector to gamma, D_γ is the gamma dose and $B(n)$ is the

sensitivity of the detector to neutrons. This section describes two techniques to overcome the fundamental problem of the dosimetry of mixed neutron-gamma fields. The first technique utilizes FNTDs that are made sensitive to neutrons with PE or ^{6}LiF as a converter on part of the detector and insensitive to neutrons on another by placing PTFE on the same FNTD. The second technique uses the volume of the crystal near the surface as the neutron and gamma sensitive detector and the deep volume as the gamma only sensitive detector. See sections 5.6 and 5.7 for discussions on depth profiles.

5.5.2 Mixed field results

FNTDs irradiated with fast neutrons, gamma and fast neutrons plus gamma were imaged and processed using the image power method described in section 5.2. The image power dependence on neutron dose for FNTDs covered with PE and PTFE is shown in Fig. 5.20. Figure 5.21 shows the image power dependence on gamma dose for FNTDs covered with PE and PTFE. The linear increase in image power behind PTFE is mainly due to the 60 keV gamma decay of the ^{241}AmBe source which contributes 2.5% of the total dose in terms of dose equivalent. The number of carbon and fluorine recoils from PTFE is only 0.3% of the number of hydrogen recoils from PE. Without additional gamma on top of the neutron irradiation, recoils from PTFE contribute approximately 10% to the signal acquired behind PTFE for irradiations with ^{241}AmBe neutrons. For the situation where a large gamma component is present, these recoils will have negligible effect.

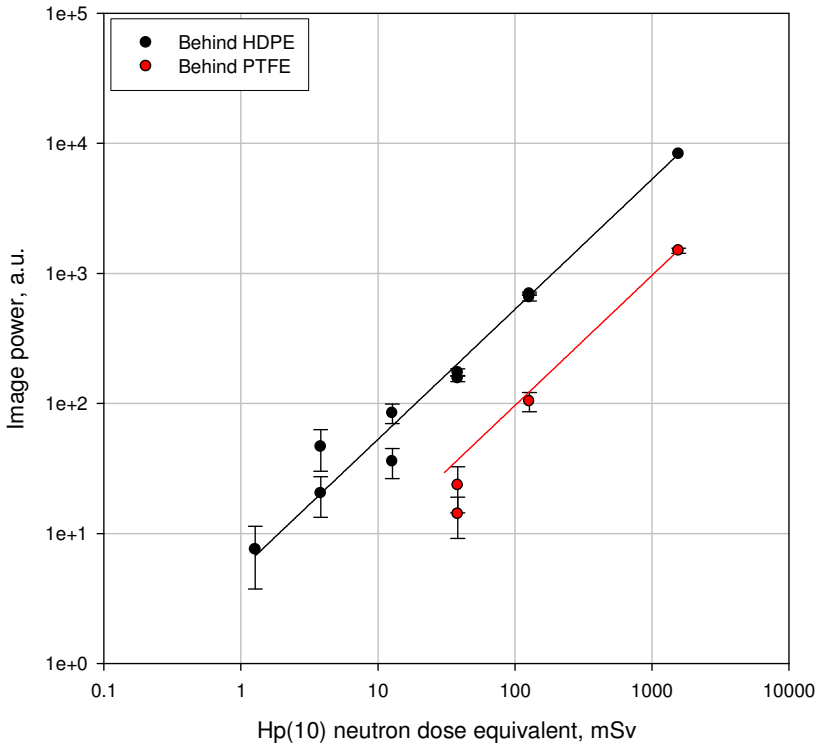

Figure 5.20 Dose dependences for FNTDs covered with PE (black symbols) and PTFE (red symbols) irradiated with ^{241}AmBe fast neutrons.

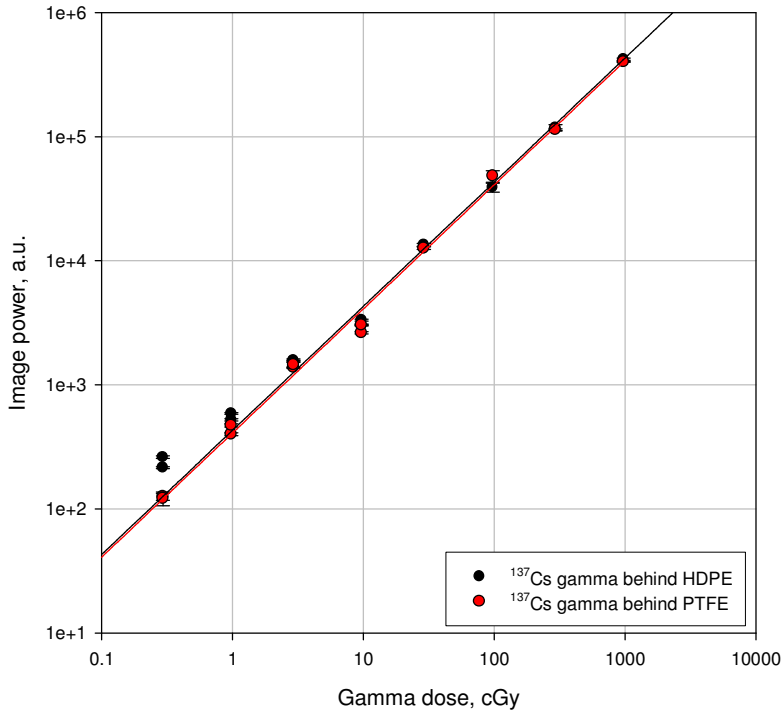

Figure 5.21 Dose dependences for FNTDs covered with PE (black symbols) and PTFE (red symbols) irradiated with ^{137}Cs gamma photons.

The image power dependence for FNTDs irradiated with gamma behind PE and PTFE are nearly collinear. The difference in slopes between FNTDs covered with PE and PTFE is 2.5% which is attributed primarily to the difference in photon absorption. The 2.5% difference was taken into account later on during processing for neutron-gamma separation.

Table 5.4 summarizes the processing of mixed field irradiations. Equation (5.8) was used to determine the neutron dose. Sensitivities of $B(n) = 7.7$ and $A(\gamma) = 42.9$ units/mSv was used to compute the final reported doses. The signal behind PTFE was corrected for the 2.5% difference in response from the HDPE converter.

In terms of dose equivalent, when the ratio of neutron dose to gamma dose is greater than 1:3, the measurement error becomes on the order of the signal obtained from neutrons making it more difficult to reliably determine the dose. As seen in Table 5.4, it is still possible to determine the neutron dose at ratios of 1:1 and 1:3, but the error is much larger. The average error in dose determination for both neutron and gamma radiation was 12.4% with the maximum bias of 40% at the 1:3 ratio. The main source of error is attributed to differences in sensitivities from detector to detector.

Table 5.4 Summary of mixed neutron-gamma irradiation processing results

Delivered neutron dose, mSv	Reported neutron dose, mSv	% error	Delivered gamma dose, mSv*	Reported gamma dose, mSv	% error
100	101	1	32.5	35.0	7.7
100	113	13	10.25	10.22	0.2
30	30	0	10.75	10.9	1.4
30	40	33	30.75	30.3	1.5
30	25	17	30.75	33.0	7.3
30	42	40	100.75	94.3	6.4

*The total equivalent dose includes 2.5% contribution of gamma dose from the ^{241}AmBe irradiation.

5.6 Neutron energy dependence

Energy dependence of a neutron detector needs to be known to accurately determine dose. All neutron detectors have a strong dependence on energy because they work on the principle of converting neutrons into charged particles via nuclear reactions. The ideal energy response for determining neutron fluence would be flat (i.e. no change with energy) and the ideal energy response for determining dose equivalent would be the same response as tissue (i.e. a quality factor-dosimeter), but most detectors have energy responses that are a convolution of the energy dependent neutron interaction cross-section of the converter and the detection efficiency of the conversion product.

Most facilities containing a neutron exposure risk will fully characterize the neutron energy spectrum in pertinent areas with Bonner spheres or other similar neutron spectrometers so the spectrum is in general known. Neutron dosimeters can then correct for their energy dependences based on a known neutron spectrum. There may be times, however, in which the spectrum is not known, or needs verification. It is therefore useful to be able to estimate the mean neutron energy to accurately estimate neutron dose. The following section characterizes and discusses not only the energy dependence, but also two novel methods of estimating the energy of incident neutrons.

5.6.1 Detection efficiency

Monoenergetic neutron irradiations were performed at four facilities, the National Physics Laboratory (NPL) in the United Kingdom, the Joint Research Centre – Institute for Reference Materials and Measurements (JRC-IRMM) in Belgium, the Radiological Research Accelerator Facility (RARAF) in Columbia University, New York and the Physikalisch-Technische Bundesanstalt (PTB) in Germany. The FNTDs irradiated at NPL and PTB were packaged in the holders containing PE and TLD 100 chips. The detectors irradiated at JRC-IRMM and RARAF were covered with 800 μm of PE only. FNTDs were also irradiated at the Landauer irradiation facility in Glenwood, Illinois and the Pacific Northwest National Laboratories (PNNL) in Washington. The FNTDs irradiated at Landauer and PNNL were packaged in the same manner as those for the NPL and PTB irradiations.

The irradiations at NPL consisted of ten neutron energies in the range of 44 keV to 5 MeV. Five detectors were exposed for each of the energies on a 30x30x15 cm^3 phantom. The reported $H_p(10)$ doses were between 0.64 mSv (44 keV) and 2.54 mSv (5 MeV). JRC-IRMM delivered monoenergetic neutrons in the range of 500 keV to 19.5 MeV. Three detectors were exposed for each of the energies. The irradiation at PTB was with 14.8 MeV neutrons and the reported dose was 2.05 mSv.

FNTDs irradiated in Landauer were exposed to fast neutrons from a bare ^{241}AmBe source. Two sets of five detectors were placed on a 30 x 30 x 15 cm^3 phantom and exposed to 2 mSv of fast neutrons. FNTDs irradiated at PNNL were

exposed to fast neutrons from a bare ^{241}AmBe source as well as to neutrons from bare and moderated ^{252}Cf sources. These detectors were exposed to a dose of 2.1 mSv.

Two competing processes affect the efficiency of FNTDs. At low energies, small recoil proton ranges limit detection, whereas at higher neutron energies, *n-p* scattering cross-section decreases as $1/\sqrt{E}$. The maximum recoil proton energy from a PE converter for a 0.2 MeV neutron irradiation is 0.2 MeV, and the maximum proton range in Al_2O_3 as calculated by SRIM 2006 (Zieglar and Biersack, 2006) is only 1.08 µm. Short range of low energy recoil protons makes it difficult to detect tracks using this technique.

FNTDs exposed to monoenergetic neutrons at NPL were scanned at a depth of 0.5 µm below the surface for the area behind PE for low energy neutrons (44 keV to 144 keV), 1 µm below the surface for higher energy neutrons (above 250 keV) and 2 µm below the surface for the area behind the LiF converter. The reason for scanning at a shallow depth is that the maximum range of recoil protons in Al_2O_3 is 0.3 µm for 45 keV neutrons. The depth behind ^{6}LiF was chosen such that the alpha particles produced in the reaction would be detectible. 100 images were acquired behind each converter area. FNTDs irradiated at Landauer and PNNL with neutrons from broad spectrum ^{241}AmBe and ^{252}Cf were imaged at a depth of 2 µm and 50 images per converter area were acquired (results are in Table 5.5).

Track densities were obtained behind both converter areas for every FNTD. The track densities behind PE and ^{6}LiF were normalized to the $H_p(10)$ dose equivalent and plotted against energy (Fig. 5.22). Mean energies of the broad spectrum neutron

sources (^{241}AmBe, ^{252}Cf and moderated ^{252}Cf) were used to plot the data (Olsher et al., 2007).

The track density from the detectors irradiated with 40 keV neutrons behind PE was only about 10% above the track density obtained from the controls sent to NPL. The control detectors had an error of 50%. It is therefore difficult, especially with the low delivered dose of 0.610 mSv, to attribute the obtained track densities to 40 keV neutrons. The amount of transient dose absorbed in the detectors is most likely too large to distinguish a small signal from the 40 keV neutrons. At the same time, track densities obtained behind ^{6}LiF converters are significant and can be used for dose determination induced by low energy neutrons.

FNTD sensitivity to low energy neutrons increases by several orders of magnitude when coupled with LiF (TLD-100) converters. The sensitivity increases as neutron energy decreases because of the ^{6}Li (n,α) reaction cross-section's energy dependence. The energy dependence of FNTDs covered with ^{6}Li does not follow the neutron capture cross section exactly because of scattered neutrons from the Albedo configuration. FNTDs can therefore serve as a reliable albedo dosimeter in addition to being an effective fast neutron dosimeter.

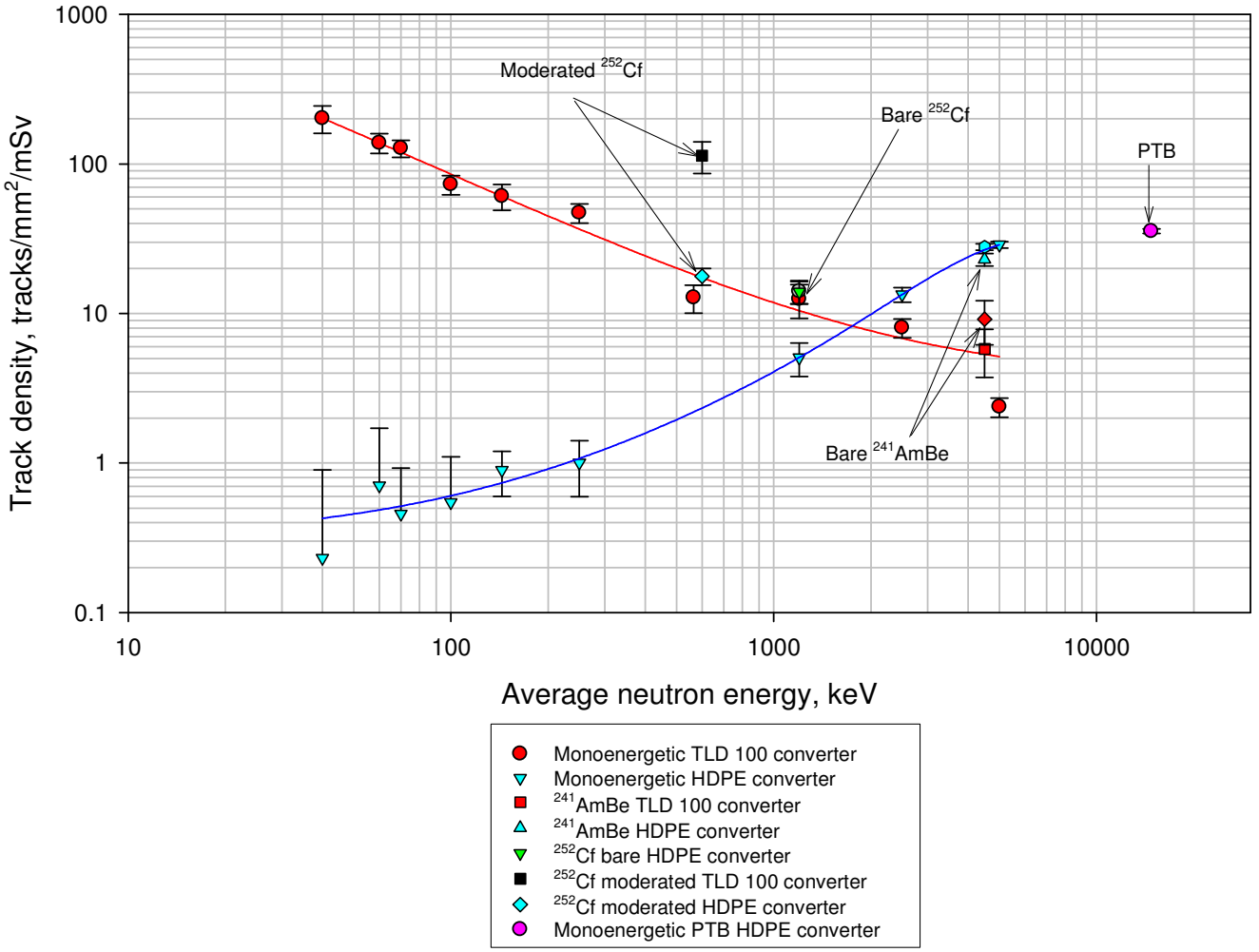

Figure 5.22 Track densities as a function of energy for monoenergetic and broad spectrum neutron irradiations at NPL, PTB, PNNL and Landauer.

Table 5.5 Summary of results from broad spectrum irradiations at Landauer and PNNL

Location	Source	Converter	Mean energy, keV	Sensitivity, tracks/mm²/mSv
Landauer	AmBe	PE	4500	23.7 ± 1.17
Landauer	AmBe	TLD 100	4500	15.47 ± 4.09
PNNL	AmBe	PE	4500	28.55 ± 1.39
PNNL	AmBe	TLD 100	4500	23.33 ± 4.36
PNNL	Cf bare	PE	1200	14.67 ± 1.51
PNNL	Cf bare	TLD 100	1200	32.26 ± 5.07
PNNL	Cf moderated	PE	600	17.44 ± 2.29
PNNL	Cf moderated	TLD 100	600	105.4 ± 13.9

Simple estimations of track detection efficiency using PE as a converter with neutron energies of 0.40, 0.144, 0.250, 0.565, 1.2, 5, 7 and 12 MeV were made by considering the energy dependent *n-p* scattering cross-section, angular dependence of recoil protons, the thickness of the PE converter and the minimum energy to create a detectible track in an FNTD. The prediction was calculated at 15 discrete energies and interpolated to obtain the efficiency between energies. The model is plotted in Fig. 5.23 with monoenergetic neutron results. This model predicts maximum detection efficiency at 10 MeV. This has not been experimentally verified due to lack of available 10 MeV neutron sources. This model is a crude approach and further modelling with Monte Carlo simulations is needed.

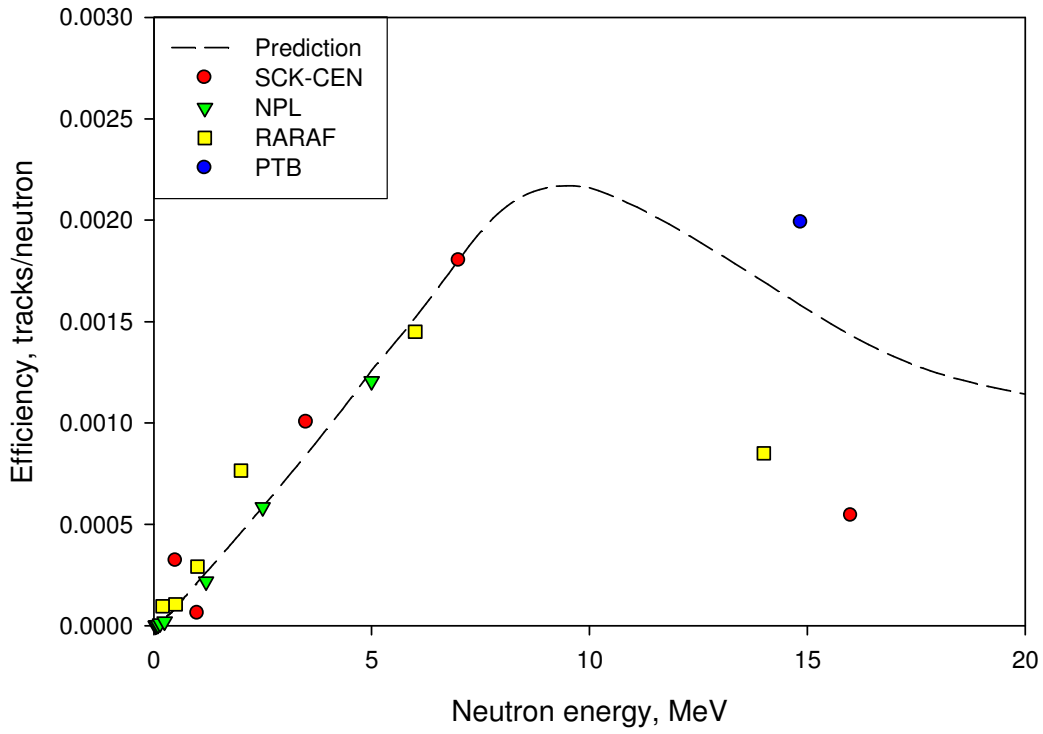

Figure 5.23 Efficiency of all monoenergetic neutron irradiations with an interpolated discrete model prediction (dashed line). The model was coerced to fit the 7 MeV irradiation from SCK-CEN.

5.6.2 Neutron energy estimation by depth profiles – track counting

FNTDs irradiated with high energy neutrons at the JRC-IRMM in Belgium were scanned at multiple depths within the crystal. FNTDs irradiated with neutrons of energy 3.5 MeV and higher were first scanned at 1 µm inside the crystal and the subsequent depths were 3.5 µm apart to a maximum depth of 80 µm. FNTDs irradiated with 0.5 MeV and 1 MeV neutrons were first scanned at a depth of 1 µm and subsequent depths were 1.5 µm apart to a maximum depth of 20 µm. Track densities at each depth were calculated and then normalized to the track density obtained for the first depth. Figure 5.24 shows the dependence of normalized track density on depth for five monoenergetic neutron irradiations.

The depth profiles show a bell-shaped behavior because recoil protons generated by relatively low energy neutrons have a short range of penetration and the depth profile shows fast decay. High energy neutrons generate longer range recoil protons and the track density reduces slower with the depth of fluorescence imaging. Data presented in Figs. 5.25 and 5.26 demonstrate how one can obtain the median energy of neutron fields (Sykora et al, 2009). Future efforts will be directed toward extracting the neutron spectrum from the depth profile of recoil protons by proper unfolding techniques. For this work, a simple method to obtain the mean energy of neutrons (500 keV to 7 MeV) was employed.

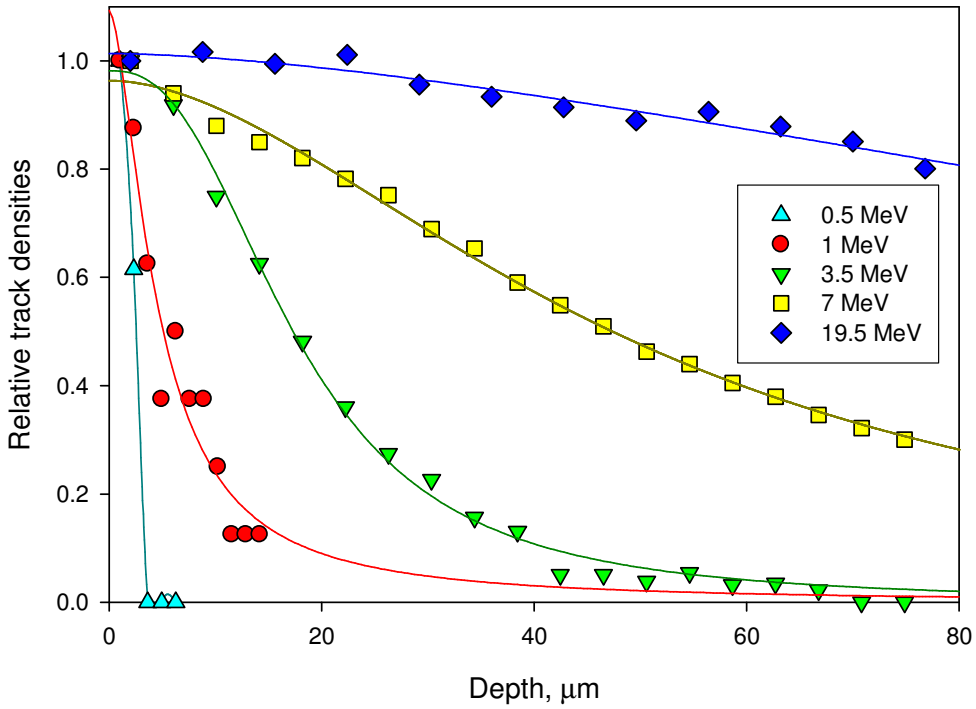

Figure 5.24 Track densities as a function of scan depth for high energy monoenergetic neutron exposures at SCK-CEN.

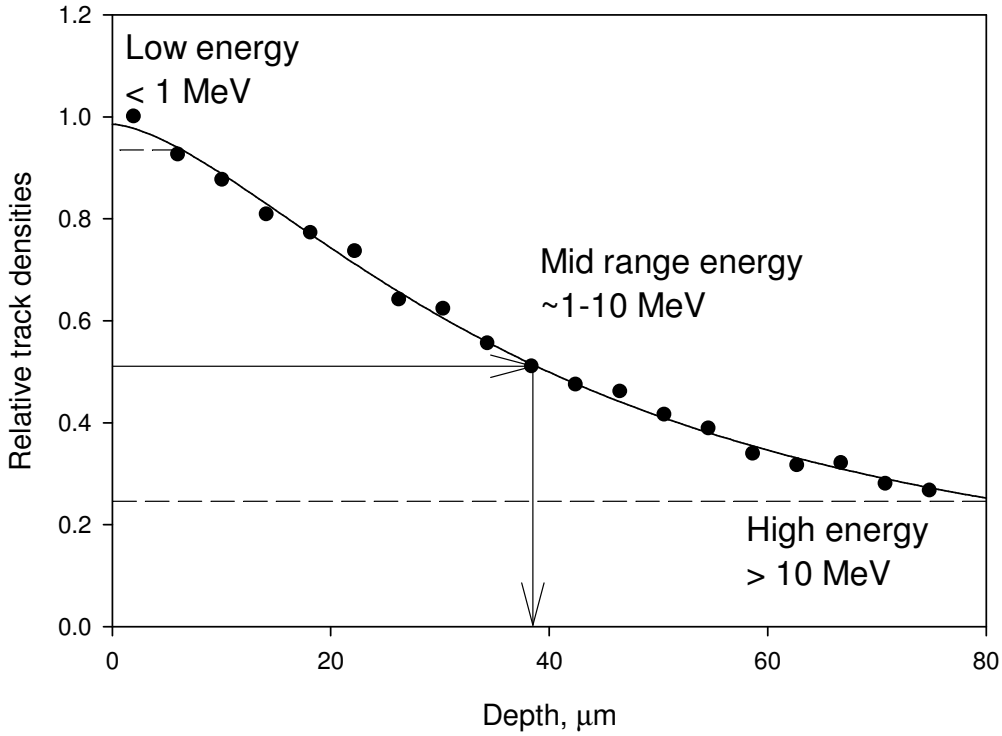

Figure 5.25 Relative track densities as a function of depth for FNTDs irradiated with ^{241}AmBe fast neutrons. This illustrates that there should be approximately 20% contribution of neutrons greater than 10 MeV while the majority lie in the 1-10 MeV range. The median energy is estimated excluding the high energy.

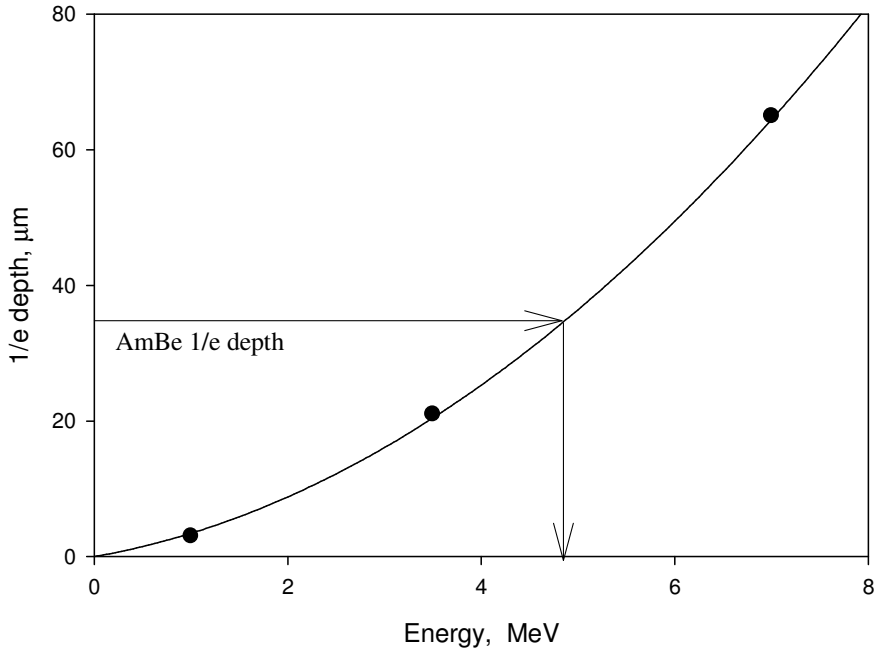

Figure 5.26 The calibration curve for the depth profile parameter (1/*e* depth), and demonstration of its ability to determine the median energy of AmBe fast neutrons.

The depth at which the track density reduces to 1/*e* (~37%) of its original value was selected as the parameter to characterize mean or median energy. This parameter was determined for the 1 MeV, 3.5 MeV and 7 MeV neutrons and plotted against the reported neutron energy in Fig. 5.26. This dependence was used as a calibration curve. The calibration curve works well for broad spectrum neutrons even though it was obtained for monoenergetic neutrons. To determine the median energy of ^{241}AmBe neutrons, the depth dependence for FNTDs irradiated with 30 mSv of fast neutrons from a bare ^{241}AmBe source was obtained (Fig. 5.25). The high energy component was subtracted and the 1/*e* depth obtained. The arrows provide an estimated median energy of 4.9 MeV which is in good agreement with the actual median energy of 4.8 MeV (Olsher et al., 2007). There is a 22% contribution of total tracks due to high energy neutrons; the ^{241}AmBe spectrum shows a significant amount of high energy neutrons agreeing with these results.

5.6.3 Neutron energy estimation by depth profiles – image power

The same energy estimation technique can be applied using image power as a parameter assuming that the dose is large enough to measure with image power. Figure 5.27 illustrates depth profiles of FNTDs irradiated with fast ^{241}AmBe neutrons and processed to obtain the average image power. The power decreases similar to the track densities in Fig. 5.25 but the power contains an increased background. The increased background is a result of accompanying gamma radiation (22.5% of the total dose) from the fission of the Beryllium nucleus. After subtraction of the gamma

background (see section 5.6.2 for a discussion of depth profiles for gamma irradiated FNTDs), the relative image power and relative track densities agree well.

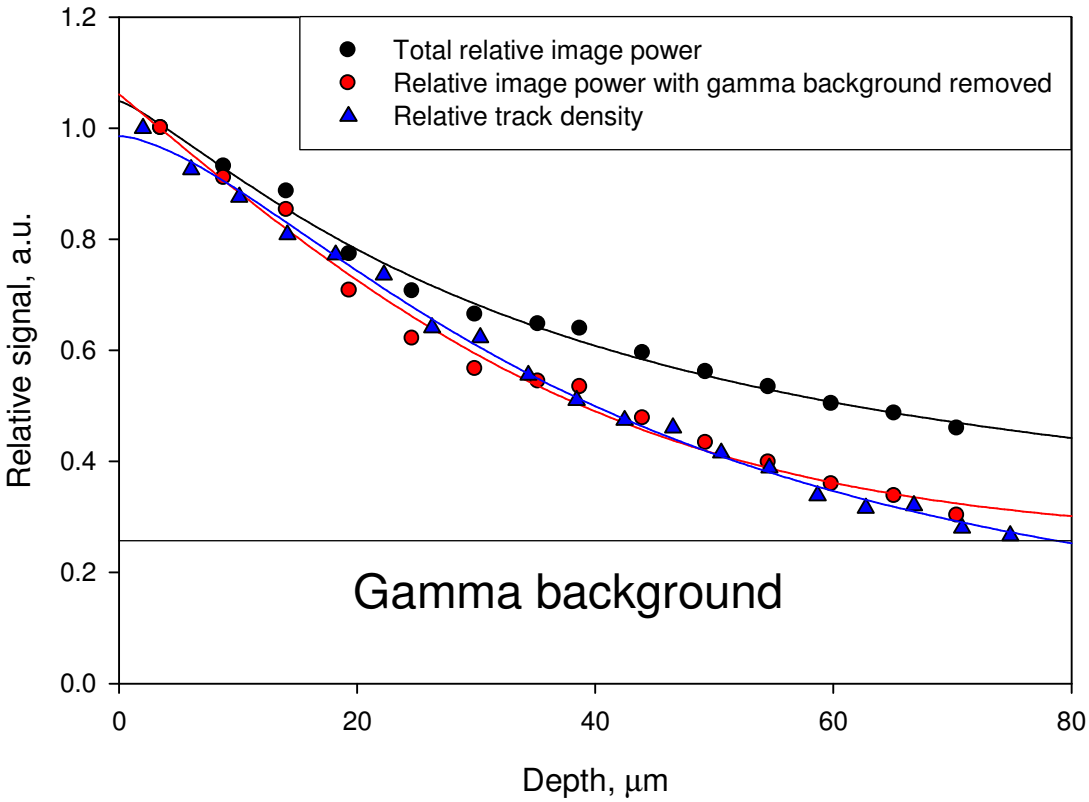

Figure 5.27 Relative image power as a function of depth in a FNTD irradiated with ^{241}AmBe fast neutrons. The expected gamma contribution to the image power is approximately 22.5%. After subtracting background (red circles), the depth profile agrees with track counting depth profiles (blue triangles).

5.6.4 Ratio of track densities

Data from the NPL irradiations were used to determine the ratio of track densities behind LiF converters to track densities behind PE which was calculated and plotted as a function of energy (Fig. 5.28). The ratio is seen to be a smooth function of energy that does not depend on the delivered dose and so it should serve as a good parameter to determine the average energy of incident neutrons within this energy range.

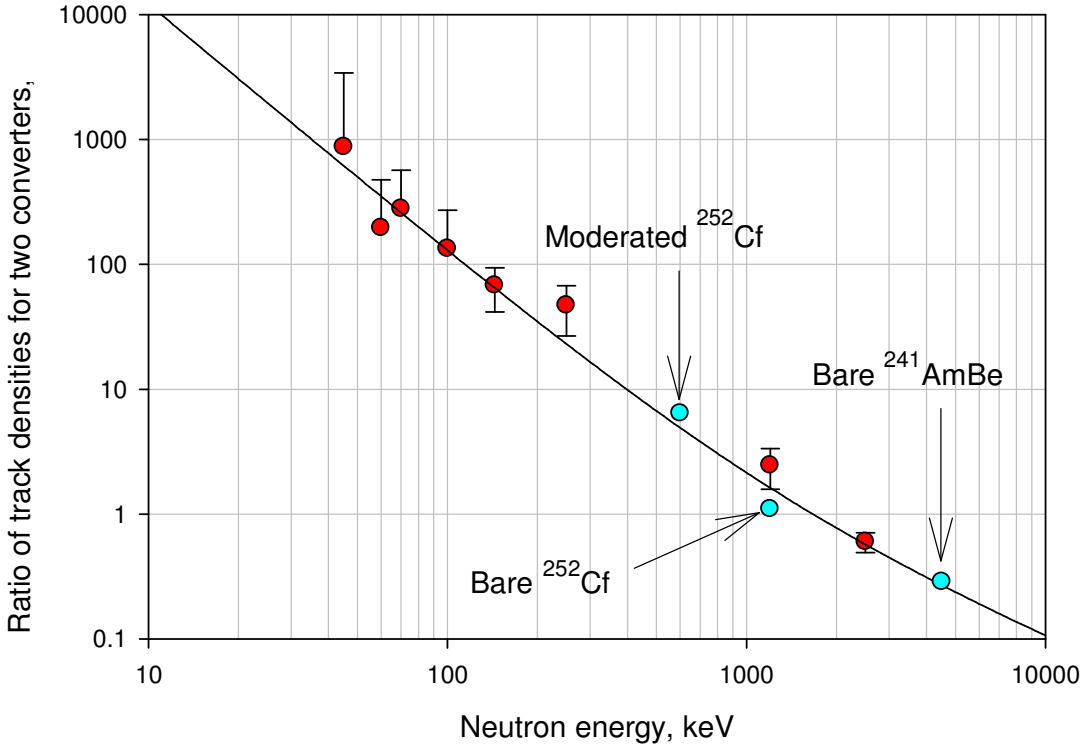

Figure 5.28 Energy dependences of calculated ratios of track densities obtained from detectors covered with PE and ^{6}LiF.

The ratio of track densities for the FNTDs irradiated at NPL with monoenergetic neutrons was used as a calibration dependence to determine the median energy of the three broad spectrum neutron sources. To estimate the energy, the track density behind ^{6}LiF was divided by the track density behind PE and compared with the calibration curve. The ratios from the broad spectrum neutrons are plotted against their known median energy as light colored circles in Fig. 5.28. Table 5.6 shows the results of neutron energy determination for broad spectrum AmBe and two ^{252}Cf sources using the calibration curve obtained from monoenergetic neutron irradiations; Table 5.6 demonstrates good agreement with the published median energy of neutrons for these sources.

Table 5.6 Energy determination of broad spectrum neutron sources using the ratio of track densities behind PE and LiF converters

Source	Published median energy, MeV	Ratio	Estimated median energy, MeV	% difference
Bare ^{241}AmBe	4.8	0.287	4.4	4.3
Bare ^{252}Cf	1.2	1.1	1.5	11
Moderated ^{252}Cf	0.6	6.4	0.52	7.1

5.7 Photon energy dependence

The energy response of detectors for photons also needs to be known in order to accurately assess the photon dose. As with neutrons, the ideal photon dosimeter will have a flat response as a function of energy so that no corrections need to be applied. All high Z detectors, however, over-respond to low energy photons because of increased photo-electric absorption of low energy photons. Al_2O_3:C over-responds to photons with energies in the range from 20 keV to 200 keV (Salasky, 2008), therefore it was necessary to determine the photon energy response of FNTDs in order to correct for the photon energy.

5.7.1 Relative response

The image power dependence on photon energy was investigated by irradiating FNTDs with X-rays of different average energies at the Landauer irradiation facility. The detectors were covered with PE and PTFE converters to obtain charged particle equilibrium near the surface of the detector. The detectors were irradiated with narrow spectrum (NS) and mid spectrum (M) x-rays providing photon energies in the range of 17 keV to 208 keV. The delivered dose varied from 9.5 cGy to 14.7 cGy so

the response was normalized to the delivered dose. To establish electron equilibrium at the surface of the Al_2O_3:C,Mg crystal, FNTDs were covered either by a 1 mm PE converter or a 1 mm layer of PTFE.

FNTDs irradiated with NS and M x-rays were imaged at a depth of 3 μm; 25 images per detector were obtained and processed to calculate the image power. The response was normalized to the image power obtained for ^{137}Cs gamma photons. All values were corrected for the expected absorption in the converter and delivered dose (given in Kerma in air). The dependence of relative image power as a function of photon energy is shown in Fig. 5.29. The energy response to x-rays is similar to regular Al_2O_3:C OSL material. Over-response is expected because the probability of the photoelectric effect increases at low energies.

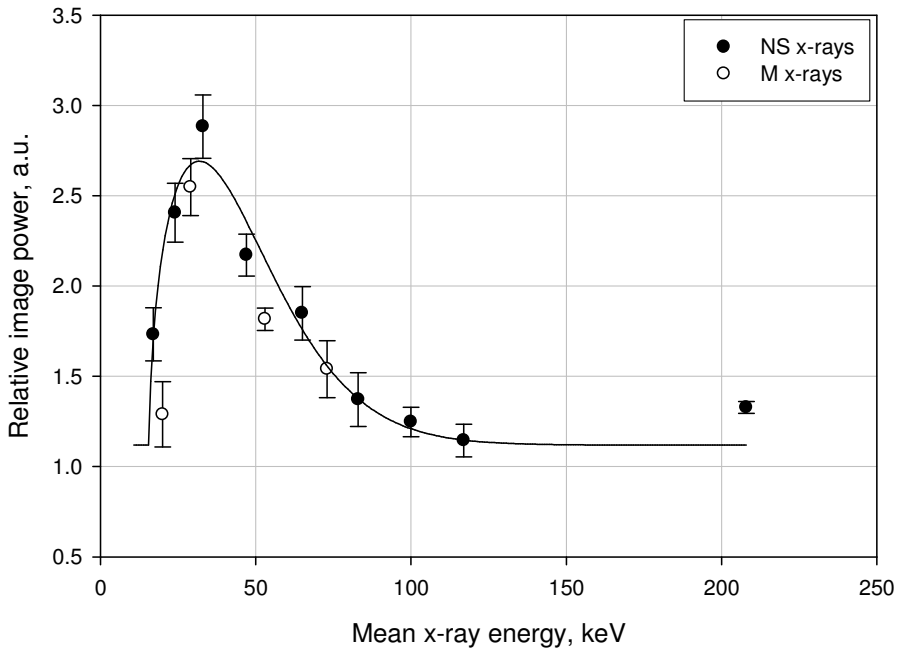

Figure 5.29 Image power dependence on photon **e**nergy for FNTDs relative to the image power obtained for FNTDs irradiated with 660 keV gamma from ^{137}Cs

5.7.2 Depth profiles

One of the methods described in section 5.6 for estimating neutron energies was acquiring dose-depth profiles, and because gamma or x-ray photons generally accompany neutrons, it was imperative verify that the image power response to photon dose as a function of depth in Al_2O_3:C,Mg followed usual absorption characteristics. FNTDs irradiated with 662 keV gamma photons from ^{137}Cs were scanned at multiple depths within the crystal. FNTDs were first scanned at 1 μm inside the crystal and the subsequent depths were 4 μm apart to a maximum depth of 80 μm. The image power at each depth was calculated and then normalized to the image power obtained for the first depth. Figure 5.30 shows the dependence of normalized power on depth for five separate gamma doses.

The power spectrum amplitude stays constant with depth for ^{137}Cs gamma. Both PE and PTFE in front of the crystals produce very similar strengths of fluorescence signal, image power and depth profiles. There is a small build-up in the first few micrometers of the detector and after that the amplitude remains constant. At 80 μm in Al_2O_3:C,Mg there should be only a fraction of a percent of 662 keV gamma photon attenuation, so nearly constant amplitude as a function of depth was expected and obtained. Figure 5.31 shows the image power as a function of depth normalized to the average image power at the second depth compared to the expected absorption of 200 keV photons in Al_2O_3. Data were normalized to the second depth because it is possible that a portion of the focal spot was outside of the detector while imaging the first depth resulting in slightly decreased image power. The relative image power agrees with the expected absorption. Most of the error was from error in spherical

aberration compensation at each depth. The build-up factor is not calculated in the expected absorption.

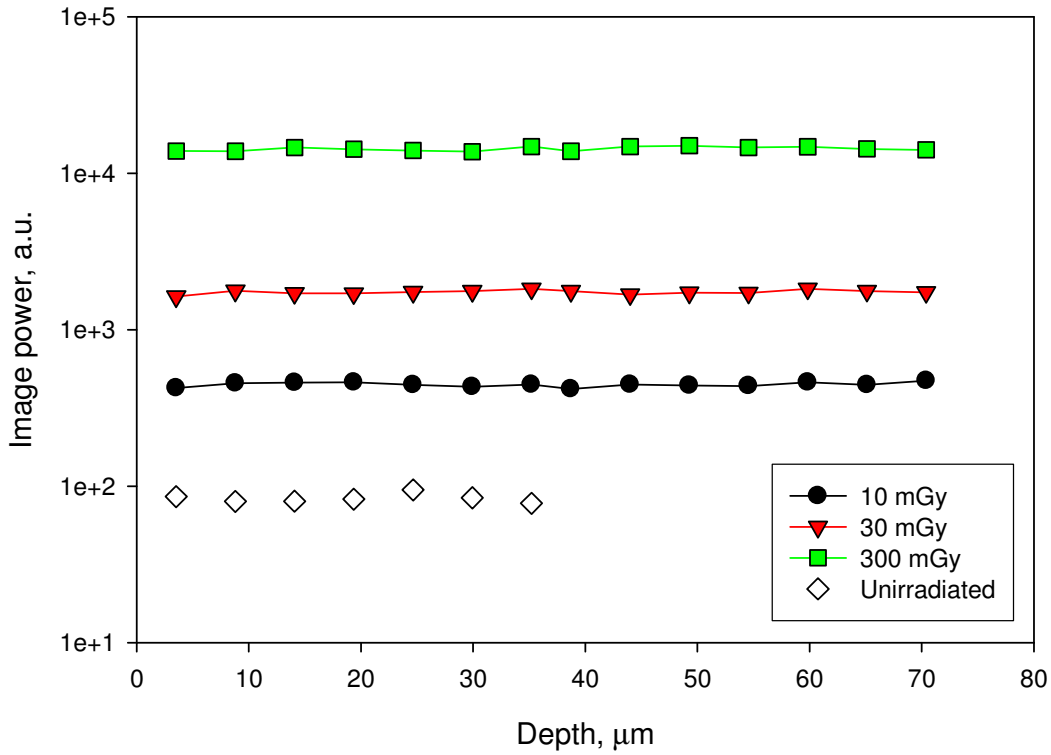

Figure 5.30 Image power as a function of depth for FNTDs irradiated with three doses of ^{137}Cs gamma photons and one unirradiated FNTD.

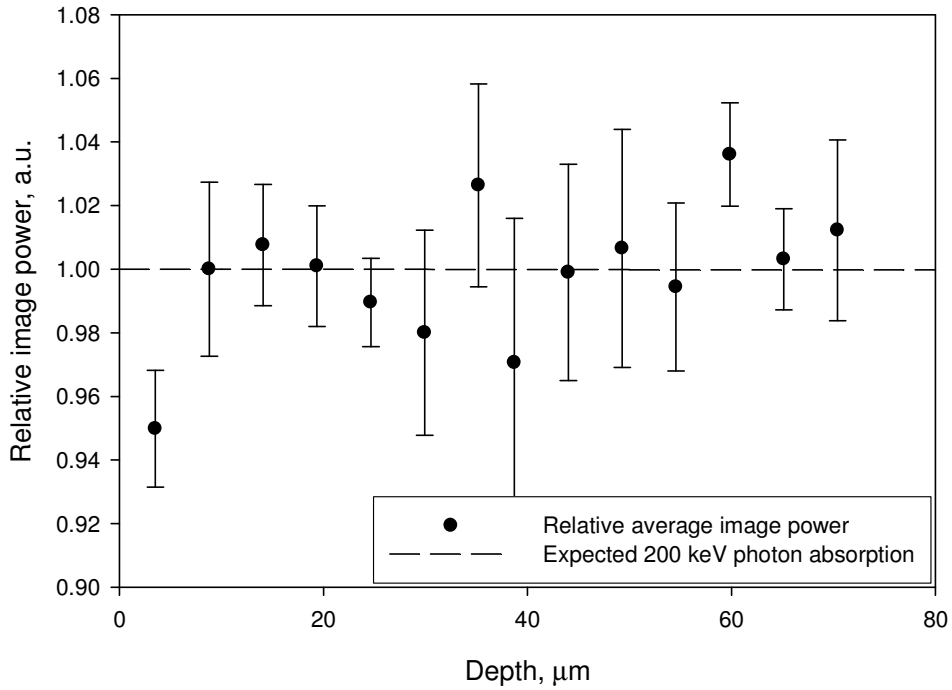

Figure 5.31 Image power relative to the point where charged particle equilibrium exists averaged over FNTDs irradiated with five doses of ^{137}Cs gamma photons. The expected absorption in Al_2O_3 is plotted as the dashed line.

An entire dose-depth distribution was obtained to demonstrate the ability of FNTDs to estimate the energy of incident photons based on their absorption in Al_2O_3. It is important to know photon energy to be able to correct for over-response demonstrated in section 5.6.1. A set of FNTDs was irradiated with 40 kVp X-rays and positioned such that the direction of incidence of the x-rays was parallel to the surface of the detector (inset in Fig. 5.32) in order to achieve scanning at greater depths in the FNTD with respect to the incident photons. Imaging across the surface of the FNTD bypassed the need to compensate for spherical aberrations. Images were acquired from top of the crystal to bottom with 10 images at every "depth". The image power as a function of depth in Al_2O_2:C,Mg is plotted in Fig. 5.32 for an unirradiated/bleached crystal (black circles) and for the x-ray irradiated crystal (red triangles).

Figure 5.32 shows an initial fast decay which is the result of the low energy portion of the X-ray spectrum. There is no build-up layer in the FNTD because of the low energy X-rays. Nearly all of the low energy x-rays were attenuated after 1.5 mm leaving only the higher energy component of the spectrum. The data in Fig. 5.32 was fit to a double exponential decay to estimate the two most dominant mean photon energies in the broad X-ray spectrum. Decay constants of the fit were compared to decay constants of calculated absorption for low energy x-rays in Al_2O_3 (Fig. 5.33). The decay constants corresponded to ~8 keV (fast decay component) and ~30-35 keV (slow decay component). Proper deconvolution (including build up, attenuation and over response due to increased photo-electric absorption) of the depth profile for x-rays in Al_2O_3 would likely give the photon energy spectrum.

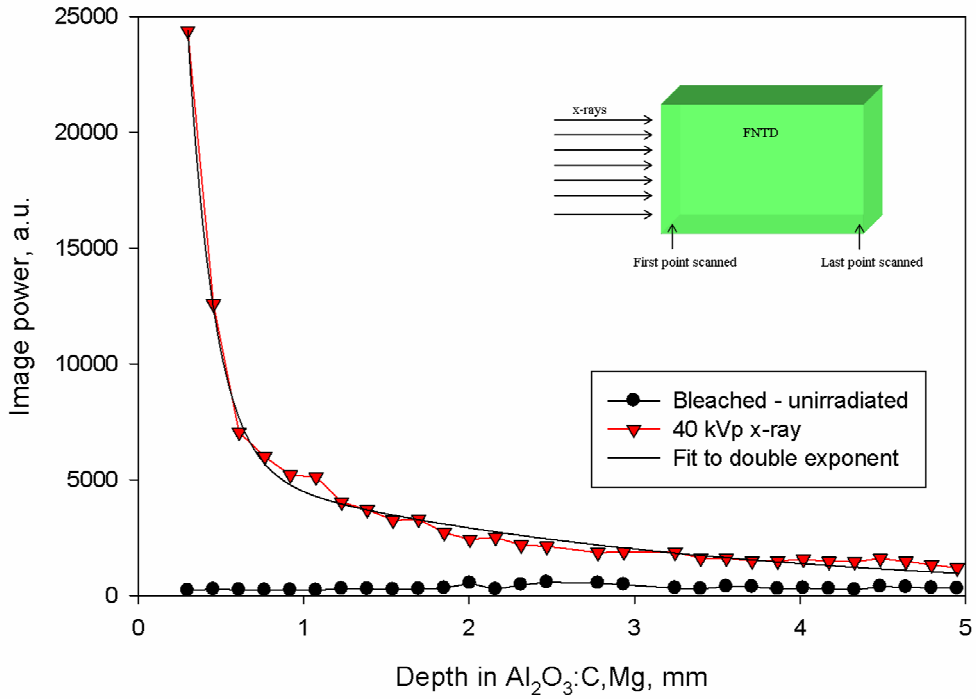

Figure 5.32 Image power dependence on depth in Al_2O_3:C,Mg for FNTDs bleached/unirradiated (black circles) and irradiated with 40 kVp x-rays (red triangles). The inset is a diagram of the irradiation geometry.

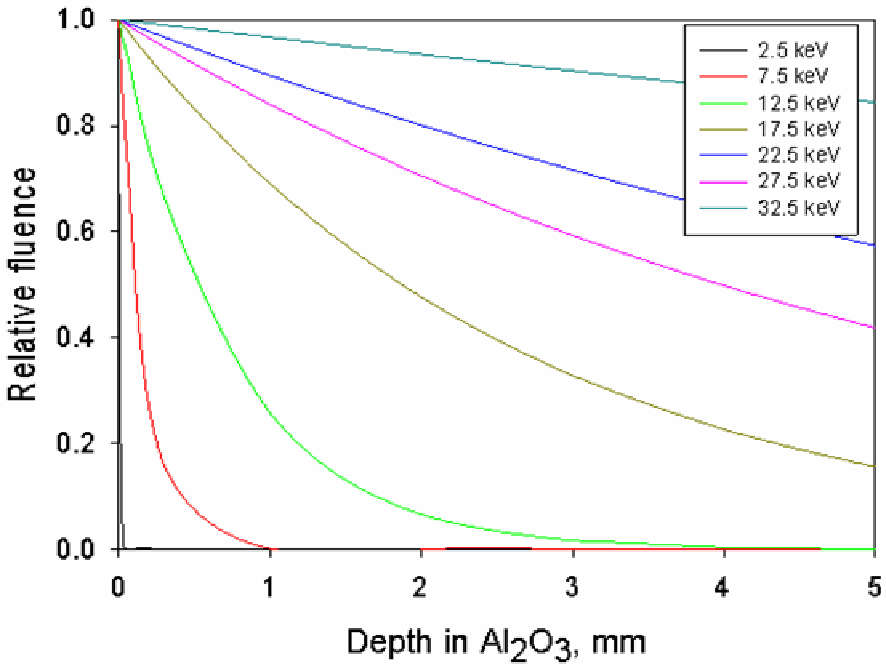

Figure 5.33 Calculated absorption of low energy photons in Al_2O_3 as a function of depth.

5.8 Angular dependence for neutrons – track counting

Dosimeters are exposed to neutrons from multiple angles in real operational conditions so the angular response of any neutron dosimeter needs to be known and preferably able to be corrected. It is for that reason that angular measurements were performed with detectors covered by PE and irradiated with the same unmoderated ^{241}AmBe source under different angles with respect to the direction of fast neutron incidence. The detectors were placed on wedged pieces of plastic that were machined to have the angle between the detector and the incident neutron beam vary from 0° (the detector surface perpendicular to the incident beam) to 90° (the detector's front surface parallel to the incident neutron beam) in 15° increments. Two detectors were irradiated at each of the seven angles. All fourteen detectors were irradiated at the same time and received a dose of 6 mSv.

The detectors were mounted on two plastic substrates with multiple angles on each substrate. It is evident from the dose dependence of detectors combined with PE and irradiated on phantom shown in section 5.2 (Fig. 5.7 and 5.8), that there is no significant contribution to the number of tracks from albedo neutrons. Figure 5.34 is the normalized track count dependence on angle of incidence for FNTDs irradiated with fast neutrons.

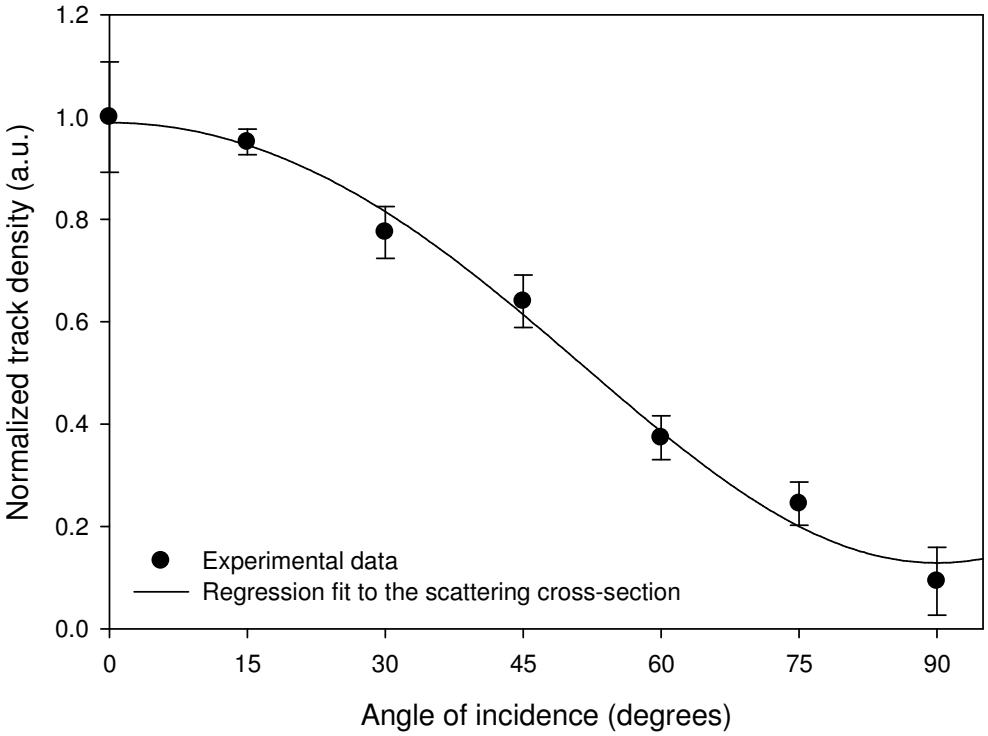

Figure 5.34 Angular dependence of FNTD response obtained after irradiations with 6.0 mSv of fast neutrons from an un-moderated ^{241}AmBe source. The data is normalized to zero angle of incidence.

The track count for all angles of irradiation was normalized to the track count obtained for the direction of incidence normal to the detector surface. The angular dependence obtained was fit to Legendre polynomials in accordance with recent experiments and Monte Carlo calculations on *n-p* scattering cross-sections for neutron energies below 15 MeV (Boukharaouba *et al*., 2001). According to the study,

Legendre polynomials for the angular dependence of the *n-p* scattering cross-section, σ_s, in the center-of-mass frame is given by

$$\sigma_s(\Theta_{cm}) = a_0 + a_1 P_1(\cos\Theta_{cm}) + a_2 P_2(\cos\Theta_{cm}), \tag{5.9}$$

where Θ_{cm} is the angle of the scattered proton with respect to the angle of incidence of the neutron, a_0, a_1, and a_2 are parameters and $P_i(\cos\Theta_{cm})$ are Legendre polynomials of order *i* and are given by

$$\begin{aligned} P_1(\cos\Theta_{cm}) &= \cos\Theta_{cm} \\ P_2(\cos\Theta_{cm}) &= \frac{1}{2}\left(3\cos^2\Theta_{cm} - 1\right) \end{aligned} \tag{5.10}$$

From simple scattering theory we can change the reference frame to the lab frame by

$$\cos\theta = \sqrt{\frac{1-\cos\Theta_{cm}}{2}}, \tag{5.11}$$

where θ is the scattering angle of the recoil proton in the lab frame. Plugging (5.9) and (5.11) into (5.9) and absorbing the constants, we are left with the scattering cross-section in the lab frame, $\sigma_s(\theta)$ given by

$$\sigma_s(\theta) = b_0 + b_1\cos^2\theta + b_2\cos^4\theta, \tag{5.12}$$

where b_0, b_1 and b_2 are fitting parameters. Regression analysis with $R^2 = 0.992$ suggests that the angular dependence of FNTD is determined by the theoretical dependence of the *n-p* scattering cross-section.

5.9 Field testing for FNTDs

5.9.1 High dose mixed field accident dosimetry – White Sands Missile Range

The need for neutron dosimeters is mainly driven by nuclear power, radiation therapy, neutron producing accelerators and military defense. Major catastrophes could happen in all of the applications listed above, but in a worst case scenario someone, or a group of people, may be exposed to large quantities of neutrons in a short period of time (nuclear explosion for example). To our knowledge there are no passive dosimeters, besides perhaps TLDs and activation foils, capable of measuring such high doses of neutrons (absorbed doses on the order of Gy's and higher) at extremely high dose rate and on top of a large gamma background. FNTDs were tested in simulated high dose rate conditions at White Sands Missile Range (WSMR) in New Mexico and compared with activation based sulfur neutron detectors, OSL detectors (for gamma) and TLDs (for gamma).

FNTDs coupled with the converter packaging containing PE and PTFE were irradiated at WSMR with high doses of neutrons from a fast burst reactor (FBR) and high doses of gamma from the relativistic electron beam accelerator (REBA). OSL detectors were exposed alongside the FNTDs to verify gamma doses in both irradiations. The dose rate was varied by the distance from the reactors and total dose was varied by the pulse width and frequency of reactor flashes. Results from neutron irradiated FNTDs were compared with sulfur activation dosimeters and FNTDs irradiated with gamma were compared with TLDs. Sulfur and TLD measurements were used as references and were performed by the WSMR staff. ICRP 60

recommends the use of absorbed dose for extremely high fluences of neutrons, so all doses were compared and discussed in terms of absorbed dose.

The contribution of gamma to the total absorbed dose after irradiation with FBR neutrons was reported to be only around 10%, but the absolute values were large. Fig. 5.35 a) is an image after irradiation with 28.6 Gy of neutrons from the FBR and Fig. 5.35 b) is an image after irradiation with 253 cGy of gamma from the REBA. It is obvious that individual tracks are indistinguishable and the level of gamma is too large so the image power must be calculated to achieve reliable dose information.

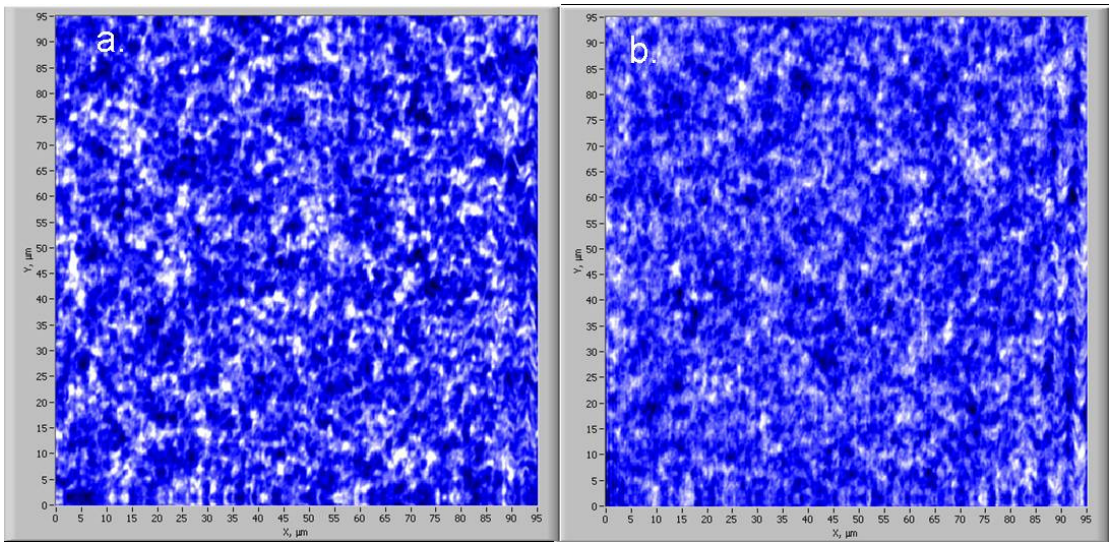

Figure 5.35 Images of FNTDs behind PE irradiated at WSMR with a) 28.6 Gy of neutrons and b) 0.25 Gy of gamma.

Doses were determined using the method described in eq. (5.8) where the FNTD + PE converter was the neutron and gamma sensitive detector and the FNTD + PTFE converter was the gamma only sensitive detector. The difference in gamma absorption between PE and PTFE was accounted for.

A neutron energy correction factor was used to determine dose because the neutron calibration was performed using fast neutrons from ^{241}AmBe, but the energy

spectrum of the FBR neutrons was known to be similar to that of ^{252}Cf. The sensitivity correction factor for the image power, $\eta_{IP}(E)$, was determined by

$$\eta_{IP}(E_n) = \frac{\eta_t(E_n)}{\eta_t(E_{cal})} \cdot \left(\frac{\bar{I}_t(E_n)}{\bar{I}_t(E_{cal})} \right)^2 \tag{5.13}$$

where E_n is the energy of incident neutrons, E_{cal} is the energy of the calibration neutrons, $\eta_t(E)$ is the track detection efficiency at a particular neutron energy and $\bar{I}_t(E)$ is the mean fluorescence intensity of recoil proton tracks induced by neutrons of energy E. The intensity factor is squared because the image power is proportional to the fluorescence intensity squared. The corrected sensitivity for the image power is then given by

$$B(n)_{corr} = \frac{B(n)}{\eta_{IP}(E_n)}. \tag{5.14}$$

The track detection efficiencies for ^{241}AmBe neutrons and ^{252}Cf neutrons are shown in section 5.5 and the average fluorescence intensities for perpendicularly incident protons as a function of energy are described in chapter 6. Mean energies of 4.4 MeV for ^{241}AmBe neutrons and 1.2 MeV for ^{252}Cf were used to determine the average fluorescence intensities. The ratio of track densities for ^{252}Cf to ^{241}AmBe is 0.56 and the squared ratio of fluorescence intensities is approximately 0.58. Equation (5.12) gives $\eta_{IP}(E)$ = 0.325. In this situation, $B(n)_{corr} = 3.08 \cdot B(n)$.

Results of neutron dose determination from FNTDs are plotted against the determined dose measured from sulfur dosimeters in Fig. 5.36. The measured gamma doses during the FBR irradiations are compared to the TLD results in Fig. 5.37 as red

symbols. Determined doses from both detectors are in agreement; small deviations were attributed to non-uniformity of the radiation field. R^2 = 0.979 for the neutron measurements, 0.944 for gamma measurements of detectors irradiated with neutrons from FBR and 0.992 for REBA gamma measurements.

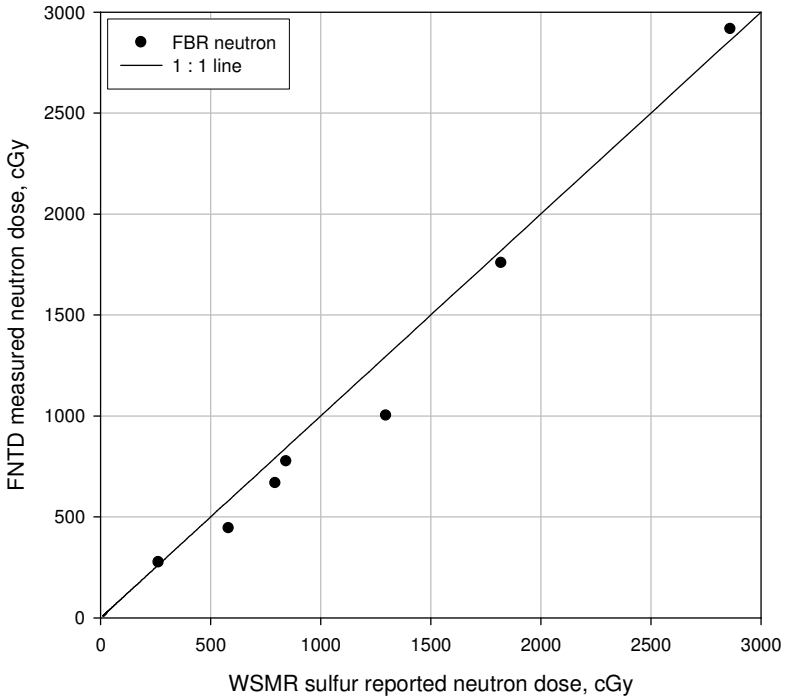

Figure 5.36 FNTD measured neutron dose correlated with the reported neutron dose from sulfur dosimeters measured at WSMR. Regression analysis yields R^2 = 0.979.

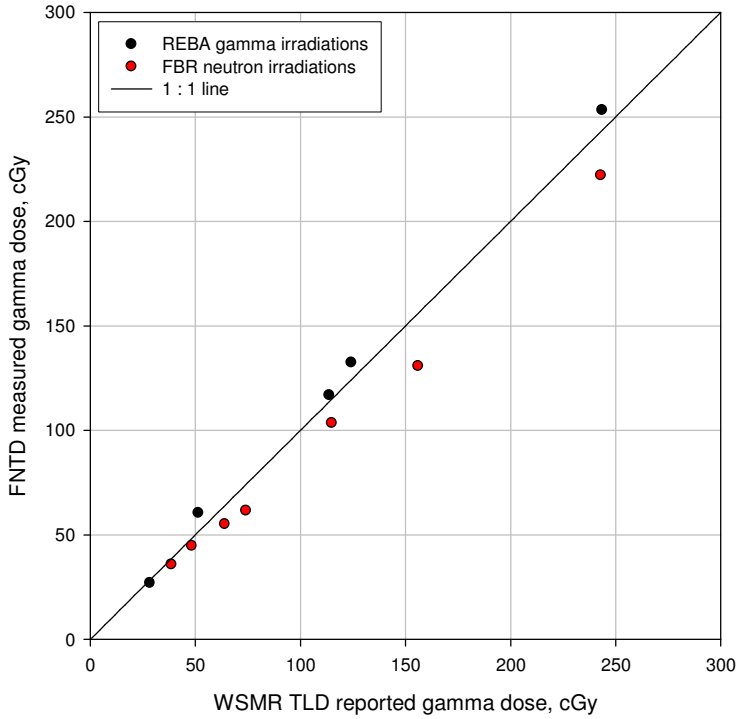

Figure 5.37 FNTD measured gamma dose correlated with the reported gamma dose from TLDs for REBA and FBR irradiations. The overall $R^2 = 0.992$.

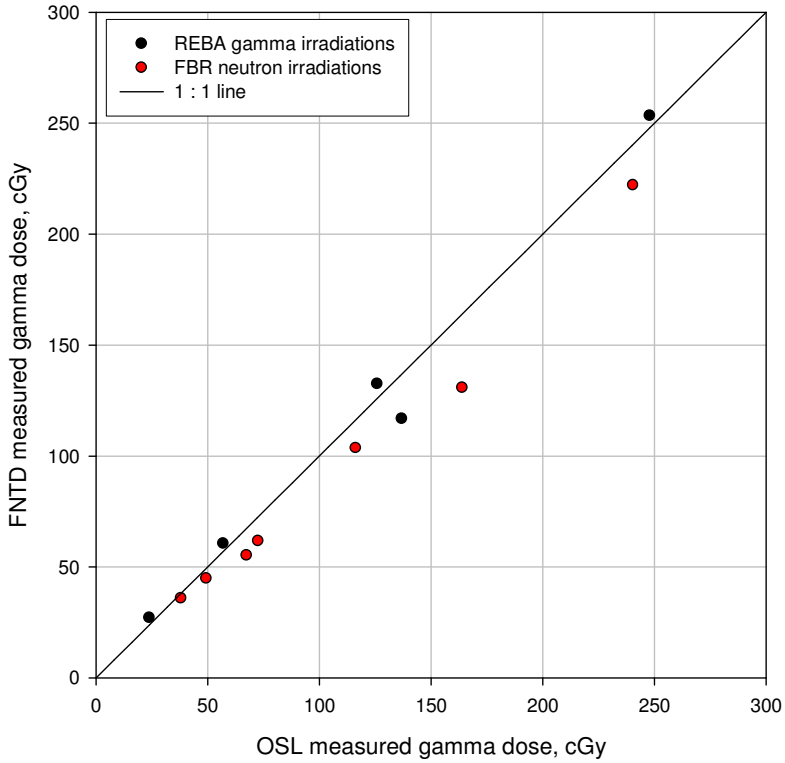

Figure 5.38 FNTD measured gamma dose correlated with the reported gamma dose from OSL for REBA and FBR irradiations. The overall $R^2 = 0.960$.

FNTD results are plotted against OSL results in Fig. 5.38. A 1:1 line is again plotted for reference. FNTDs agree well with OSL detectors. Overall, FNTDs showed good agreement with Sulfur activation foils, TLDs and OSL detectors. The ability of FNTDs to determine high doses of neutrons as well as high doses of gamma makes FNTD technology an excellent candidate for high dose accident dosimetry.

5.9.2 Neutron dose measurements in the workplace - AREVA

FNTDs were tested at AREVA in France in a blind comparison with CR-39 and CODEBADGE active dosimeters; OSL film was placed with the FNTDs to measure gamma dose. FNTDs were irradiated alongside the other dosimeters in various locations in proximity to a neutron source. Doses determined from the CODEBADGE (CB) dosimeters were reported by AREVA and the CR-39 detectors were processed by Marc Million of Landauer Europe (LCIE) in Paris, France. Thirty FNTDs were packaged in the PE holders with TLD100 chips. FNTDs were imaged and processed using track counting. An area of 3.2 mm^2 was scanned.

Tracks were counted and related to dose by eq. (5.3). The neutron energy spectrum was assumed to be similar to that of D_2O moderated ^{252}Cf so the sensitivity was taken to be 17 tracks/mm^2/mSv behind PE and 105 tracks/mm^2/mSv behind TLD100. Table 5.7 is a statistical analysis (Student's T-test) of all measurements performed. The doses obtained for FNTDs and CR-39 agree, but are almost a factor of 2 lower than the active detectors. Most FNTDs behind TLD100 agree within 8 % of the CR-39 detectors.

Table 5.7 Comparison of data acquired at AREVA nuclear power station for OSL detectors, FNTDs covered with PE and ^{6}Li (TLD 100) converters, CR-39 PNTDs and Codebadge electronic dosimeters

		Location 1				Location 2				Location 3		
OSL Average dose in mrad	Test #'s	1,2,3	4,5,6	7,8,9		10,11,12	13,14,15	16,17,18		19,20,21	22,23,24	25,26,27
	Stdev	52.46	8.98	6.63		2.16	5.93	2.90		20.85	22.16	49.47
	Mean	**169.00**	**76.17**	**54.50**		**41.33**	**53.00**	**43.00**		**73.33**	**110.17**	**101.17**
	Stdev/mean	0.31	0.12	0.12		0.05	0.11	0.07		0.28	0.20	0.49
	Conf. Int. 95%	130.32	22.30	16.46		5.37	14.74	7.20		51.79	55.04	122.89
	Relative Conf. Int	0.771	0.293	0.302		0.130	0.278	0.167		0.706	0.500	1.21
FNTD/PE converter Average dose in mSv	Test #'s	1,2,3	4,5,6	7,8,9		10,11,12	13,14,15	16,17,18		19,20,21	22,23,24	25,26,27
	Stdev	0.06	0.06	0.08		0.16	0.05	0.11		0.14	0.13	0.13
	Mean	**0.27**	**0.20**	**0.26**		**0.19**	**0.17**	**0.28**		**0.24**	**0.39**	**0.27**
	Stdev/mean	0.22	0.30	0.31		0.84	0.29	0.39		0.58	0.33	0.48
	Conf. Int. 95%	0.15	0.15	0.20		0.41	0.14	0.27		0.35	0.32	0.32
	Relative Conf. Int	0.558	0.779	0.984		2.212	0.782	0.981		1.480	0.815	1.19
FNTD/^{6}LiF converter Average dose in mSv	Test #'s	1,2,3	4,5,6	7,8,9		10,11,12	13,14,15	16,17,18		19,20,21	22,23,24	25,26,27
	Stdev	0.03	0.04	0.05		0.01	0.06	0.04		0.02	0.02	0.03
	Mean	**0.25**	**0.25**	**0.28**		**0.22**	**0.28**	**0.25**		**0.28**	**0.17**	**0.22**
	Stdev/mean	0.12	0.16	0.18		0.05	0.21	0.17		0.07	0.11	0.14
	Conf. Int. 95%	0.07	0.09	0.14		0.04	0.16	0.09		0.06	0.04	0.08
	Relative Conf. Int	0.264	0.354	0.481		0.166	0.585	0.378		0.216	0.236	0.386

LCIE CR-39 Average dose in mSv	Test #'s	1,2,3	4,5,6	7,8,9		10,11,12	13,14,15	16,17,18		19,20,21	22,23,24	25,26,27
	Stdev	0.04	0.05	0.04		0.03	0.05	0.08		0.02	0.05	0.02
	Mean	**0.22**	**0.22**	**0.17**		**0.21**	**0.30**	**0.25**		**0.32**	**0.29**	**0.23**
	Stdev/mean	0.18	0.21	0.21		0.16	0.18	0.32		0.07	0.18	0.07
	Conf. Int. 95%	0.10	0.11	0.09		0.09	0.13	0.20		0.06	0.13	0.04
	Relative Conf. Int	0.45	0.52	0.52		0.41	0.44	0.81		0.18	0.46	0.18
Electronic CODE-BADGE Average dose in mSv	Test #'s	1,2,3	4,5,6	7,8,9		10,11,12	13,14,15	16,17,18		19,20,21	22,23,24	25,26,27
	Stdev	0.01	0.01	0.05		0.03	0.02	0.01		0.04	0.03	0.01
	Mean	**0.45**	**0.47**	**0.46**		**0.39**	**0.51**	**0.51**		**0.65**	**0.59**	**0.46**
	Stdev/mean	0.03	0.02	0.10		0.07	0.04	0.02		0.06	0.04	0.02
	Conf. Int. 95%	0.03	0.03	0.12		0.07	0.05	0.02		0.10	0.07	0.02
	Relative Conf. Int	0.06	0.06	0.26		0.17	0.10	0.05		0.15	0.11	0.05

Table 5.8 is a comparison of the average 95 % relative confidence interval (estimation of precision) for all of the dosimeters. The most precise were the CB dosimeters followed by FNTDs covered with ^{6}LiF, CR-39 and the least precise were FNTDs covered with PE. FNTDs covered with ^{6}LiF were more precise than those covered with PE because the sensitivity of the FNTD-^{6}LiF combination is more than 6 times larger than the FNTD-PE configuration. Similarly, CR-39 is more sensitive to 600 keV neutrons than the FNTD-PE configuration, but less sensitive than the FNTD-TLD100 configuration explaining their relative differences in precision.

Table 5.8 95% relative confidence interval for dosimeters used in AREVA neutron tests.

Dosimeter	OSL	FNTD-PE	FNTD- TLD100	CR-39	CB
95% RCI	0.485	1	0.34	0.44	0.11

5.9.3 Out-of-field in-vivo IMRT neutron dosimetry

With the increasing survival times of cancer patients after external radiotherapy it becomes more important to estimate the dose of secondary radiation to tissue outside of the target volume in order to minimize the risk of damaging healthy tissue. In treatments involving photon energies higher than 10 MV it becomes more difficult to estimate the out-of-field dose because part of it will be due to photoneutrons generated both in the linac head and in the patient. FNTDs and neutron sensitive OSL (OSLN) detectors (Yukihara et al, 2008) were used to measure the out-of-field neutron dose to the lower lung in 18 MV 3D conformal, IMRT and RapidArc (RA) treatments for prostate cancer.

FNTDs were covered with PE and either TLD100 or TLD600 chips and placed beside OSL film (for gamma dose determination) and OSLN film (neutron + gamma) in rectal catheters. The catheters were inserted into an Alderson-Rando anthropomorphic phantom and an IMRT thorax phantom from CIRS Inc. The thorax phantom allowed for easy placement of the catheters in the lower right lung.

Irradiations were performed at Copenhagen University Hospital in Denmark by Dr. Marianne Aznar and Ms. Sidsel Damkjaer. Irradiations were generated from actual patient treatment plans using 18MV RA, IMRT and 3D conformal treatments. Treatment doses were delivered to the prostate region of the phantom (Fig. 5.39 and 5.40). 4 treatments were delivered per set of detectors. The field size in the RA and IMRT are comparable so it is acceptable to neglect differences in the out-of-field dose due to the field size.

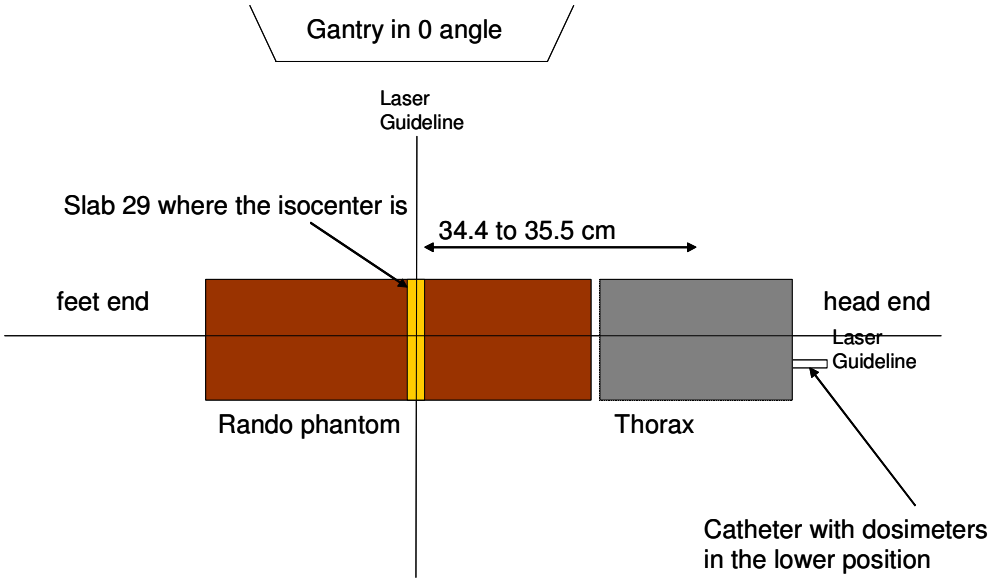

Figure 5.39 Schematic of irradiation conditions during RA, IMRT and 3D conformal treatments depicting the location of the detectors with respect to the isocenter of the treatment.

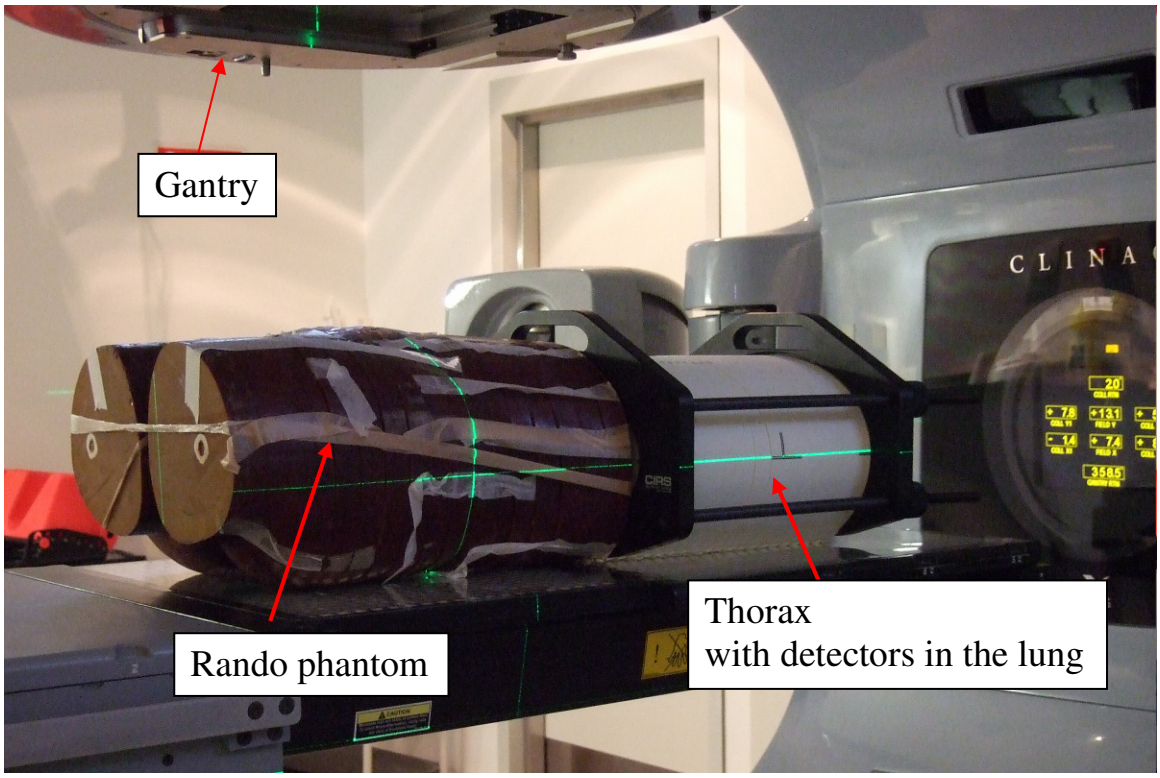

Figure 5.40 Photograph of the conditions during irradiation. The location of the detectors is noted in the photograph.

FNTDs and OSLN were calibrated at PTB using a ^{252}Cf neutron source behind a scattering cone to moderate the peak neutron energies to 200 keV in accordance with average measured photoneutron energies from an 18 MV LINAC of 266 keV (Howell et al, 2005). The detectors were irradiated free-in-air so the calibration dose was in units of H*(10) (ambient dose equivalent). Personal dose equivalent, or $H_p(10)$, would have been a better quantity because the treatment measurements were in-vivo and neutrons will be moderated by the body, but irradiation on phantom was not available at the time of calibration. Doses reported here are in terms of H*(10).

FNTDs were imaged and processed in track counting mode to determine the track density and the OSL/OSLN detectors were readout using a pulsed OSL reader developed

at Landauer. Acquired images had dimensions of 100 x 100 μm^2 and a total area of 2 mm^2 was scanned. Images were automatically processed in track counting mode. Neutron dose was determined from OSLN using a similar method to eq. (5.8) where the regular OSL film determines the gamma dose such that the gamma contribution can be subtracted from the total signal obtained from the OSLN detectors.

Table 5.9 Statistical analysis of FNTDs, OSLN and OSL dosimeters irradiated out of field and in-vivo in a phantom during prostrate treatments using 18 MV 3D conformal, IMRT and Rapid Arc treatments. Mean doses are reported in ambient dose equivalent per treatment (4 treatments) and ambient dose equivalent per monitor unit (MU).

Detector	Treatment	Mean dose/treatment, mSv	Mean dose/MU, μSv	Error	95% confidence interval	Relative confidence interval
FNTD +TLD100 (neutron)	3D Conformal	2.604	10.588	0.070	0.135	0.052
	IMRT	3.368	9.150	0.456	0.877	0.260
	RA	4.008	9.950	0.263	0.505	0.126
OSLN (neutron)	3D Conformal	2.121	8.620	0.708	1.363	0.643
	IMRT	3.365	9.140	0.314	0.604	0.180
	RA	3.883	9.423	0.663	1.275	0.328
OSL (gamma)	3D Conformal	1.602	6.513	0.223	0.429	0.268
	IMRT	1.221	3.311	0.071	0.136	0.111
	RA	1.594	3.869	0.476	0.916	0.575

Doses and statistical analysis of the data obtained behind all detectors are presented in Table 5.9. Mean doses are the averages of 5 FNTDs irradiated in the lung position in the phantom. Both FNTDs and OSLN detectors showed similar results suggesting the determined dose are accurate. Relatively low numbers for 95%

confidence intervals relative to the mean imply that the precision for all detectors irradiated was also good.

Attempts to measure the out-of-field neutron dose in various organs made by Kry et al at the M.D. Anderson Cancer Center show similar results to FNTDs and OSLN detectors. Kry et al (2005) measured the neutron dose equivalent of conventional 18 MV IMRT treatments to be 7.1 μSv/MU which is only 25% different from the FNTD and OSLN estimated neutron dose equivalent of 9.15 μSv/MU. Factors such as exact placement of the detector, treatment plan, gantry angles, lay out of the room and calibrations could all contribute to the small difference in numbers. Kry also reported that neutrons made up 55% of the total dose equivalent (neutrons plus gamma) in the center of the lung (Kry et al, 2005). FNTD and OSL measurements show that neutrons contribute approximately 73% of the total dose equivalent in the lung. Results from both these measurements and Kry's measurements suggest that more dosimetry of out-of-field photoneutrons is needed to properly estimate the risk to healthy tissues which is a problem that, as was shown here, FNTDs can address.

5.10 Conclusions

The goal of this investigation was to demonstrate that FNTDs can be used as reliable neutron dosimeters. Thousands of detectors were irradiated to fully characterize FNTDs for use in neutron dosimetry. Dose dependences were obtained for several FNTD-converter combinations. The dose response was linear throughout the entire range of

investigated doses for both fast and thermal neutrons. It was also demonstrated that FNTD have high sensitivity and good fast to thermal neutron discrimination.

A new method of measuring fast neutrons and photon radiation has been proposed and tested. The new method utilizes high spatial resolution and the imaging capabilities of FNTD technology as well as new, more sophisticated, image processing routines.

The image power was found to be proportional to the dose of both neutron and photon radiations in a wide dynamic range. Total dose linearity was shown to span over 5 orders of magnitude by combining the new image power method with track counting. The image power processing method extends the linear dose response range at least one order of magnitude as it accounts for overlapping tracks.

A method of determining neutron dose on top of relatively large gamma doses was developed using image power as a parameter to determine both neutron and gamma doses. It was shown that it is possible to separate neutron to gamma doses at ratios down to 1:3 in terms of dose equivalent (1:30 in absorbed dose).

FNTDs were characterized in monoenergetic neutron fields from 40 keV to 14.8 MeV. Relatively simple methods of determining the median energy of neutron fields have been demonstrated. One method compares track densities behind two converters: PE, which is efficient for fast neutron conversion and ^{6}LiF, which is efficient for low energy neutrons. The second method is mostly applicable to fast neutrons and determines median energy by measuring the penetration depth of recoil protons. Both methods show good agreement with accepted values for standard broad spectrum neutron sources.

FNTDs also show promise for operating as neutron spectrometers. FNTDs could provide a good alternative to track-etch detectors sometimes used for neutron

spectrometry. It is strongly suggested to continue investigating FNTDs for neutron spectrometry including development of proper unfolding routines and Monte Carlo simulations for verification.

The energy response of FNTDs was expected to depend on fast neutron converter thickness because the recoil proton loses energy in the converter and fails to reach the FNTD. Higher energy neutrons generate higher energy recoil protons that penetrate the converter and interact with the crystal. It would be beneficial to investigate the effects of using thin PE converters to effectively flatten the energy dependence for high neutron energies. A thin fast neutron converter can help simplify deconvolution. Conversely, thicker converters should be investigated to increase sensitivity to high energy (greater than 10 MeV) neutrons. Monte Carlo calculations also need to be performed to compare with experimental data. Monte Carlo modeling of the FNTD dosimeter package is also needed to find the optimum dosimeter design.

Obtaining reliable depth profiles and ratio of track densities required a large number of tracks which equates to high doses or a large number of images to acquire. This can be practically problematic as the dosimeters must be exposed or read-out over long periods of time to acquire enough statistics. The median energy estimation methods only work for neutron energies equal to or greater than 100 keV where recoil protons can easily be identified. A possible solution for estimating energies of neutrons with lower energies is to use the ratio of track densities for a combination of converters with different energy dependent neutron capture cross-sections such as ^{6}Li and ^{10}B.

Gamma results were shown to agree with TLDs and OSL detectors during high dose irradiations. FNTDs will probably not replace TLDs or OSL detectors as gamma

dosimeters because the low dose limit for spatial frequency analysis is still too large (~500 μSv for FNTDs compared to ~10 μSv for OSL) and the readout method is much more complex making it inefficient and expensive for gamma dosimetry. It is suggested to investigate the OSL properties of Al_2O_3:C,Mg to be able to measure precise X-ray or gamma doses as well as neutrons and heavy charged particles in specialized fields such as space dosimetry where there is a mixture of many types of radiation.

FNTDs were proven to be effective in several practical scenarios including high dose accident dosimetry, in nuclear processing workplaces and in out-of-field radiation therapy neutron dosimetry.

CHAPTER VI

INVESTIGATION OF OTHER APPLICATIONS

FNTDs were originally investigated for neutron detection and as LET spectrometers for heavy charged particles (HCP) (Akselrod et al, 2006). Our research continued this original work, but because FNTD technology was brand new, it was important to investigate other promising applications. Many new applications for FNTDs have become viable throughout the course of this research. Spatial frequency analysis of the images, for example, has brought about several new approaches to dosimetry using FNTDs, most notably beta and photon dosimetry; x-ray and gamma dosimetry have already been discussed in detail in chapter 5.

Investigating other applications can also lead to discoveries for applications to neutron dosimetry. As an example, energy corrections to the image power for high dose neutron dosimetry (section 5.8.1) were made possible by investigating proton energy spectroscopy (section 6.2). Applications such as microdosimetry are relevant to neutron dosimetry (see section 6.8). Other applications may also identify limitations in the current approach to neutron dosimetry which could lead to better solutions in the future. New studies focused on feasibility of FNTDs in immediately practical fields like projectile fragmentation, inertial confinement fusion diagnostics, dosimetry for radiotherapy, microbeam imaging, and microdosimetry

6.1 Heavy charged particle spectroscopy

Radiotherapy, space dosimetry, nuclear physsics and radiation protection are all areas that require the ability to distinguish particles of varying LET. Plastic nuclear track detectors (PNTDs) are currently the predominant passive LET spectrometer, but differences in chemical etching, the chemical etching process itself and disagreement in how to process data have left some researchers searching for alternative technologies.

One proposal for an alternative LET spectrometer is FNTDs. Several papers have been published on the topic of using FNTDs for HCP spectroscopy (Akselrod, G.M. et al. 2006 and Sykora et al. 2008a). These papers demonstrated that the fluorescence intensity of the HCP track was dependent upon the LET of the incident particle. Fluorescence intensity depends on the number of F_2^+(2Mg) color centers created within the track as a result of radiochromic transformation of F_2^{2+}(2Mg) centers which increases as the amount of energy deposited along the track increases. The amount of energy deposited in a specific volume (ionization density) determines the number of electron-hole pairs created. The fluorescence intensity of the track therefore depends on the ionization density of the incident charged particles. The main parameter used for determining LET or ionization density was the fluorescence intensity of the tracks.

The fluorescence response to HCPs can be explained by track structure theory and microdosimetry (see sections 2.2 and 2.3). Stochastic deposition of energy within the particle's track causes variance in fluorescence intensity along the track as demonstrated in Fig. 6.1. Figure 6.1 is an image of an FNTD irradiated with 400 MeV/amu ^{84}Kr and 290 MeV/amu ^{12}C parallel to the crystal surface, but perpendicular to each other.

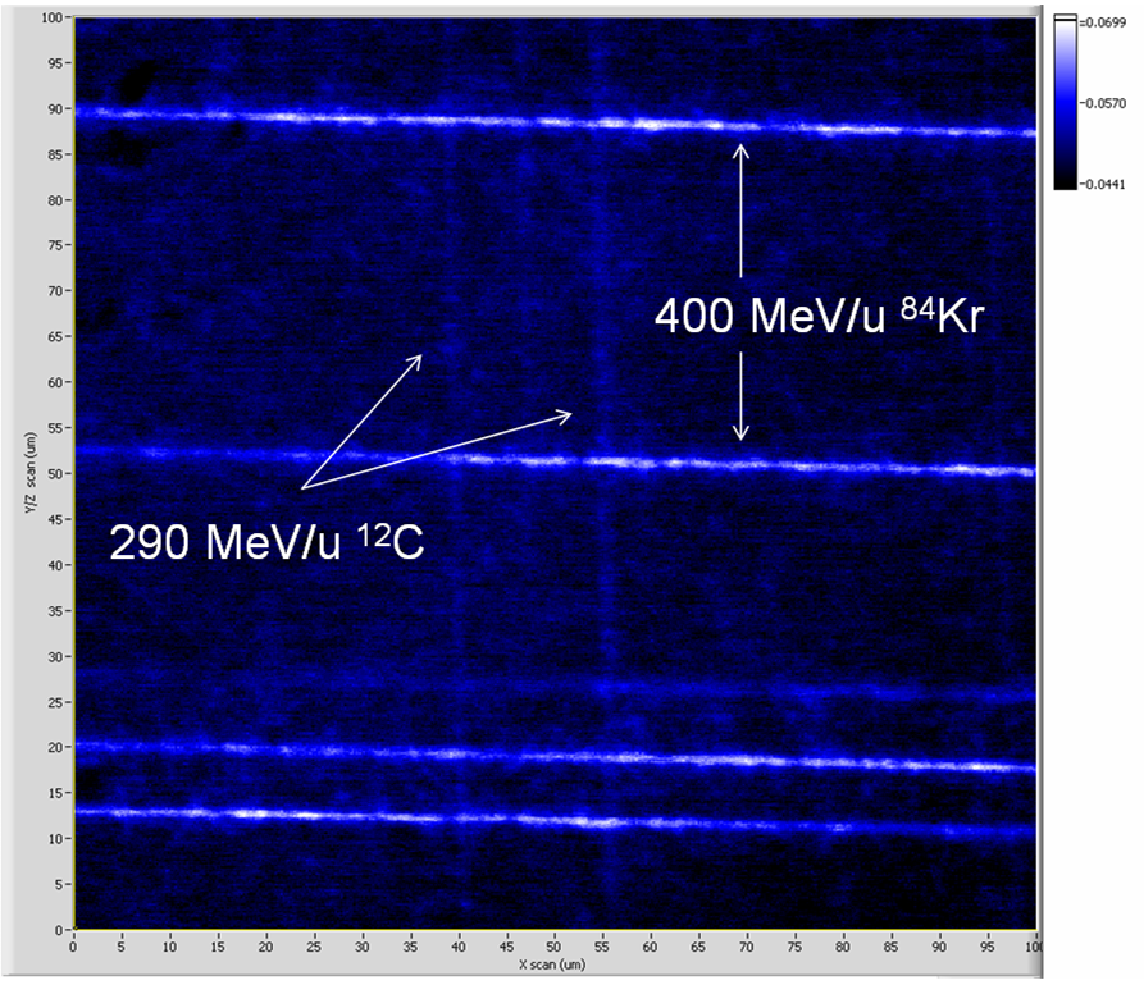

Figure 6.1 100x100µm^2 image of an FNTD irradiated with 400 MeV/amu ^{84}Kr and 290 MeV/amu ^{12}C parallel to the surface of the FNTD but perpendicular to each other. The image demonstrates stochastic deposition of energy within the detector by the varying intensities within one track.

6.1.1 Experimental methods common to all HCP studies

Table 6.1 outlines parameters of heavy charged particle irradiations and the irradiation facilities. Individual irradiations will be discussed as pertinent information in the ensuing subsections. For reliable statistical analysis, 25 to 50 images (depending on particle fluence) were acquired and processed to obtain at least 3000 tracks for each type of ion. Individual fluorescence tracks were identified by an image processing program as

bright objects on dark background and were automatically processed. The track counting efficiency was determined to be nearly 100%. The fluorescence intensity of each track was measured as discussed in chapter 4. Fluorescence intensity was defined as the maximum fluorescence signal above the background fluorescence (background is caused by the residual concentration of F_2^+(2Mg) centers in the crystal prior to irradiation).

Low LET particles have track diameters on the order of a few angstroms to tens of nanometers (Cuccinota et al, 1995) which is smaller than the lateral size of the diffraction limited focal spot (~600 nm) of the FNTD imaging system. Therefore, tracks from low LET particles all appear to be the size of the focal spot. In fact, fluorescence track diameter begins to increase for ions with $LET_{\infty}H_2O$>100 keV/μm (see Fig. 6.7).

The readout and processing methods described in chapter 4 allowed for measurements of fluorescence intensity, track diameter and the ion range. If the track was within the volume of the single crystal detector and within the working distance of the imaging optics, then the ion range was determined. Throughout this chapter, fluorescence intensities are labeled in arbitrary units (a.u.) and are normalized relative to the mean fluorescence intensities of tracks caused by irradiation with a standard 5.11 MeV alpha source.

Table 6.1 List of ions and their parameters used for HCP spectroscopy calibrations

Facility	Ion	Energy, MeV/amu	LET H_2O, keV/μm	LET Al_2O_3, keV/μm	LET after wedge*, keV/μm	Z/β
HIMAC	^{1}H	30	1.93	6.07		4.05
	^{1}H	40	1.51	4.83		3.53
	^{1}H	55	1.17	3.76		3.05
	^{1}H	70	0.967	3.12		2.73
	^{1}H	160	0.526	1.71		1.92
	^{4}He	150	2.2	6.82	11.4	4
	^{12}C	6	257.4	783.5		53.1
	^{12}C	135	20.8	64.5		12.3
	^{12}C	290	12.6	39.1		9.27
	^{16}O	383	19.74	61.2	307.7	11.3
	^{20}Ne	371	31.7	98.4	374.6	14.3
	^{28}Si	444	57	177	316	19
	^{28}Si	1000	43.4	134.5		16
	^{40}Ar	500	92.2	285	529.2	23.7
	^{56}Fe	6	3128	9521		23.2
	^{56}Fe	120	431	1336	4153	56
	^{56}Fe	500	182	564	1825	34.2
	^{84}Kr	400	395.5	1226		50.4
	^{132}Xe	187	1345	4169	8767	97.5
Brookhaven	^{28}Si	5000	41.97	137		14.2
	^{56}Fe	500	182	564		34.2
	^{56}Fe	1000	147	456		29.67
RARAF	^{1}H	0.3	51	143.6		39.57
	^{1}H	0.59	32.8	99.5		28.22
	^{1}H	1.5	19.9	58.8		17.71
	^{1}H	3	12.1	32.4		12.54
MIT	^{1}H	0.694	29.7	91.2		26.02
	^{1}H	1	24.0	74.6		21.68
	^{1}H	1.6	19.1	56.3		17.15
	^{1}H	2.2	15.5	45.0		14.63
	^{1}H	2.87	12.6	37.0		12.82
	^{1}H	4.16	9.40	28.5		10.66
	^{1}H	7.05	6.18	19.2		8.21
	^{1}H	10.29	4.34	14.0		6.81
	^{1}H	13.56	3.64	11.4		5.95
MD Anderson	^{1}H	72.5	0.960	3.08		2.69
	^{1}H	100	0.730	2.39		2.34
	^{1}H	160	0.526	1.71		1.92
	^{1}H	200	0.454	1.48		1.77
	^{1}H	250	0.395	1.29		1.63

*Values are listed if a wedged absorber was used for that ion.

6.1.2 Fluorescence intensity dependence on LET

New experiments related to LET spectroscopy of HCPs motivated by the needs of current radiation research were investigated. Experiments were performed with the new FNTD reader described in chapter 4. A full calibration of the detectors' response to LET of HCPs was performed by irradiating FNTDs with energetic charged particles at HIMAC with a range of LET from 0.4 to 8767 keV/μm. The response of FNTDs to varying LET was demonstrated by measuring Bragg peaks of ions after propagating through wedged absorbing materials.

6.1.2.1 Experimental details

FNTDs were exposed to a variety of heavy ions from 250 MeV ^{1}H with $LET_{\infty}H_2O$ = 0.395 keV/μm ($LET_{\infty}Al_2O_3$ = 1.23 keV/μm) to 187.5 MeV/amu[7] ^{132}Xe with $LET_{\infty}H_2O$ = 1350 keV/μm ($LET_{\infty}Al_2O_3$ = 4170 keV/μm) at HIMAC as part of the National Institute of Radiological Sciences collaborative research program and at MD Anderson Cancer Center in Houston. One set of detectors was irradiated "bare" (no absorbing medium other than the crystal itself) while the other was irradiated behind metal wedge absorbers made of aluminum, brass or copper (Fig. 6.2). The wedge absorbers were designed so that the incident ions reach their maximum range at a known depth within the wedge. The detector was positioned on the back of the wedge in such a way that both primary tracks and secondary fragment tracks could be imaged both in front of and behind the Bragg peak. For example, the range of 444 MeV/u ^{28}Si in brass is about 27 mm, so the wedge was made 35 mm along the beam axis. As a result of using

[7] The units MeV/amu represent energy per nucleon so 187.5 MeV/amu ^{132}Xe has energy of 187.5 MeV/amu × 132 amu = 2.475×10^{4} MeV.

wedged absorbers, the range of $LET_{\infty}H_2O$ was from 0.4 keV/µm for 250 MeV ^{1}H (bare) to 8767 keV/µm for 187.5 MeV/u ^{132}Xe behind the wedge absorber. A total of 25 LET values were measured within that range. In addition, detectors were irradiated at the NASA Space Radiation Laboratory (NSRL) heavy ion facility at the Brookhaven National Laboratory (BNL) with 1 GeV/amu ^{28}Si and 1 GeV/amu ^{56}Fe. All detectors irradiated at BNL were exposed bare (without wedge absorbers). Table 6.1 lists all relevant details pertaining to HCP exposures including the irradiation facility, the ion, energy, $LET_{\infty}H_2O$, $LET_{\infty}Al_2O_3$, and Z/β.

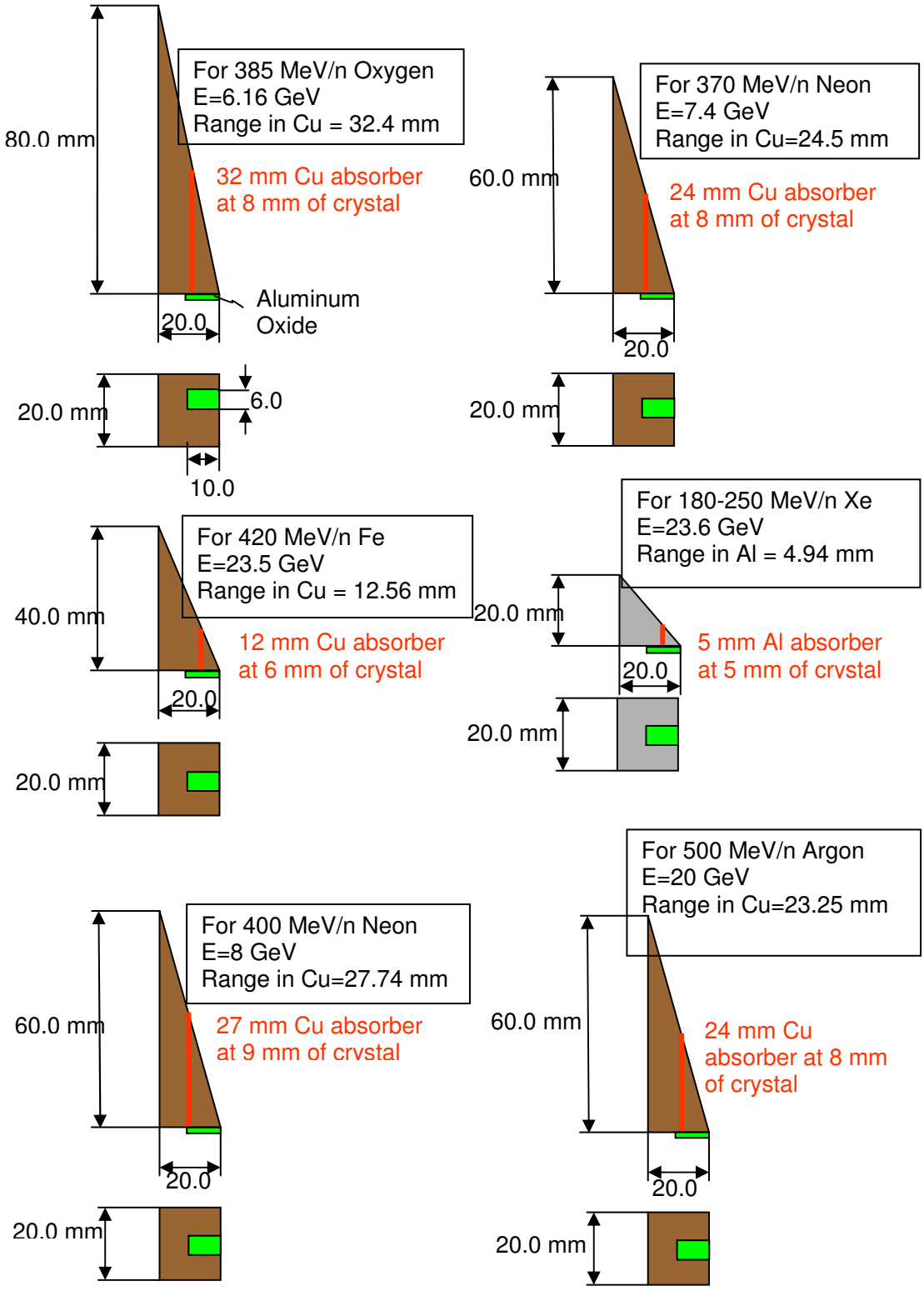

Figure 6.2 Diagram of the wedged absorbers designed for irradiation with heavy charged particles. The red line represents the estimated location of the Bragg peak in the wedge.

6.1.2.2 Results and discussion

Figure 6.3 shows two 50x50 μm^2 images from FNTDs exposed to 5.1 MeV alphas ($LET_{\infty}H_2O$ = 90 keV/µm) and 187.5 MeV/amu ^{132}Xe ($LET_{\infty}H_2O$ = 1350 keV/µm). The images illustrate the influence of LET on the observed fluorescence intensity and track diameter. As LET increases, the fluorescence intensity and track diameter increase.

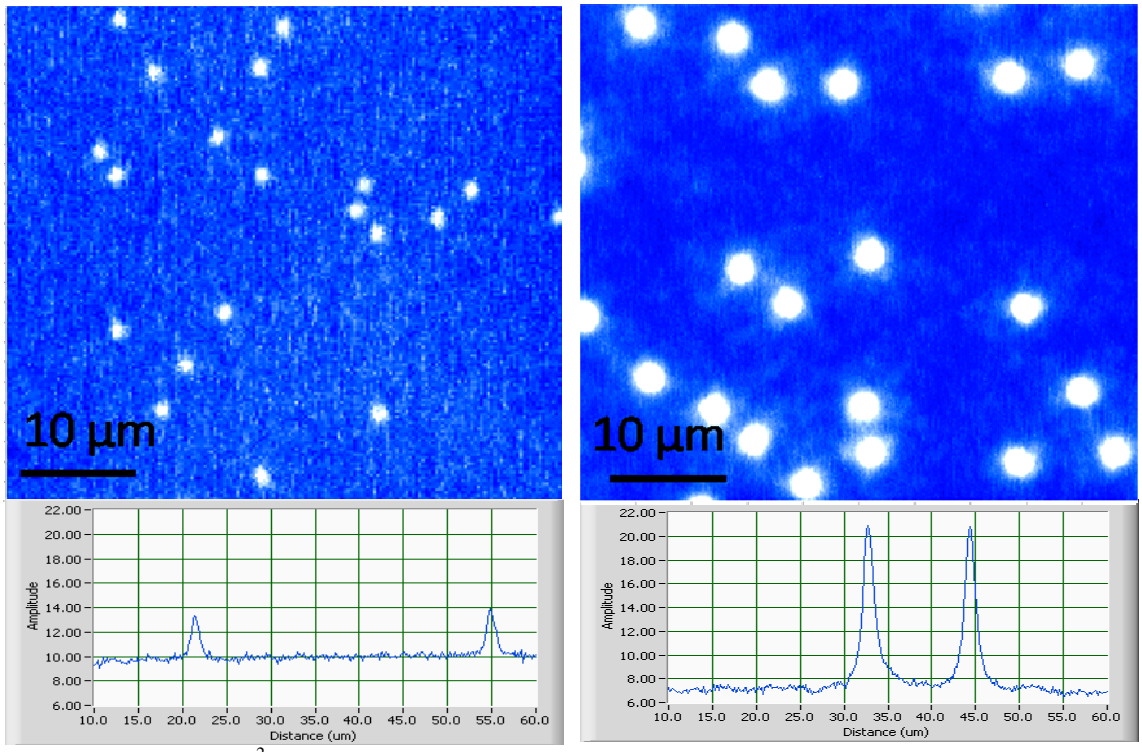

Figure 6.3 a) 50x50 μm^2 images of FNTDs irradiated with 5.1 MeV alpha particles with $LET_{\infty}H_2O$ = 90 keV/µm (left) and 187 MeV/amu ^{132}Xe with $LET_{\infty}H_2O$ = 1350 keV/µm (right) and b) corresponding cross-sections of individual tracks.

To illustrate the spectroscopic capabilities of FNTD technology, fluorescence intensity histograms were obtained for seven different ions. All images were acquired at a depth of 5 µm below the surface of the detector. Figure 6.4 depicts histograms of fluorescence intensity for ^{56}Fe ions having three different energies. 1 GeV/amu ^{56}Fe with $LET_{\infty}H_2O$ = 147 keV/µm produces the lowest fluorescence intensity. 500 MeV/amu and 120 MeV/amu ^{56}Fe ions, with $LET_{\infty}H_2O$ = 182 keV/µm and 431 keV/µm respectively,

have higher fluorescence intensities. Similarly three well separated peaks were obtained for ^{12}C ions having 6 MeV/amu ($LET_{\infty}H_2O$ = 257 keV/μm), 135 MeV/amu, ($LET_{\infty}H_2O$ = 12.6 keV/μm) and 290 MeV/amu ($LET_{\infty}H_2O$ = 20.8 keV/μm).

Figure 6.5 shows fluorescence intensity distribution histograms for seven ions having different Z, energies and LET. The histograms clearly demonstrate the ability of FNTDs to distinguish tracks caused by incident particles with differing $LET_{\infty}H_2O$ values. The full-width at half maximum (FWHM) of the peaks defines the spectral resolution of the technology. Each peak in the distributions was fit to a Gaussian function with FWHM between 16% and 17% of the mean fluorescence amplitude for every ion except for ^{132}Xe for which the width was 21%. Figure 6.6 shows the spectral width of the distribution normalized to mean fluorescence intensities for the ions shown in Fig. 6.5. The ^{132}Xe peak is broadened partially because of straggling in the incident ion beam and its strong interaction with air due to the large atomic number number of Xe ions (Z=54). The largest contributing factor in the width of the distributions is the statistical fluctuation in energy deposition along the track.

Akselrod et al (2006b) has shown that the width of the peaks can be decreased approximately by a factor of 1.5 by imaging tracks at seven depths within the crystal and by averaging their respective intensities. The current confocal imaging system described in chapter 4 restricts track averaging in depth to only 75 μm which is not sufficient to completely average the statistical energy deposition.

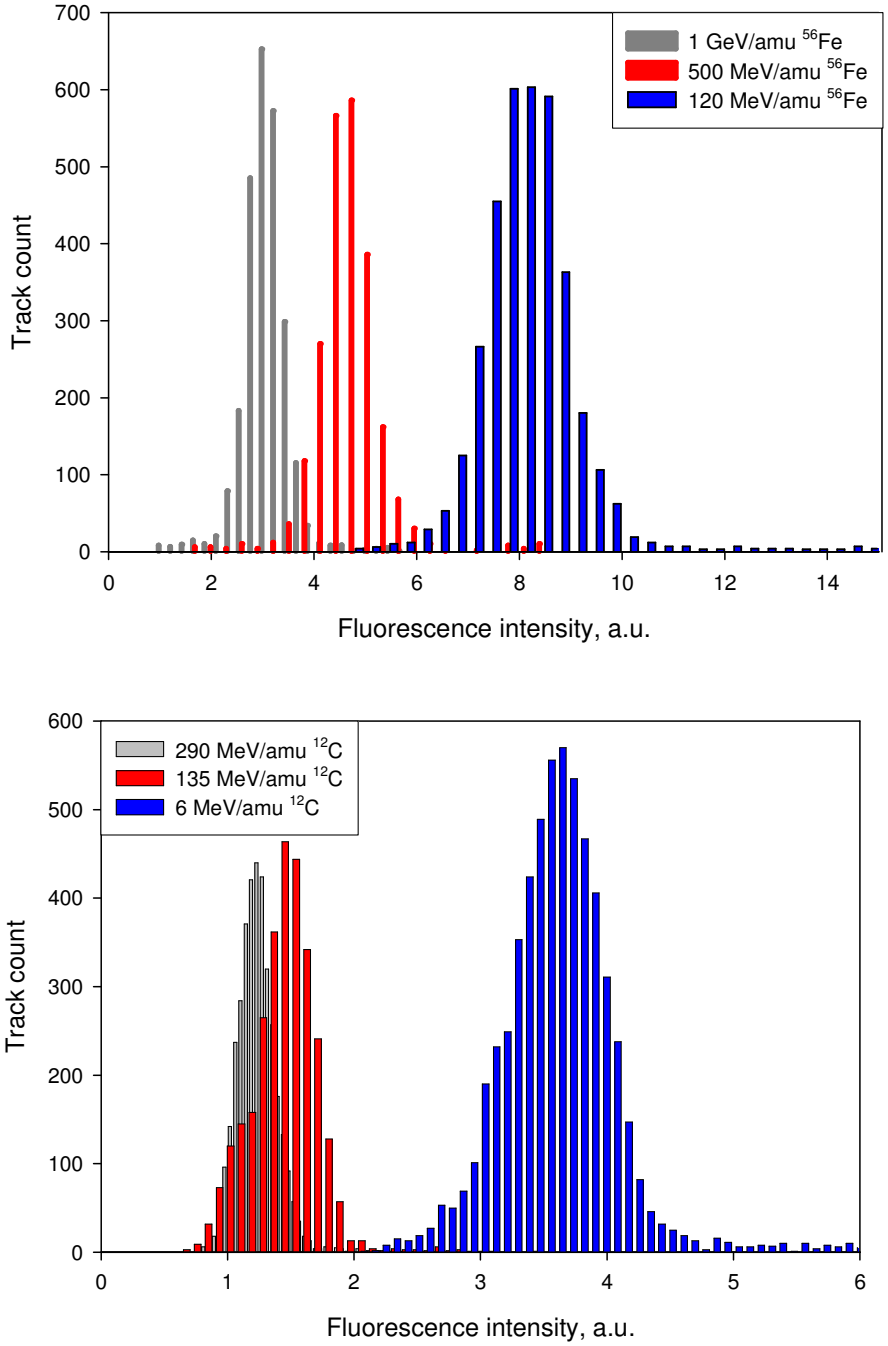

Figure 6.4 Track frequency histograms of ^{56}Fe with three different energies ($LET_{\infty}H_2O$ = 147, 182 and 431 keV/µm) (top) and ^{12}C with three energies (($LET_{\infty}H_2O$ = 12.6, 20.8 and 257.4 keV/µm).

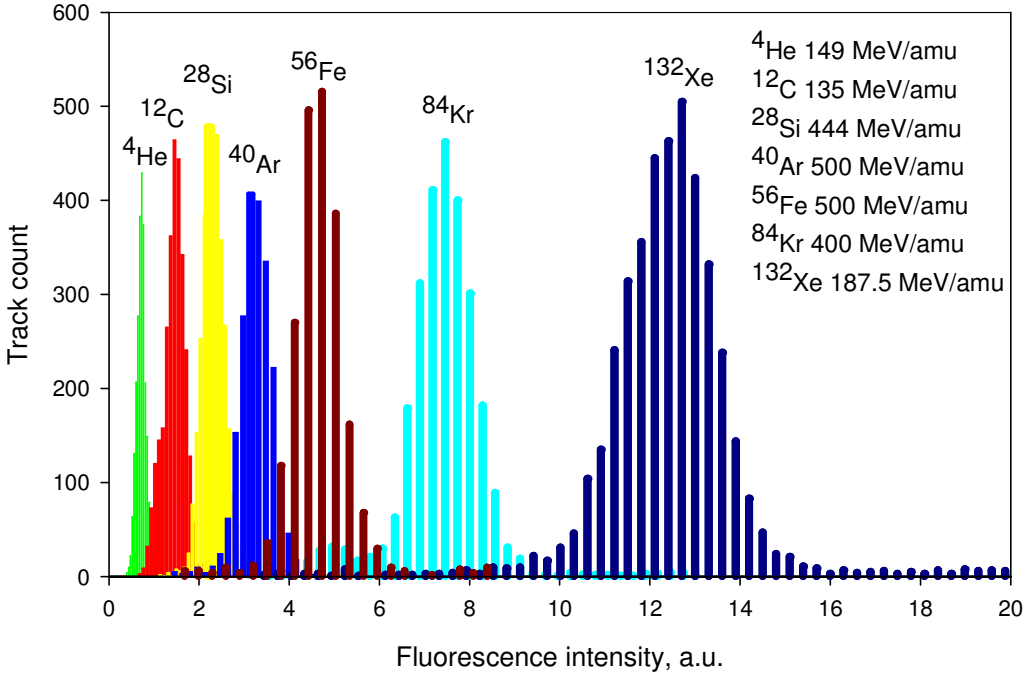

Figure 6.5 Fluorescence intensity distributions for seven high energy ions incident on bare FNTDs.

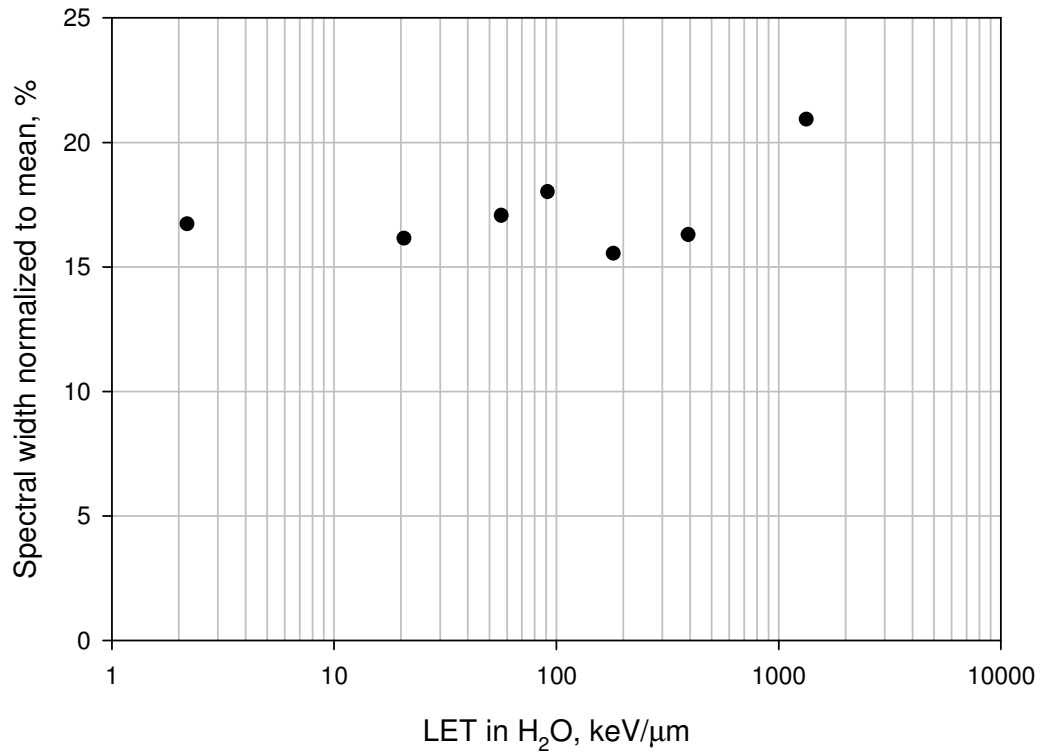

Figure 6.6 Dependence of spectral width (defined by the Full-width at half maximum) of the fluorescence intensity distributions normalized to mean intensity on $LET_{\infty}H_2O$ for the seven ions shown in Fig. 6.5.

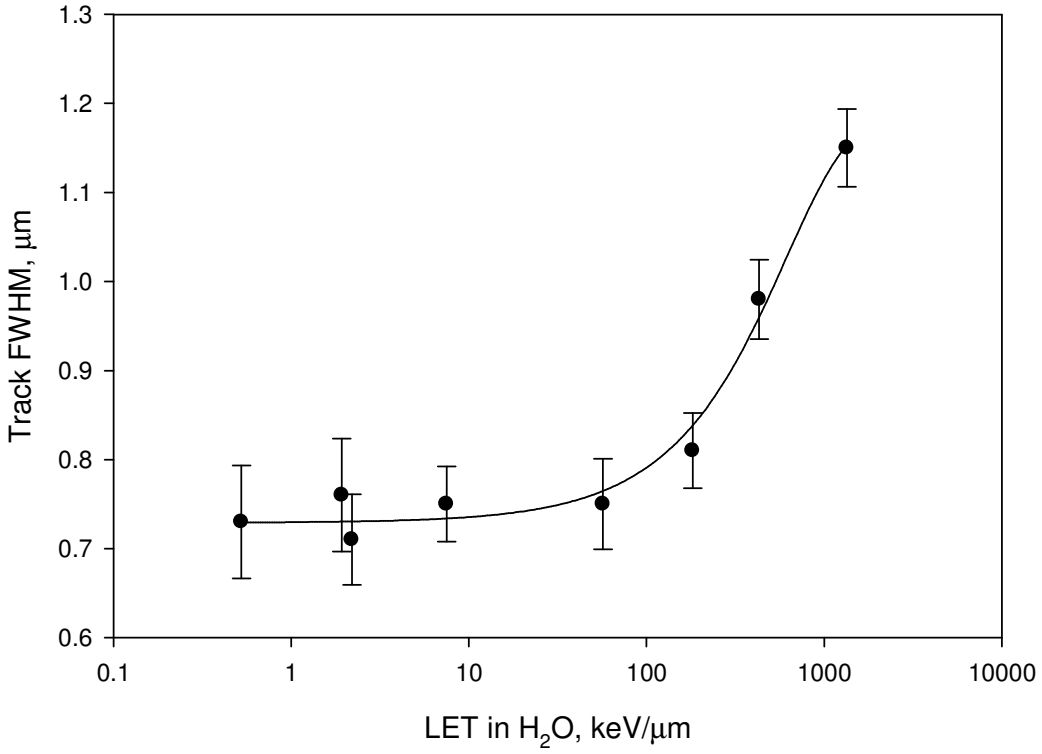

Figure 6.7 Dependence of the full-width at half maximum of tracks in FNTDs on the $LET_{\infty}H_2O$ showing constant width for ions with $LET_{\infty}H_2O$<100 keV/µm.

A significantly wider range of LET can be obtained by slowing incident ions with absorbers and by measuring fluorescence track intensity at various depths along the Bragg curve within the detector. Bragg curve measurements were carried out in FNTDs exposed to eight different heavy ion beams. The fluorescence images were obtained at intervals of 160 µm starting from the edge of the detector aligned with the thin edge of the wedged absorber (see Fig. 6.2). The slope of the wedge determined the absorber thickness and thus the position on the crystal where the Bragg peak occurred. Figure 6.8 presents Bragg curves obtained by measuring the mean fluorescence amplitude of tracks corresponding to a specific depth within the wedged absorber. For comparison, LET as a function of absorber thickness was calculated using SRIM-2006 (Ziegler and Biersack,

2006). The mean fluorescence amplitude obtained without the absorber was used to normalize the fluorescence amplitudes. Simulations using TRIM-2006 (Ziegler and Biersack, 2006) (shown as red lines in Fig. 6.8) are in reasonable agreement with experimental data. The locations of the Bragg peak for each ion were in good agreement with the calculations, with the exception of 144 MeV/u ^{4}He. A more detailed investigation of the response of FNTD to energetic ^{4}He is planned for future studies.

The wedge absorber experiment using the 187.5 MeV/n ^{132}Xe beam permitted the maximum $LET_{\infty}H_2O$ to be extended from 1350 keV/μm to 8767 keV/μm. $LET_{\infty}H_2O$ of the ions incident on FNTDs after penetrating through the wedged absorbers were estimated by calculating the energy loss in the absorber according to:

$$E_f = E_0 - \int_0^t \frac{dE}{dx} dx \tag{6.1}$$

where E_0 is the initial energy of the incident ions, dE/dx is the energy loss (stopping power) in the absorber and t is the thickness of the absorber at the point of measurement. Calculated $LET_{\infty}H_2O$ for ions in the Bragg peak was used in Fig. 6.9.

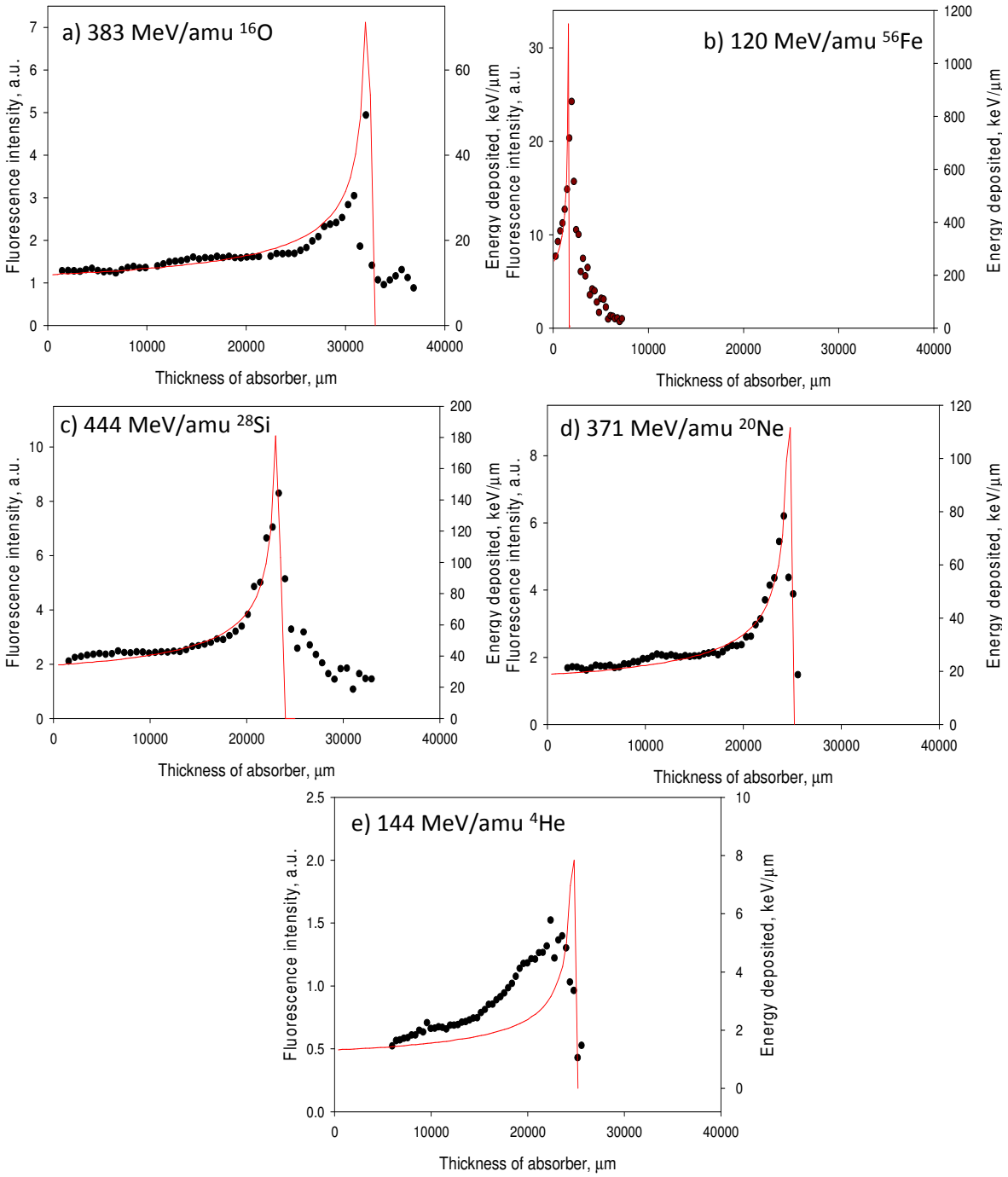

Figure 6.8 Bragg curves obtained for four different ions: a) 383 MeV/amu ^{16}O, b) 120 MeV/amu ^{56}Fe, c) 444 MeV/amu ^{28}Si, d) 371 MeV/amu ^{20}Ne and e) 144 MeV/amu ^{4}He. The solid lines are the result of simulations using TRIM-2006 (Ziegler and Biersack, 2006) whereas the symbols indicate experimental fluorescence intensities obtained by processing FNTD images.

In addition to extending the maximum obtainable LET, the data obtained from detectors behind the wedges showed some tracks beyond the Bragg peak position. These tracks have different diameters and fluorescence intensities. The data indicates that some incident ions fragmented inside the absorber and penetrated through the wedge beyond the maximum range of the primary ions (see section 6.1.2).

The fluorescence intensity dependence on LET for all heavy ion beams used in this study, both bare and behind wedged absorbers is illustrated in Fig. 6.9. Fluorescence intensity dependence on LET is nonlinear and the continuing increase in fluorescence intensity indicates that the detector has not saturated even at an $LET_{\infty}H_2O$ = 8767 keV/μm. Some deviations from a smooth dependence are probably due to slight variations in crystal properties (i.e. concentration of F_2^{2+}(2Mg) color centers). Calibration measurements performed on each detector after irradiation with the same particles of a known LET should allow one to correct for this color center concentration difference.

LET is a parameter that is strongly dependent on the properties of the absorbing medium. Fluorescence intensities were plotted against Z/β which is used to describe ionization density independent of the absorbing medium, (Fig. 6.10), where Z is the effective charge of the ion and β is the relativistic ion velocity which is calculated from:

$$T = m_0 c^2 \left[\frac{1}{\sqrt{1-\beta^2}} - 1 \right], \tag{6.2}$$

T is the kinetic energy of the particle, and m_0c^2 is the rest energy of the ion. It is evident that the fluorescence intensity dependence on Z/β is a linear relationship. A similar linear dependence of Z/β on etch rate (v_t/v_b-1) was demonstrated over a smaller range of Z/β for PNTDs by Ogura, *et al*. (2001).

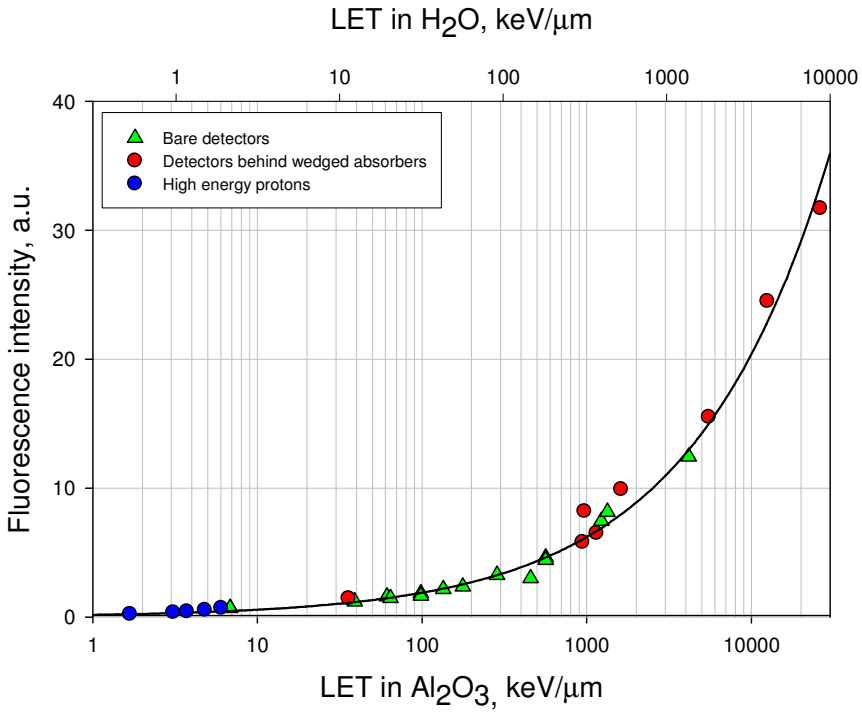

Figure 6.9 Fluorescence intensity dependence on LET_∞ in Al_2O_3 (bottom axis) and H_2O (top axis). High energy protons are included for completeness (see section 6.1.3).

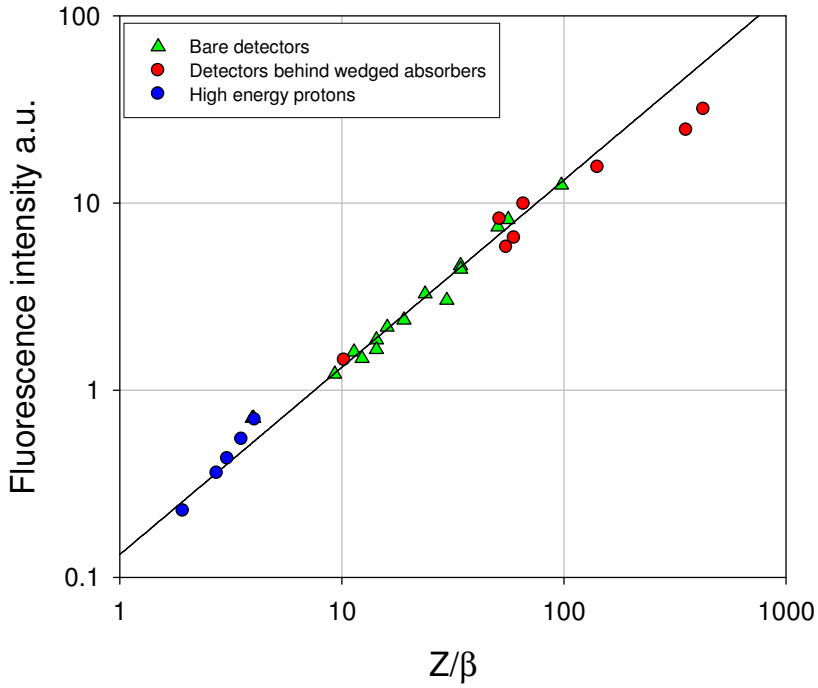

Figure 6.10 Fluorescence intensity dependence on Z/β for heavy charged particles. High energy protons are included for completeness (see section 6.1.3).

6.1.3 Fragmentation

Fragmentation of incident ions and target material occurs with certain probabilities (fragmentation cross section) as a result of interaction of the ion with the target. It is important to understand and quantify fragmentation because fragments can deposit extra dose that is not accounted for when estimating risk to heavy ion therapy patients or astronauts. PNTDs and several active detectors are currently being used to determine fragmentation cross-sections (Zeitlin et al, 2006, Flesch et al, 1999 and Ota et al, 2008) so FNTDs can potentially serve as a detector to determine fragmentation cross sections.

Several detectors were irradiated behind varying thicknesses of PMMA with 290 MeV/amu C and 150 MeV/amu He. The purpose of the PMMA was to initiate fragmentation of the incident ions. The detectors were imaged and processed to obtain frequency distributions (histograms of track counts) of track fluorescence intensity.

Figure 6.11 is a compilation of track frequency distributions of FNTDs exposed during the fragmentation experiments. The distributions were deconvolved assuming that the FWHM of the distribution for each ion was proportional to its mean fluorescence intensity and a best-fit was performed by adjusting the peak heights in the distribution. Deconvolution demonstrates the ability to distinguish tracks caused by fragments and primary ions. All of the histograms obtained have the same features with different relative peak heights and shifted centers (because of slowing in the PMMA). Fragments were seen and distinguished in all irradiations. Deuterons may account for the larger peak height for H relative to He.

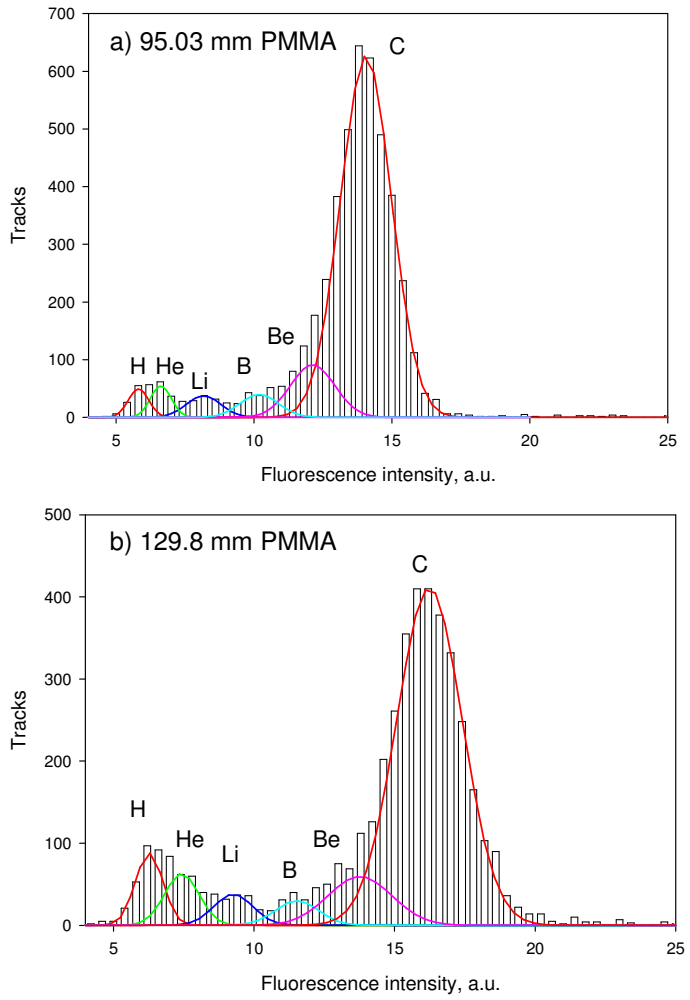

Figure 6.11 Fluorescence intensity frequency distributions for 290 MeV/amu ^{12}C incident on a) 95.03 mm and b) 129.8 mm of PMMA. The bars are data and the lines represent deconvolution of the data.

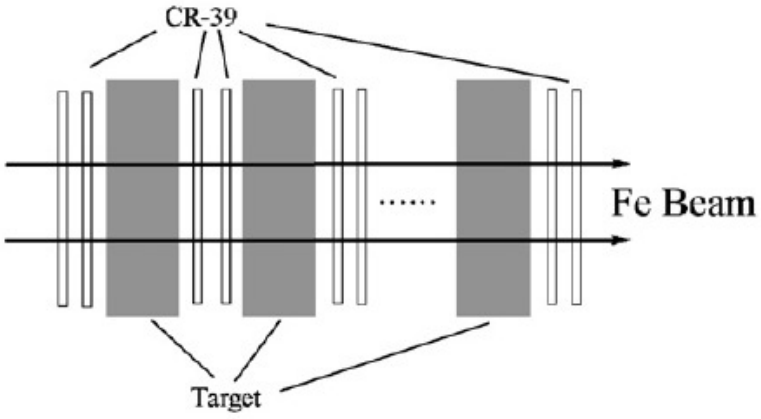

Figure 6.12 Configuration of CR-39-target stacks used to determine fragmentation cross-sections of high energy heavy ions.

Individual peaks were indistinguishable meaning the charge resolution for FNTDs is not yet good enough. Charge resolution may improve using pre-treated FNTDs (see section 5.3), imaging more depths and using multiple detectors as done with CR-39 (Fig. 6.12 and 6.13) (Flesch et al, 1999 and Ota et al, 2008).

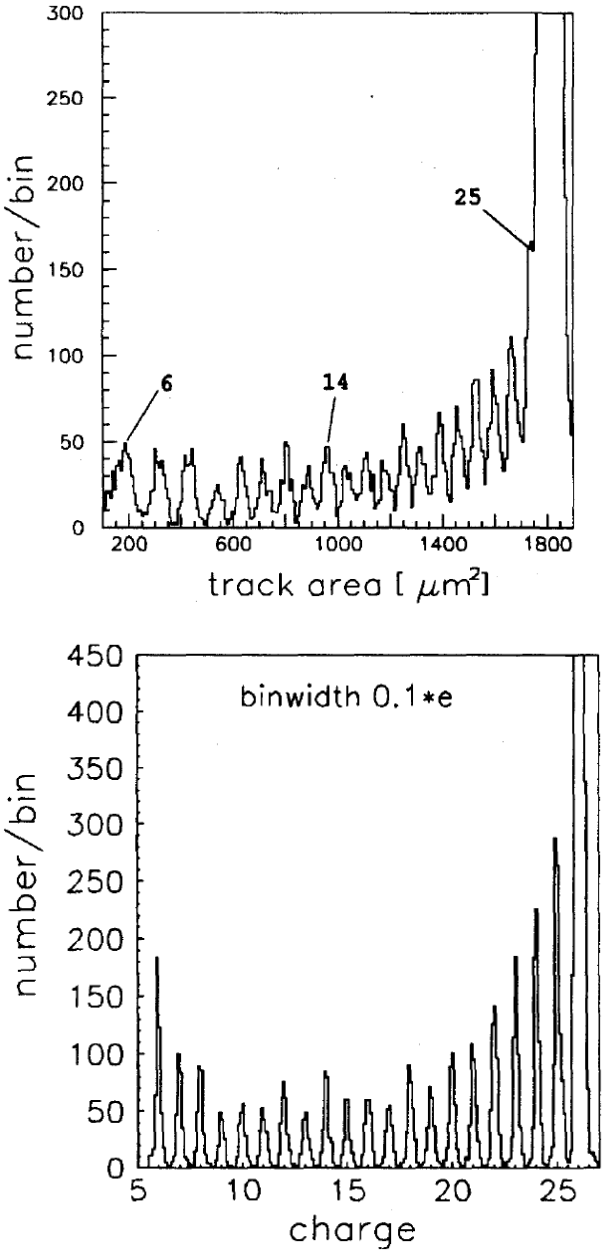

Figure 6.13 (Top) Track distribution obtained by Flesch et al (1999) from a single sheet of CR-39 downfield from a Cu target irradiated with 700 MeV/u Fe and (bottom) charge distribution of the fragments after track tracing through the whole stack of CR-39 detectors.

Most fragmentation cross-section measurements have been motivated by space dosimetry and so the majority of data from CR-39 available for comparison with FNTDs is on fragmentation of Fe ions on metal targets because of the significant presence of Fe in the GCR spectrum (Benton and Benton, 2001). It is difficult to compare the distributions from Flesch and Ota to distributions using FNTDs because the experimental conditions were very different.

Figure 6.13 demonstrates excellent charge resolution of CR-39 for fragments of 700 MeV/u Fe in an 11 mm thick layer of Cu. It appears that CR-39 has good charge resolution for ions with Z>5 using this ion tracking technique and it is possible that FNTDs will exhibit similar performance. The results of Flesch and Ota also indicate that it is difficult for CR-39 to resolve, or even detect, ions with Z<6 at these energies. FNTDs have the ability to detect low LET particles making them good candidates for detection of low Z fragments. It is suggested to continue investigation into the ability of FNTDs to determine fragmentation cross-sections by first repeating the same irradiations and techniques used by other groups such as Flesch and Ota. The fragmentation cross-sections of ions incident on Al_2O_3:C,Mg should also be determined to separate fragments from the target and fragments from the detector.

6.1.4 Spectroscopy of proton beams

Protons play a vital role in radiation therapy, space exploration and nuclear physics. Assessment of potential biological risk (or benefits) of proton interaction in the body is needed because of the popularity of proton therapy facilities for treating cancer and because of the large contribution of high energy protons in galactic cosmic rays (Benton et al, 2001.). Nuclear sciences such as fusion experiments require proton

spectroscopy as a diagnostic tool because protons are common reactants and products (Seguin et al, 2003).

Applications like proton therapy, space exploration and nuclear sciences require the ability to detect a range of proton energies from 100 keV to greater than 1 GeV (Seguin et al, 2003, Suit and Urie, 1992 and Benton and Benton, 2001) which is often difficult using one type of detector. FNTDs, having demonstrated a unique ability to measure low and high LET particles, provide a new potential solution for proton spectroscopy. This section discusses the use of FNTDs in proton spectroscopy with energies from 300 keV to 250 MeV.

6.1.4.1 Experimental methods

Irradiations of FNTDs as well as CR-39 PNTDs were performed with monoenergetic protons at the Radiological Research Accelerator Facility (RARAF) of Columbia University. Twenty-seven FNTDs and PNTDs were exposed to protons of a fluence of around 2 x 10^4 mm^{-2} with energies of 0.3, 0.59, 1.5 and 2.9 MeV. The proton irradiations were performed at a normal angle of incidence to the detector surface. Results of etching and processing of CR-39 detectors were provided by Mark Salasky at Landauer, Inc.

FNTDs were also irradiated at the Massachusetts Institute of Technology (MIT) using a Van de Graff generator to produce monoenergetic protons, alpha particles and tritons from D^3He and DD reactions (Table 6.2). 20 FNTDs were irradiated behind aluminum absorbing filters to reduce proton energies. Six FNTDs were irradiated behind a 1.5 μm thick layer of Mylar™ film to study fluorescence intensity distributions of tracks for the three DD reaction products. Mylar was used to stop the ^3He ion of the DD

reaction before reaching the FNTD Energies and nuclear reactions used in this study are presented in Table 6.2. Initial energies were measured using a surface barrier detector and the energies after the absorbers were calculated using SRIM. Another set of FNTDs were exposed to high energy protons produced at the HIMAC from 30 MeV to 250 MeV.

Table 6.2 Nuclear reactions common in inertial confinement fusion (Seguin et al, 2003). These reactions were used to test FNTD response to protons and determine if they can distinguish ^{3}He and alpha particles.

Primary reactions	$D+D \rightarrow T^*[1.01\ MeV]+p^*[3.02\ MeV]$	(1)
	$D+D \rightarrow n[2.45\ MeV]+{}^{3}He^*[0.82\ MeV]$	(2)
	$D+{}^{3}He \rightarrow \alpha^*[3.6\ MeV]+p^*[14.7\ MeV]$	(3)
Secondary reactions	$T[\leq 1.01\ MeV]+D \rightarrow \alpha[6.7\text{-}1.4\ MeV]+n[11.9\text{-}17.2\ MeV]$	(4)
	${}^{3}He[\leq 0.82\ MeV]+D \rightarrow \alpha[6.6\text{-}1.7\ MeV]+p^*[12.6\text{-}17.5\ MeV]$	(5)

6.1.4.2 Low energy protons

FNTDs irradiated at RARAF with low energy protons were imaged to obtain fluorescence intensities and proton range. Comparison of delivered fluences that were calculated from the accelerator instrumentation data and the measured FNTD track density yields detection efficiency of nearly 100% for protons within the investigated energy range. Discrepancies between delivered and measured fluences are between 0.3% and 8% for different samples and might be caused by errors in irradiation time and beam instrumentation coupled with statistical fluctuations of the requested low fluences.

Figure 6.14 shows the dependence of fluorescence intensity on proton energy. As with the high energy HCP irradiations, the spread in amplitudes is probably due to two main factors: an uneven distribution of color centers between detectors and the stochastic deposition of energy by the protons.

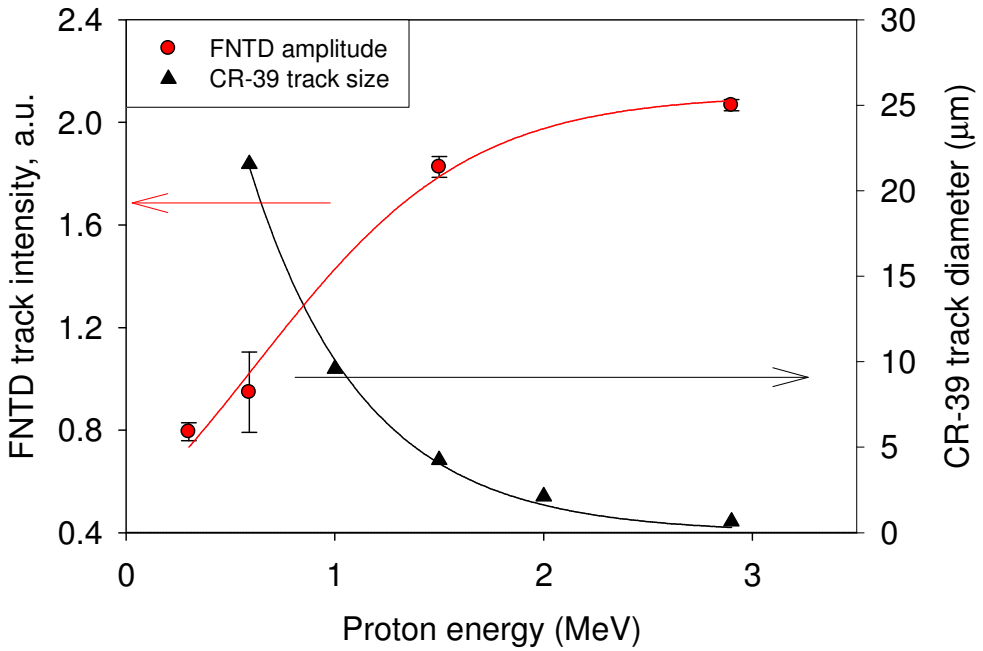

Figure 6.14 Comparison of track parameters for CR-39 (track diameter – black triangles) and FNTDs (fluorescence intensity- red circles).

FNTDs were compared to CR-39 detectors exposed in the same experiment (Fig. 6.14). The pit diameter of proton tracks decreases exponentially with proton energy. For FNTDs, the measured track diameter does not change with proton energy because the track core is on the order of a few nanometers whereas the FWHM of the point-spread function of the excitation beam is on the order of several hundred nanometers. All tracks appear to be ~1 μm in diameter for protons penetrating perpendicular to the detector surface (see *combined results* below for a more detailed discussion).

It is possible to measure the range of low energy protons in Al_2O_3:C,Mg with FNTD technology because they stop at relatively shallow depths in Al_2O_3 (see Table 6.3). The range of protons was measured by initially acquiring images at large distances apart in the axial direction to locate the vicinity in which the protons stop. Images were then acquired at 0.3 μm intervals until the majority of tracks had disappeared. Table 6.3 is a comparison of the measured range of protons to calculated values using SRIM-2006. All

values agree within 2 %. Measuring the range of protons was determined to be a more accurate form of low energy proton spectroscopy than using fluorescence amplitudes.

Table 6.3 Proton ranges for 4 energies as measured in Al_2O_3:C,Mg compared to the calculated ranges from stopping power tables of SRIM-2006 for protons irradiated at RARAF.

Energy, MeV	Measured range, μm	Calculated range, μm	% error
0.30	1.7	1.7	0
0.59	4.3	4.25	1.1
1.50	16.7	16.5	1.21
3.00	49.0	49.9	1.8

Another set of FNTDs were exposed to reaction products detailed in Table 6.2 at MIT. 200 images with dimensions of 100x100 μm^2 were acquired per FNTD to obtain enough tracks for reliable statistics. 50 different areas were scanned with 4 images per area at different depths in the detector incremented by 3.5 μm. Images at different depths were taken to average the stochastic variation of energy deposition within each individual track and to determine the range of lower energy protons. For FNTDs irradiated with protons of energy greater than 1.6 MeV, the position of every track within the first image was correlated with the coordinates of the same track on the other three images. Fluorescence intensities were averaged for tracks that matched in all four images. The FWHM of the distributions was reduced approximately by a factor of 2 using this procedure. FNTDs irradiated with low energy protons (1.00 MeV and lower) were only imaged at three different depths and in increments of 1.8 μm.

Fluorescence intensity dependence on proton energy was obtained (Fig. 6.15) to demonstrate the spectroscopic capabilities of FNTDs for protons in the energy range from 0.6 MeV to 13.8 MeV. The energy dependence of these FNTDs agrees with the proton irradiations done at the RARAF irradiation facility. The energy dependence has its

maximum at 3 MeV, dividing the dependence in two parts, low energy (~3 MeV and lower) and high energy (<3 MeV). These two parts are separable by determining the range of the protons in Al_2O_3 similar to the range measurements done for the RARAF irradiations. Track fluorescence intensity dependence on proton energy is discussed more in detail below in section 6.1.4.4

Intensity distributions were plotted as histograms (Fig. 6.16) to analyze the results and to define the spectroscopic resolution of the fluorescence intensity technique. FNTDs irradiated with 1.6 MeV and 2.27 MeV protons also show a second peak on the left side of their histograms. This second peak most likely comes from the 14.6 MeV protons of the secondary reaction (Equation 5 from Table 6.2). The peak widths are larger in comparison to the peak widths of the monoenergetic heavy ion beams obtained from HIMAC irradiations. Increased width is a likely result of the use of Mylar and aluminum to slow down the protons. Any material between the FNTD and the beam source will broaden the energy spectrum of the incident ions.

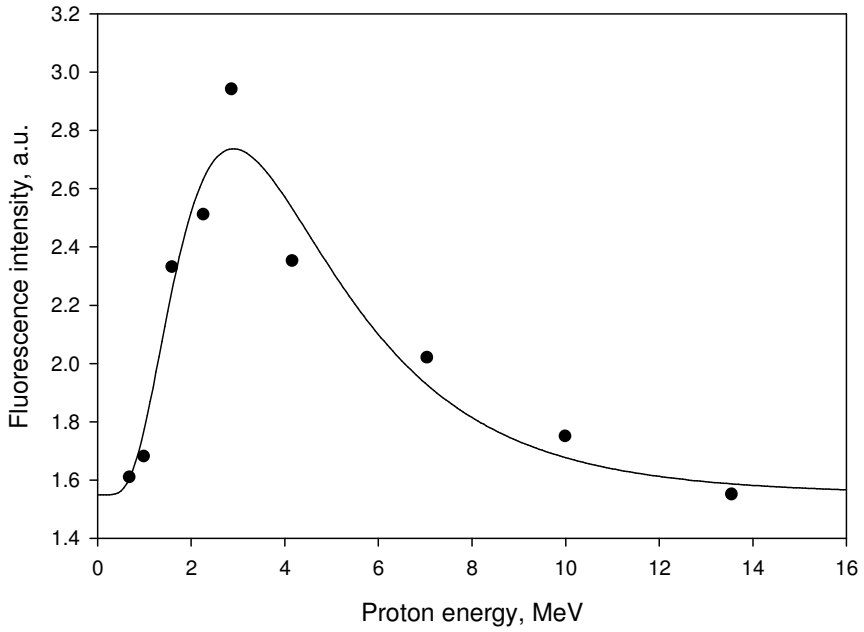

Figure 6.15 Fluorescence intensity dependence on proton energy for FNTDs irradiated at MIT.

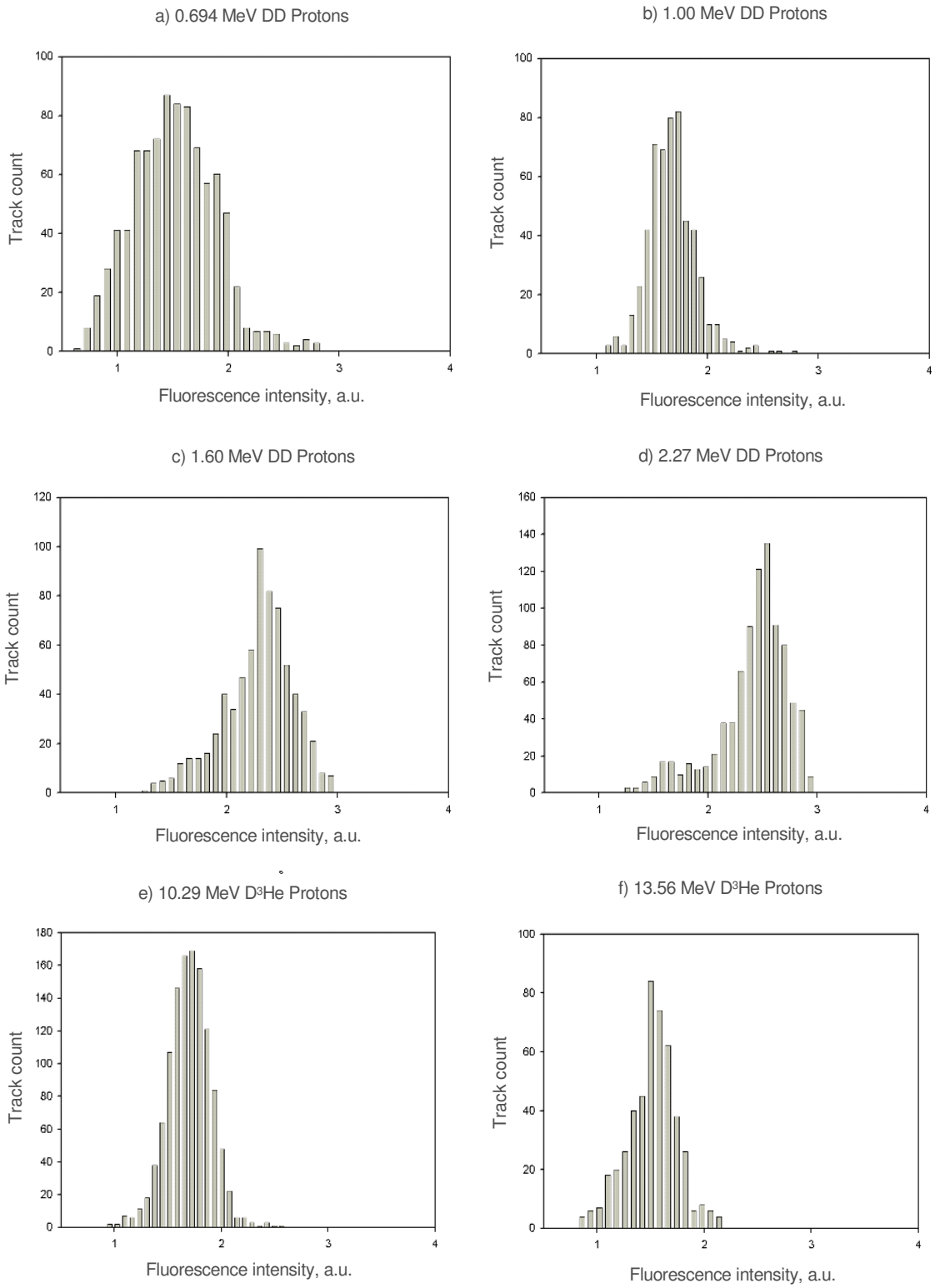

Figure 6.16 Intensity distributions for FNTDs irradiated with DD and D^3He reaction products. The distribution for the FNTD irradiated with 0.694 MeV DD protons was obtained without averaging in depth.

6.1.4.3 High energy protons

The response of FNTDs to high energy protons was characterized to determine if FNTDs could detect low LET charged particles for space and radiation therapy applications. FNTDs irradiated with high energy protons at NIRS, in Japan, were imaged and fluorescence intensities of tracks were correlated through 7 axial fields and averaged to reduce the FWHM of the histograms. Figure 6.17 shows the fluorescence intensity distributions for tracks created by high energy protons. Each peak was fit to a Gaussian function with FWHM between 9% and 12% of the mean fluorescence intensity all energies. It is possible that the widths could be further decreased by averaging more layers through a larger volume of the crystal. Figure 6.18 shows the dependence of fluorescence intensity on proton energy. The fluorescence intensity of the tracks decreases as a smooth function of energy. The most notable result is the ability of FNTDs to easily detect high energy protons with $LET_{\infty}H_2O$ below 0.5 keV/µm.

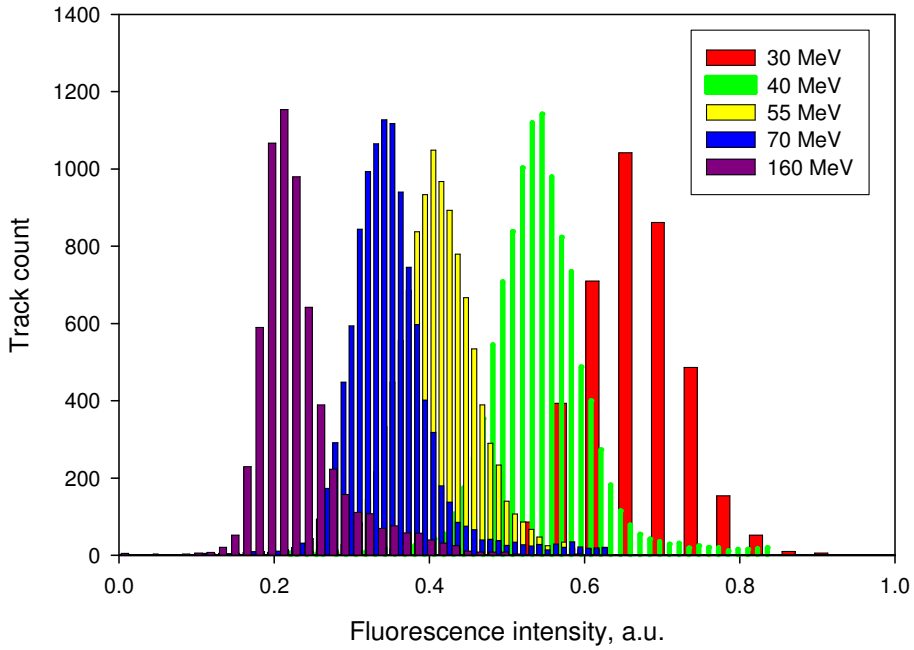

Figure 6.17 Fluorescence intensity distributions for 30, 40, 55, 70 and 160 MeV protons after averaging each track through a series of 7 depths decreasing the FWHM of the distributions by a factor of 1.5.

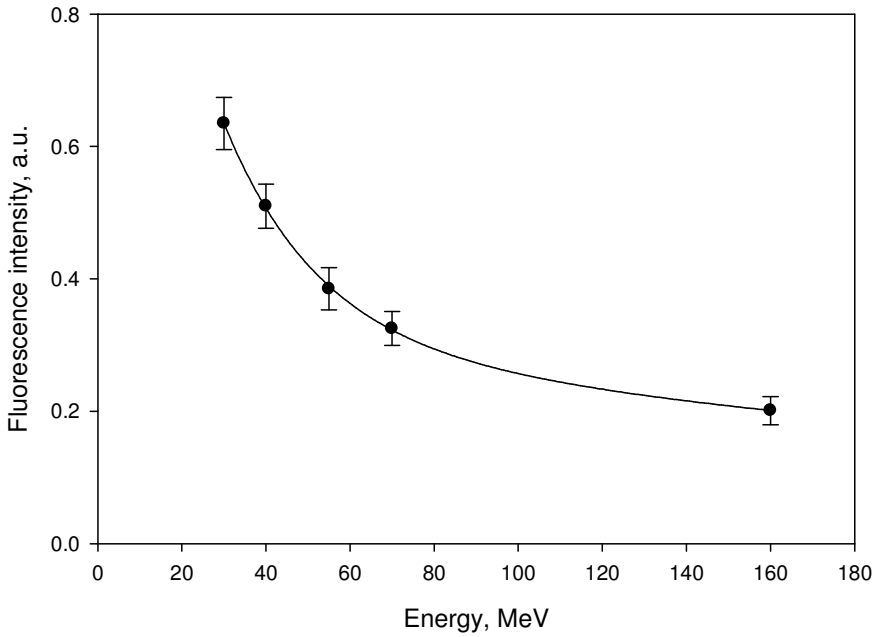

Figure 6.18 Mean fluorescence intensity dependence on incident proton energy. Irradiations were performed at NIRS.

6.1.4.4 Discussion of proton irradiations results

The general fluorescence intensity dependence on proton energy in FNTDs contains two distinct sections (Fig. 6.19 and 6.20). Tracks created by protons with energy ≥ 3MeV fit the LET dependence (Fig. 6.20) discussed in section 6.1.2 (see Fig. 6.8). The low energy region (E < 3 MeV) shows different behavior. The fluorescence intensity of low energy protons increases as a function of energy until it reaches it maximum near 3 MeV. This behavior may be common for protons that have ranges in Al_2O_3 shorter than the depth of focus (~5 μm), but protons with energies above 0.7 MeV will travel further than 5 μm in Al_2O_3.

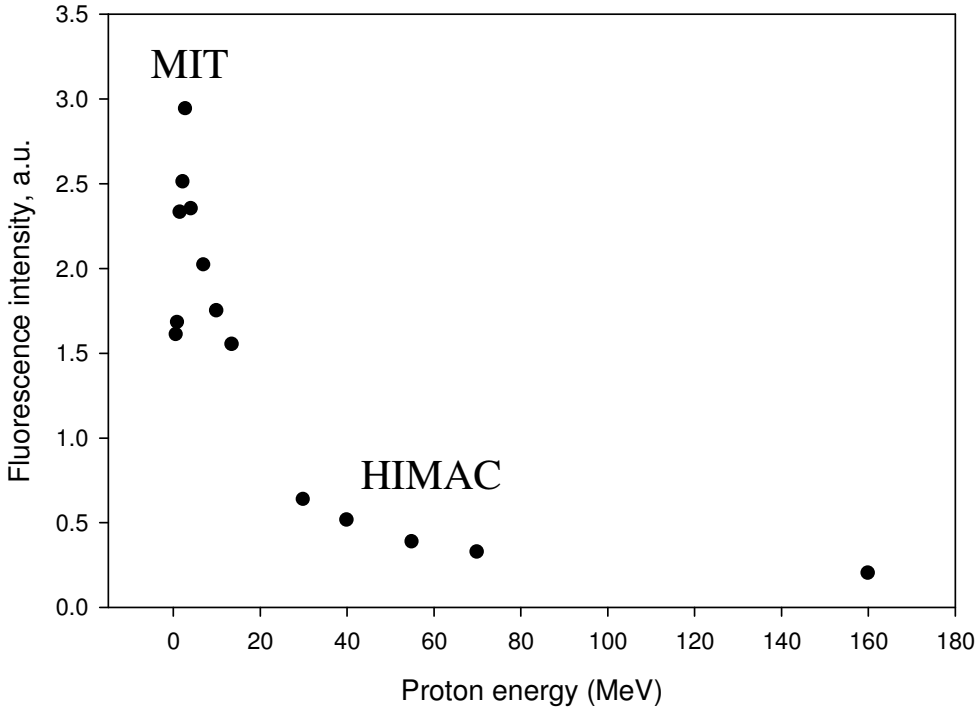

Figure 6.19 Combined fluorescence track intensity dependence on proton energy for FNTDs irradiated with protons of energy 0.5 MeV to 160 MeV.

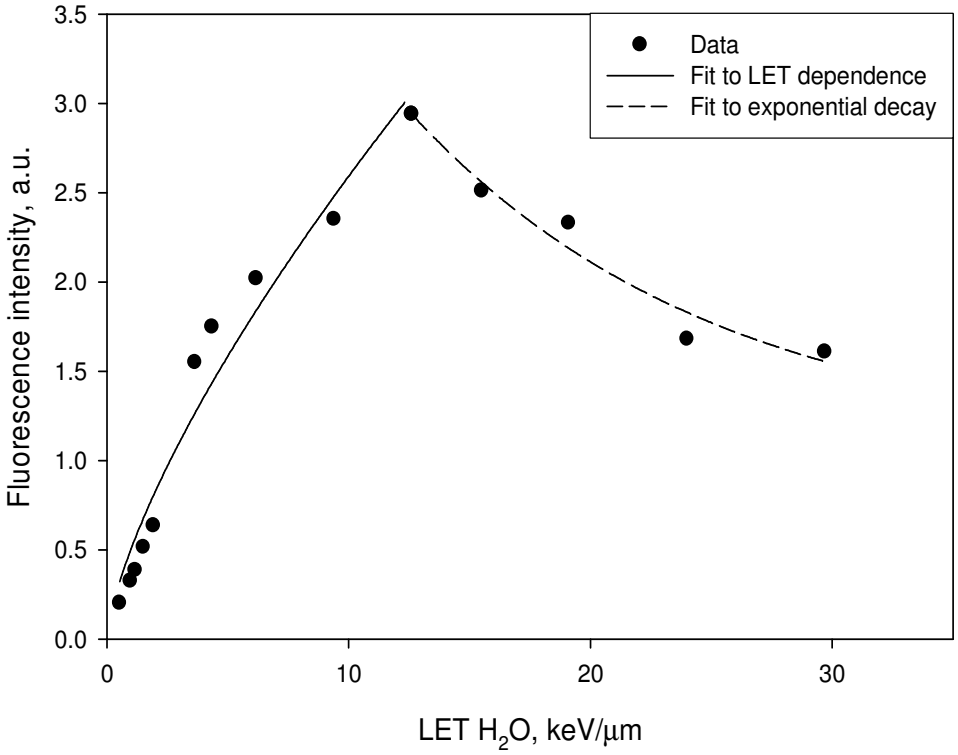

Figure 6.20 Combined fluorescence track intensity dependence on $LET_{\infty}H_2O$ for FNTDs irradiated with protons of energy 0.5 MeV to 160 MeV. Data for protons with $LET_{\infty}H_2O$ below 14 keV/µm were fit to the same functional dependence determined by HCP irradiations in section 6.1.2 (solid line).

One possible explanation for the increase in fluorescence intensity with energy is that all local F_2^{2+}(2Mg) color centers are saturated and the low energy protons impart so little energy to electrons that they do not travel sufficient distance to be captured by available F_2^{2+}(2Mg) color centers thus leaving a large number of electrons unavailable for capture. The range-energy relationship (eq. 2.28) established in section 2.5 gives a maximum electron range in Al_2O_3 of only 158 nm for a proton with energy of 2.2 MeV which means that the vast majority of delta electrons will travel less than a few nanometers. If this is indeed the case, then varying the concentration of F_2^{2+}(2Mg) color centers ought to change the energy at which the maximum fluorescence intensity on the energy dependence occurs.

The theory that F_2^{2+}(2Mg) color centers saturate is supported by data obtained by irradiating FNTDs having different concentrations of color centers with 5.11 MeV alpha particles. The maximum range for delta electrons ionized by a 5.11 MeV alpha particle in Al_2O_3 is 392 nm (again, the vast majority of delta electrons will stop within a few nanometers). Fluorescence intensity dependence on color center concentration is shown in Fig. 6.21. The data are fit to a one-site saturation curve. Fluorescence intensity increases with color center concentration until it reaches a maximum. Maximum fluorescence intensity occurs when there are enough color centers to capture available electrons.

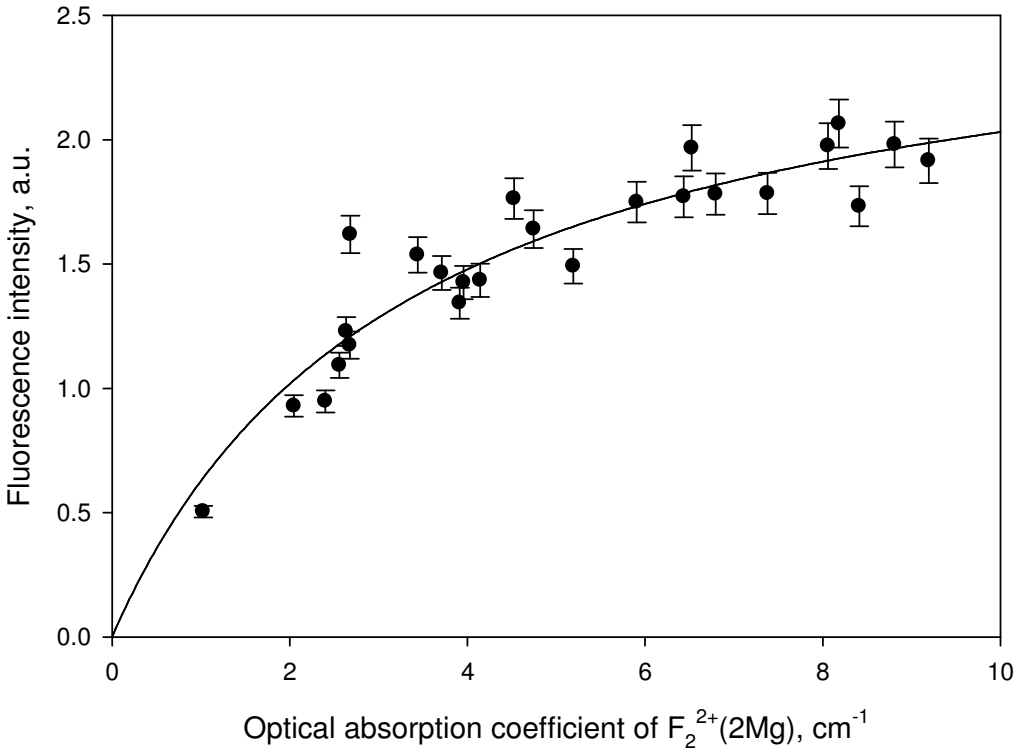

Figure 6.21 Fluorescence intensity dependence on color center concentration for FNTDs irradiated with 5.11 MeV alpha particles providing evidence that F_2^{2+}(2Mg) centers are locally saturated with low energy delta electrons. Optical absorption coefficient is a measure of the concentration of absorbing centers.

6.1.5. LET spectroscopy in inertial confinement fusion experiments

The main purpose of irradiating FNTDs with low energy protons at MIT, discussed above, was to determine if FNTDs would work for spectroscopy of heavy charged particles produced during inertial confinement fusion (ICF) experiments. To test this, FNTDs covered with a thin Mylar foil (used to stop primary 0.8 MeV ^{3}He ions) were irradiated with multiple charged particles produced by the primary reactions described in Table 6.2.

The histogram for FNTDs irradiated with 2.87 MeV protons, 0.405 MeV tritons and 2.59 MeV alpha particles shows that three peaks can be deconvolved (Fig. 6.22). The small peak on the left (peak 1) corresponds to the 14.6 MeV protons created by the D^{3}He

reaction (secondary protons), the middle peak (peak 2) corresponds to 2.59 MeV alpha particles also created by the secondary D^3He reaction and the large peak on the right (peak 3) corresponds to the 2.87 MeV protons (primary protons). The ratio of the number of 2.87 MeV proton tracks to the number of alpha tracks is the same ratio as measured by the surface barrier detector used during the irradiation which is 10:1. The number of alpha particles and secondary protons were approximately the same as measured on the surface barrier detector. Tritons are visible on the first image near the surface, but are stopped in Al_2O_3 at a shallower depth than the second imaging plane. It is possible to count the number of tritons by determining the range of the particles.

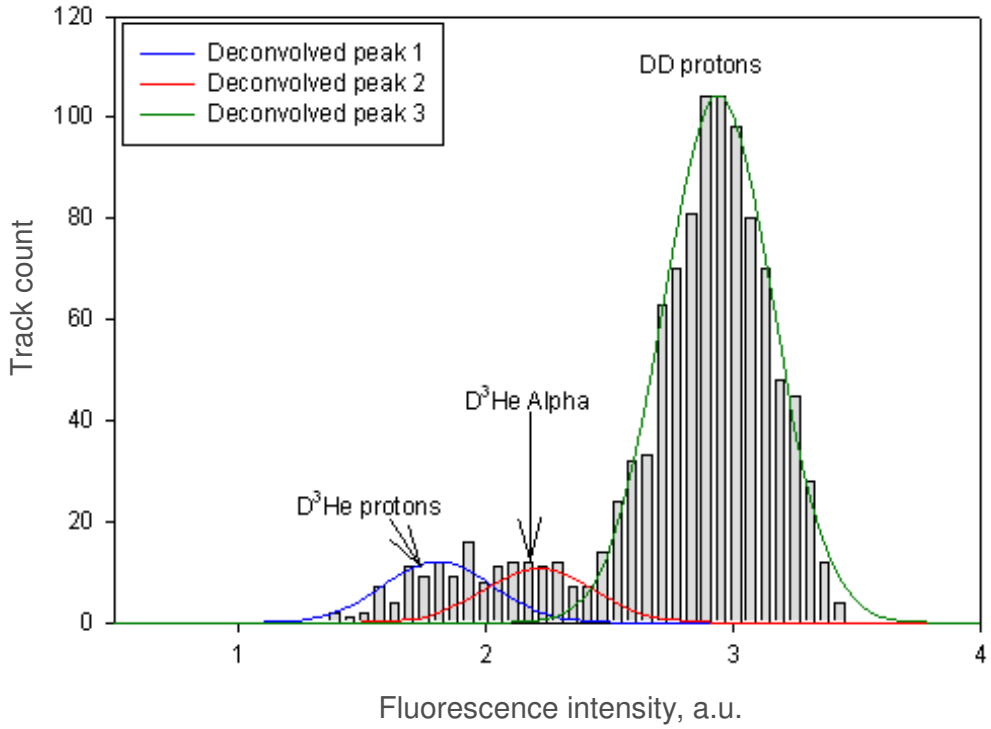

Figure 6.22 . Deconvolution of the distribution of detector 74-561 irradiated with 2.87 MeV DD protons, 2.59 MeV D^3He alphas, 14.6 MeV D^3He protons and 0.405 MeV tritons.

This initial study demonstrated that FNTDs can be used as a spectroscopic tool for ions resulting in DD and D^3He reactions that commonly occur in ICF experiments.

Combining track range and fluorescence intensity data will provide accurate results. The major problem with using FNTDs in ICF is that there are high fluences of x-rays generated during the reactions. Typical x-ray spectra during implosion of the CH sphere were provided by MIT and the total x-ray dose estimated at the detector was calculated to be approximately 2185 Gy. 25 μm thick Ta foil would reduce the x-ray dose to 0.022 mGy, which would have minimal effect on the FNTD. FNTDs would only be able to measure protons with energies greater than 3 MeV because lower energy protons will be absorbed in the Ta. In order to avoid the x-ray problem completely, FNTDs can be used in place of CR-39 in a magnet spectrometer (Seguin et al, 2003).

6.2 Quality assurance in proton therapy beams

Quality assurance (QA) of proton therapy beams is required for all treatment facilities. Precise calculations and measurements are required to ensure the correct dose delivery to the volume of the tumor and minimize dose to other parts of the body. Ionization chamber measurements are currently used as a "golden standard" to verify the accuracy of Monte Carlo simulations. Ionization chambers, however, provide only data to calculate air kerma and do not provide information on LET or lineal energy. Due to the relatively low LET of high energy protons, the radiation weighting factor used for proton therapy is 1.1 when compared to photon dose (Attix, 1986). The problem is that the biological effect in the Bragg peak is larger due to increasing LET of the proton at the end of its range. FNTDs may be a potential candidate for QA of proton fields within the

pristine and spread out Bragg peaks because of their strong LET response which is why FNTDs were investigated as possible QA detectors.

6.2.1 Experimental methods

The response of FNTDs to protons with energies suitable for radiotherapy was tested for quality control of radiotherapy beams at the MD Anderson Cancer Center in Houston. FNTDs were irradiated alongside OSL detectors with protons in the energy range of 100 to 250 MeV. Irradiations are listed in Table 6.4. FNTDs were cut and polished in the form of 4 x 6 mm^2 plates to study the response of FNTDs to 100, 160, 200 and 250 MeV protons propagating perpendicular to the surface of the crystal.

FNTDs were irradiated with approximately 100 mGy of high energy protons corresponding to large fluences (~1×10^8 cm^{-2}). At these doses, tracks overlap making it impossible to extract data from individual tracks (Fig. 6.23). Image processing using spatial frequency analysis (see sections 4.3 and 5.4) was performed. 50 images were acquired for each detector and the image powers were averaged. Image power was shown to be linearly dependent on absorbed dose for both gamma and neutron radiations in chapter 5.

Table 6.4 Details of high energy proton irradiations performed at MD Anderson Cancer center. Depth is the thickness of the solid water phantom at which the detectors were placed.

Energy (MeV)	Depth (cm)	MU/Dose
100	0.0	13.06
	4.0	13.06
	4.6	13.06
	4.1	13.06
	4.2	13.06
	4.3	13.06
160	0.0	14.39
	11.6	14.39
	12.5	14.39
	12.7	14.39
	13.0	14.39
	13.6	14.39
200	0.0	15.9
	18.0	15.9
	18.5	15.9
	18.7	15.9
	19.0	15.9
	20.0	15.9
250	0.0	15.3
	27.5	15.3
	27.8	15.3
	28.2	15.3
	28.5	15.3
	30.0	15.3
^{60}Co	-	100 mGy

6.2.2 Results and discussion

Figure 6.23 shows images from FNTDs irradiated with 160 MeV protons at every position in the water phantom. The fluorescence intensity of tracks increases along the Bragg curve (images b-e) as demonstrated in section 6.1.2. Target fragments are seen after the Bragg peak (image f). Figure 6.24 compares the image powers of FNTDs to results obtained with OSL detectors, ionization chamber measurements, TRIM (Zieglar and Biersack, 2006) simulations and Monte Carlo calculations (performed by Dr. Gabriel

Sawakuchi). The data are normalized to the entrance values for each detection and simulation method.

Figure 6.24 shows good agreement between ionization chamber and OSL data while the power spectrum analysis of FNTDs yielded a response in the Bragg peak approximately two times larger than the ionization chamber and OSL. TRIM and Monte Carlo simulations are seen to be in better agreement with FNTD results. The efficiency of Al_2O_3:C OSL detectors has been seen to decrease as LET of the incident particle increases due to saturation of the signal in the track (Sawakuchi et al, 2008). Fluorescence intensity (and therefore image power) of charged particle tracks continuously increases as the LET of charged particles increases (see section 6.1) explaining the difference between OSL and FNTD results. Assuming the simulations are correct, it would appear that the ionization chamber exhibit under-response similar to OSL detectors. Agreement between simulations and FNTD data suggests that FNTDs are good candidates for QA of protons therapy beams.

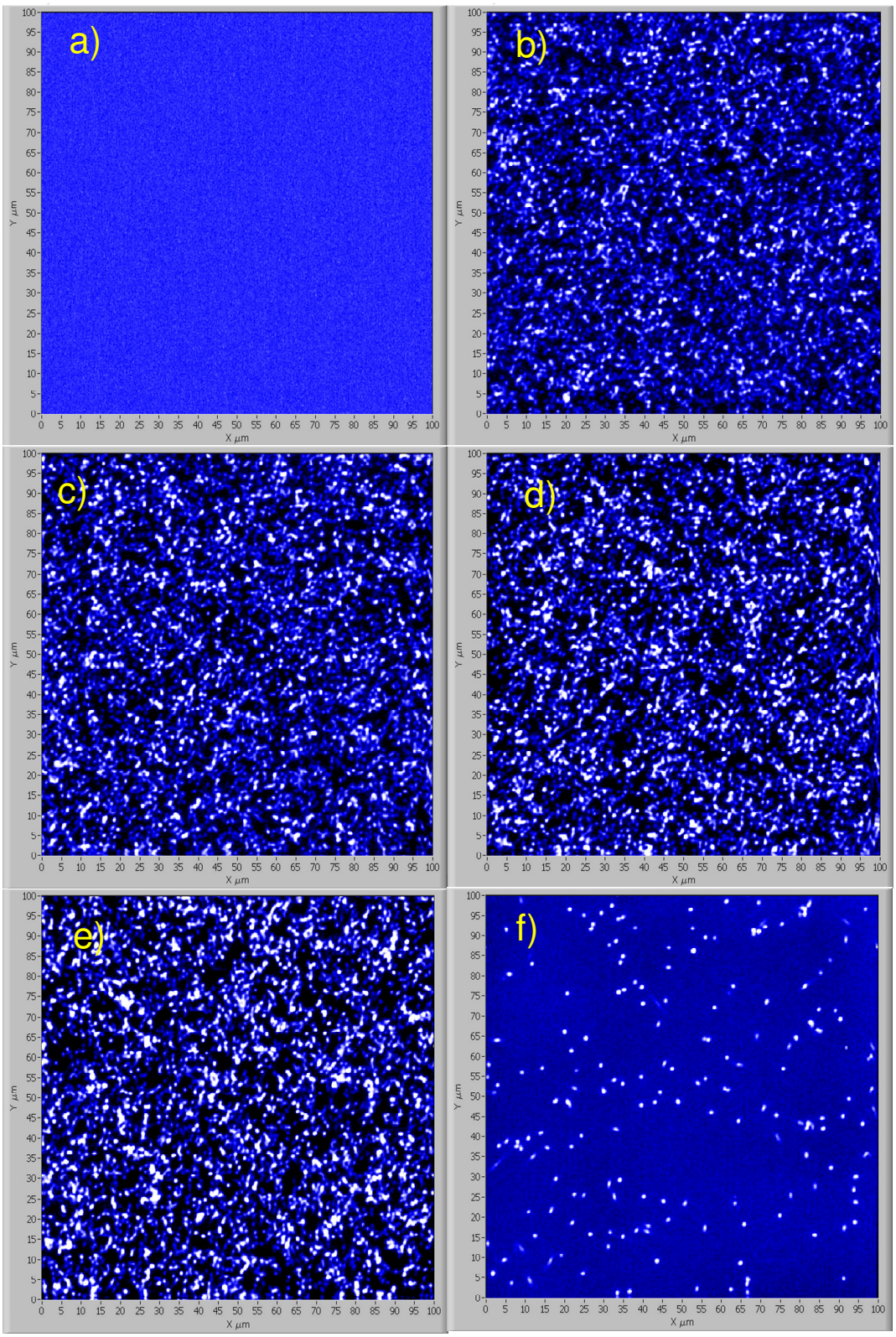

Figure 6.23 Images of FNTDs irradiated with 160 MeV protons; a) is an unirradiated control, b) is at 11.6 cm, c) 12.5 cm, d) 12.7 cm, e)13.0 cm and f) 13.6 cm (beyond the Bragg peak) depth in a solid water phantom.

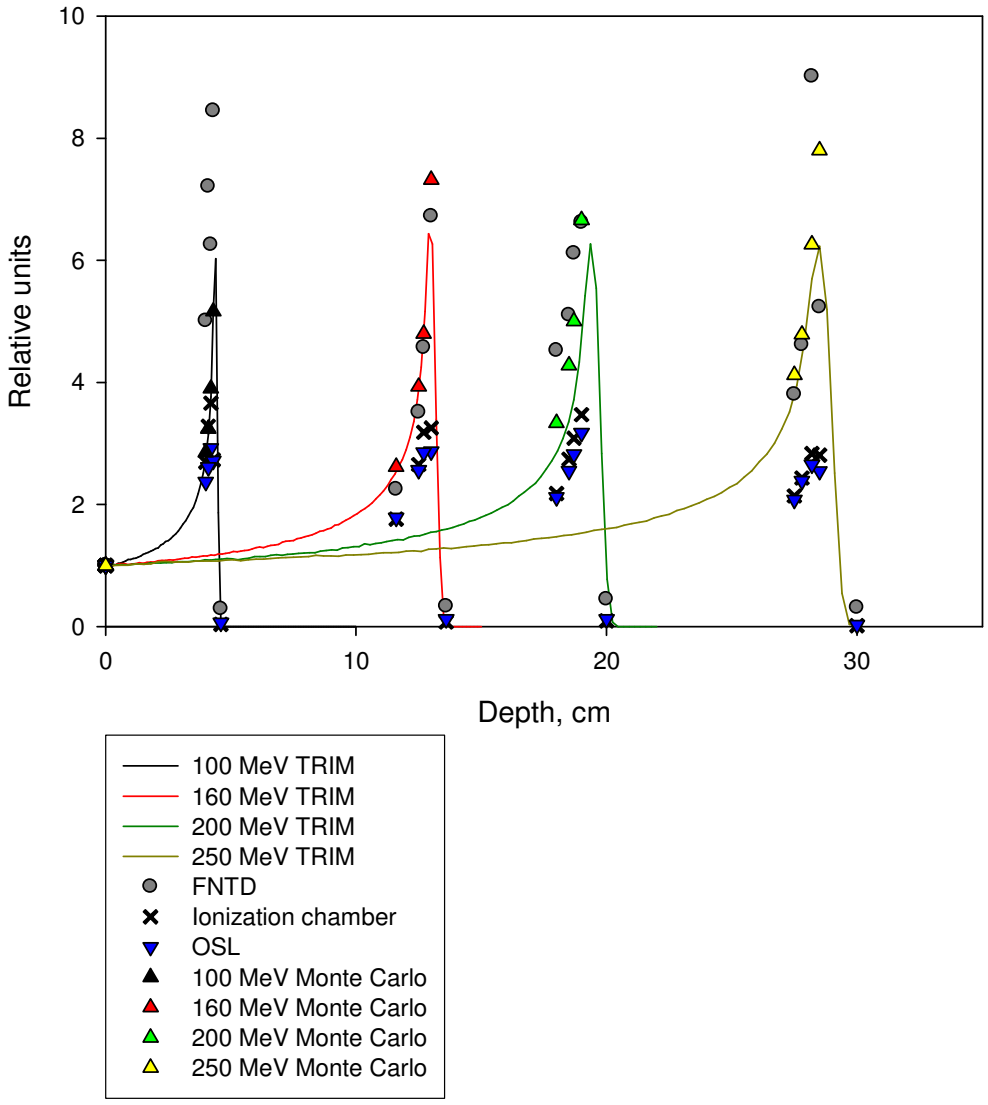

Figure 6.24 FNTD responses as a function of depth in a solid water phantom for high energy protons irradiated at MD Anderson Cancer Center compared to TRIM energy deposition simulations, Monte Carlo calculations (courtesy of Dr. Gabrielle Sawakuchi), ionization chamber and OSL measurements. All data were normalized to the entrance value (i.e. FNTD results were normalized to the image power obtained on detectors irradiated on the entrance surface of the solid water phantom).

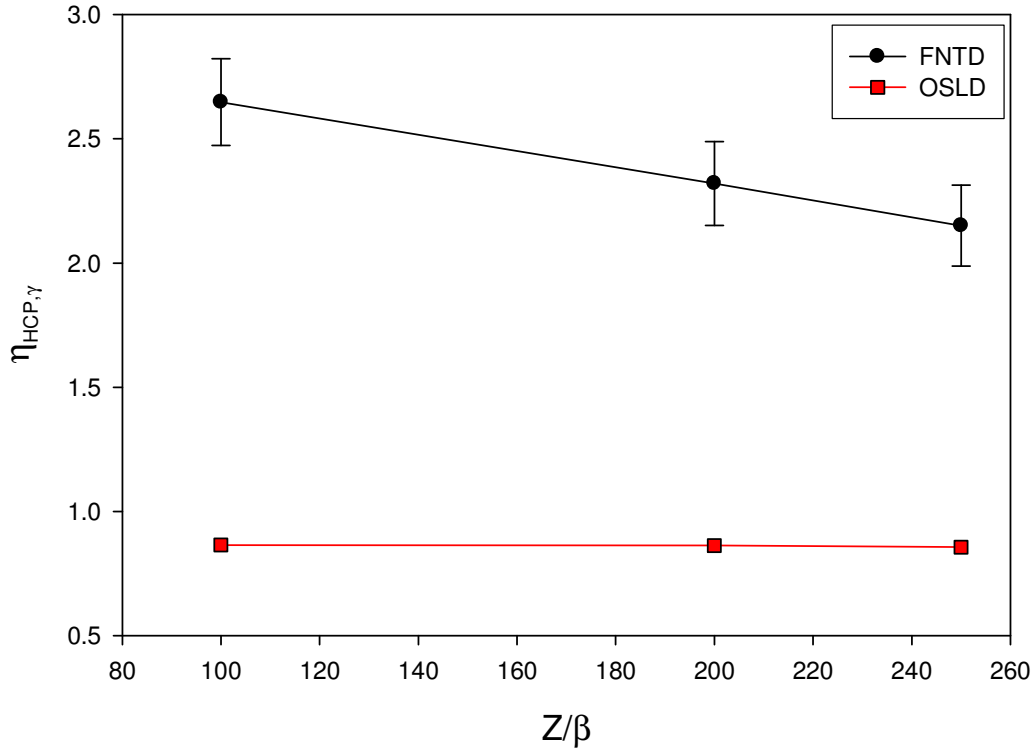

Figure 6.25 Relative efficiency of FNTDs and OSL detectors for protons irradiated at the entrance surface of the solid water phantom relative to ^{60}Co gamma as a function of proton energy.

FNTDs and OSL detectors irradiated with ^{60}Co gamma photons were measured and compared with the proton irradiated detectors. Figure 6.25 shows the relative efficiencies for FNTDs and OSL detectors as functions of proton energy. Relative efficiency for HCPs, η_{HCP}, is defined as

$$\eta_{HCP,\gamma} = \frac{\left(\frac{S_{HCP}}{D_{HCP}}\right)}{\left(\frac{S_{\gamma}}{D_{\gamma}}\right)} \tag{6.3}$$

where, S_{HCP}, is the signal per unit dose of HCPs, D_{HCP}, S_{γ} is the signal per unit reference dose, D_{γ}, (in this situation the reference is ^{60}Co gamma). The relative efficiencies for OSL detectors measured during this study are comparable to those obtained by

Sawakuchi et al (2008). The relative efficiencies for FNTDs are greater than two and increase as proton energy decreases which opposes the typical OSL response.

The purpose of this investigation was to determine if FNTDs could be used for QA in proton therapy. At this stage of the research it is difficult to say with certainty where FNTDs will be most helpful, but comparison with simulations would suggest that FNTDs provide good estimations of LET. Perhaps FNTDs can provide estimates of LET (and thus quality factor) to supplement ionization chamber measurements.

6.3 FNTDs for beta dosimetry

Beta particles generated during the decay of ^{85}Kr (687 keV maximum and average of 251 keV) and ^{90}Sr/^{90}Y (2.27 MeV maximum and 550 keV average) have similar energy distribution of secondary electrons to gamma radiation. The difference in the gamma and beta irradiations is that gamma generates secondary electrons throughout the entire crystal volume whereas the beta particles of lower energies penetrate less into the crystal. The question is whether or not the fluorescence images due to the overlapping of many beta tracks produce results similar to gamma induced signal near the surface of the detector.

To compare the response of FNTDs to beta and gamma, the detectors were irradiated at Landauer Inc. with beta particles from ^{85}Kr and ^{90}Sr/^{90}Y isotopes with 3 and 10 cSv doses delivered in terms of surface dose equivalent Hp(0.07). Bare FNTDs were also irradiated at Oklahoma State University with beta from a ^{90}Sr/^{90}Y source with doses in the range of 48 μSv to 1.6 cSv. The detectors were scanned at a depth of 3.5 μm and

processed using spatial frequency analysis. Images from beta irradiated detectors have the same appearance as images from detectors irradiated with photons (Fig. 6.267) and exhibited similar dose response characteristics. Figure 6.27 shows the image power dependence on dose equivalent for FNTDs irradiated with beta and gamma. FNTD response to beta and gamma are nearly identical. The lowest detectible dose using spatial frequency analysis is 480 µSv.

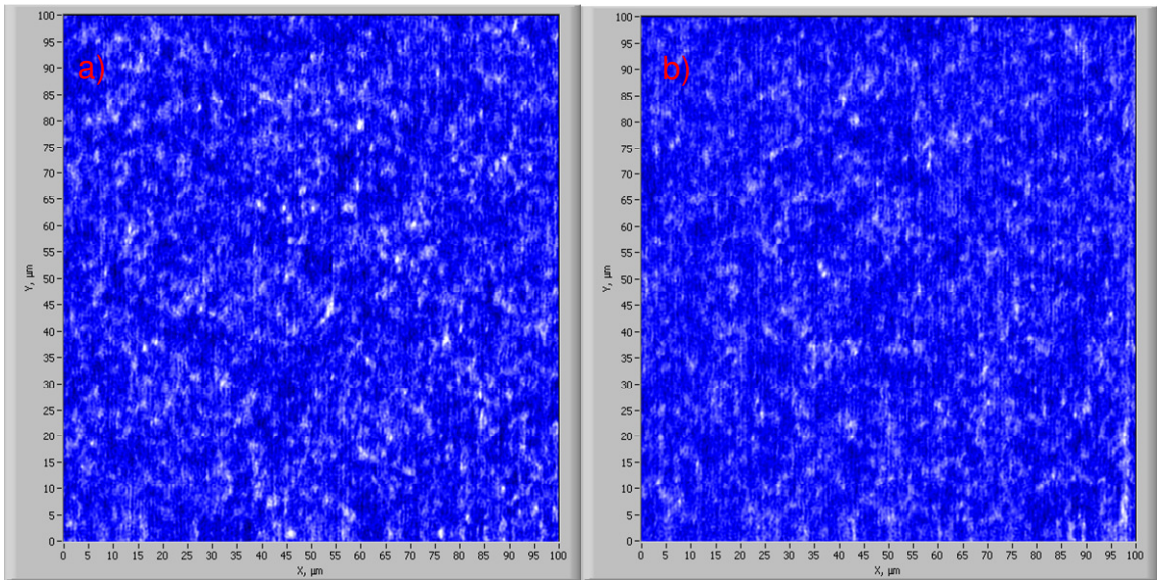

Figure 6.26 Images of FNTDs irradiated with a) beta from the decay of $^{90}Sr/^{90}Y$ and b) gamma from ^{137}Cs.

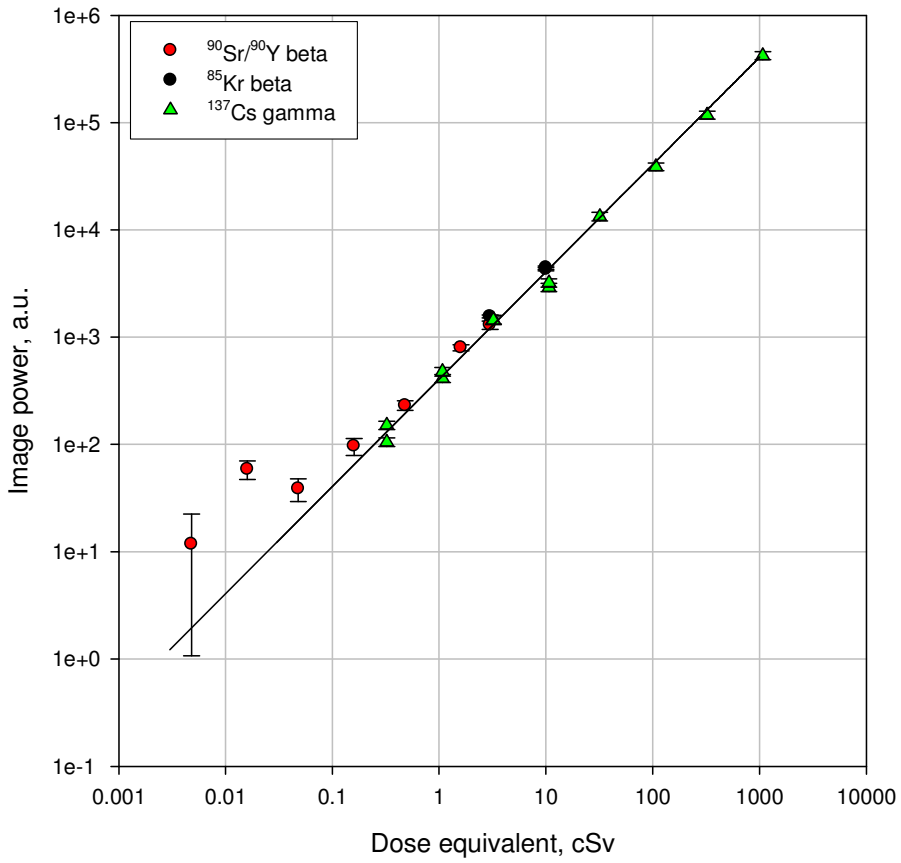

Figure 6.27 Dose dependences from irradiations with from $^{90}Sr/^{90}Y$ and ^{85}Kr beta and ^{137}Cs gamma for bare FNTDs.

6.4 X-ray microbeam diagnostics

Microbeam radiation therapy (MRT), utilizing high intensity synchrotron radiation, is currently in a pre-clinical phase and is being studied specifically for the treatment of brain tumors in infants (Brauer-Krisch et al, 2005 and 2009). In MRT, the tumor is irradiated with unusually high doses of x-rays (several hundred Gy) in a short amount of time but in highly localized "slices" (sheets of x-rays with full-width at half-maximum from 25 µm to 100 µm and spaced 100 µm to 400 µm center to center) providing what is called spatial fractionation (Brauer-Krisch et al, 2009). The principle

of MRT is that normal brain tissue, particularly in developing systems (i.e. children), has high tolerance to radiation delivered in small volumes due to regeneration of damaged cells and blood vessels. Therefore, peak doses of several hundred Gy can be delivered to the tumor and surrounding healthy tissue with no permanent damage to healthy tissue as long as the valley doses remain below a threshold determined by a number of parameters (Brauer-Krisch et al, 2005) that will not be discussed here. It is therefore essential to be able to accurately determine the dose in the valley of the microbeam, or more importantly, the peak-to-valley dose ratio.

The peak-to-valley dose gradient should be very steep so that high spatial resolution is needed to accurately determine doses. FNTDs provide radiation field imaging with extremely high spatial resolution down to 600 nm and positioning down to 100 nm. FNTDs are investigated here as a possible solution to determining peak-to-valley dose ratio and also determining precisely the dose gradient in the microbeam.

6.4.1 Irradiations

FNTDs were exposed to homogeneous and microbeam radiation at the European Synchrotron Radiation Facility (ESRF) to test the ability of FNTDs to image x-ray microbeams. Table 6.5 lists the irradiation details. The detectors were irradiated on a 5 x 5 x 5 cm^3 PMMA phantom. Images of 200 x 200 μm^2 with a resolution of 1024 x 1024 pixels were processed to obtain average fluorescence intensity and fluorescence intensity corresponding to both peak and valley doses. The FWHM for several microbeams was estimated from the image intensity profiles.

Table 6.5 List of irradiations performed at ESRF for calibrations and microbeam exposures.

Irradiation Type	Dose Delivered
Homogeneous	2 Gy
	5 Gy
	10 Gy
	30 Gy
Microbeam	2 Gy
	5 Gy
	25 Gy
	50Gy
	400 Gy
	600 Gy

6.4.2 Results and discussion

All FNTDs used in this study had background fluorescence that was not radiation induced and was subtracted from the total signal in order to process only the signal caused by irradiation of the crystal. Figure 6.28 shows the dose dependence of the radiation induced fluorescence signal. Fluorescence intensity has a sub-linear dependence on the delivered dose consistent with previous photon irradiations (section 5.2.2). These results also agree with the results of radiochromic transformations discussed in chapter 3.

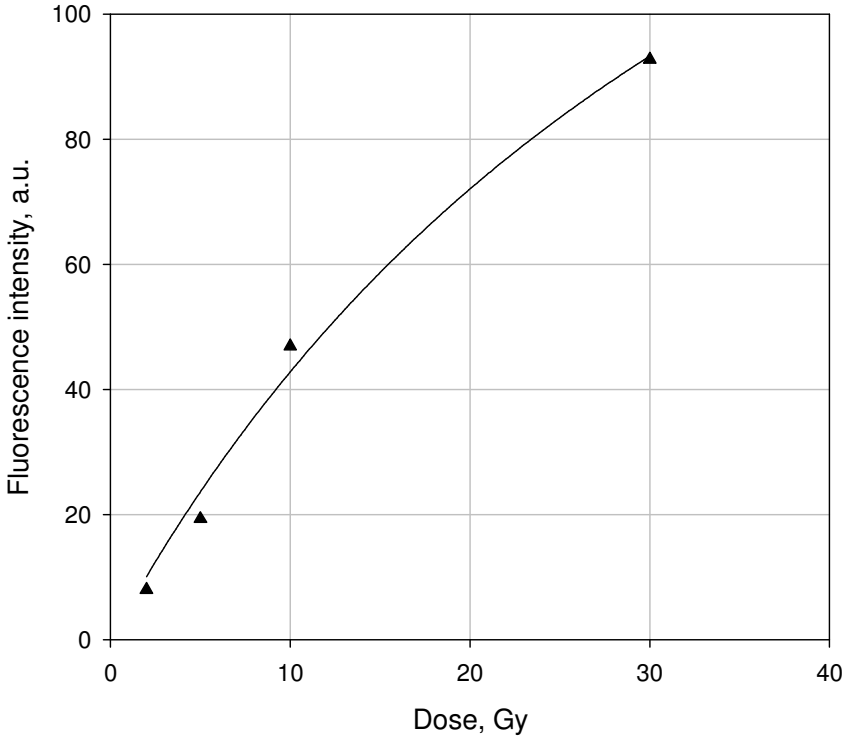

Figure 6.28 Mean fluorescence intensity dependence on dose for homogeneous synchrotron x-rays.

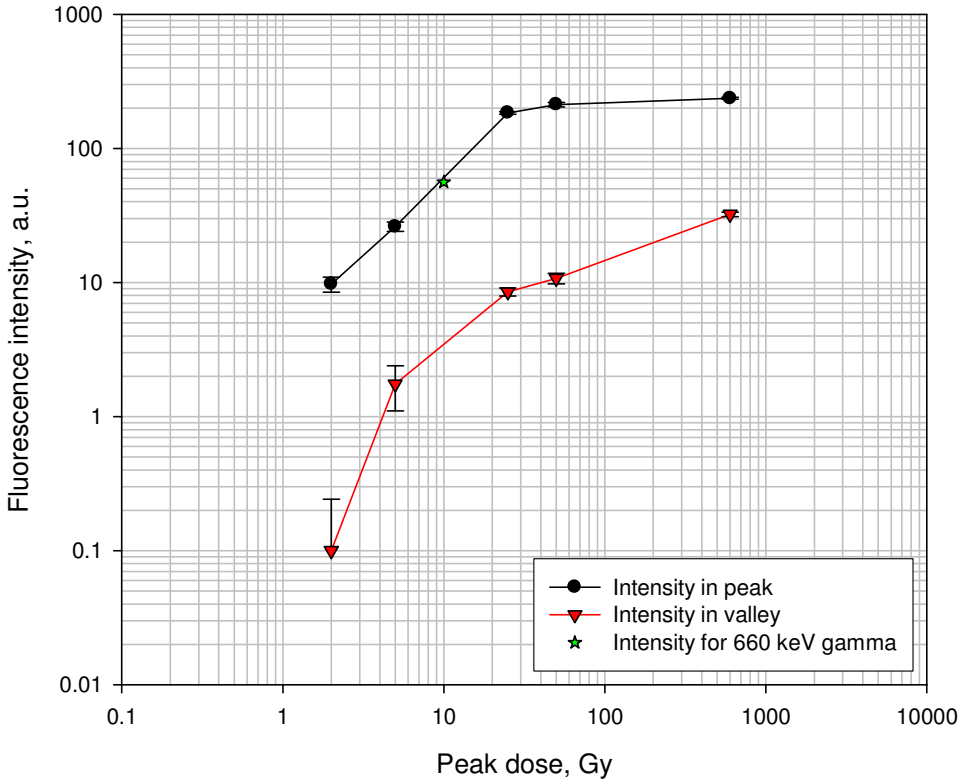

Figure 6.29 Dose dependence of average fluorescence intensity in the peak and valley positions for all microbeam irradiated FNTDs.

The samples irradiated with the modulated microbeam at ESRF were imaged with a field size of 200×200 μm^2. Fluorescence intensities in the peaks and valleys are plotted as a function of peak dose in Fig. 6.29. The dynamic range of FNTDs did not allow for the measurement of both peak and valley doses from the same detector with high accuracy. Valley doses were estimated from the detectors subjected to high dose irradiations of 400 and 600 Gy, whereas peak doses were obtained from the samples irradiated to 2, 5, 25 and 50 Gy. The fluorescence signal at the peak position in the detector irradiated to 400 and 600 Gy was saturated as seen in Fig. 6.30. The ratio of fluorescence signal between peak and valley is approximately 10 for both 25 and 50 Gy exposures. A ratio of 10:1 in signal corresponded to a peak to valley dose ratio of approximately 20 (from the calibration dose dependence). Valley fluorescence signal was not distinguishable from the background for the peak dose of 2 Gy, but there was a small amount of valley signal seen from the 5 Gy dose suggesting that the crystal used for these irradiations is sensitive down to around 0.25 Gy assuming that there is about 1/20 of peak dose delivered in the valley. Uncertainty and variation of the background fluorescence signal increases the uncertainty of the valley dose for small doses of radiation.

More fluorescence signal was measured in the valley of the sample irradiated with 400 Gy than that of the sample irradiated with 600 Gy. The sheets of microbeams produced during the 400 Gy irradiation were only 200 μm apart whereas the beams for the 600 Gy irradiation were 400 μm apart. The beam separation should have a direct effect on the dose delivered in the valley because the shape of the microbeam profile causes more overlap as the sheets of radiation are moved closer together.

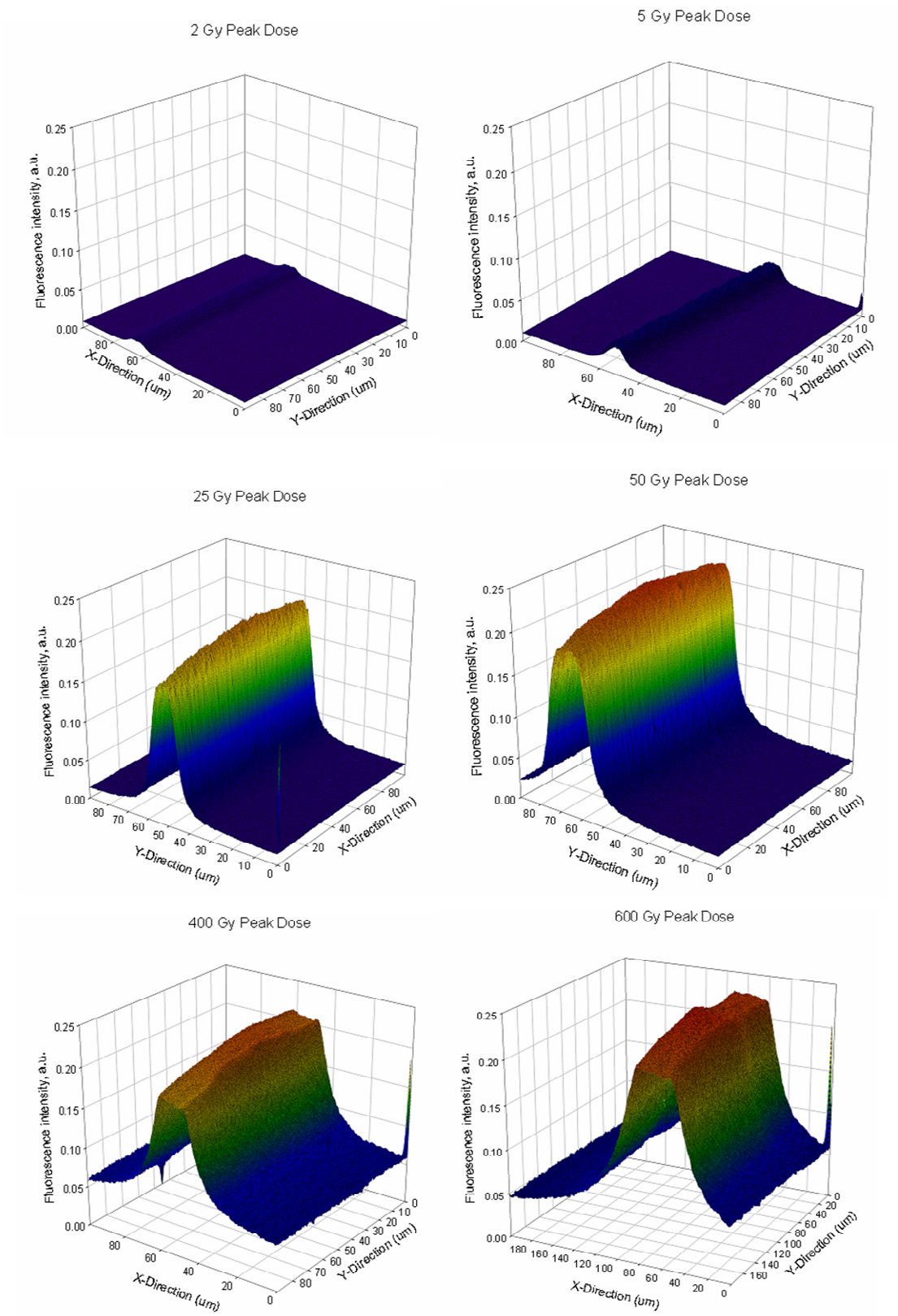

Figure 6.30 Three-dimensional intensity profiles of FNTDs irradiated with synchrotron microbeam radiation. The doses are labeled above each profile. Partial saturation has already occurred at 50 Gy peak dose.

The FWHM of the microbeam for peak doses of 2, 5 and 25 Gy was found to be 27.0, 26.1 and 25.6 μm respectively agreeing with the reported FWHM of 26 μm. For the two higher doses (400and 600 Gy) FWHM can not be correctly estimated because of the saturation of the fluorescence signal at the peak position. The images of the microbeams produce steep fluorescence gradients. At high doses, (above the saturation level) the peak is a flat-top profile. Figure 6.31 shows the profiles of microbeam irradiations for all six peak doses.

High resolution imaging of microbeam radiation allowed for precise determination of the FWHM and center to center distances of the microbeam radiation. Accurate dose profiles can be obtained with relatively low peak dose below 100 Gy. The low limit of detection was around 0.25 Gy because FNTDs that were manufactured and irradiated before the optimization process described in chapter 3 were used for these irradiations. New FNTDs with better uniformity and sensitivity are currently being irradiated at ESRF with more microbeam x-rays. The new spatial frequency analysis (image power) technique was suggested and should be able to provide more accurate peak to valley dose measurements by calculating the modulation transfer function.

Most treatment plans require doses larger than 100 Gy which FNTDs cannot currently measure, but QA for peak-to-valley dose ratio can be determined at doses below the saturation level of FNTDs. FNTD technology has shown promise for application in microbeam imaging making it worth further investigations.

6.5 Neutron microbeam imaging

One of the most recent research topics in radiobiology is utilization of neutron microbeams with a spot size of 10-15 μm in diameter. Neutron microbeams are realized by hitting a thin gold target with a focused proton beam generating neutrons. The neutrons have a maximum energry of 60 keV but the majority are between 20 and 40 keV (Marino, 2009). In the current state of the technology, only wide beams of neutrons are possible.

FNTDs were used to image neutron beams "focused" to a point approximately 1 mm in diameter at RARAF. Water soluble lithium carbonate ($^6Li_2CO_3$) was used as a converter. Powdered $^6Li_2CO_3$ was dissolved in water with concentrations of 0.004 g/ml. The solution was then applied to the polished surface of the FNTD. The FNTD was heated to 80°C on a hotplate to aid in dissociation of the $^6Li_2CO_3$ from the water. Several drops of solution were applied and dried to create a film of $^6Li_2CO_3$ that varied in thickness from 5 μm to 50 μm.

FNTDs were covered with either 1 mm thick enriched ^6LiF or 5-25 μm thick layers of enriched $^6Li_2CO_3$ and irradiated with neutrons. The entire FNTD was imaged and track density was determined for multiple 100 x 100 μm^2 images. Track densities were mapped to the position on the FNTD. The mapping procedure is essentially imaging of the neutron field. Figure 6.31 shows the track densities for an FNTD covered with 1 mm thick ^6LiF chip and irradiated with the neutron microbeam for 3 hours. The current

resolution of the neutron field imaging is 100 µm, but resolution down to 1 µm is achievable by analyzing smaller areas in the images.

The diameter of the central spot was measured to be 1.5 mm with significant scatter occurring up to 0.5 mm beyond that. Tracks were observed throughout the entire crystal which is most likely the result of scattered neutrons. Only a few tracks were observed on FNTDs covered with ^{6}LiF and $^{6}Li_2CO_3$ that were irradiated for a shorter period of time (40 minutes or less).

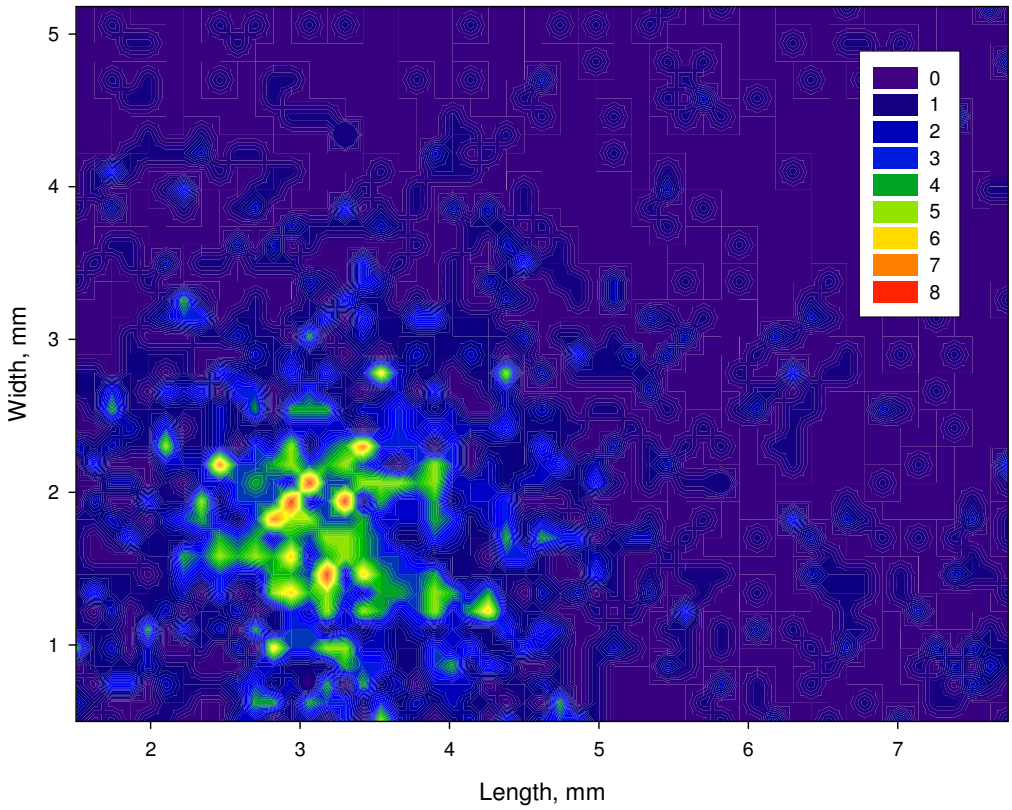

Figure 6.31 Image of a neutron microbeam field incident on an FNTD covered with 1 mm of enriched ^{6}LiF.

6.6 Microdosimetry

6.6.1 Lineal energy

Fluorescent nuclear track detector technology combines luminescent Al_2O_3:C,Mg with laser scanning confocal microscopy to image radiation induced ionizations with diffraction limited optical resolution. High resolution imaging provides microscopic information on energy deposition events on less than a micrometer scale. It is hypothesized that FNTD data are inherently microdosimetric.

Three-dimensional imaging capabilities allow for analysis of individual tracks in a spherical site with a 1 μm diameter. Assuming the energy deposited in the spherical site can be calculated based on the parameters obtained through image analysis, the lineal energy can be calculated using the length of the track segment in the spherical site ($y = \varepsilon/l$). A proposed method of calculating the energy deposited in a volume of interest is by measuring the fluorescence intensity at all points in the sphere.

It is assumed that the fluorescence intensity is directly proportional to the number of radiochromically transformed F_2^+ (2Mg) color centers which is the number of electrons captured by F_2^{2+}(2Mg) color centers after irradiation. The energy needed to create one electron-hole (e-h) pair (W) in semiconductors and dielectrics is estimated to be equal to two energy gaps, so for Al_2O_3, W is approximately 20 eV. The energy deposited resulting in ionizations can be calculated by multiplying the number of e-h pairs by the energy required to produce one pair. In other words, the energy imparted in the crystal can be calculated by

$$\varepsilon = N_{e-h} W \tag{6.4}$$

where $N_{e\text{-}h}$ is the number of electron-hole pairs generated. Let A be the fluorescence intensity at a point in the site and k be a proportionality constant, then

$$N_{e-h} = \frac{n}{\sigma_n} = \frac{A}{k\sigma_n} \tag{6.5}$$

where n is the density of F_2^{2+}(2Mg) color centers and σ_n is the fraction of electrons generated that get trapped in the F_2^{2+}(2Mg) color centers, i.e. the electron capture cross section for F_2^{2+}(2Mg) color centers (this can be thought of as an analog to charge collection efficiency in proportional counters). Therefore, the energy imparted is

$$\varepsilon = \frac{A}{k\sigma_n} W. \tag{6.6}$$

The proportionality constant will need to be determined by calibrating the FNTD and data acquisition system. The lineal energy is then

$$y = \frac{A}{lk\sigma_n} W \tag{6.7}$$

It would generally be assumed that the number of radiochromically transformed color centers is proportional to the amount of energy deposited (a constant electron capture cross section), however fluorescence intensity was observed to change non-linearly with LET and dose (sections 3.3, 5.7.2 and 6.1). Non-linearity of fluorescence intensity must therefore be considered. Empirical studies have shown that the fluorescence intensity of charged particle tracks in FNTDs varies as $\sqrt{\varepsilon}$, where ε is the deposited energy resulting in ionizations (taken from fitting the photon dose dependence and LET dependence). Therefore the amount of energy deposited is determined empirically by considering its relationship to the fluorescence intensity, i.e.

$$A = s\sqrt{\varepsilon}, \tag{6.8}$$

where the constant, *s,* depends on the imaging system and FNTD sensitivity. The energy deposited is

$$\varepsilon = \left(\frac{A}{s}\right)^2 \tag{6.9}$$

and so the lineal energy is

$$y = \frac{1}{l}\left(\frac{A}{s}\right)^2 \tag{6.10}$$

The procedure described above for obtaining the lineal energy applies directly to the lineal energy in Al_2O_3. There needs to be a conversion from the lineal energy in Al_2O_3 to lineal energy in tissue. Tissue equivalent conversion factors have been applied in other detectors that are not tissue equivalent such as silicon-on-insulator microdosimeters (Bradley et.al., 2001 and Wroe, et al., 2007). ICRU 36 recommends applying a conversion factor, ζ, which is the ratio of stopping powers of tissue to the absorbing material. ζ is usually applied to the mean chord length, *l*, i.e.

$$< l >_{Tissue} = \frac{< l >_{Al_2O_3}}{\zeta}. \tag{6.11}$$

Therefore, the tissue equivalent lineal energy can be calculated as

$$y_{Tissue} = \frac{\varepsilon}{< l >_{Tissue}} = \frac{A}{k\sigma_n} W \frac{\zeta}{< l >_{Al_2O_3}} \tag{6.12}$$

or more appropriately

$$y_{Tissue} = \left(\frac{A}{s}\right)^2 \frac{\zeta}{< l >_{Al_2O_3}}. \tag{6.13}$$

Figure 6.32 shows a plot of the energy dependent conversion factor, ζ for both silicon and Al_2O_3 for protons with energies in the range of 0.01 MeV to 10 MeV calculated based on data for tissue, Si and Al_2O_3 from SRIM 2006.

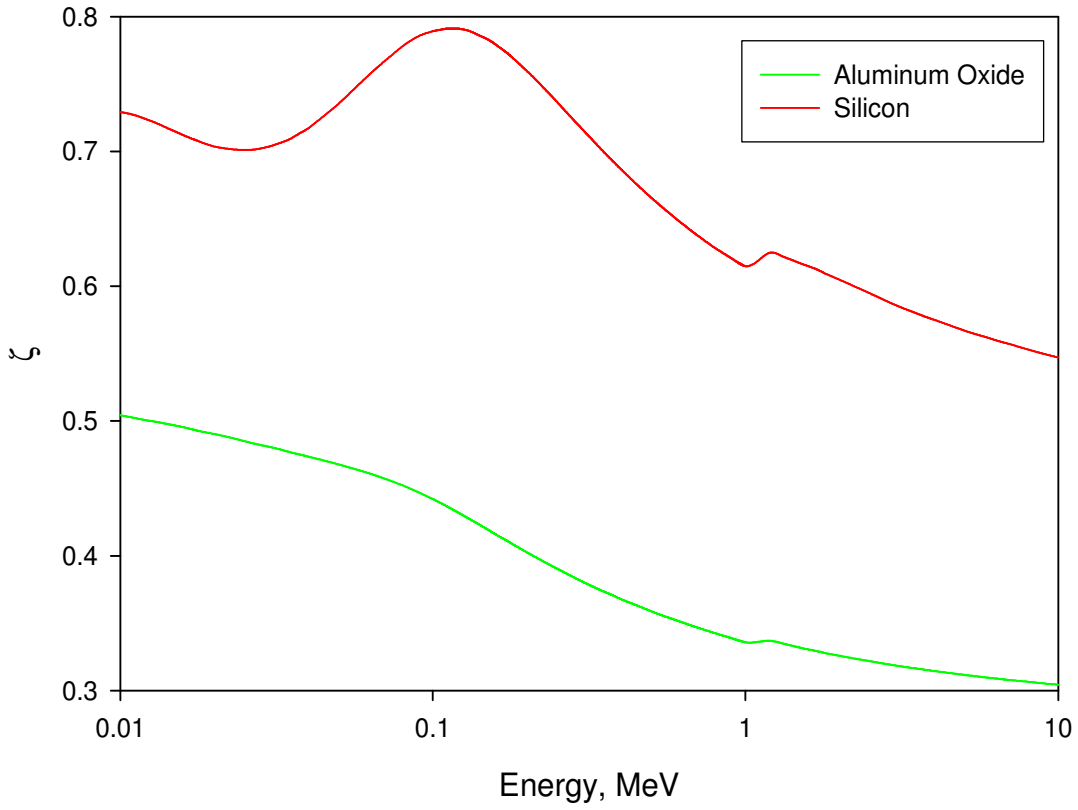

Figure 6.32 Energy dependent tissue equivalent correction factor, ζ for Al_2O_3 (green line) and Si (red line).

6.6.2 Linear energy spectra

Perhaps a more readily available application for FNTDs is the determination of the linear energy spectrum, *Ld*(*L*) (Spurny et al, 1996). The difference between linear energy and lineal energy is that linear energy assumes that the absorbed dose is due to charged particle tracks that travel in a straight line and have constant energy loss in the material (LET assumption) (Rossi and Zaider, 1996). This approach approximates the true interaction events (lineal energy transfer) by using the average value of LET.

Determining the LET of an incident particle can be achieved by measuring the fluorescence amplitude of the track. Fig. 6.9 was used as a calibration to obtain the LET of unknown incident particles. The LET can then be determined and a track frequency histogram can be plotted. The dose, *d(L)* is calculated by equation (2.22). The same can be done for the dose equivalent, *h(L)*, by multiplying by the quality factor, *Q(L),* i.e.

$$h(L) = Q(L)d(L)\,. \tag{6.14}$$

The LET frequency distribution for fragmented ^{12}C ions in 95.03 mm of PMMA is shown in Fig. 6.33 and its corresponding linear energy dose distribution is seen in Fig 6.34. The contribution to the total dose is obtained by integrating the linear energy spectrum. It is obvious that the majority of the dose is delivered by the primary carbon ions. The amount of heavy recoils from the PMMA is small (~0.6% of the total tracks) but the linear energy spectrum shows that they contribute approximately 3.5% to the total dose. In contrast, the amount of fragmented ions is relatively large (~30% of the total tracks) but the actual contribution to the dose is only 2.5%.

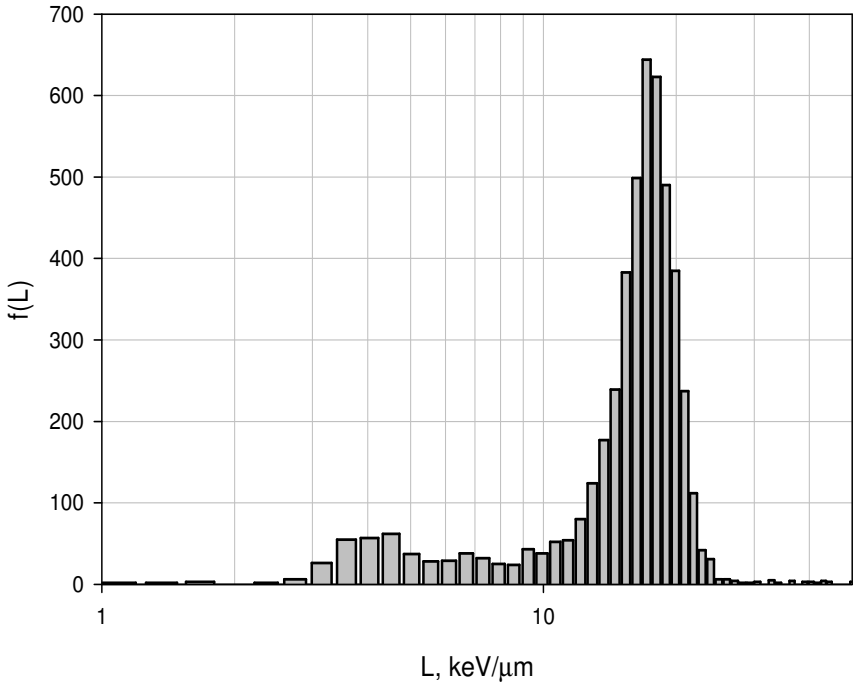

Figure 6.33 LET frequency distribution for FNTDs irradiated with 290 MeV/amu ^{12}C behind 95.03 mm of PMMA. The fluorescence intensity was converted into L using the LET dependence in Fig. 6.9.

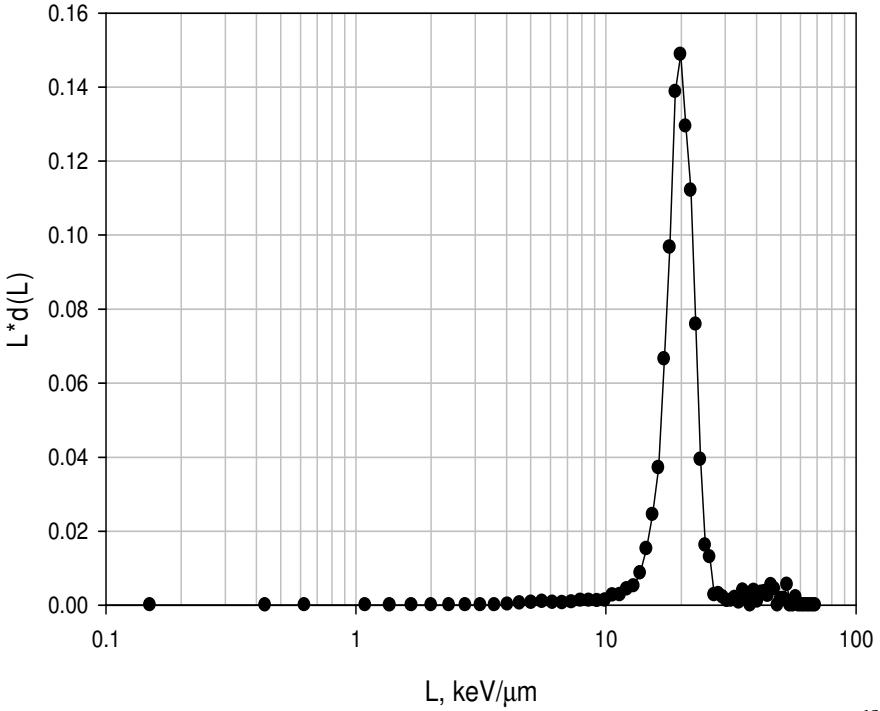

Figure 6.34 Linear energy dose distribution for FNTDs irradiated with 290 MeV/amu ^{12}C behind 95.03 mm of PMMA.

6.6.3 Effect of site size on FNTD data

The effect of site size on the linear energy spectrum obtained from FNTD images was investigated by processing images with squares of different areas to simulate change in site size. The volume of the site was calculated by assuming the focal spot was uniform along the axial depth of focus thus giving a rectangular site. The focal spot was constant at 1.5 μm in the axial direction and the lateral dimensions were varied from 0.5 μm to 4 μm. Images of FNTDs irradiated with 10 mGy of gamma from ^{137}Cs, 5.1 MeV alpha particles and 120 MeV/u ^{56}Fe were processed in this way; the results are presented in Fig. 6.35. Figure 6.36 is a comparison of all three irradiations processed with a 1.5 μm^3 site size. Conversion to actual lineal energy is investigated below.

Microdosimetric analysis of FNTDs irradiated with alpha particles and ^{56}Fe ions demonstrates that increasing site size begins to approximate individual track analysis (measuring fluorescence intensity of individual tracks). As the site size is decreased, the number of low intensity (low LET) events increases. This phenomenon is expected because the probability of multiple energy deposition events per site decreases leading to an overall decrease in energy deposition per site. The integrals of the microdosimetric spectra are expected to remain constant for each specific type of radiation because the total energy deposition in the imaged area is constant.

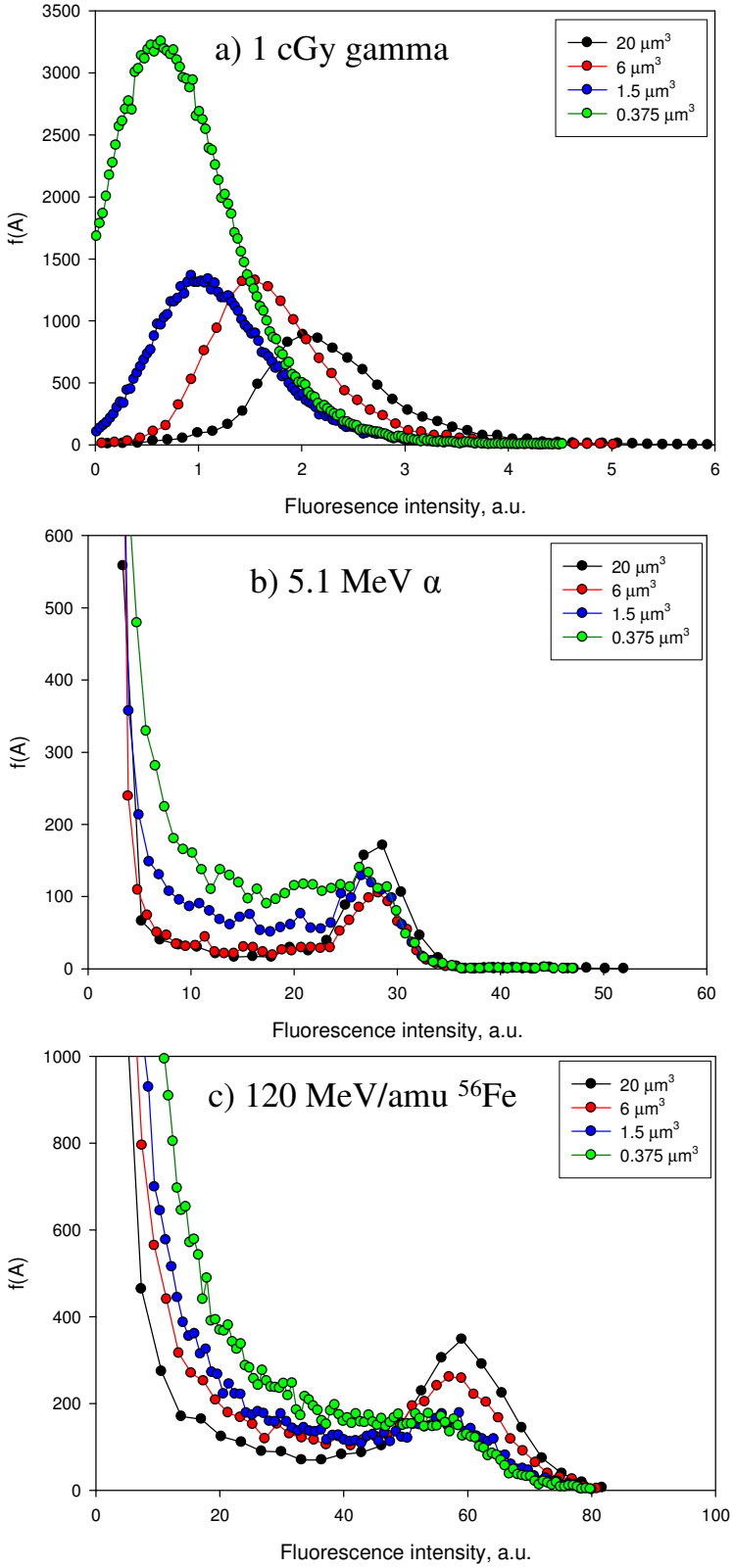

Figure 6.35 Fluorescence intensity spectra with site sizes of 0.375, 1.5, 6 and 20 µm^3 for FNTDs irradiated with a) 1 cGy of gamma from ^{137}Cs, b) 5.1 MeV alpha particles and c) 120 MeV/amu ^{56}Fe.

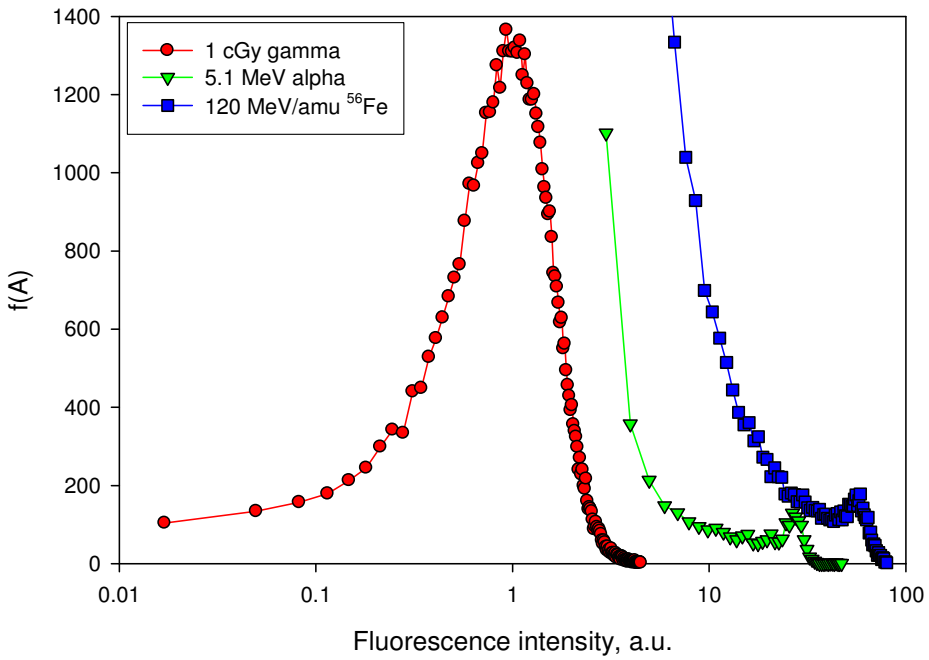

Figure 6.36 Comparison of fluorescence intensity spectra for 1 cGy of gamma (red circles), 5.1 MeV alpha (green triangles) and 120 MeV/amu ^{56}Fe for a site size of 1.5 µm^3.

6.6.4 Comparison of FNTDs with TEPCs

Lineal energy spectra obtained by Dicello, Wasiolek and Zaider (1991) using walled and wall-less tissue-equivalent proportional counters (TEPCs) are presented in Fig. 6.37. Dicello's results from 500 MeV/u Fe using walled (surrounded by a solid shell that shields delta electrons that are generated from outside of the sensitive area) and wall-less (no delta electron shielding) TEPCs were normalized to the total energy deposited (i.e. the integrals of the two spectra are the unity). Data using a wall-less TEPC indicates much higher contribution from low LET secondary delta electrons than its walled counter part as expected. Wall-less detectors approximate the true microdosimetric spectrum much better than walled detectors because they are more similar to actual biological systems where secondary electrons are not shielded.

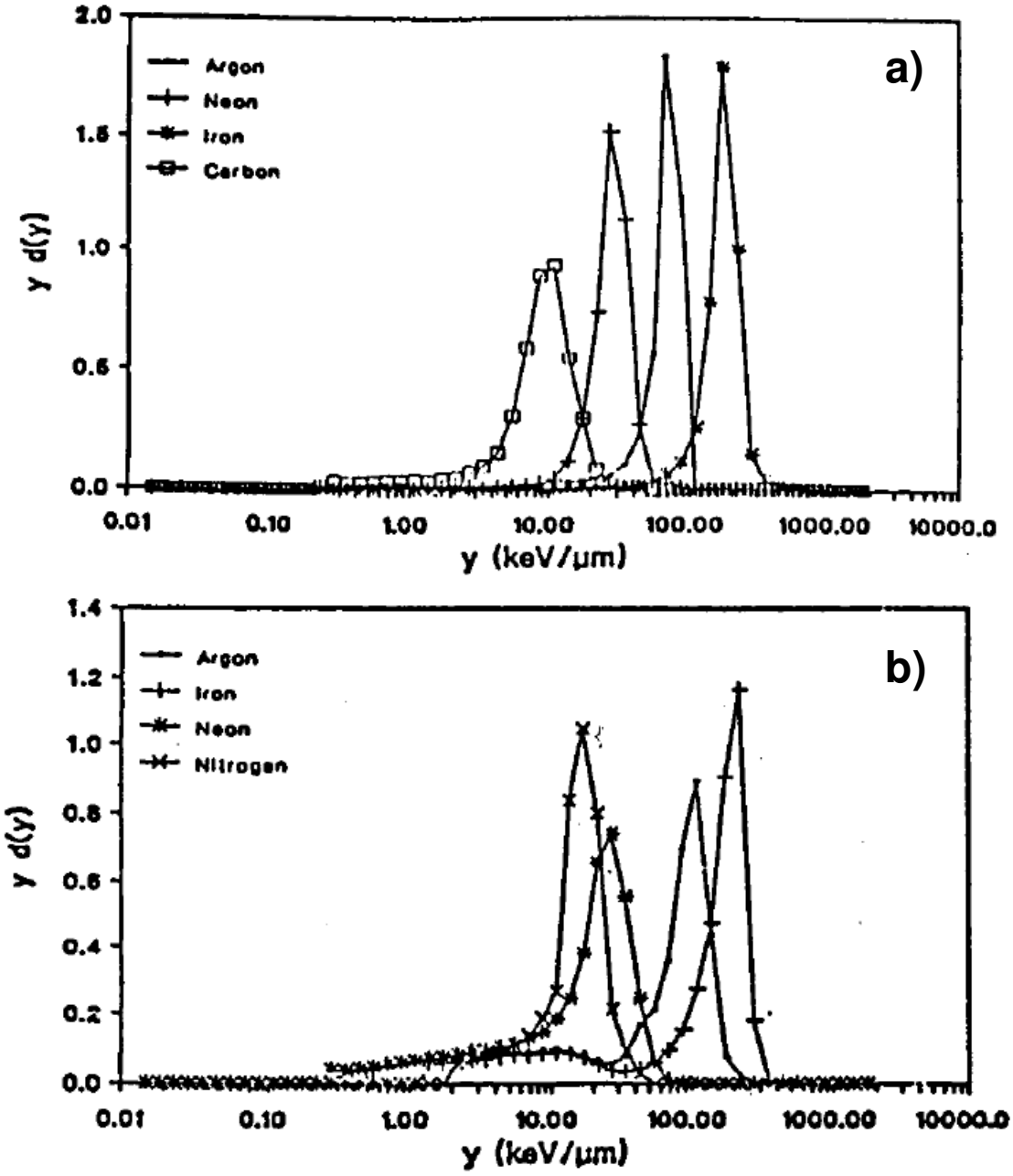

Figure 6.37 Microdosimetric spectra of 570 MeV/u Ar, 535 MeV/u Ne, 500 MeV/u Fe and 400 MeV/u C using a walled TEPC a) and a wall-less TEPC b) (Dicello et al, 1991). The data are normalized to total energy deposited. The contribution from low LET secondary delta electrons is much greater with the wall-less TEPC.

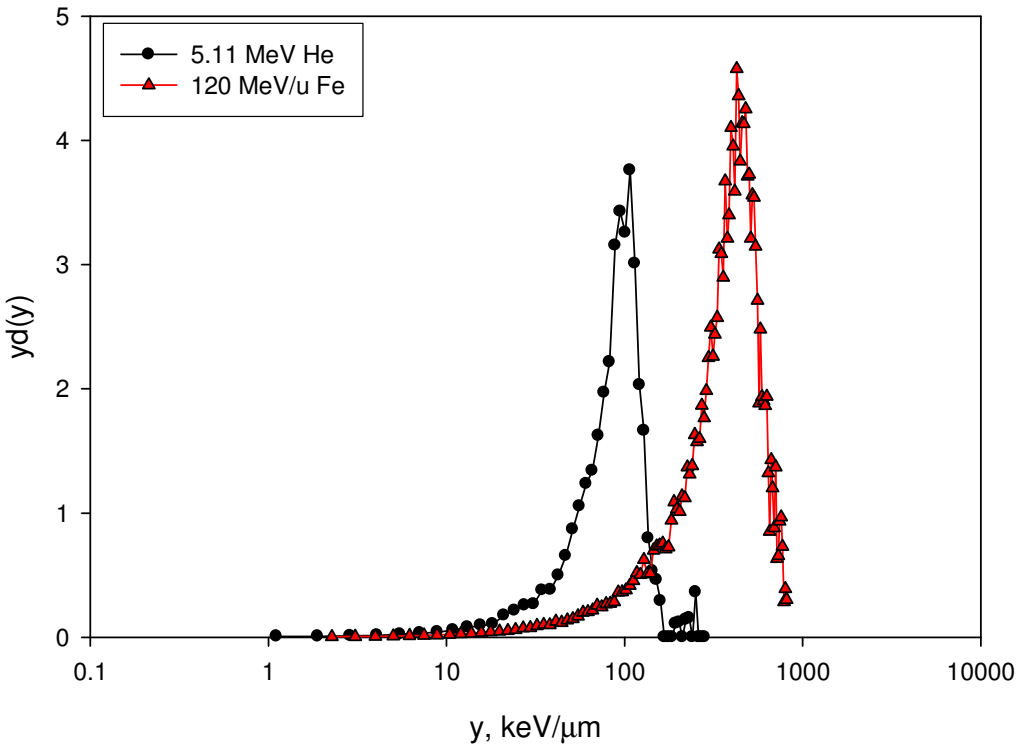

Figure 6.38 Microdosimetric spectra of 5.11 MeV alpha particles and 120 MeV/u Fe using FNTDs processed with a site size = 0.375 μm^3. The lineal energies were calculated using eq. (6.10). The data are normalized to total energy deposited.

Lineal energy spectra in Fig. 6.38 agree well with data obtained by Dicello, Wasiolek and Zaider (1991). Data from FNTDs (Fig. 6.38) are more similar to the walled TEPC data. The contribution from low LET delta electrons is not as apparent in the FNTD data as in the wall-less TEPC data. FNTDs are effectively wall-less detectors because delta electrons are not shielded from any sensitive volume of the detector, so it is expected that their results will agree with the wall-less TEPC more so than the walled, but this is currently not the case. One reason for this is that, presently, FNTDs are "self-shielding" meaning that most delta electrons stop in Al_2O_3:C,Mg before reaching a distance away from the track core greater than the diffraction limited resolution. As resolution is increased, the contribution from secondary delta electrons should become

more apparent. Increasing sensitivity of the FNTD should also make the delta electron contribution more apparent.

FNTDs have four disadvantages that hinder their microdosimetric prospects: 1) tissue equivalence is impossible to achieve using Al_2O_3:C,Mg, 2) the site size is limited by optical constraints (i.e. diffraction limited resolution), 3) they are not sensitive enough to measure single delta electron energy deposition events and 4) multiple deposition events in the same volume of the FNTD will register as one event with energy equal to the sum of the individual deposition events. Tissue equivalence can be accounted for by using the tissue conversion factor eq. (6.11) and there are techniques such as stimulated emission depletion (Hell, 2004) that break the diffraction barrier and allow for resolution of tens of nanometers; other forms of microscopy such as near-field microscopy would also be worth investigating. Sensitivity to single energy deposition events is one of the most challenging problems for FNTD technology to overcome in which more studies of the role of defects in Al_2O_3:C,Mg is needed. As a passive detector, FNTDs cannot overcome the fourth problem presented above; the best solution would again be to increase optical resolution as much as possible to decrease the volume of the site thus decreasing the probability of multiple energy deposition events. Despite the challenges, FNTD technology still appears as a strong candidate for microdosimetry with the ability to not only determine the amount of energy deposited, but also the spatial distribution of energy deposition.

6.7 Conclusions

Since FNTD technology is new and has never before been investigated in detail, it was necessary to determine further courses of study for FNTDs. FNTDs have proven to be effective for multiple applications including HCP spectroscopy (with uses in space dosimetry, radiation therapy, fusion diagnostics and fragmentation cross section determination), radon detection, beta dosimetry, microbeam field imaging and microdosimetry. Our research has opened up a wide variety of new research topics. It is suggested to carry on with the applications discussed above as separate research topics.

HCP spectroscopy was demonstrated by determining the dependence of fluorescence intensity on LET and Z/β for a wide range of ions from H to Xe. Spectroscopic capabilities of this new method were demonstrated for energetic heavy ions of $LET_{\infty}H_2O$ ranging from 0.4 to 8767 keV/μm with no signs of saturation. So far, the biggest problem with the FNTD approach to HCP spectroscopy is its spectral resolution. In order to be effective as an LET spectrometer, the spectral resolution of FNTDs should be improved by at least a factor of 5 to be equivalent to the CR-39 resolution reported by Flesch. The ability of FNTDs to provide multiple parameters (fluorescence intensity, variation of intensity within the track, track width and range) to extract information from fluorescence tracks ought to be exploited. Multi-parameter analysis along with material improvement should improve the LET spectral resolution.

Another suggested detailed study includes continuing investigation into the ability of FNTDs to determine fragmentation cross-sections by first repeating the same irradiations and data processing techniques used by other groups such as Flesch and Ota. The

fragmentation cross-sections of ions incident on Al_2O_3:C,Mg should provide separate data on fragments from the target and fragments from the detector.

The basic physics of track interaction, energy deposition and charge trapping in FNTDs needs to be understood in order to extract their optimal performance. Proton energy dependences (section 6.2) and color center coloration dependences have provided some clues into track formation in FNTDs suggesting two restrictive factors, limited color center concentration which is a material constraint and limited electron-hole pair production which is an energy deposition limitation. Multi-variable analysis of fluorescence intensity, color center concentrations and ionization density of incident radiation ought to provide insight into track formation mechanisms in Al_2O_3:C,Mg.

FNTDs were investigated as a QA detector for proton therapy and microbeam radiation therapy. Large sensitivity to changes in LET make FNTDs good candidates to supplement ionization chamber data in proton therapy. Treatment plans in MRT require doses larger than 100 Gy which FNTDs cannot currently measure, but QA for peak-to-valley dose ratio can be determined at doses well below the saturation level of FNTDs.

Despite the challenges, FNTD technology still appears as a strong candidate for microdosimetry. Insensitivity to single energy deposition events and integration of multiple energy deposition events are the most demanding problems. Studies of the basic physics of Al_2O_3:C,Mg needs to be performed to increase FNTD sensitivity. The best possible solution to limit the observation of multiple energy deposition events would be to increase optical resolution as much as possible to decrease the volume of the site thus decreasing the probability of multiple events in the same volume.

CHAPTER VII

CONCLUSIONS

Fluorescent nuclear track detector technology was developed and investigated as a multi-purpose radiation dosimeter. The goals of this work were to investigate luminescence mechanisms of Al_2O_3:C,Mg, develop new instrumentation for FNTD readout, to perform full characterization of FNTDs for neutron dosimetry and investigate any other possible applications of fluorescence based detectors. The primary objective was to fully develop FNTDs as neutron dosimeters which included solving the problem of determining neutron dose in the presence of large gamma dose.

Development of a new, more useful, neutron dosimeter required investigations into a broad range of topics. In order to create a practical, commercially viable technology, one needs to understand the fundamental properties of the material used as a radiation sensor, namely luminescence characteristics of Al_2O_3:C,Mg and its LET spectroscopic capabilities. As the investigation progressed, several problems presented themselves including interference of gamma induced fluorescence with recoil proton tracks which predicated a study of FNTD response to X-ray and gamma photons. Finding the solution to X-ray and gamma dosimetry with FNTDs opened several avenues to other applications such as beta dosimetry, high dose neutron dosimetry and proton therapy QA. Work on these new applications helped, in turn, to identify and solve some problems related to

neutron dosimetry. For example, a neutron energy correction factor needed to process high doses of neutrons using the image power was obtained from the results of investigations in proton spectroscopy.

Another example of positive feedback between different research topics was investigation of the average intensity of gamma induced fluorescence versus gamma dose. It was found that average fluorescence intensity was a non-linear function of dose. The same nonlinearity was found for the LET dependences of fluorescence intensities of tracks created by heavy charged particles, as well as changes in absorption bands in Al_2O_3:C,Mg after exposure to X-rays.

Radiochromic transformations of optically active defects in Al_2O_3:C,Mg were studied to explain non-linear dose response of FNTDs. Optical spectroscopy provided several key results for understanding electronic processes in Al_2O_3:C,Mg. Important results included the assignment of luminescence centers to particular defects based on results of thermal- and photo-conversion experiments and identifying how those particular luminescence centers change when trapping electrons or holes.

Combining the results from optical spectroscopy, image analyses of photon induced fluorescence, LET dependences, proton energy dependence and alpha track intensity as a function of F_2^{2+}(2Mg) center concentration allowed us to hypothesize that fluorescence intensity is a function of F_2^{2+}(2Mg) center concentration, ionization density and the amount of energy imparted to delta electrons. Both non-linearity and early saturation of fluorescence intensity were explained by assuming F_2^{+}(2Mg) centers act as hole traps rather than electron traps.

Detailed discussions of major conclusions and future work are found in the appropriate chapters. The following is a list of the major accomplishments of this thesis work:

1. Identification and assignments of color centers to excitation/emission bands were performed for single and double oxygen vacancy defects in Al_2O_3:C,Mg as a result of thermal, photochromic and radiochromic transformations.
2. A new laser scanning confocal fluorescence imaging system and image processing routines were developed.
    a. This system exhibited performance sufficient for automatic processing of large numbers of FNTDs at 4 seconds acquisition time per image.
    b. The imaging system was designed for automatic spherical aberration compensation for imaging the crystal at different depths for determining the range and energy of recoil protons.
    c. A cross-correlation technique was implemented for automatic track recognition.
    d. A new image processing technique was developed using spatial frequency analysis for determining doses due to neutrons, photons, betas and heavy charged particles and extending the useful dose range.
3. Several thousand detectors were irradiated and imaged in order to fully characterize FNTDs for neutron dosimetry.
    a. Dose linearity for FNTDs covered with PE, TLD 600 enriched with ^{6}Li, TLD 100 with natural abundances of ^{6}Li and ^{10}B loaded Teflon was shown to cover ~4 orders of magnitude in track counting mode.

b. The new image power parameter was shown to be linearly proportional to dose for all types of radiation tested in this study, most notably neutrons and gamma.

c. Combining track counting and image power allowed for a linear dose range of approximately 6 orders of magnitude for neutron dosimetry.

d. The saturation dose for FNTDs was found to be at least 1000 times greater than that of CR-39.

4. Neutron-gamma separation was accomplished by applying spatial frequency analysis and a dosimeter configuration consisting of an FNTD in contact with two neutron sensitive converters (PE or ^{6}LiF) and a third converter insensitive to neutrons (PTFE). It was demonstrated that:

   a. For higher doses, neutron to gamma ratios of 1 to 3 in terms of dose equivalent (1 to 30 in terms of absorbed dose) can be separated.

   b. Neutron-gamma discrimination is 100% if the total gamma dose is less than 20 mSv because recoil proton tracks are still detectible.

5. The neutron energy dependence of FNTDs covered with PE and ^{6}LiF converters to fast neutrons (E_n > 40 keV) was fully characterized and new procedures for estimating median neutron energies were as follows:

   a. The ratio of track densities between the slow and fast neutron converters demonstrated median energy with 11% error from the published data.

   b. Dose-depth dependences from neutron irradiated FNTDs in both track counting and image power modes demonstrated agreement within 2%

from the published median energy of ^{241}AmBe neutrons and also correctly showed the presence of high energy neutrons in the field.

6. "Blind test" irradiations of FNTDs and other well established neutron and gamma dosimeters were performed in neutron and gamma fields confirming that FNTDs provide reliable results.
7. Capabilities of FNTD technology for heavy charged particle spectroscopy were demonstrated by determining the dependence of fluorescence intensity on LET and Z/β for a wide range of ions from H to Xe.
    a. Spectroscopic capabilities of this new method were demonstrated for energetic heavy ions of $LET_{\infty}H_2O$ ranging from 0.4 to 8767 keV/μm with no signs of saturation.
    b. Bragg peaks were obtained for a total of eight different types of ions using metal wedged absorbers extending the investigated LET range and showing obvious evidence of ion fragmentation.
    c. FNTDs showed promising results for use in fragmentation studies.
8. FNTDs were used to image X-ray microbeam radiation with high spatial resolution where peak to valley dose ratios, the width of the microbeam and center to center distances were determined using fluorescence intensity distributions.
9. Preliminary investigations of FNTD technology for microdosimetry, proton therapy, microbeam diagnostics, accident dosimetry, charged particle spectroscopy for inertial confinement fusion and space dosimetry demonstrate that FNTDs can be applied in many fields requiring passive radiation dosimetry.

Fluorescent nuclear track detector technology has proven to be a versatile radiation detection tool with applications in every major radiation field. As a result of the studies presented in this thesis, the most immediate application for FNTD technology is neutron dosimetry as it is nearly ready for national accreditation. The results of this investigation can be of particular importance to radiobiology, radiotherapy, space dosimetry and nuclear reaction diagnostic experiments.

The readout process of FNTDs is completely optical and non-destructive, allowing for multiple readouts of the same detector. Detectors are reusable after optical bleaching. FNTDs also allow for fast automatic scanning and dose determination. The most deficient problem with using FNTDs for neutron dosimetry was gamma induced signal interfering with neutron induced tracks which was successfully solved. The essential characteristics of neutron dosimeters (dose linearity, dosimeter configuration, energy dependence, angular dependence and neutron-gamma discrimination) were thoroughly tested. Key additions of this work to FNTD technology included neutron-gamma separation, methods to estimate median neutron energy and the extension of dynamic dose range to cover approximately 6 orders of magnitude.

REFFERENCES

Akselrod, M.S., Lucas, A.C., Polf, J.C. and McKeever, S.W.S., (1998) Optically stimulated luminescence of Al_2O_3. *Radiat. Meas*. **29**, 391-399.

Akselrod, M. S. and Mckeever, S. W. S. (1999). A radiation dosimetry method using pulsed optically stimulated luminescence. *Radiat. Prot. Dosim*. **81**, 167-176.

Akselrod, M. S. (2003a). Recording of holographic gratings in photochromic Al_2O_3:C,Mg crystals. *Proc. Of SPIE* **5069**, 258-263.

Akselrod, M. S., Akselrod, A. E. Orlov, S.S. Sanyal, S., and Underwood, T.H. (2003b). New aluminum oxide single crystals for volumetric optical data storage. *Proc. Of SPIE* **5069,** 244-246.

Akselrod, M. S., Akselrod, A. E. Orlov, S.S. Sanyal, S., and Underwood, T.H. (2003c). Fluorescent Aluminum Oxide Crystals for Volumetric Optical Data Storage and Imaging Applications. *J. of Fluorescence*, **13** (6), 503-511.

Akselrod, M. S, Orlov, S. S. and Akselrod, G.M. (2004). Effect of anisotropy, color center concentration and recording parameters on volumetric optical data storage in aluminum oxide single crystal media. *Proc. of SPIE* **5380**, 320-327.

Akselrod, G. M., Akselrod, M. S., Benton, E. R, and Yasuda, N., (2006a) A Novel Al_2O_3 Fluorescent Nuclear Track Detector for Heavy Charged Particles and Neutron*., Nucl. Instr. Meth. B* **247,** 296-306.

Akselrod, M. S., Yoder, R. C., and Akselrod, G. M., (2006b) Confocal Fluorescent Imaging of Tracks from Heavy Charged Particles Utilizing New Al_2O_3:C,Mg crystals. *Rad. Prot. Dosim*. **119** (1-4), 357-362.

Akselrod, M. S. and Akselrod, A. E., (2006c). New Al_2O_3:C,Mg crystals for radiophotoluminescent dosimetry and optical imaging of tracks produced by heavy charge particles. *Rad. Prot. Dosim*. **119** (1-4), 218-221.

Attix, F.H.(1986) *Introduction to Radiological Physics and Radiation Dosimetry*. John Wiley & Sons, Inc., NJ.

Bartlett, D.T., (2008). 100 years of solid state dosimetry and radiation protection dosimetry. *Radiat. Meas.* **43**, 133-138.

Benton, E.R. and Benton, E.V. (2001). Space radiation dosimetry in low-Earth orbit and beyond. *Nucl. Instr. and Meth. B* **184**, 255-294.

Benton, E.R., Benton, E.V. and Frank, A.L. (2001). Neutron dosimetry in low-Earth orbit using passive detectors. *Radiat. Meas*. **33**, 255-263.

Benton, E.V., Ogura, K., Frank, A.L., Atallah, T.M. and Rowe, V. (1986). Response of different types of CR-39 to energetic ions. *Nuclear Tracks* **12**, 79-82.

Bøtter-Jensen, L., McKeever, S.W.S, Wintle, A.G., (2003). *Optically Stimulated Luminescence Dosimetry*. Elsevier, Amsterdam.

Boukharaouba, N., Bateman, F.B., Brient, C.E., Carlson, A.D., Grimes, S.M., Haight, R.C., Massey, T.N., and Wasson, O.A.. (2001). Measurement of the n-p elastic scattering angular distribution at E_n=10 MeV. *Phys. Rev. C* **65** 014004.

Bradley, P.D., Rosenfeld, A.B., Zaider, M., (2001). Solid state microdosimetry. *Nucl. Instr. Meth. B* **184**, 135-157.

Bramblett, R.L., Ewing, R.I. and Bonner, T.W., (1960) A new type of neutron spectrometer. *Nucl. Instr. and Meth.*. **9**, 1-12.

Brauer-Krisch, E., Siegbahn, E.A. and Bravin, A., (2005). Gafchromic film measurements of microbeam radiation therapy (MRT). *IFMBE Proc*. **25**, 174-177.

Brauer-Krisch, E, Requardt, H., Brochard, T., Berruyer, G., Renier, M., Laissue, J.A. and Bravin, A., (2009). New technology enables high precision mulitslit collimators for microbeam radiation therapy. *Rev. Scien, Instr.* **80** published online DOI: 10.1063/1.3170035.

Brewer, J.D., Jeffries, B.T. and Summers, G.P., (1980). Low-temperature fluorescence in sapphire. *Phys. Rev*. *B* **22**, 4900-4906.

Butts, J.J. and Katz, R. (1967) Theory of RBE for heavy ion bombardment of dry enzymes and viruses. *Radiat. Res*. **30**, 855-871.

Chatterjee, A., and H. J. Schaefer. (1976) Microdosimetric structure of heavy ion tracks in tissue. *Radiat. Environ. Biophys.* **13**, 215–227.

Cooley, J.W. and Tukey, J.W. (1965) An algorithm for the machine calculation of complex Fourier series. *Math. Comput*. **19**, 297-301.

Cucinotta, F.A., Katz, R., Wilson, J.W., Dubey, R.R., (1996). Radial dose distributions in the delta-ray theory of track structure. *AIP conference proceedings.* **362**, 245-265

Diaspro, A. (Ed.), (2002). *Confocal and two-photon microscopy: Foundations, applications, and advances*, Wiley, New-York.

Dicello, J.F., Wasiolek, M. and Zaider, M. (1991). Measured microdosimetric spectra of energetic ion beams of Fe, Ar, Ne and C: limitations of LET distributions and quality factors in space research and radiation effects. *Trans. on Nucl. Sci*. **38**, 1203-1209.

Evaluated Nuclear Data File (ENDF) Retrieved June 2009 from http://www-nds.iaea.org/exfor/endf.htm

Evans, B.D. and Stapelbroek, M., (1978). Optical properties of the F^+ center in crystalline Al_2O_3. *Phys. Rev. B* **18**, 7089-7098.

Evans, B.D., Pogatshnik, G.J. and Chen, Y., (1994). Optical properties of lattice defects in α- Al_2O_3. *Nucl. Instr. and Meth. B*, **91**, 258-262.

Evans, B.D., (1995). A review of the optical properties of anion lattice vacancies and electrical conduction in α- Al_2O_3: their relation to radiation-induced electrical degradation. *J. of Nuc. Mater*. **219**, 202-223.

Flesch, F., Hirzebruch, S.E., Huntrup, G., Roecher, H., Streibel, T., Winkel, E. and Heinrich, W., (1999). Fragmentation cross section measurements of iron projectiles using CR-39 plastic nuclear track detectors. *Radiat. Meas*. **31**, 533-536.

Fowler, W.B., (1968). *Physics of Color Centers*. Academic Press, New York, NY.

Golovchenko, A.N., Skvarc, J., Yasuda, N., Ilic, R., Tretyakova, S.P., Ogura, K., Murakami, T., (2001). Total charge-changing and partial cross-section measurements in the reaction of 110 MeV/u ^{12}C with paraffin. *Radiat. Meas.* **34**, 297-300.

Goodhead, D.T. (2006). Energy deposition stochastics and track structure: what about the target?. *Radiat. Prot. Dosim*. **122**, 3-15.

Harrison, J.D. and Streffer, C., (2007). The ICRP protection quantities, equivalent and effective dose: their basis and application. *Radiat. Prot. Dosim*. **127**, 12-18.

Hell, S.W. (2004). Strategy for far-field optical imaging and writing without diffraction limit. *Phys. Lett. A* **326**, 140-145.

Henderson, B. and Imbusch, G.F. (1989) *Optical Spectroscopy of Inorganic Solids*. Oxford University Press, Oxford.

Howard-Flanders, P., (1958). Physical and chemical mechanisms in the injury of cells by ionizing radiations. *Adv. Biol. Med. Phys*. **6**, 553–603.

Howell, R.M, Ferenci, M.S., Hertel, N.E., Fullerton, G.D., Fox, T. and Davis, L.W., (2005) Measurements of secondary neutron dose from 15 MV and 18 MV IMRT. *Radiat. Prot. Dosim.,* **115**, 508-512.

Huang, K. and Rhys, A., (1950). Theory of light absorption and non-radiative transitions in F-centres. *Proc. of Royal Soc. of London A*, **204**, 406-423.

ICRP. 1990 Recommendations of the International Commission on Radiological Protection. Technical Report 60, International Commission on Radiological Protection, Oxford, UK.

ICRU Report 36, (1983). Microdosimetry. International Commission of Radiation Units and Measurements, Betheda, MD.

Katz, R. (1978). Track structure theory in radiobiology and radiation protection. *Nucl. Track Detect*. **2**, 1-28.

Kellerer, A.M., and Hahn, K., (1988) Considerations on a revision of the quality factor. *Rad. Res*. **114**, 480-488.

Kiefer, J., and H. Straaten.(1986) A model of ion track structure base on classical collision dynamics. *Phys. Med. Biol.* **31**, 1201–1209,

Knoll, G.F. (2000). *Radiation detection and measurement* 3rd ed. John Wiley & Sons, Inc., NJ.

Kobetich, E. J., and R. Katz. (1968) Energy deposition by electron beams and delta rays. *Phys. Rev.* **170**, 391–396.

Kry, S.F., Salehpour, M, Followill, D.S., Stovall, M., Kuban, D.A., White, R.A., Rosen, I.I. (2005). Out-of-field photon and neutron dose equivalents from step-and-shoot intensity-modulated radiation therapy. *Radiation Oncology Biol. Phys*. **62**, 1204-1216.

Kulis, P.A., Springis, M.J., Tale, I.A., Vainer, V.S. and Valbis, J.A. (1981). *Phys. Status Solidi B* **104**, 719.

La, S.Y., Bartram, R.H. and Cox, J., (1973) The F^+ center in reactor-irradiated aluminum oxide. *J. Phys. and Chem. of solids.* **34**, 1079-1086.

Lee, K.H. and Crawford, J.H., (1979) Luminescence of the F-center in sapphire. *Phys. Rev. B* **15**, 3217-3221.

Marino, S. (2009) Private communication.

Martynovich, E.F., Baryshnikov, V.I. and Grigorov, V.A., (1985) Room-temperature lasing the visible region on color centers in Al_2O_3. *Sov. Tech. Phys. Lett*. **11**, 81.

Milster, T.D., Upton, R.S. and Luo, H., (1999). Objective lens design for multiple-layer optical data storage. *Opt. Eng*. **38**, 295-301.

Mitchell, E.W.J., Rigden, J.D. and Townsend, (1960). *Philos. Mag*. **5**, 1013-1027.

Nikjoo, H., Uehara, S., Emfietzoglou, D., Cucinotta, F.A., (2006). Track-structure codes in radiation research. *Radiat. Meas*. **41**, 1052-1074.

Ogura, K., Asano, M., Yasuda, N. and Yoshida, M., (2001) Properties of TNF-1 track etch detector. *Nucl. Instr. and Meth. B,* **185**, 222-227.

Olsher, R. H., McLean, T. D., Mallett, M. W., Seagraves, D. T., Gadd, M. S., Markham, R. L., Murphy, R. O., Devine, R.T. (2007). Characterization of neutron reference fields at US department of energy calibration fields. *Radiat. Prot. Dosim*. **126**, 52-57.

Ota, S., Kodaira, S., Yasuda, N., Benton, E.R., Hareyama, M., Kurano, M., Sato, M., Shu, D. and Hasebe, N., (2008) Tracking method for the measurement of projectiles charge changing cross-section using CR-39 detector with a high speed imaging microscope. *Rad. Meas*. **43**, 195-198.

Pogatshnik, G.J., Chen, Y. and Evans, B.D., (1987) A model of lattice defects in sapphire. *Trans. on Nucl. Sci*., **34**, 1709-1712.

Ramirez, R., Tardio, M., Gonzalez, R., Chen, Y. and Kokta, M.R., (2005) Photochromism of vacancy-related defects in thermochemically reduced α-Al_2O_3:Mg single crystals. *Appl. Phys. Lett*. **86**.

Ramirez, R., Tardio, M., Gonzalez, R., Munoz Santiuste, J.E. and Kokta, M.R., (2007) Optical properties of vacancies in thermochemically reduced Mg-doped sapphire single crystals. *J. Appl. Phys*. **101**.

Reitz, G. (2006) Past and future application of solid-state detectors in manned spaceflight. *Radiat. Prot. Dosim*. **120**, 387-396.

Rossi, H.H. and Rosenzweig, W. (1955) Measurements of neutron dose as a function of linear energy transfer. *Rad. Res*. **2**, 417-425.

Rossi, H.H., Zaider, M. (1991) Elements of microdosimetry. *Med. Phys*. **18**, 1085-1092.

Rossi, H.H., Zaider, M., (1996) *Microdosimetry and Its Applications*. Springer-Verlag, Berlin.

Russ, J.C. (2007) *The Image Processing Handbook* 5th ed. CRC Press, Boca Raton.

Salasky, M. (2006 and 2008) Private communication.

Santa Cruz, G.A., Palmer, M.R., Matatagui, E., Zamenhof, R.G. (2001a) A theoretical model for event statistics in microdosimetry. I: Nonuniform distribution of heavy ion tracks. *Med. Phys*. **28**, 988-996.

Sanyal, S. and Akselrod, M.S. (2005). Anisotropy of optical absorption and fluorescence in Al_2O_3:C,Mg crystals. *J. Appl. Phys*. **98**, 033518.

Sawakuchi, G. O. (2008) Characterization and modeling of relative luminescence efficiency of optically stimulated luminescence detectors exposed to heavy charged particles. *Ph.D. Dissertation*. Oklahoma State University.

Seguin, F.H, Frenje, J.A., Li, C.K., Hicks, D.G., Kurebayashi, S., Rygg, J.R., Schwartz, B.E., Petrasso, R.D., Roberts, S., Soures, J.M., Meyerhofer, D.D., Sangster, T.C., Knauer, J.P., Sorce, C., Glebov, V.Yu, Stoeckl, C., Philips, T.W., Leeper, R.J., Fletcher, K. and Padalino, S. (2002). Spectrometry of charged particles from inertial-confinement-fusion plasmas. *Rev. Sci. Instrum*. **74**(2), 975-995.

Springis, M.J. and Valbis, J.A. (1985). *Phys. Status Solidi B* **132**, K61.

Spurny, R., Bednar, J., Johansson, L., Saetherberg, A., (1996). LET spectra of secondary particles in CR 39 track etch detectors. *Radiat. Meas*. **26**, 645-649.

Stabin, M. (2006) Nuclear medicine dosimetry. *Phys. Med. Biol*. **51**, 187-202.

Stepanov, B.I. and Gribkovskii, V.P. (1968) *Theory of Luminescence*. London.

Sykora, G.J., Akselrod, M.S., Salasky, M., Marino, S.A., (2007). Novel Al2O3:C,Mg fluorescent nuclear track detectors for passive neutron dosimetry. *Radiat. Prot. Dosim.* **126**, 278-282.

Sykora, G.J., Akselrod, M.S., Benton, E.R., Yasuda, N. (2008a) Spectroscopic properties of novel fluorescent nuclear track detectors for high and low LET charged particles. *Radiat. Meas*. **43**, 422-426.

Sykora, G.J., Akselrod, M.S., Salasky, M., (2008b) Properties of novel fluorescent nuclear track detectors for use in passive neutron dosimetry. *Radiat. Meas*. **43**, 10017-1023.

Sykora, G.J., Akselrod, M.S. and Vanharave, F, (2009) Performance of fluorescent nuclear track detectors in monoenergetic and broad spectrum neutron fields. *Radiat. Meas.* **44**, 988-991.

Suit and Urie, (1992). Proton beams in radiation therapy. *J. Nucl. Cancer Institute* **84**, 155-164.

Tardio, M., Ramirez, R., Gonzalez, R., Chen, Y. and Kokta, M.R., (2003) Photochromic effect in magnesium-doped α- Al_2O_3 single crystals. *Appl. Phys. Lett*. **83**, 881-883.

Tippins, H.H., (1970). Charge-transfer spectra of transition-metal ions in corundum. *Phys. Rev. B* **1**, 126-135.

Vij, D.R. (1998) *Luminescence of Solids*. Plenum Press, New York.

Waligorski, M.P.R., Hamm, R.N. and Katz, R. (1986). The radial distribution of dose around the path of a heavy ion in liquid water. *Nucl. Tracks and Radiat. Meas.* **11**, 309-319.

Walker, A.J. (2006). Techniques for radiation measurements: microdosimetry and dosimetry. *Radiat. Prot. Dosim*. **122**, 369-373.

Welch, L.S., Hughes, A.E. and Pells, G.P., (1980). Polarised luminescence of an aggregate defect centre in Al_2O_3. *J. Phys. C* **41**, 533-536.

Wilks, R.S., Desport, J.A. and Smith, J.A.G. (1967). *J. Nucl. Mater*. **24**, 80.

Wroe, A., Rosenfeld, A., Reinhard, M., Pisacane, V., Ziegler, J., Nelson, M., Cucinotta, F., Saider, M., Dicello, J. (2007). Solod state microdosimetry with heavy ions for space applications. *IEEE Transactions on nuclear science*, **54**, 2264-2271.

Yukihara, E.G., Mittani, J.C, Vanhavere, F. and Akselrod, M.S. (2008) Development of new optically stimulated luminescence (OSL) neutron dosimeters. *Radiat. Meas.***43**, 309-314.

Zeitlin, C., Guetersloh, S.B., Hilbronn, L.H. and Miller, J. (2006) Measurements of materials shielding properties with 1 GeV/nuc ^{56}Fe. *Nucl, Instr. and Meth. B.* **252**, 308-318.

Zhang, C. X., X. W. Liu, M. F. Li, and D. L. Luo (1994) Numerical calculation of the radial distribution of dose around the path of a heavy ion. *Radiat. Prot. Dosim.* **52**, 93–96.

Ziegler, J.F., Biersack, J.P., Littmark, U., 2003. The Stopping and Range of Ions in Solids. Pergamon Press, New York. http://www.srim.org/

VITA

Garrett Jeffrey Sykora

Candidate for the Degree of

Doctor of Philiosophy

Dissertation: PHOTO- AND RADIOCHROMIC TRANSFORMATIONS IN Al_2O_3:C,Mg FLUORESCENT NUCLEAR TRACK DETECTORS AND HIGH RESOLUTION IMAGING OF RADIATION FIELDS

Major Field: Physics

Biographical:

Personal:

Born in Omaha, NE, United States on April 08, 1983.

Education:

Received Bachelor of Science in Physics from Creighton University in Omaha, Nebraska, United States in May 2004. Completed the requirements for the Doctor of Philosophy in Physics at Oklahoma State University, Stillwater, Oklahoma in May, 2010.

Experience:

Undergraduate research assistant at Creighton University, United States 2002-2004. Physics teaching assistant at Creighton University, United States, Summer 2003 and 2004. Physics recitation teaching assistant at Oklahoma State University, United States, Fall 2004. Graduate research assistant at Oklahoma State University, United States in conjunction with Landauer, Inc. 2004-2010.

Name: Garrett Jeffrey Sykora Date of Degree: May, 2010

Institution: Oklahoma State University Location: Stillwater, Oklahoma

Title of Study: PHOTO- AND RADIOCHROMIC TRANSFORMATIONS IN Al_2O_3:C,Mg FLUORESCENT NUCLEAR TRACK DETECTORS AND HIGH RESOLUTION IMAGING OF RADIATION FIELDS

Pages in Study: 270 Candidate for the Degree of Doctor of Philosophy

Major Field: Physics

Scope and Method of Study: The goal of this work was to develop fluorescent nuclear track detectors (FNTD) based on aluminum oxide doped with carbon and magnesium (Al_2O_3:C,Mg) as a multi-purpose radiation detection technology. The study focused on the optical properties of Al_2O_3:C,Mg as well as on the dosimetry of neutrons and mixed neutron-gamma fields utilizing a high resolution imaging system built as part of this research. A detailed investigation of optical properties using optical absorption and photoluminescence spectroscopy, radiation interaction in the sensitive volume, dose and energy response to different types of radiation and new applications of FNTDs was performed. This work demonstrated progress in all aspects of FNTD technology including basic material research, instrumentation development, new data and image processing, and characterization of FNTDs in multiple radiation fields including neutrons, gammas, X-rays, betas and heavy charged particles.

Findings and Conclusions: Identification and assignment of color centers to excitation/emission bands were performed for single and double oxygen vacancy defects in Al_2O_3:C,Mg as a result of thermal, photochromic and radiochromic transformations. A new laser scanning confocal fluorescence imaging system and image processing routines were developed exhibiting performance sufficient for automatic processing of large numbers of FNTDs at an acquisition time of 4s per image. A new image processing technique was developed using spatial frequency analysis which was shown to be linearly proportional to dose for all types of radiation tested in this study, most notably neutrons and gamma. Neutron-gamma separation was accomplished by applying spatial frequency analysis and a dosimeter configuration consisting of an FNTD in contact with two neutron sensitive converters (polyethylene or ^{6}LiF) and a third converter insensitive to neutrons (polytetrafluoroethylene). Investigations of FNTD technology for charged particle spectroscopy, microdosimetry, proton therapy, microbeam radiation therapy, accident dosimetry, fusion diagnostics and space dosimetry demonstrate that FNTDs can be applied in many fields requiring passive radiation dosimetry.

ADVISER'S APPROVAL: Dr. Mark Akselrod